Microstructural Changes as a Time Temperature Indicator in Cobalt Superalloys and a NiCoCrAlTaY coating

by

David L Oates

Institute of Polymer Technology and Materials Engineering
Loughborough University

Submitted in partial fulfilment of the requirements for
the award of Doctor of Philosophy

July 2007

Acknowledgements

I would like to sincerely thank my supervisor, Professor Rachel Thomson, for her guidance and support throughout the course of my PhD studies.

I am grateful to RWE npower for their sponsorship and to Dr Jonathan Wells, my industrial mentor, for his important contributions to my work and his constant support.

I am indebted to Dr Geoff West for the work carried out on my behalf on the FIB SEM, TEM and PEELS and to Mr John Bates for the early TEM work.

I would also like to sincerely thank Kath, Matthew and Robert for their tolerance, encouragement and support.

All negatives are positives

(Professor Rachel Thomson 2005)

Abstract

Gas turbines in power generation systems use both nickel and cobalt-based superalloys for vanes, blades, discs and combustion chamber components. Cobalt-based superalloys have the advantage over nickel based superalloys in that they have a higher thermal conductivity and hence a greater thermal shock resistance, a greater resistance to thermal fatigue and also a better corrosion resistance. However, in some applications coatings have to be applied to such alloys because of their poor oxidation resistance. The creep strength of cobalt-based superalloys depends primarily on solid solution strengthening and the interaction between the hard carbides and alloy defects, such as dislocations and stacking faults.

There is a need to develop an understanding of the microstructural changes that occur in cobalt-based superalloys, with both time and temperature, for life prediction, refurbishment and failure investigations.

A programme to assess the effects of ageing at temperatures between 800 and 1050°C for up to 25,000 hours has been carried out on two cobalt-based superalloys, FSX 414 and MAR M509, and one high cobalt (~19 wt.%) nickel based superalloy NP 222. A second programme using the same ageing conditions has investigated a NiCoCrAlTaY coating, Amdry 997, on a MAR M509 cobalt superalloy substrate both with and without inter-carbidic oxidation.

For the three superalloys, a number of microstructural features were examined systematically with increasing time and temperature exposure. These included determination of the identity and amount of the second phases present within the microstructure, characterised using optical, scanning and transmission electron microscopy and X-ray diffraction of extracted carbides. It was therefore possible to determine microstructural maps as a function of increasing thermal exposure. In particular, measurements of the width of the denuded/oxidised layers on the exposed surfaces of the samples showed a reasonable trend and could be used to predict operating temperature or time. In addition, for FSX 414 the presence of Laves and σ phase would allow the prediction of a maximum operating temperature, whereas the length of η phase needles, which form in NP 222, would allow the prediction of operating temperature or time. For NP 222, the reduction in the measured mean hardness between 800 and 950°C could provide a coarse prediction of operating temperature but would also require detailed examination of the microstructure to confirm that the samples additionally contained γ'.

Thermodynamic predictions were used to correlate the phases predicted to be present at thermal equilibrium with the microstructural observations. Current thermodynamic equilibrium software packages include cobalt but are not optimised for cobalt-based superalloys. However, by using a nickel superalloy thermodynamic database it has been possible to compare the equilibrium predictions with the phases found in the samples.

The results obtained, using the JMatPro software, did in the majority of cases, predict the phases formed and in general did predict the composition of the phases. However, there were

some discrepancies between the identity of the predicted thermodynamic equilibrium phases and the phases found within the samples. The thermodynamic equilibrium calculations were also used to provide a useful insight into the diffusion of key elements in the coated samples.

The aged, coated samples showed that the presence of inter-carbidic oxidation (ICO) in the MAR M509 substrate local to the coating reduced coating life, measured by the presence of β (NiAl), by approximately one third. Measurements of the aluminium diffusion profile in the coating and the MAR M509 substrate showed no significant differences between the 'ICO' and 'no ICO' samples that would account for the reduced life of the 'ICO' samples. However, selected area diffraction patterns obtained using transmission electron microscopy in conjunction with site specific sample preparation, confirmed the presence of an alumina layer around the 'ICO' phase. It is considered that the increased diffusion of aluminium from the coating is a result of the formation of the alumina layer around the 'ICO' phase. The investigation of the coating on the MAR M509 substrate without 'ICO' showed that β was still evident in the coating after 25,000 hours at 800°C. At ageing temperatures above 800°C coating life reduced to less than 15,000 hours at 850-900°C. Measurement of the width of the inner denuded layer formed in the coating adjacent to the MAR M509 substrate showed a relationship with time and could be used to predict the operating temperature, given a known operating history.

For the cobalt superalloys further work is required to identify the effects of composition variations within the specified alloy limits on the formation of secondary phases in FSX 414 and the growth of η needles in NP 222. The samples in this work were aged at a constant temperature, and therefore the effect of thermal cycling and composition on the width of the denuded/oxidised layer requires further investigation. This research has generated a large amount of data and has identified a number of areas where a correlation exists between the microstructural observations and the time and temperature experienced, and has demonstrated the potential for some of these features to be used as a "time temperature indicator"

Table of Contents

List of Figures

List of Tables

1 Introduction

In its simplest form the gas turbine system consists of three main sections: a compressor, a combustor and a turbine. In operation, air is drawn into the compressor which increases the air pressure and air temperature. The compressed air is transferred to the combustion chamber where it is mixed with the fuel and burnt at a constant pressure. The hot high pressure gases leave the combustion chamber and are expanded through the turbine to produce mechanical power. This power is used to drive the compressor, turbine auxiliaries and the electrical generator which produces electrical energy. The low pressure gases then leave the turbine exiting to atmosphere. Most of the early machines were aero derivatives used by power generators for limited peak power generation. Typical efficiency values for the simple cycle are ~39%, increasing to ~59% in the combined cycle gas turbine (CCGT). In the CCGT the hot exhaust gases from a power generating gas turbine are used to raise steam in a heat recovery steam generator (HRSG). The steam from the HRSG is used to drive a steam turbine to generate electrical power or for process heating.

The major factor determining the thermal efficiency of a CCGT is the turbine inlet temperature which is limited by the availability of materials with high temperature strength and oxidation/corrosion resistance at the turbine operating temperature. In the current industrial gas turbines the inlet temperature is typically 1260°C to 1300°C, and the bulk metal temperature of the first stage vanes, typically 800°C, is dependant on the amount of cooling air used. The current programme of work is primarily concerned with cast cobalt-based superalloys used for first stage gas turbine vanes.

Cobalt-based superalloys have the advantage over nickel based superalloys in that they have a higher thermal conductivity and hence a greater thermal shock resistance and greater resistance to thermal fatigue. Cobalt-based superalloys also have a better corrosion resistance. However, in some applications coatings have to be applied to components because of the poor oxidation resistance of the cobalt-based superalloys. The cobalt superalloys are strengthened by carbide precipitation. Primary carbides form at grain boundaries during solidification, which inhibit grain boundary sliding, whereas fine secondary carbides, precipitated during ageing or service at elevated temperature, pin dislocations and harden the alloy matrix and contribute to strengthening.

The creep strength of cobalt-based superalloys depends primarily on solid solution strengthening and the interaction between hard carbides and alloy imperfections such as dislocations and stacking faults. Cobalt-based superalloys lack a precipitation hardening mechanism to match the $\gamma'(Ni_3Al)$ strengthening found in the nickel based superalloys and, as a result cobalt-based superalloys are used for stationary components in gas turbines.

There is a need to develop an understanding of the microstructural changes that occur in cobalt-based superalloys, with both time and temperature, for life prediction, refurbishment and failure investigations.

The current research programme has assessed the effects of ageing at temperatures between 800 and 1050°C for up to 25,000 hours on two cobalt-based superalloys, FSX 414 and MAR M509, and one high cobalt (19 wt.%) nickel based superalloy NP 222. A second programme has assessed the effects of ageing at temperatures between 800 and 1050°C for up to 25,000 hours on a NiCoCrAlTaY coating, Amdry 997, on a MAR M509 substrate. It is intended to develop a process based upon the microstructural changes that can be utilised to allow the prediction of the effective operating temperature.

Chapter 2 reviews the literature available on cobalt-based superalloys and the coatings used to protect the components as turbine inlet temperatures increase. Chapter 3 discusses in some detail the various experimental techniques which have been used including hardness, optical microscopy, scanning electron microscopy (SEM), energy dispersive spectroscopy (EDS) and X-ray diffraction (XRD). In addition transmission electron microscopy (TEM) selected area diffraction of thin foils prepared from the bulk SEM samples by focused ion beam (FIB) milling using a dual beam (FEG-SEM/FIB) system has allowed the identification of a number of unknown phases. Thermodynamic equilibrium calculations were carried out for all of the materials by means of software package JMatPro(1) developed by Thermotech.

Chapters 4, 5 and 6 present and discuss the outcome of the experimental work carried out to characterise alloy FSX 414, a conventionally cast cobalt-based superalloy, NP 222 a conventionally cast γ' (~20%) strengthened nickel based superalloy with a high level ~19 wt.% of cobalt and MAR M509 a high carbon, high strength, vacuum cast cobalt-based superalloy respectively. Chapter 7 presents and discusses the outcome of the experimental work carried out on NiCoCrAlTaY coated samples of MAR M509, with and without inter-carbidic oxidation (ICO), focusing on; the phase changes within the coating, the interaction between the coating and the substrate, and the effect of 'ICO' on coating life. The conclusions drawn from this work are presented in Chapter 8, together with a discussion of the possible areas for further work.

2 Literature Survey

2.1 General Introduction to Cobalt-based Superalloys

A superalloy can be defined as an alloy usually based on Group VIIIA elements specifically designed for elevated temperature service, where high surface stability and the ability to withstand severe mechanical stresses are needed(2).

The first cobalt-based alloy used for high temperature applications was HS 21, a cobalt-chromium-molybdenum casting alloy derived from the dental prosthetic alloy Vitallium. The alloy was initially used to produce blades in turbo-superchargers for piston engines in the 1930's and then for blades and vanes in the first gas turbine engines of the 1940's. In the late 1940's and early 1950's the wrought alloy S-816 was used for forged turbine blades, combustion liners and after burner tail pipes(2,3). Further development has been limited by the cost and the limited availability of cobalt. Cobalt-based superalloys have therefore tended to take a secondary position to nickel based superalloys. This is clearly shown by the alloy X40 a cast cobalt-nickel-chromium-tungsten alloy developed by R.H.Thielemann in 1943 and still in use today for gas turbine vanes(2,3).

The reasons for the continued use of both wrought and cast cobalt-based superalloys are(2):

- A higher melting temperature and corresponding flatter stress rupture curve than iron and nickel based superalloys.
- The higher chromium content gives superior hot corrosion resistance in contaminated gas turbine atmospheres.
- In general cobalt-based superalloys have a higher thermal conductivity and hence a greater thermal shock resistance and greater resistance to thermal fatigue than nickel based superalloys. At 538°C the thermal conductivity of MAR M509 is 27.9 $Wm^{-1}K^{-1}$, Inconel 738 is 17.7 $Wm^{-1}K^{-1}$ (4).

The cobalt-based superalloys are designed around a cobalt-chromium matrix with chromium contents in the range 18 to 35 wt.% and carbon contents from 0.25 to 1.0 wt.%. If not used in the as-cast or forged condition, components are heat treated to control carbide precipitation.

The alloy's strength is derived from solid solution and precipitation strengthening. Solid solution strengthening results principally from the additions of chromium, tantalum, niobium and tungsten, whereas precipitation strengthening is obtained primarily from carbides formed with chromium and tantalum. The strength of cobalt-based superalloys is inversely related to the carbide particle size and directly related to the volume fraction of carbides.

It is reported that in service at high temperatures the carbide particles coarsen and finer carbides precipitate leading to depletion of alloying elements from the matrix(5).

2.2 Application of Cobalt-based Superalloys

Figure 2.1 illustrates a typical example of an industrial gas turbine engine. Cobalt-based superalloys are used in land based gas turbines in the combustor, transition duct and vanes (Figure 2.2). Cobalt-based superalloys are not used for blades due to the superior creep strength of nickel based superalloys.

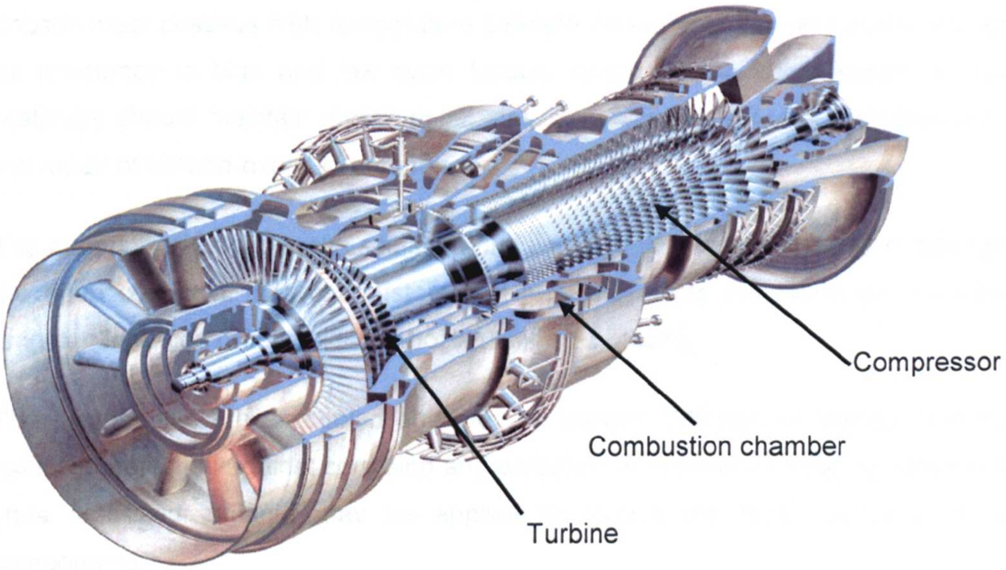

Figure 2.1 Example of industrial gas turbine engine used for power generation(6)

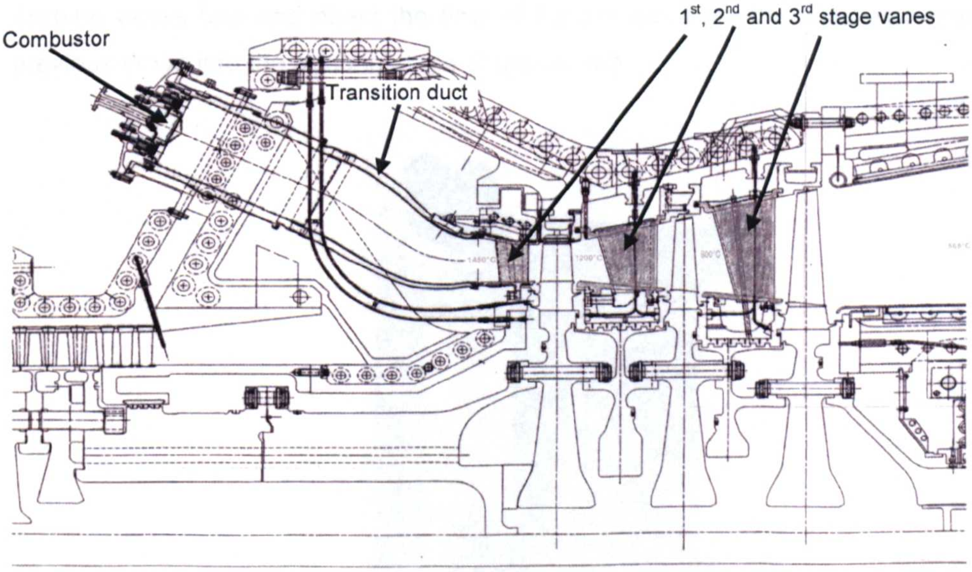

Figure 2.2 Cross section through a can-annular gas turbine.

2.2.1 Combustor and transition duct

Air enters the combustion chamber from the compressor at a pressure of ~20 bar and a temperature of ~500°C. The combustor is designed to contain the flame and to allow mixing of the hot gases from the flame with further air to control the gas temperature and emissions. The transition duct directs the hot gases to the first stage guide vanes.

The combustor components are subject to the hottest gases in the turbine and hence the largest thermal cycles during the start up and shutdown of the turbine. For the type of service seen in land based gas turbines nickel and cobalt-based superalloys are used. The materials chosen must possess high temperature strength including tensile and creep strength, as well as resistance to high and low cycle fatigue, oxidation and carburisation. In addition, the materials should maintain metallurgical stability in service to avoid embrittlement and allow the repair of service-exposed components.

The materials are used in the solution annealed condition or with the higher strength alloys in the aged condition. The combustors and transition ducts are fabricated from sheet using tungsten inert gas (TIG) welding, spot welding and brazing.

The components are air cooled and may be coated. Diffusion or overlay coatings may be used for protection against corrosion and oxidation. A thermally insulating ceramic top coat of yttria stabilized zirconia may be applied to reduce the metal temperature on cooled components.

2.2.2 Turbine vanes

Turbine vanes turn and direct the flow of the hot gas from the combustor/transition duct or previous stage into the rotating stage of the turbine.

Figure 2.3 Photograph of MAR M509 First stage vane.

The first stage inlet guide vanes (Figure 2.3) are subject to the highest gas temperature and thermal stresses in the turbine but lower mechanical stresses than the rotating blades. In large industrial gas turbines the vanes are air cooled to keep the bulk metal temperatures below 800°C. The use of cooling air is limited as it impacts on the overall turbine efficiency. The high temperature strength and oxidation resistance of cobalt-based superalloys allows vanes to operate at higher temperatures with less cooling air than nickel based superalloys. In addition to high temperature strength, the vane material requires creep strength to resist distortion caused by gas loading and thermal stress, low cycle fatigue strength to resist the cyclic thermal strains, and oxidation and corrosion resistance. For later stage vanes, the choice of alloys used is a balance between alloy strength and the amount of cooling required.

Stationary vanes are currently produced as single or multiple airfoil investment castings. Castings are precision cast in air (FSX 414) or for the higher strength cobalt-based superalloys (MAR M509) vacuum cast. However, dependant upon the requirements of the OEM, vacuum casting may be stipulated for FSX 414.

The cobalt-based superalloys used for vanes (Table 2.1)(4,7) are solid solution strengthened by the addition of tungsten and tantalum and precipitation hardened by the formation of carbides of chromium tantalum and titanium. Chromium is important for oxidation and corrosion resistance. Components may be used as-cast or in the heat treated condition. The heat treatment is generally limited to solutioning and ageing to control carbide precipitation.

During their life time the vanes will be refurbished a number of times. This will be discussed in Section 2.9.

	C	Fe	Ni	Cr	Co	W	Ta	Ti	Al	Zr	B
X40	0.5	1.5	10.0	25	Bal	7.5					
X45	0.25	2.0	10.5	25	Bal	7.0					0.01
FSX 414	0.25	2.0	10.5	29.5	Bal	7.0					0.012
MM 509	0.6	1.0	10.0	21.5	Bal	7.0	3.5	0.2		0.5	0.01
ECY 768	0.6	1.0	10.0	23.5	Bal	7.0	3.5	0.2	0.15	0.05	0.01

Table 2.1 Nominal composition of cobalt-based turbine vane alloys (wt.%)(4,7).

2.3 Microstructure

Cobalt-based superalloys are normally characterised by a face-centred cubic (FCC) matrix containing second phases.

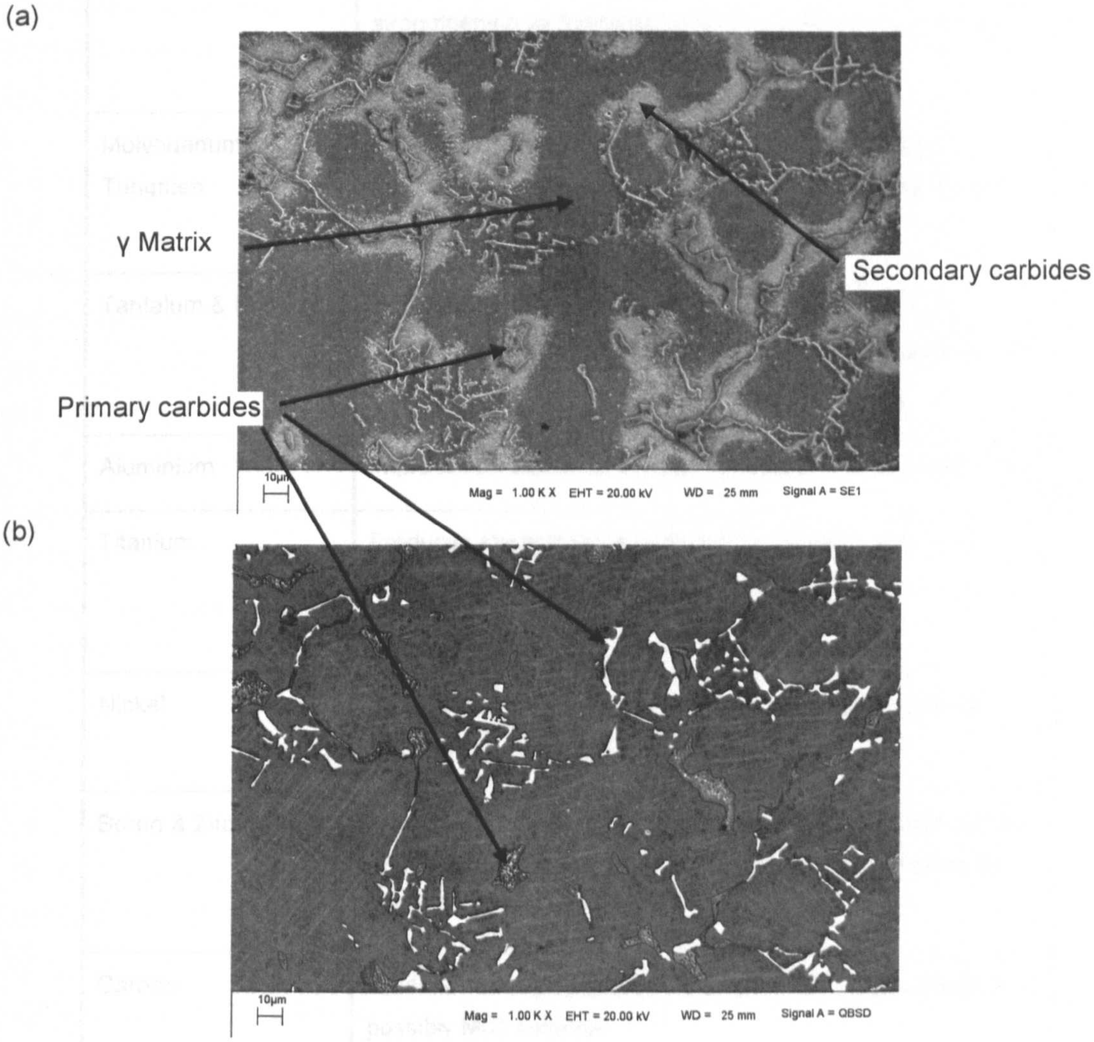

Figure 2.4 SEM images showing the microstructure of cobalt-based superalloy (a) secondary electron (SE) (b) backscatter (BSE) modes.

Although the second phases are usually carbides (Figure 2.4) with a variety of compositions, precipitation of other intermetallic compounds are also observed. The effects of different alloying elements on cobalt-based superalloys are detailed in Table 2.2[2,3,8,9].

Element	Effect (Where M refers to the alloy addition)
Chromium	Improves oxidation and hot corrosion resistance, produces strengthening by formation of M_7C_3 and $M_{23}C_6$ carbides. Can form harmful intermetallic compounds (σ).
Molybdenum & Tungsten	Solid-solution strengtheners; produce strengthening by formation of intermetallic compound Co_3M and carbides M_6C and MC.
Tantalum & Niobium	Solid-solution strengtheners; produce strengthening by formation of intermetallic compound Co_3M, γ and carbides MC and M_6C.
Aluminium	Improves oxidation resistance; formation of intermetallic CoAl.
Titanium	Produces strengthening by formation of MC carbide and intermetallic Co_3Ti with sufficient nickel produces strengthening by formation of intermetallic Ni_3Ti.
Nickel	Stabilises FCC form of matrix; produces strengthening by formation of intermetallic Ni_3Ti.
Boron & Zirconium	Produces strengthening by effect on grain boundaries and by precipitate formation; zirconium produces strengthening by formation of MC carbides.
Carbon	Produces strengthening by formation of MC, M_7C_3, $M_{23}C_6$ and possibly M_6C carbides.
Yttrium & Lanthanum	Increase oxidation resistance.

Table 2.2 Effects of different alloying elements on cobalt-based superalloys(2,3,8,9).

2.3.1 Solid solution strengthening

A solid solution is a solid, homogenous mixture of two or more elements. The solute atoms are present on either substitutional or interstitial sites in the matrix. Their presence can influence the mechanical properties of the metal by affecting the lattice parameter such that dislocations are impeded. The properties that can be changed by solute atoms include the lattice parameter, modulus, stacking fault energy and electron density of the alloy.

Common solid solution elements in cobalt-based superalloys are chromium, tungsten, tantalum and molybdenum. Rausch(10) confirmed that in cobalt-based superalloys containing

15 – 25% chromium, additions of tungsten, tantalum and molybdenum improved substantially the 925°C yield strength.

2.3.2 Carbides

Cobalt-based superalloys are strengthened primarily by the precipitation of cubic, non-coherent carbide particles(2). To promote the formation of carbides, the carbon content of cobalt-based superalloys is higher than in both nickel and iron based superalloys.

In the as-cast condition, cobalt-based superalloys contain primary carbides located at grain boundaries and interdendritic regions. Primary carbides in cobalt-based superalloys are metastable, and ageing or subsequent service at high temperature causes their degeneration and induces secondary carbide precipitation(11). The primary carbides inhibit grain boundary sliding at elevated temperatures, while fine secondary carbides pin dislocations and harden the alloy matrix and thus contribute significantly to strength. Carbide precipitation can occur on deformation generated stacking faults reducing the matrix ductility and is one of the reasons cobalt-based superalloys are restricted in use to static rather than rotating parts(12). Carbides in cobalt-based superalloys can be divided into chromium rich M_3C_2, M_7C_3 and $M_{23}C_6$ and refractory element rich MC and M_6C carbides(2). The chromium rich carbides typically contain cobalt, tungsten or molybdenum as substitutes for chromium.

Optimum mechanical properties are obtained through a balance between the carbides at the grain boundaries and those in the matrix. Grain boundary carbides, regardless of type, should be present as discrete particles. Continuous carbide networks at grain boundaries reduce impact ductility and creep rupture properties. During service all cobalt-based superalloys suffer some loss of ductility from carbide precipitation, as a result of the removal of carbon from solution(13). Service at high temperatures can result in the formation of undesirable acicular carbides and lamellar carbides which can also form during slow cooling from the solution heat treatment temperature(14).

2.3.2.1 MC carbide

MC carbides form during solidification as discrete 'blocky' particles. The strongest MC forming elements are hafnium, zirconium, tantalum, niobium and titanium. The carbides are extremely stable and are generally distributed throughout the alloy in both matrix and intergranular positions. The more stable carbides (hafnium and zirconium) may form in the melt and can be found at the interstices of the dendrites. Tantalum carbides and niobium carbides usually form in the "Chinese-script" morphology suggesting precipitation later in the solidification sequence(2). In high chromium cobalt-based superalloys the MC carbides can, under long term service exposure degenerate to $M_{23}C_6$ carbide, producing a secondary hardening effect(2).

2.3.2.2 $M_{23}C_6$ carbide

$M_{23}C_6$ carbides are found in superalloys with a high chromium/carbon ratio(5). They can form during solidification, ageing heat treatments and in service.

$M_{23}C_6$ may form as a primary precipitate during solidification and is found, in most commercial superalloys, as an interdendritic precipitate within the secondary dendrite arms and is the last phase to freeze. This produces a lath structure consisting of alternate sheets of $M_{23}C_6$ and the γ matrix.

The strengthening role of $M_{23}C_6$ is as a fine secondary precipitate throughout the matrix. The carbide can preferentially precipitate along stacking faults and twin boundaries at low temperatures. This can have an adverse effect on low temperature ductility especially in cast superalloys with $C > 0.5$ wt.% (2).

2.3.2.3 M_6C carbide

M_6C carbides are generally found in the low chromium content superalloys in which the molybdenum and or tungsten levels exceed 4-6 at.%. The carbides exhibit excellent temperature stability, which is beneficial for grain size control during the fabrication of wrought materials. The M_6C carbides usually occur as M_3M_3C or M_4M_2C. M_6C carbides may also transform to $M_{23}C_6$ carbide or may form as a decomposition product of MC carbide(2).

$$MC + \text{austenite} \rightarrow M_6C \text{ (e.g. } TaC + (Co,Ni,Cr,C) \rightarrow (Co,Ni)_4(Cr,Ta)_2C)$$

Jiang et al(11) investigated the formation of a tungsten rich phase in a modified X40 directionally solidified alloy. The alloy was modified by the addition of tantalum, titanium and zirconium and in the as-cast condition contained M_7C_3 and MC primary carbides.

Ageing of the alloy resulted in the precipitation of fine secondary $M_{23}C_6$ carbides and a tungsten rich phase on the surface of the M_7C_3 carbide. In general M_6C carbide forms only when the tungsten and or molybdenum content exceed 4-6 at.% which was not met in alloy X40. Transmission Electron Microscopy (TEM) of thin foils confirmed that the tungsten rich phase was M_6C. Jiang concluded that the formation of the M_6C was as a result of the addition of tantalum, titanium and zirconium to the alloy which induced the formation of primary MC carbides with a high tungsten content. The subsequent decomposition of the MC carbide produced a segregated zone where the tungsten and/or molybdenum content exceeded 4-6 atomic % enabling the precipitation of the M_6C, with the surface of the neighbouring MC carbide acting as a heterogeneous nucleation site.

2.3.2.4 M_7C_3 carbide

M_7C_3 is trigonal in structure and forms at low chromium/carbon ratios(5) usually as Cr_7C_3 and can be involved in the formation of σ in some superalloys.

Lane and Grant(15) proposed that Cr_7C_3 was metastable and decomposed into $Cr_{23}C_6$ through an in situ reaction

$$23Cr_7C_3 \rightarrow 7Cr_{23}C_6 + 27C$$

Subsequently the carbon atoms diffuse locally into the alloy matrix combining with more chromium to form fine precipitates.

$$6C + 23Cr \rightarrow Cr_{23}C_6$$

Jiang at al(16,17) investigated the relationship between the degeneration of primary M_7C_3 carbide and the precipitation of $M_{23}C_6$ in a directional solidified (DS) cobalt alloy, after ageing at 850°C for 100 hours. Jiang proposed a similar reaction to Lane and Grant(15) based on metallographic observation.

$$23M + 6C \rightarrow M_{23}C_6$$

where M is mainly chromium.

2.3.3 Intermetallic compounds in cobalt-based superalloys

The strengthening of cobalt-based superalloys by the precipitation of intermetallic compounds is secondary when compared to carbide strengthening. The intermetallic phases found in cobalt-based superalloys are detailed in Table 2.3(3).

Compound	Structure
Co_3 (Mo, W, Ta, Nb)	HCP ordered
Co_3Ti, β Co_3Ta	FCC ordered
Co_2 (Mo, W, Ta, Nb)	Hexagonal Laves phase (TCP)
Co_7 $(Mo, W)_6$	Rhombohedral – Hexagonal Mu (μ) phase (TCP)
Co_2 (Ta, Nb, Ti)	Cubic Laves phase (TCP)
Co_2 $(Mo, W)_3$	Sigma (σ) phase (TCP)
CoAl	Cubic ordered
$(Co, Ni)_3(Al, Ti)$	FCC, ordered
Co_3Ti	HCP

Table 2.3 Intermetallic phases found in cobalt-based superalloys(3).

Precipitation hardening of cobalt-based superalloys by means of intermetallic phases of the γ' type has been demonstrated in the Co-Cr-Ti and Co-Cr-Ta systems(9,10). However, the high temperature instability of the γ' formed in these systems has prevented them from achieving commercial status(8).

Topologically close packed phases (TCP) found in cobalt-based superalloys are sigma (σ), mu (μ), and Laves (Table 2.3). TCP phases occur when the solubility limit of the austenite matrix is exceeded primarily by a combination of chromium and refractory element additions(2). These phases usually precipitate near grain boundaries where concentrations of chromium and refractory elements may be high. Additionally, they can denude the matrix of elements such as chromium, which reduces corrosion resistance. The phases can precipitate in both acicular and blocky morphologies. The acicular morphology is generally considered undesirable with regard to crack initiation and propagation through the microstructure. The presence of TCP phases is generally considered to be deleterious, reducing strength and ductility at service temperatures as well as a severe loss of low temperature ductility(2).

$M_{23}C_6$ carbides have a complex cubic structure, which, if the carbon atoms were removed, would closely approximate the structure of σ. Coherency between $M_{23}C_6$ carbides and σ is high; σ often nucleates on $M_{23}C_6$ carbides(2).

2.4 Heat Treatment

The heat treatment of cobalt-based superalloys is principally used for control of carbide precipitation. Typical heat treatment involves the solutioning of M_6C, $M_{23}C_6$ and part of the MC carbides at around 1150°C, followed by ageing in the 870-980°C range to precipitate a variety of carbides, the major one being $M_{23}C_6$(12). However, the commercial heat treatments do not bring about complete carbide precipitation and more carbides are formed during service, in particular at dislocations and deformation stacking faults(2). Cast cobalt-based superalloys are not usually solutioned but may be given a stress relief and/or ageing heat treatment. When required, ageing is carried out at 760°C to promote the formation of discrete $M_{23}C_6$ carbides.

2.5 Thermodynamic Calculations

2.5.1 Introduction

Thermodynamic calculations on complex, multi component alloys are becoming more common in metallurgical research, in part replacing the reliance on printed phase diagrams which have been used to represent the equilibrium structure of binary, ternary and occasionally higher order systems. The use of computer aided thermodynamic phase diagram calculations (CALPHAD) has been developed such that using suitable thermodynamic data, it is now possible to predict the equilibrium concentration of phases present in a multi-component alloy of specified composition as a function of temperature and pressure. The thermodynamic models used are based on sound physical principles, hence, parameters from several well defined systems may be combined to calculate the equilibria with confidence in considerably more complex systems. The CALPHAD approach for superalloys, has been used in the development of new alloys, in the selection of processing conditions for existing or new alloys, and to evaluate the long term metallurgical stability of alloys.

In this programme of work thermodynamic modelling has been carried out using a commercially available software package. I will only briefly touch on the mathematics behind thermodynamic modelling and will discuss the operation of the package in the experiment methods (Chapter 3.9).

2.5.2 Modelling multicomponent equilibria

The chemical equilibrium of an alloy system may be determined by minimising the total free energy of the system with respect to the amount and composition of the phases present, at fixed pressure in the case of Gibbs free energy or fixed volume in the case of Helmholtz free energy. Conventionally, Gibbs free energy is used in the CALPHAD approach(18).

When the Gibbs energy, G, of the system is at a minimum, the chemical potentials of the components are equalised throughout the system. Equilibrium can therefore be computed by minimising the Gibbs energy of the system,

$$G = \sum_{i=1}^{p} n_i G_i^{\varphi} = \text{minimum}$$

where n_i is the number of moles, and G_i^{φ} is the Gibbs energy of phase i. A thermodynamic description of a system requires the assignment of thermodynamic functions for each phase. The CALPHAD method employs a variety of models to describe the temperature, pressure, and concentration dependencies of the free-energy functions of the various phases. The contributions to the Gibbs energy of a phase can be written as

$$G^{\varphi} = G_T^{\varphi}(T,x) + G_p^{\varphi}(p,T,x) + G_m^{\varphi}(T_C,\beta_o,T,x)$$

where $G_T^{\varphi}(T,x)$ is the contribution to the Gibbs energy by the temperature (T) and the composition (x), $G_P^{\varphi}(p,T,x)$ is the contribution of the pressure (p), and $G_m^{\varphi}(T_c,\beta_0,T,x)$ is the magnetic contribution of the Curie or Néel temperature (T_C) and the average magnetic moment per atom (β_0). The temperature dependence of the concentration term of G_T^{φ} is usually expressed as a power series of T.

$$G = a + bT + cT\ln(T) + \sum d_n T^n$$

where a, b, c, and d_n are coefficients, and n are integers. To represent the pure elements, n is typically 2, 3, -1, and 7 or -9[75]. This function is valid for temperatures above the Debye temperature; in each of the equations in the following models describing the concentration dependence, the G coefficients on the right-hand side can have such a temperature dependence. Frequently, only the first two terms are used for the representation of the excess

Gibbs energy. For multi-component systems, it has proven useful to distinguish three contributions from the concentration dependence to the Gibbs energy of a phase, G^{φ}

$$G^{\varphi} = G^{0} + G^{ideal} + G^{xs}$$

The first term, G^0, corresponds to the Gibbs energy of a mechanical mixture of the constituents of the phase; the second term, G^{ideal}, corresponds to the entropy of mixing for an ideal solution, and the third term, G^{xs}, is the so-called excess term.

In summary to produce an equilibrium calculation by the CALPHAD method the Gibbs energies of all potential phases are expressed as a function of temperature and composition. The total Gibbs energy is then given by the weighted sum of the Gibbs energies of the individual phases. By minimising this total, the phases present at equilibrium can be identified.

At the present time only the nickel based superalloy database is commercially available for use with the current software packages and may be of limited use for cobalt-based superalloys(19). Berthod et al(20,21) have developed a database for cobalt-based superalloys using the Thermo-calc software. The database used is the SSOL (SGTE) database incorporating the binary and ternary thermodynamic descriptions of Ta-C, Ta-Ni, Ta-Cr, Ta-Co, Co-Ta-C and Ni-Cr-Ta from the available literature. The results of high temperature (1000-1300°C) short time experiments on cobalt-based superalloys have been compared with the calculated results. Investigated were the phases present, the molar fraction of each phase present and the solidus temperature. The results indicate a good agreement for the microstructural evolution with a quantitative disagreement between the results which is considered as a problem of using surface fractions measured on the samples compared with volume fractions obtained from the calculation. Differential thermal analysis of the solidus temperature was 50°C higher than the database calculated value. It was concluded that the difference could be attributed to the lack of accuracy of the database.

2.6 Corrosion/oxidation

Gas turbine components are subjected to hot corrosion and high temperature oxidation. Hot corrosion can be either Type I, which results from condensation of alkali sulphates which form as liquid salts on the vane surface, or as low temperature or Type II hot corrosion, which results from the formation of low melting eutectic compositions of alkali metal sulphates and base metal sulphates that result in the dissolution of the protective surface oxide layer. Figure 2.5(22) is a schematic of the range of temperatures in which these types of environmental attack occur. It should be noted that there are some variations in the temperature ranges reported in the literature. This variation is due to the dependence of the attack upon the specific chemistry of the base metal and the gas stream.

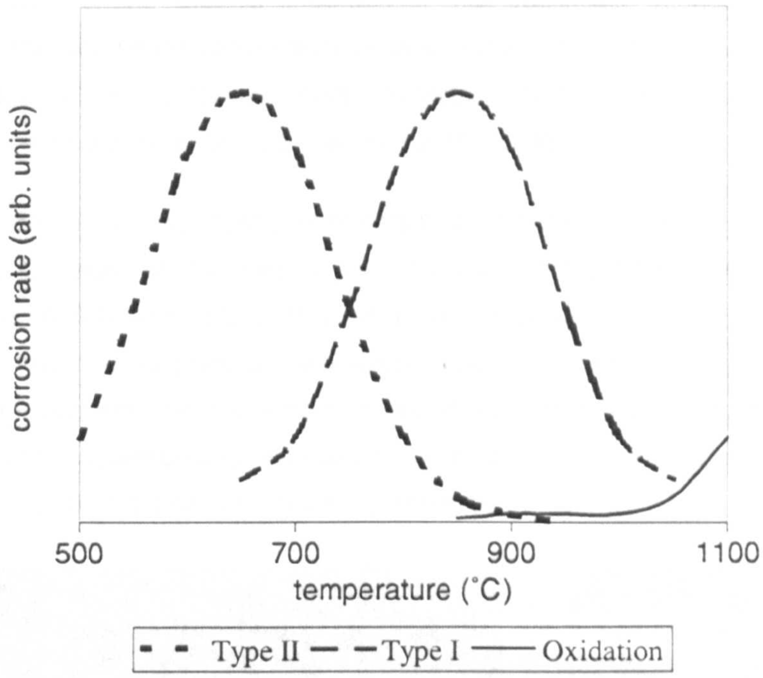

Figure 2.5 **Schematic representation of rate-temperature curves for Type II hot corrosion, Type I hot corrosion and oxidation(23).**

2.6.1 Hot corrosion

Hot corrosion (Figure 2.6), hot sulphidation or Type I corrosion results from the condensation of alkali sulphates (sodium sulphate Na_2SO_4 or potassium sulphate K_2SO_4), which form as liquid salts on the vane surface in service. The molten salts dissolve the protective oxide layer at temperatures between 750 and 950°C(24,25,26). With the breakdown of the protective oxide, sulphur is able to diffuse into the alloy surface layer where chromium sulphide can form. The by products of this reaction eventually prevent the formation of an adherent protective oxide allowing more oxygen into the surface resulting in rapid oxidation rates with the formation of a thick porous outer oxide layer, an intermediate layer of internal oxide particles mixed with depleted alloy and an inner region containing internal sulphide particles(8). The major source of sulphur is the fuel, particularly distillate fuels, and the alkali arises from the inlet air, especially on coastal sites; sulphates may also be ingested directly with the air. With the use of clean fuels such as natural gas and with good filtration practice hot corrosion should not be a major problem for large land based turbines.

Chromium is the most effective alloying element for improving the hot corrosion resistance of superalloys. In order to attain good resistance to Type I corrosion, a minimum of 15 wt.% chromium is required in nickel based superalloys and a minimum of 25 wt.% chromium in cobalt-based superalloys(27). Type I hot corrosion can reduce the rupture life, fatigue life and ductility of the base metal; the severity of the degradation is dependant on temperature, environment, stress and the metal composition(28).

The microstructure of the alloy is important in that secondary phases may lead to an accelerated attack along phase boundaries or by selective attack of one phase. Enhanced hot corrosion of superalloys containing coarse refractory metal carbides has been identified where the coarse refractory metal carbides intersect the metal surface(27).

Type II or low temperature hot corrosion occurs in the temperature range 595 to 815°C. It is caused by the formation of low melting point eutectics of alkali metal sulphates and base metal sulphates ($NiSO_4$ and $CoSO_4$) this results in the dissolution of the protective surface oxide layer(23). The melting point of the eutectic mixture is lower than that of pure sodium sulphate. Type II corrosion results in pitting of the metal surface, a porous layered scale, low levels of base metal depletion and few internal sulphide particles. At the temperature of Type II attack, internal sulphidisation is not normally observed.

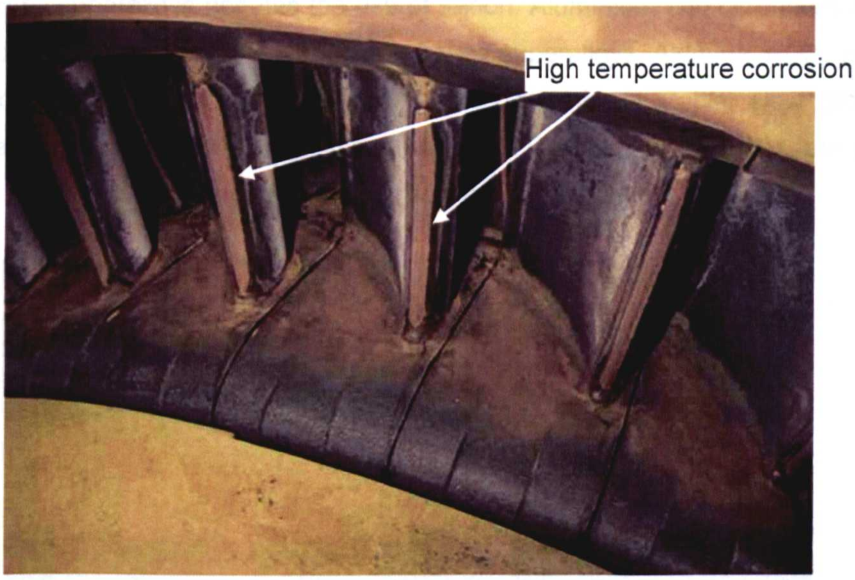

Figure 2.6 Photograph of first stage vanes showing high temperature corrosion.

As with hot corrosion, low temperature corrosion can significantly reduce the stress rupture life, fatigue life and ductility of the base metal. The formation of an adherent chromium oxide (Cr_2O_3) scale will protect the component from Type II corrosion. Al_2O_3 scales are readily attacked as a result of the pH of the molten sulphate.

Cobalt-based superalloys are, in general, more resistant to Type I corrosion than nickel based superalloys. This may result from the higher melting temperature of the Co-Co_4S_3 eutectic (877°C) in comparison to the Ni-Ni_3S_2 eutectic (645°C). In addition, the diffusivity of sulphur in cobalt-based superalloys is approximately 100 times lower than in nickel based superalloys(29). Cobalt-based superalloys are, however, more susceptible to Type II corrosion than nickel based superalloys.

If high temperature hot corrosion is evident in a gas turbine then low temperature hot corrosion can occur on cooler sections of the same component and on downstream components. Features of both types of corrosion may be evident in the transition region of 730 – 850°C. It is difficult to control the attack of components that cycle in this transition region as different oxide scales provide protection in each regime.

2.6.2 Oxidation

High temperature oxidation is the formation of an oxide scale due to interaction between the combustion environment and the component (Figure 2.7). Oxidation resistance in superalloys is essentially the result of the formation, by selective oxidation, of an external scale that forms a protective layer over the surface. To be effective the oxide layer must limit the diffusion of the oxidising element and oxygen through the oxide to comparatively slow rates(30). Aluminium, chromium and silicon are the only elements whose oxides are sufficiently protective and have an affinity for oxygen to allow selective oxidation(31). The high melting point required by superalloys negates the use of silicon. Aluminium and chromium form Al_2O_3 or Cr_2O_3 respectively on nickel, cobalt and iron based superalloys. Alumina, Al_2O_3, is the most protective oxide at temperatures above 900°C. It is chemically stable, slow growing and provides an effective barrier to inward oxygen transport. Chromia, Cr_2O_3 offers less protection than alumina above 850°C where chromia can sublime to CrO_3.

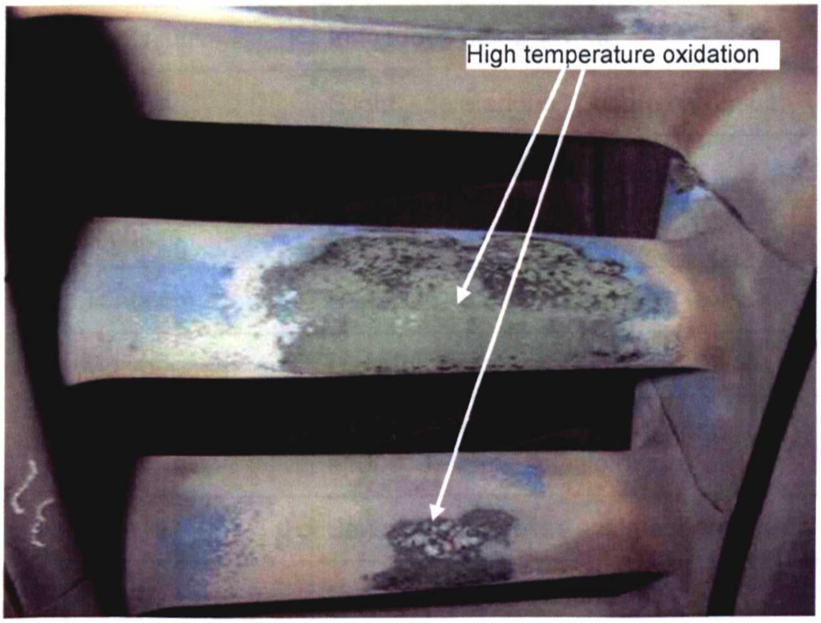

Figure 2.7 Photograph of coated vanes showing evidence of high temperature oxidation.

Factors which may affect the rate of oxidation are alloy composition, surface condition, gas environment and cyclic oxidation resulting in the formation of oxide scale cracks and spallation. Cracking and spallation will eventually lead to depletion of the protective oxide forming element, and hence, break down in the oxide layer and formation of less protective oxides when other elements within the alloy oxidise preferentially.

Cobalt-based superalloys cannot contain sufficient aluminium to form an alumina protective oxide layer whilst maintaining the required mechanical properties(30). Cobalt base superalloys instead utilise the formation of a Cr_2O_3 protective oxide layer. The oxidation resistance of cobalt-based superalloys generally increases with the chromium concentration, with the oxidation resistance of alloys with less than 20% chromium being comparatively poor. Refractory elements such as tungsten and molybdenum have favourable effects on the selective oxidation of chromium (Table 2.4)(5). However, when the oxidation of chromium is no longer preferential, the oxidation of tungsten and molybdenum occurs at an increased rate due to the development of a less protective oxide scale(30).

Oxidation occurs preferentially at carbides close to the surface. The only protective scale that can form over carbides is chromia, however this cracks easily(30). To minimise this form of degradation, the carbides in superalloys should be small and discontinuous.

Alloying element	Probable effect of addition on the oxidation behaviour of a Co(20-30)Cr base material
Titanium	Innocuous at low levels
Zirconium	Innocuous at low levels
Carbon	Slightly deleterious; Ties up chromium
Vanadium	Harmful, even at 0.5%
Niobium	Harmful, even at 0.5%
Tantalum	Beneficial to moderate (<5%) levels
Molybdenum	Harmful; forms volatile oxides
Tungsten	Innocuous below 1000°C, Harmful >1000°C; forms volatile oxides
Yttrium	Beneficial; improves scale adherence
Nickel	May be slightly deleterious
Manganese	Beneficial; induces the formation of spinels
Iron	Tends to induce spinel formation

Table 2.4 Role of alloying additions to cobalt base materials oxidation(5).

2.7 High Temperature Oxidation, Corrosion and Temperature Resistant Coatings

Cobalt-based superalloys were initially used in the uncoated condition but are increasingly used with coatings to provide protection of the base metal from oxidation and corrosion and to limit the diffusion of harmful species into the substrate. The reasons for using coatings are to provide:

- protection from high temperature oxidation
- protection from high temperature corrosion
- reduction in metal temperatures to prevent thermal fatigue
- protection of the parent metal from erosion.

Coatings are consumable, in that the coatings oxidise or corrode during operation and are replaced during refurbishment.

The coatings used can contain high levels of aluminium, chromium and, to a lesser extent, silicon, all of which can form a continuous, adherent, dense oxide scale when exposed to oxygen at high temperature. Aluminium forms the stable, coherent, Al_2O_3 oxide, chromium the protective Cr_2O_3 oxide. However, in the early stages of oxidation meta-stable oxides (θ, δ, γ alumina) and oxides of the major alloying additions may form until the stable, protective oxide is established(32). The protective oxide layer forms a barrier at the gas/component interface and increases in thickness with time; the growth is typically exponential with temperature (15°C increase in temperature doubles the growth rate). The protective oxide layer can be brittle and can spall as a result of thermal cycling and mechanical damage. Spallation (Figure 2.8) reduces the thickness of the oxide layer and can increase the rate of oxidation of the oxide forming elements that diffuse from the coating to reform the scale. When the oxide forming elements in the coating fall below a critical level, for sustaining a stable oxide layer, discontinuous breakaway oxidation occurs with a resultant rapid degradation of the coating and subsequently the substrate.

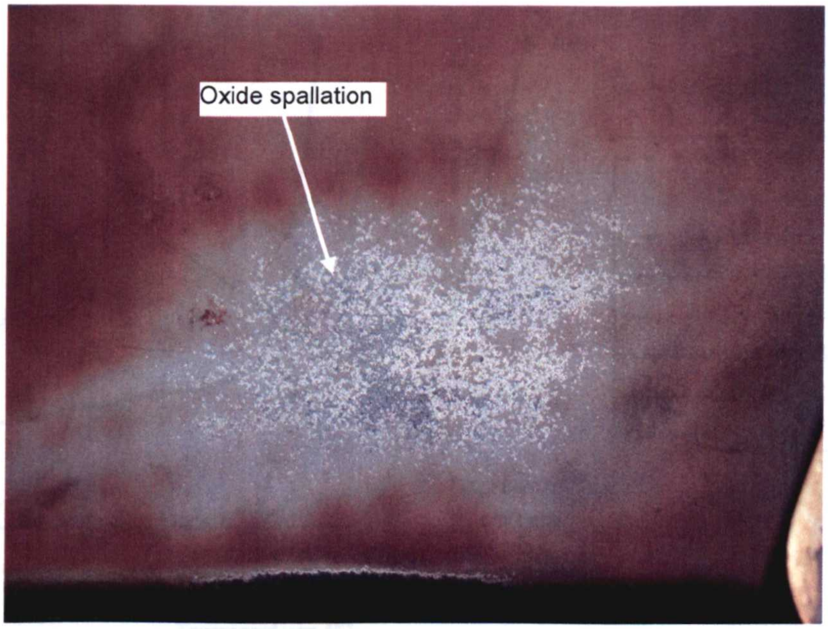

Figure 2.8 Photograph of oxide spallation on the pressure side of a gas turbine blades.

When alloyed with aluminium in the coating, chromium reduces the level of aluminium required to form a protective Al_2O_3 oxide. When alloyed with nickel, cobalt, aluminium and silicon, chromium makes coatings resistant to hot corrosion. For high temperature hot corrosion (Type I) 15 to 20% chromium is required, for low temperature hot corrosion (Type II) 25 – 40% chromium is required(33).

Prior to reviewing the different types of coatings and combinations that exist it is important to consider their mechanical properties. In general the tensile, compressive and creep properties of the base metal are not affected by the coating because the coating is only a small fraction of the total. Fatigue resistance can be affected in that cracks in the coating can propagate into the base metal. Coating failure through coating and metal cracking can lead to "onion-bulbing", typically seen in diffused aluminide coated components. Reducing the aluminium content of the coating would improve the coating ductility, but this would however, reduce the oxidation resistance of the coating. It is therefore important to identify the potential failure mechanisms in the component/coating system to ensure that an inappropriate coating is not chosen. The ductile/brittle transition temperature (DBTT) gives a measure of the coating's ductility as a function of temperature and hence its propensity to cracking (Figure 2.9)(34).

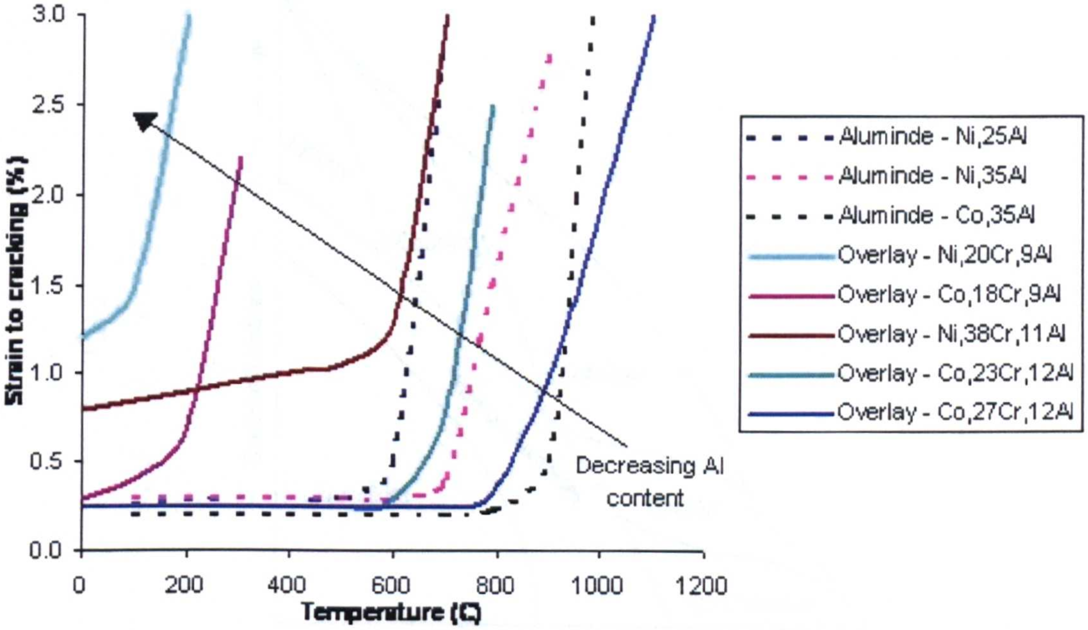

Figure 2.9 The effect of aluminium content on the ductile/brittle transition temperature of a coating(34).

In general the lower the DBTT the lower the oxidation resistance. A balance must be made therefore between oxidation resistance and mechanical properties (Figure 2.9).

The crack resistance of the coating is dependent on the thermal stresses during operation. During start-up and at elevated temperatures the coating is placed under compressive stresses, whereas during shutdown (or trip) the coating is subject to tensile stresses – the coating's mechanical properties are better under compressive loading. The tensile stresses during a shutdown can lead to cracking in the coating and to spallation of the aluminium oxide protective scale. The consensus view is that where the protective oxide scale is less than 10μm it is unlikely to spall, whereas at thicknesses greater than 10μm spallation will occur(22).

Figure 2.10(35) is an attempt to graphically identify the optimum coating with reference to the particular application.

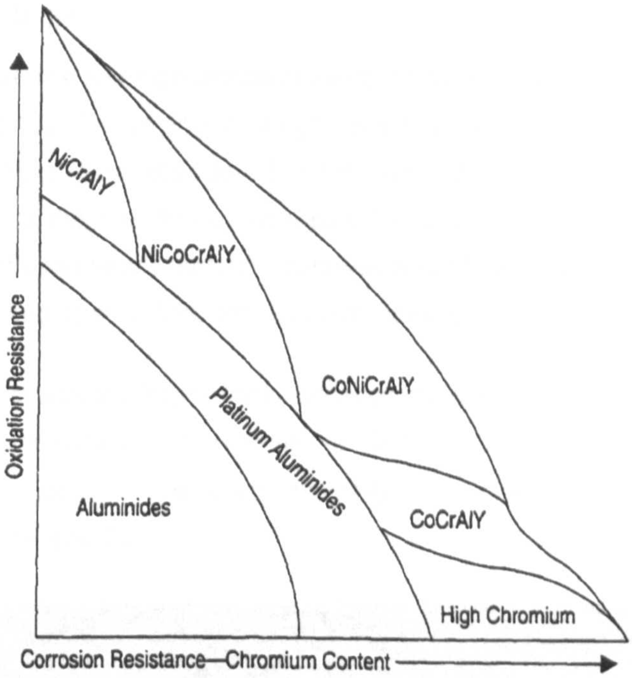

Figure 2.10 Schematic illustration of coating composition as related to oxidation and corrosion resistance[36].

Chromising offers the best resistance to hot corrosion (both Type I and II), while for oxidation NiCrAlY-NiCoCrAlYs offer the best protection. This is a simplification and does not take into account other elements that are added to the coating to improve the coating's properties.

Although numerous variants of high temperature coatings are in use, they usually fall into one of three generic types[25]:

- Diffusion coatings – formed by the surface enrichment of an alloy with aluminium (aluminide), chromium (chromised) or silicon (siliconised). In some systems combinations of these elements are possible, i.e., chromium-aluminised or silicon-aluminised.

- Overlay coatings – these are a family of corrosion resistant alloys specifically designed for high temperature surface protection. Often referred to as MCrAlY coatings; where M is the alloy base metal, normally Ni or Co or a combination of these two; Cr is chromium; Al is aluminium and Y is yttrium.

- Thermal barrier coatings – this family of coatings are designed to insulate the substrate from the heat of the gas path and thereby reduce the rate of oxidation and creep. They are a composite coating system consisting of an outer ceramic coating (usually 6-12 wt.% yttria partially stabilised zirconia) overlaid over an oxidation resistant bond coat. The bond coat is typically a MCrAlY overlay coating or a diffusion aluminide coating.

2.7.1 Diffusion coatings

Diffusion coatings were the first high temperature coatings to be used and the process is still widely used (Figure 2.11). The original coatings were brittle and were prone to cracking as a result of thermal cycling. The addition of other elements, notably platinum and silicon, improved the ductility of the coating but increased the cost. The method relies on diffusion, during a carefully controlled heat treatment, between a coating deposited on the surface and cobalt/nickel from the substrate to form an aluminide coating (Table 2.5).

Aluminide coatings are typically 65μm thick, although thicknesses in the range 25 - 100μm have been used. Typical service temperatures are 800 – 1100°C. For severe hot corrosion conditions chromised coatings are used, typically 20 - 50μm thick, operating in the temperature range 600 – 870°C.

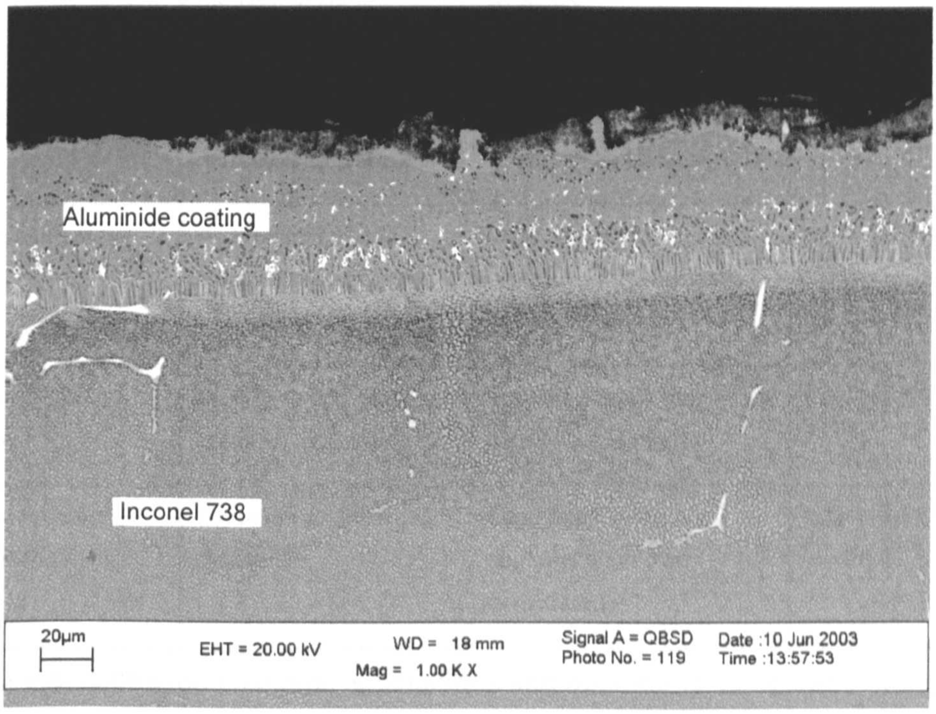

Figure 2.11 SEM BSE image of an aluminide coating on IN 738 substrate.

Coating type	**Application**	**Comments**	**Operational temperature range**
Aluminide	High oxidation resistance.	Very brittle, can lead to cracking in the base metal.	600-1100°C
Chromide	High corrosion resistance.	Poor in oxidation at high temperature, can lead to cracking.	600-870°C
Chromium-aluminide	High corrosion and medium oxidation resistance.	Alternative coatings available.	600-870°C
Silicon-aluminide	High oxidation and corrosion resistance.	Improved crack resistance to aluminised coatings.	600-1100°C
Platinum-aluminide	High oxidation and corrosion resistance.	Very brittle, can lead to cracking in the base metal.	600-1150°C
Platinum-silicon-aluminide	High oxidation and corrosion resistance.	Improved crack resistance over Pt/Al coatings.	600-1150°C
Platinum, Paladium, Platinum/Rhodium	Oxidation and corrosion resistance.	Expensive, alternative coatings should be considered.	600-1150°C

Table 2.5 Diffusion coatings, applications and operational temperature ranges(22).

The major drawback for the industrial use of diffusion coatings is that there is experience of cracks in the coatings that subsequently lead to cracks within the base metal, which can lead to 'onion-bulbing' oxidation in the base metal. It is very difficult to determine if a crack on the surface of a component is contained within the diffusion layer or if it runs into the base metal.

Diffusion coatings can make good bond-coats for TBC coatings. However, due to their brittle nature diffusion coatings have limited application in gas turbines which would be regularly cycled. Platinum modified aluminide coatings provide good TBC adhesion in turbines which experience high levels of thermal cycling. However, on industrial gas turbines this would be very expensive and the process tends to be covered by a patent limiting the number of companies that can apply the coatings.

During service aluminide diffusion coating are consumed in two distinctly different ways: Aluminium diffuses to the surface to form a continuous alumina protective scale which as a result of thermal cycling eventually cracks and spalls. Aluminium diffuses into the base material causing a depletion of the aluminium in the coating. Once the level of aluminium falls below 4-5 wt.%, there is thought to be insufficient aluminium to allow the formation of the alumina scale and oxidation of the base material occurs(2).

The two processes employed for diffusion coating are pack cementation or chemical vapour deposition. In pack cementation the component is placed in a pack that consists of a powdered mixture of the elemental addition (aluminium or chromium or an alloy of aluminium or chromium), a halide activator salt (ammonium halide) and an inert diluent such as alumina.

On heating in an inert atmosphere to a temperature in the range 700°C-1100°C for 2 to 24 hours, the metal powder and activator react to form a vapour. This vapour in turn reacts with the surface of the component forming either an intermetallic coating (CoAl or NiAl depending on the substrate) or an enriched surface layer in the case of chromising. Coatings are classified as low temperature high activity (LTHA) where inward diffusion occurs or high temperature low activity (HTLA) where outward diffusion of the base metal elements (Ni or Co) occurs. Subsequent heat treatments may be required to further diffuse the coating.

Platinum or rhodium modified aluminide coatings are a modification of the pack cementation process incorporating a thin platinum or rhodium layer (6µm thick) electroplated on to the surface of the component. The component is then aluminised with the aluminium activity modified such that the outer layer of the coating contains most of the platinum or rhodium in the form of aluminium containing intermetallic $PtAl_2$ or $RhAl_2$ the platinum modification is generally used for nickel based superalloys and the rhodium modification for cobalt-based superalloys. These coatings show significant improvements in hot corrosion resistance in the temperature range 800 - 950°C and moderate improvements in oxidation resistance at higher temperatures.

In the chemical vapour deposition process the parts are loaded into a retort in a furnace. A precursor gas, typically HCl, or a mixture of HCl and HF, in the aluminising process, is passed over a source of aluminium in a separate evaporator under closely controlled temperature, pressure and flow rate to generate gaseous aluminium chloride or fluoride. The gas is introduced into the coating chamber where it reacts with the surface of the component. By pumping the vapour through the inside of the parts the internal passages can be coated.

2.7.2 Overlay coatings

Overlay coatings act in a similar manner to diffusion coatings; they provide a thermally grown oxide (TGO) layer that protects the coating and the base metal from further attack by either oxidation or corrosion. The coatings offer both good oxidation and corrosion resistance and are less prone to cracking than diffusion coatings.

Overlay coatings are formed from an alloyed material containing elements necessary to form an adherent protective scale. The coating alloy composition is selected to provide a balance between oxidation resistance, corrosion resistance and coating ductility. The common coatings are known as MCrAlY, M being nickel or cobalt with chromium, aluminium and yttrium. The matrix of the coating is nickel or cobalt with chromium in solution. Aluminium forms NiAl or CoAl in the coating, yttrium is an oxygen active element added to improve the adhesion of the oxide scale and decrease oxidation rates.

The different types of MCrAlY coatings are used as follows(37);

NiCrAlY	high temp. applications > 900°C
CoCrAlY	medium temp. (700°C to 900°C)
FeCrAlY	moderate temp. < 700°C

Overlay coatings are deposited thicker than diffusion coatings typically 125 - 200μm thick with thicknesses up to 300μm on some commercial applications.

In most commercial coatings the main phases present in the microstructure are γ-Ni and β-NiAl, however depending on the composition and service temperature additional phases α-Cr, σ-CoCr and γ'-Ni_3Al and other intermetallic phases may be present(38). The TGO formed removes aluminium and chromium from the coating leading to changes in the microstructure, predominantly the dissolution of the β-NiAl phase, followed by the depletion of the γ'-Ni_3Al in the coating. The rate of aluminium consumption is increased by high oxide growth rates and spalling of the alumina scale. Commercial coatings contain oxygen active elements (yttrium) which are present as intermetallic compounds. Yttrium is considered to aid adhesion by scavenging tramp levels of sulphur from the coating/TGO interface and reducing scale growth by forming blocking oxide phases within the TGO grain boundaries, limiting the inward transport of oxygen(39). The distribution of the yttrium rich phases can be affected by the coating process. In high oxygen content coatings the yttrium will be tied up in finely dispersed oxide particles reducing the yttrium available in solution. If the yttrium content in solution reduces below a critical level, the effects of yttrium on scale growth and adherence is lost(40).

In addition to the diffusion of aluminium to the outer surface, interdiffusion between the coating and substrate material occurs. This interdiffusion results in aluminium loss from the coating to the base metal, the formation of new phases at or near the coating substrate interface and diffusion of substrate alloying elements into the coating altering the coating mechanical properties and oxidation performance. Diffusion of aluminium from the coating into the base alloy, in most cases leads to a γ′ rich layer and an intermediate pure γ layer. However, with high chromium active coatings the diffusion of chromium from the coating and refractory alloys from the base alloy into the coating can result in the precipitation of brittle intermetallic compounds in the interdiffusion zone(40).

The two common methods of deposition are physical vapour deposition (PVD) and plasma spraying. Electron beam physical vapour deposition (EB-PVD) is the most common physical vapour deposition method for coating superalloys. The process involves the vaporisation, in a vacuum, of a continuously fed ingot with a high voltage electron beam. The vaporised atoms move in a straight line from the molten ingot to the parts to be coated which are rotated and tilted within the vapour cloud with the metal condensing out on the preheated substrate surface(2). The part is usually heated to temperatures around 800 - 1100°C which also allows a metallurgical bond to form between the coating and substrate. Typical deposition rates are 6μm min^{-1} but can be up to 75μm min^{-1}. On completion of the coating process a diffusion heat treatment is generally applied to improve the bond. Glass bead peening is frequently used to close areas of unbonded columnar grain structure(2).

For spray deposited coatings (air-plasma, low pressure plasma and high velocity oxyfuel combustion spraying) the coating material is an alloyed powder that is heated and the molten or partially molten droplets are accelerated on to the part to be coated. The molten particles, or droplets, strike the substrate surface at a high velocity and solidify on contact. The coating is attached to the substrate by the mechanical interlocking of the coating and the substrate. The surface of the substrate is roughened by grit blasting prior to spraying. Deposition rates of 200 - 400μm/min are possible. A diffusion heat treatment is used to promote diffusion between the coating and the substrate.

Both EB-PVD and plasma spraying are line of sight processes and therefore can be problematic for complex shapes. These two processes cannot coat internal passages, in contrast to aluminising.

Following the application of the coating the component is normally heat-treated to homogenise the coating and produce a chemical bond, i.e. an inter-diffusion region, between the coating and the base metal. Typically the thickness of this region is 10-15μm. An example of an overlay-coating is given in Figure 2.12.

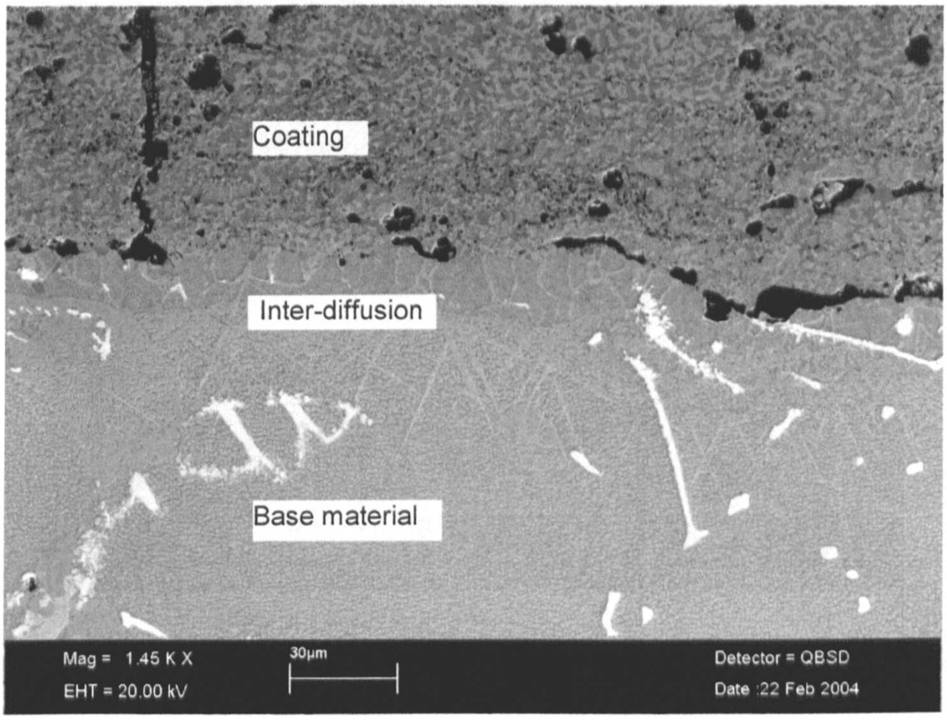

Figure 2.12 SEM BSE image of the inter-diffusion region between a MCrAlY coating and a nickel based superalloy substrate.

The main active scale-forming element in overlay coatings is again aluminium, but in overlay coatings the aluminium content is 6-12 wt.% compared to diffusion coatings where the aluminium content is 24-35 wt.%. This would suggest that the overlay coatings are not as effective at resisting oxidation however, this is not the case. Chromium improves oxidation resistance by increasing the activity of aluminium. An addition of 10 wt.% chromium will enable Al_2O_3 scale (Figure 2.13) formation down to aluminium levels of 5 wt.%(2). The increased ductility of the coatings allows the TGO to grow to 15-20 µm before reaching the critical thickness and spalling off(41).

In service, degradation of the coating occurs both by the loss of TGO and by diffusion of aluminium into the base metal. Once the aluminium content of the surface of the coating is less than ~4 wt.% the coating life has effectively been fully consumed and the oxidation of the coating will be almost as rapid as the base metal. At this point the component should be refurbished.

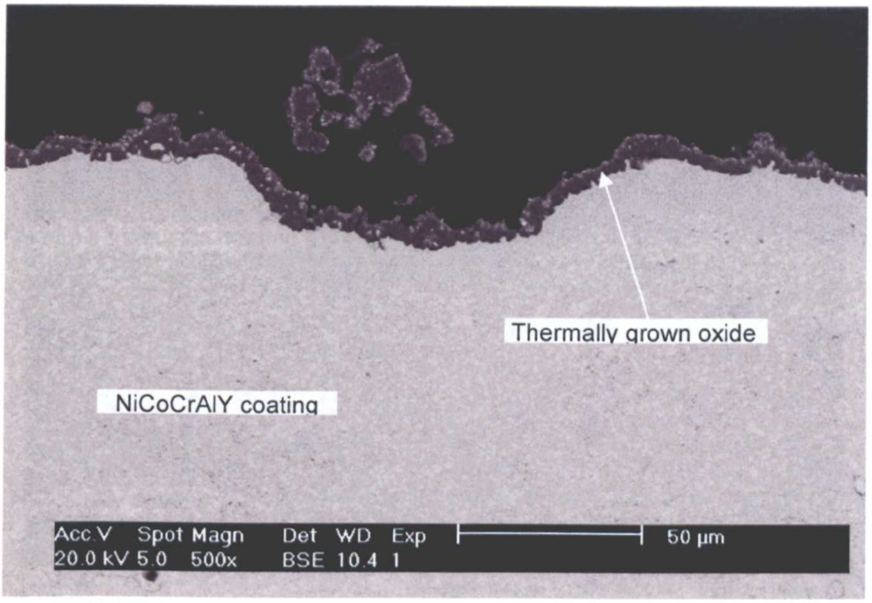

Figure 2.13 SEM BSE image of a thermally grown oxide on NiCoCrAlY coating.

It should be noted that while exclusive formation of Al_2O_3 is often possible (except for the incorporation at grain boundaries of oxides of the active element addition, yttrium for example), growth of Cr_2O_3 scales will usually be accompanied by oxidation products of Mn, Si, Ti and similar elements if present within the substrate alloy or coating. The presence of such dopants may significantly affect the protective nature of the thermally grown oxide.

Over-aluminising is a process where the overlay coating is over coated with an aluminium diffusion coating (Figure 2.14). This greatly increases the life of the coating by enhancing the aluminium reservoir in the coating. However, over-aluminising makes the outer surface of the coating brittle and it is often found that the component fails earlier as a result of fatigue cracking or brittle failure as a result of thermal shock in the over-aluminising layer. These failures would probably not have occurred if the component had not been over-aluminised. The over-aluminised coating fails normally by crack formation, diffusion of aluminium into the overlay coating and by spallation of the TGO, in much the same way as a standard diffusion coating. However, once the surface aluminide coating has been degraded what remains is the overlay coating, which then continues to offer oxidation resistance. The coating then continues to degrade as an overlay coating.

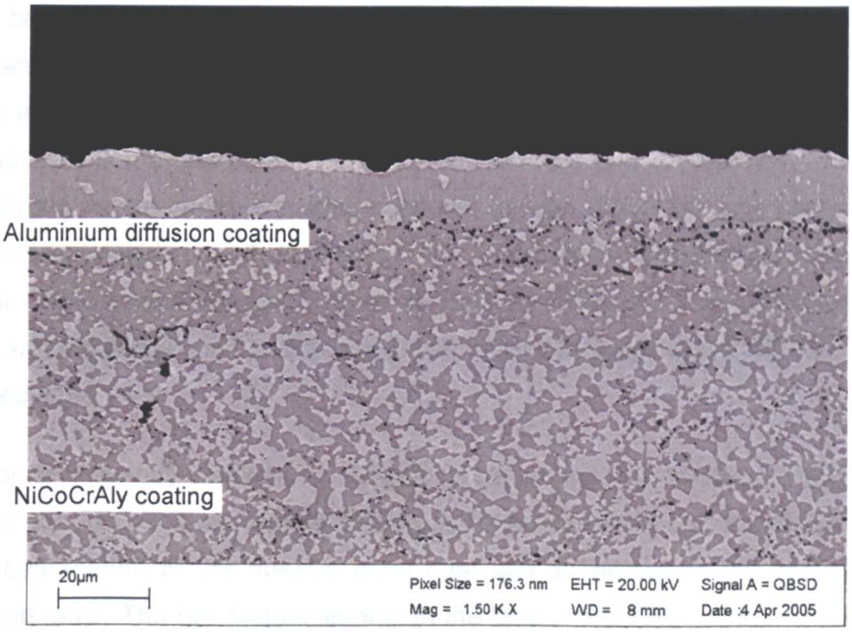

Figure 2.14 SEM BSE image of an over-aluminised NiCoCrAlY coating.

2.7.3 Thermal barrier coatings

In a number of situations it may be necessary to limit the temperature of cooled components by the provision of a Thermal Barrier Coating (TBC) i.e. an insulating layer. For the TBC to function efficiently there must be sufficient cooling to ensure that the temperature drop through the TBC is attained. Components which are not cooled would not benefit from the application of a TBC. TBCs of all types (whether air plasma sprayed (APS), dense vertically cracked (DVC) APS, or EB-PVD) have very low thermal conductivity coefficients and so reduce the surface metal temperature significantly.

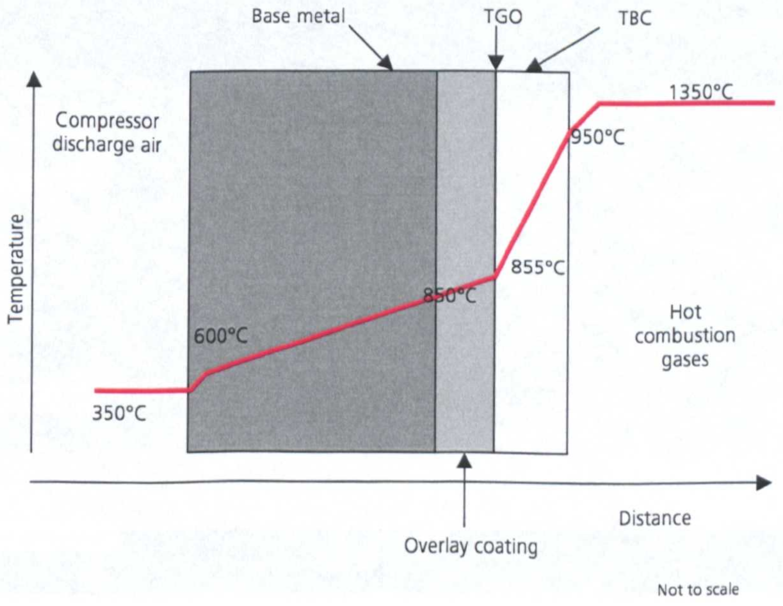

Figure 2.15 Typical temperature profile through a TBC coated component[(22)].

A thermal barrier coating (TBC) is formed from two layers; a metallic inner layer, the bond coat (BC) and a ceramic insulating outer layer. The bond coat is a MCrAlY overlay coating or a diffusion aluminide coating as previously described. The purpose of the bond coat is to improve the adhesion of the ceramic coat to the substrate and prevent oxidation of the base metal substrate, as the ceramic coating conducts oxygen. The TBC coat comprises zirconia (ZrO_2) stabilised by additions of yttria Y_2O_3 (7 wt.%) to prevent the volume change that occurs as a result of the phase change in pure zirconia at 1170°C(2). The ceramic has a higher reflectivity and a thermal conductivity one to two orders of magnitude lower than the nickel or cobalt-based superalloy.

For diffusion and overlay coatings, coating life is determined by chemical degradation of the coating. For the TBC coating the life limiting factor is considered to be the loss of the TBC such that degradation of the metallic bond coat and subsequently the substrate occur at unacceptable rates. The two factors leading to the loss of the TBC coating are spallation and erosion. Spallation occurs by delamination of the TBC from the bond coat. Two major factors controlling spallation are bond coat oxidation and the strain generated by thermal expansion mismatch during cooling between the TBC and the bond coat/substrate(42).

APS TBCs are the cheapest TBC coatings available on the market and are typically used on stationary components where mechanical stresses are much lower than in rotating blades, a typical microstructure is shown in Figure 2.16. On combustors, the hottest parts will be coated with a TBC in order to reduce the metal temperature by 50-100°C. The adhesion of the TBC to the bond coat is critical for acceptable life of the coating. With APS coatings the bond coat may have a poorly developed TGO layer; porosity may be too high; bonding between TBC particles may be poor which can lead to spallation or blistering of the TBC.

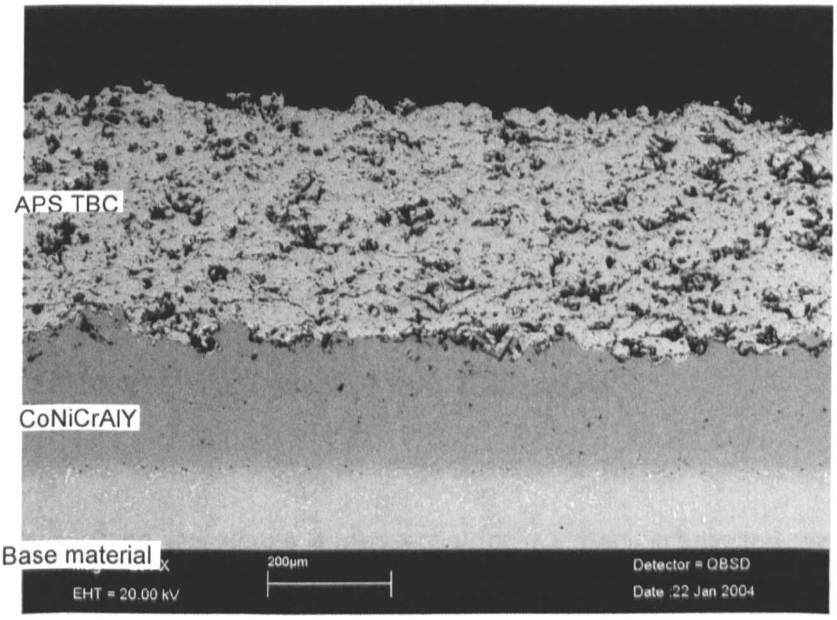

Figure 2.16 SEM BSE image showing an APS TBC coating on a CoNiCrAlY overlay coating.

EB-PVD TBCs have mainly been used in aero gas turbines but are now being increasingly applied to industrial gas turbines as an alternative to APS TBC. The microstructure of a typical EB-PVD TBC is shown in Figure 2.17. In this case the coating thickness is ~150μm or approximately half the thickness of a typical APS coating.

As with APS TBCs the EB-PVD coating reduces the temperature of the base metal, however, the reduction in temperature is normally only half to two-thirds that obtained using APS coatings. The porosity and cracking present in the APS coating decrease the thermal conductivity of the coating when compared to the EB-PVD coating. The increase in metal temperature of the component needs to be considered and compared with the advantage of improved adhesion of the TBC. It may therefore be appropriate to coat the blade with an EB-PVD TBC and the vanes and other stationary components with APS TBC. One further advantage exists with the use of EB-PVD coatings – cooling holes in the component do not have to be masked when the coating is being deposited. This is because the coating process is a line of sight process and the coating thickness rapidly reduces.

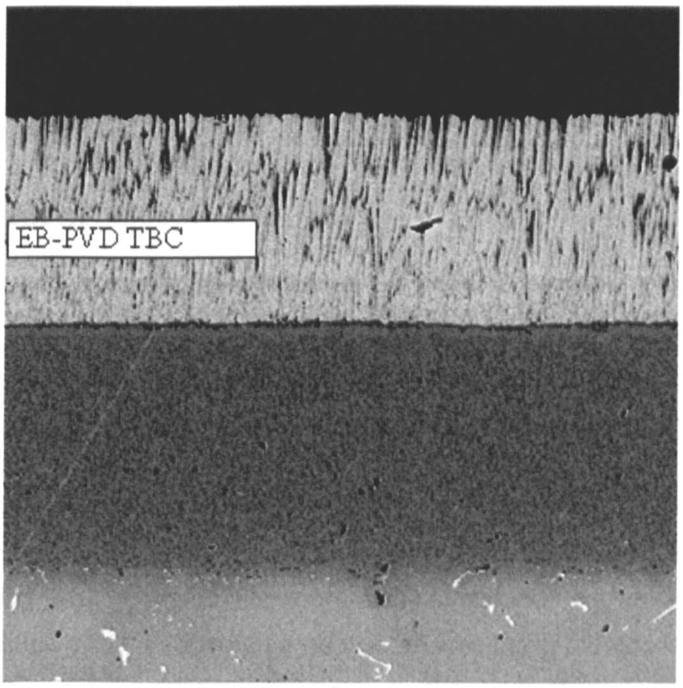

Figure 2.17 SEM BSE image of an EB-PVD TBC coating.

2.8 Welding

Weld repair and joining techniques are essential for the manufacture and overhaul of gas turbine vanes. Repairs of casting defects, hot tears and shrinkage porosity, repair of service generated thermal fatigue cracks, and the joining of nozzle assemblies, are the main area of concern. The manual Tungsten Inert Gas (TIG) and Electron Beam (EB) welding techniques are the most commonly used welding processes(43).

The weldability of wrought and cast cobalt-based superalloys is considered to be generally good. However, the highly segregated, high strength cast cobalt-based superalloys are prone to hot cracking. Hot cracking will generally occur within a critical high temperature range when thermal stresses due to welding induced strains are superimposed onto a microstructure with a limited plastic strain capability as a result of the formation of a low melting point phases or micro constituents. Hot cracking is normally associated with the HAZ but can occur in the weld metal in high heat input welding processes(43). Segregation along the centre line of the weld bead in both tungsten inert gas and to a lesser degree electron beam welding leads to hot cracking and poor thermal fatigue cracking resistance. This can be limited in tungsten inert gas welds by using pulsed arc tungsten inert gas welding which breaks up the columnar grain orientation found in both tungsten inert gas and electron beam welds.

Filler alloys should melt at a lower temperature than the incipient melting point of the substrate and be free of liquid-metal embrittling segregates. The weld metal should exhibit a slow strength recovery during solidification and cooling, have good high temperature ductility and be metallurgically compatible with the substrate(43). The use of low carbon filler wires reduces the tendency for the precipitation of carbide stringers at grain boundaries that can increase crack propagation rates in thermal fatigue.

2.9 Refurbishment

The components used in gas turbines are refurbished a number of times before being scrapped. It is this ability to rework the components and return them to service that allows the high cost of cobalt and nickel based superalloys to be deferred over a number of service cycles. It is therefore important to have an understanding of the refurbishment cycle:

Stripping – the remaining coating is removed from the component. This can be achieved through acid stripping or by mechanical means. Acid stripping leaches aluminium from the oxide and the coating, making the coating more brittle; it can then be removed by grit blasting. The acid-soak/grit blast cycle is repeated a number of times until the coating is fully removed. Final remnants of the coating can be removed by belt grinding. There are a number of other chemical processes available that ensure that a specific thickness of material is removed; these are more applicable to components with complex geometries and cooling arrangements. A heat-tint is applied to ensure that the coating has been removed; the component is heated in a furnace, the coating tends to produce a straw tint that is easily recognisable against the blue base metal tint. With acid stripping some of the base material is removed, typically 60 μm thick.

Heat treatment – the component is heat-treated to remove any residual stress that may exist and to dissolve any precipitates that may have formed during service. It is important to know the component's base metal condition so that the chosen heat-treatment is the correct one. A small sample is usually taken to confirm the level of degeneration of the metallurgical structure and hence if the component can be reclaimed or scrapped.

Inspection – the component is inspected using the appropriate NDT technique to determine the extent and position of any cracking.

Welding/brazing – welding and brazing may have to be performed on the component. Any welding is carried out using approved procedures and consumables. Care is taken to ensure that the component is not over-heated and that residual stresses are not generated. Brazing may be undertaken to build-up low-stressed regions of the component. This may take the form of a coupon, sheet or powder. Brazing is generally carried out above the solution heat treatment temperature. Following any welding a heat-treatment is carried out to relieve any stress that may have been produced from the repair. A further NDT inspection is then carried out.

Preparation – before coating, the component is masked and cleaned. The mask prevents cooling holes, the root and other sensitive regions of the component from being coated. Cleaning is very important because grease and dirt from the environment, and especially fingerprints, will prevent the coating from bonding properly to the metal surface.

Coating – prior to coating it is important that the coating process is first qualified because the coating thickness is based upon the weight gain and not the measured thickness. It is good practice to use dummy components (or scrap components) to determine the coating parameters for whatever coating process is being used. This is normally done by applying small metal tabs to the dummy component. These are then sectioned so that the coating thickness and quality can be measured. Once the parameters have been determined, the program for the coating machine is fixed. A test piece is then coated before each shift or following any change in the coating process. Any change to the coating (e.g., thicker coating in a specific region) requires a full qualification procedure to be undertaken.

Heat-treatment – this is undertaken following the coating process and is normally done in vacuum or under nitrogen. The heat-treatment improves the bond between the coating and the base metal, chemically homogenises the coating and relieves any stresses that may exist within the coating. Following heat-treatment it is normal to carry out controlled shot-peening of the component to reduce the surface roughness (this is not carried out for components that are to be further coated with an APS TBC where surface roughness is critical for TBC adhesion).

The current programme of work has been carried out on two cobalt-based superalloys, FSX 414 and MAR M509 and a high cobalt (19 wt.%) nickel superalloy NP 222.

2.10 FSX 414

FSX 414 is a General Electric (GE) patented alloy with modest rupture strength and excellent oxidation and hot corrosion resistance. The alloy was first marketed in May 1968 and was the preferred choice for all production first stage vanes and some later stage vanes in GE machines(7). FSX 414 was derived from alloys X40 and X45 with lower carbon levels than X40 and a higher chromium content 30% against 25% and slightly lower tungsten. The lower carbon levels improve weldability, the higher chromium content increases oxidation/corrosion resistance. Published literature for this alloy is limited.

2.10.1 Composition

The compositional limits are shown below (Table 2.6):

Co	Cr	Ni	W	C	Mn	Si	B	Fe	S	P
Bal.	28.5- 30.5	9.5- 11.5	6.5- 7.5	0.2- 0.3	1.0 max.	1.0 max.	0.005- 0.015	2.0 max.	0.04 max.	0.04 max.

Table 2.6 FSX 414 Compositional limits (wt.%).

2.10.2 Microstructure and heat treatment

The as-cast microstructure contains eutectic $M_{23}C_6$ carbides formed at the grain boundaries and within the γ matrix. Two forms of eutectic carbide are evident: a coarser eutectic consisting of $M_{23}C_6$ carbide particles in a matrix of γCo, and a finer eutectic consisting of γCo particles in an $M_{23}C_6$ carbide matrix. $M_{23}C_6$ carbide in this alloy exists as $Cr_{21}W_2C_6$(44,45). As a result of heat treatment or service the carbides can be partially solutioned and precipitated as more finely divided particles around the original carbides. The primary carbides retard slip and grain boundary migration. The secondary $M_{23}C_6$ carbides pin dislocations that harden the matrix(5).

The heat treatment generally specified for this alloy(44) is 1150°C for 4 hours, furnace cool to 935°C and then hold for 10 hours, furnace cool to below 540°C, air cool to room temperature. The hold at 1150°C stabilises the alloy through a homogenising effect. The furnace cool to 935°C is to control the precipitation of $M_{23}C_6$, the furnace cool to 540°C is to limit distortion of complex castings. Bicego et al(46) identified the solutioning and ageing heat treatment as 4 hours at 1150°C cool, and 4 hours at 980°C followed by a furnace cool.

2.10.3 Thermal ageing

Morrow et al(47) found in FSX 414 samples aged for 1,000 hours at 815°C that secondary carbide precipitated in the γ dendrites in areas adjacent to the interdendritic eutectics. These secondary carbides showed directional patterns characteristic of Widmanstatten carbide precipitation or carbide precipitation on stacking faults.

The investigations by Foster and Sims(44) found that the $M_{23}C_6$ carbides spheroidise and agglomerate modestly in service. Spheroidisation and agglomeration is more rapid under stress. Platelets of $M_{23}C_6$.carbide can form after long exposure at 820°C.

Steinberg et al(14) examined uncoated first stage FSX 414 vanes which had operated at a turbine inlet gas temperature of 1000°C. They found that as the material overages, the carbides grow and the shape changes until there are continuous carbides at the grain boundaries, and acicular and lamellar carbides within the matrix. The acicular and lamellar carbides reduce the material's toughness, the grain boundary carbides provide crack paths for thermal fatigue.

Exceeding the chromium and tungsten composition limits can result in the formation of σ or π phases which would be deleterious. This is the reason the tungsten content was lowered by 0.5 wt.%(44).

Haafkens(48) identifies two different stages of in service degeneration in FSX 414, the dissolution of the fine $M_{23}C_6$ and the formation of brittle phases of η and σ (Figure 2.18). Both η and σ embrittle the material and cause subsequent difficulties during repair welding. The conditions under which the η and σ formed and the position of the micro section with respect to coatings or oxidation are not detailed. A solution treatment and ageing heat treatment removed η and σ with reprecipitation of $M_{23}C_6$ carbide in the matrix.

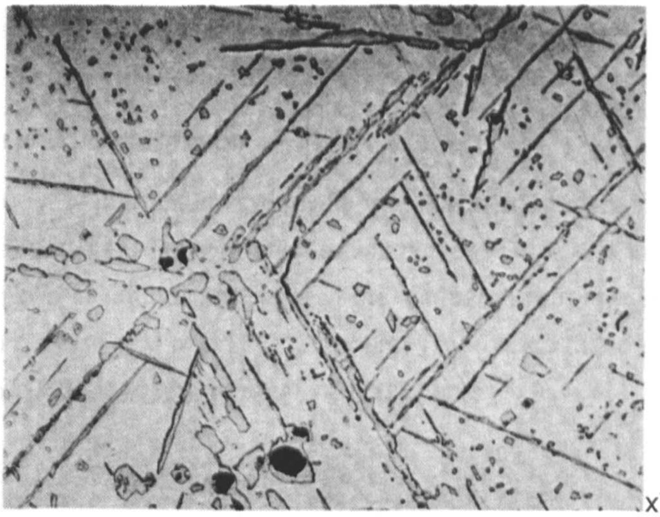

Figure 2.18 Photographic micrograph of degenerated FSX 414 microstructure showing brittle phases of η and σ (48).

Mezzedimi et al(45) discuss the experience gained from optical and SEM observation of FSX 414 nozzles removed from service. The report identifies image analysis using backscattered electrons as a method capable of estimating the exposure of FSX 414 components at different temperatures. Reference is made to the segregation of tungsten carbides which appear bright in the SEM in backscatter. Bicego et al(46) in a report dealing with the analysis of high temperature fatigue and creep damage in FSX 414 turbine nozzles details the examination of a first stage nozzle removed from service after 20,000 hours and 50 starts. A finite element thermal analysis calculation predicted the leading edge maximum operating temperature as 984°C. A microstructural examination of samples from the leading edge confirmed the presence of an outer oxidised band ~0.15 mm wide with chromium and cobalt oxides followed by an inner band ~0.85mm wide with a modified microstructure involving swelling of the secondary carbides as well as the disappearance of the "blocky" eutectic carbides which had begun to segregate into new chromium rich and tungsten rich carbides. Of interest is the observation that the cooled inner surface, showed similar microstructural changes to a depth of 0.3mm, while the area between the two bands appears unchanged. Pratesi et al(49) evaluated the microstructure of ~6,000 hour stress rupture tests at 950°C and 1000°C and a FSX 414 nozzle which had been in service for 35,000 hours. The report concentrates on the high atomic number carbides which appear white in backscatter electron imaging mode. A comparison of the 950°C and 1,000°C stress rupture specimens showed fewer and larger heavy metal carbides in the 1000°C sample when compared to the 950°C sample. Samples from the nozzle showed the shape and distribution of the carbides were not the same in different parts of the vane. The variations in the carbides are described through wall in a section taken from the "nose". At this point the heavy metal carbides are evident at the inner surface immediately below the inner oxidised layer. At the mid point through wall the heavy metal carbides are almost circular and aligned along the grain boundaries. At the outer surface, below the oxidised layer, identified as about 950°C a reduction in the heavy metal carbides is noted. In summary the report notes the difference in the carbides between the stress rupture samples and the nozzle and indicates that with further evaluation there may be a relationship with life/and or residual life based on the number or area of the white spots.

2.10.4 Oxidation and hot corrosion

The addition of 4 wt.% chromium improved the oxidation resistance of FSX 414 when compared with X40 and X45. The oxidation resistance of FSX 414 is three to eight times that of the other two alloys in natural gas firing in the temperature range 980-1090°C. At 980°C X45 will oxidise to a depth of 3 mm in 6,000 hours. To produce this depth of oxidation at the same temperature in FSX 414 would require 40,000 hours(50).

2.10.5 Rejuvenation and repair

Work by T F Chase and A M Beltran(43) shows that hot cracking during welding is primarily associated with carbide precipitation. The eutectic $M_{23}C_6$ carbides melt in the fusion zone during welding. On resolidification the carbides enhances brittle crack propagation.

The filler metals used for welding are L-605 and FSX 414 electrodes. The weldability of FSX 414 after service is equal to that of X45 and exceeds that of X40(43).

2.11 GT 222

This literature review will consider the available information on GTD 222 an alloy similar to NP 222 investigated in this work. GTD 222 is a vacuum cast, γ′ strengthened nickel superalloy developed by General Electric (GE). The alloy has a high level of cobalt 18.5-19.5 wt.% similar to Inconel 939. Published literature for this alloy is limited. Schilke(7) states that the alloy was developed in response to the need for improved creep strength in stage 2 and 3 vanes above that offered by FSX 414. In addition to the improved creep strength GE claim improved low temperature hot corrosion resistance and as a result of the low volume fraction of γ′ in the alloy better weldability than nickel based superalloys used for turbine blades. For stage 2 applications the vanes are coated with an aluminide coating to provide added oxidation resistance(7).

Investigations into the effects of cobalt in nickel based superalloys by Tien et al(51) on Udimet 700 (Co 17 wt.%) concluded that the role of cobalt is subtle and difficult to discern. It impacts slightly on the partitioning of the elements between the γ matrix and the γ′ precipitate and carbide phases. Depending on the heat treatment, cobalt is seen to promote creep and stress rupture resistance or to have no effect. Work by Nathal et al(52) on MAR-M247 (Co 10 wt.%) a high strength cast alloy and Maurier et al(53) on Waspaloy (Co 13 wt.%) a moderate strength wrought alloy concluded that cobalt promotes fewer carbides by stabilising the MC type carbides instead of the $M_{23}C_6$ type carbides. Cobalt widens the solid solution temperature range and contributes to γ′ coarsening. Coutsouradis et al(8) stated that the principle purpose of adding cobalt is related to mechanical properties or phase stability rather than oxidation or corrosion resistance.

2.11.1 Composition

United States Patent 4,810,467 is considered to describe alloy GTD 222. The preferred melt chemistry range is detailed in Table 2.7(54):

Ni	Co	Cr	W	Al	Ti	Nb	Ta	B	Zr	C
Bal	18.8 19.5	22.2 22.8	1.8 2.2	1.1 1.3	2.2 2.4	0.7 0.9	0.9 1.1	0.005 0.015	0.005 0.02	0.08 0.12

Table 2.7 GTD 222 Compositional limits (wt.%)(54).

2.11.2 Microstructure and heat treatment

GTD 222 is a gamma prime strengthened alloy. The alloy exhibits a primary MC carbide (Ta, Ti, Nb) and chromium rich $M_{23}C_6$ grain boundary carbide. The MC carbide precipitates during or shortly after solidification. The $M_{23}C_6$ carbide precipitates during ageing as a semi-continuous film, which results in lower stress rupture strength(55). The alloy is vacuum heat treated in two stages 1130°C for four hours followed by 785°C for 8 hours(56). Banik et al(55) looked at the effect of carbon, homogenisation and solution heat treatment on the mechanical properties and microstructure. They found that the homogenisation did not improve high temperature stress rupture strength.

2.11.3 Thermal ageing

The affects of thermal ageing were studied by Seavers and Beltran(56) on heat treated blank charpy impact specimens at 760°C and 870°C for up to 8,000 hours. The charpy tests were conducted at room temperature and showed a reduction in charpy energy with time at temperature, the maximum reduction occurring after 1,000 hours. The samples aged at 870°C showed an increase in charpy energy with exposure time peaking at 4,000 hours and decreasing to a minimum at 8,000 hours. The results were considered to show GTD 222 at 870°C is slowly over aged with exposure time with environmentally induced embrittlement affects dominating after 4,000 hours.

2.11.4 Oxidation and hot corrosion

Seavers and Beltran(56) reported the results of small burner rig tests carried out on GTD 222. Hot corrosion tests were carried out using doped diesel oil containing 1% sulphur and 125ppm sodium at a fuel to air ratio of 50:1. The samples were air quenched to room temperature every 50 hours. Oxidation tests were carried out in undoped natural gas combustion products. Metallographic measurements were made to determine average surface metal loss and maximum subsurface penetration, including internal oxidation or sulphidisation. The tests showed that GTD 222 is more resistant to Type II corrosion at 730°C than FSX 414. However, with increasing temperature and a shift to Type I hot corrosion FSX 414 had superior resistance to corrosion. The natural gas oxidation tests showed the oxidation resistance and the rate of internal oxidation of FSX 414 to be better than GTD 222 above 870°C. Aluminide coatings are recommended for temperatures above 870°C.

2.11.5 Rejuvenation and repair

Gamma prime strengthened nickel based superalloys exhibit sensitivity to strain age cracking when welded. The chemical composition of GTD 222 was balanced to provide good weldability in thick sections while retaining high creep and fatigue strength with good castability(56). The alloy definition of weldability as provided by Prager and Shira(57) indicates that GTD 222 is within the weldable range (Figure 2.19).

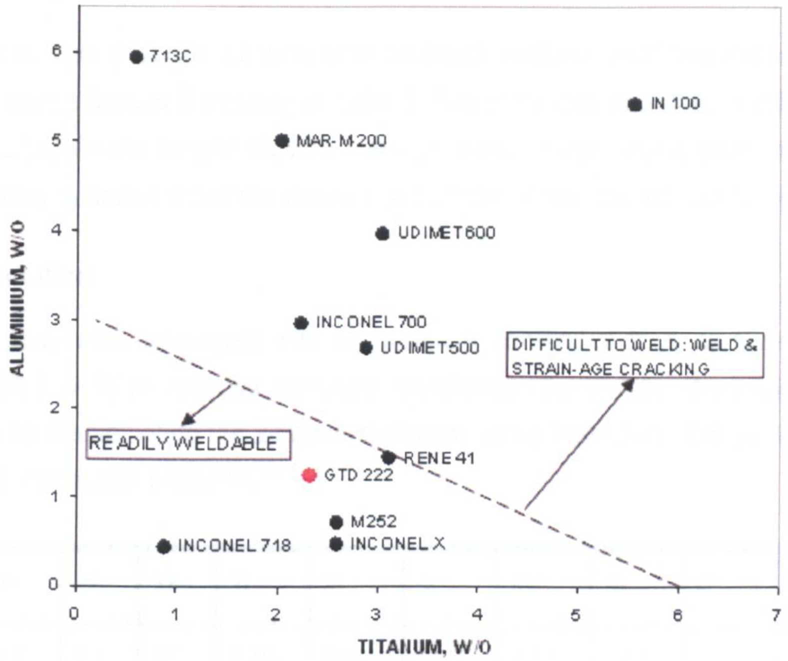

Figure 2.19 Diagram showing the weldability of nickel based alloys as a function of aluminium and titanium content with some common nickel based alloys marked(57).

Tungsten inert gas arc welding trials using Nimonic 263, GTD 222 and Waspaloy filler metals showed that the room temperature, 650°C and 760°C tensile strength of all three filler materials exceeded that of cast GTD 222. Short time cross weld stress rupture tests at temperatures between 785°C and 930°C failed in the weld with the Waspaloy tests at 825°C and 865°C failing in the HAZ. U groove patch tests for the Nimonic 263 and GTD 222 were acceptable after post weld heat treatment and simulated service at 760°C for 3,000 hours. The Waspaloy weldments showed minor HAZ fissuring. No post age cracking was noted on the samples.

2.12 MAR M509

MAR M509 is a high strength, carbide-strengthened, vacuum cast cobalt-based superalloy developed by Martin Metals Company in 1964-5. The alloy was primarily developed as a gas turbine vane alloy where longer service lives at lower stress levels were required(58,59,60). Currently the alloy is used for turbine vanes in a number of land based gas turbines(61).

2.12.1 Composition

Originally the alloy was developed with a chromium content of 21.5 wt.% which was later increased to 23.5 wt.% to improve oxidation resistance (Table 2.8). Castability of the alloy was improved by manipulating the zirconium content down from 0.4%-0.6 wt.% to 0.15 wt.% to avoid mould interaction problems(59,60).

Co	Cr	Ni	W	Ta	Ti	Zr	C	Mn	Si	B	Fe	S
Bal.	21.0-24.0	9.0-11.0	6.5-7.5	3.0-4.0	0.15-0.25	0.40-0.60	0.55-0.65	0.10 max.	0.40 max.	0.01 max.	1.50 max.	0.015 max.

Table 2.8 MAR M509 Compositional limits (wt.%).

In MAR M509 tungsten and chromium are solid-solution strengtheners; carbon, tantalum, titanium, zirconium and chromium are carbide formers. The carbides formed in MAR M509 are MC carbides rich in tantalum, titanium and zirconium, and $M_{23}C_6$ carbides rich in chromium. Chromium also plays an important role in controlling the oxidation and hot corrosion resistance of the alloy. Nickel is added to stabilize the FCC matrix(2).

2.12.2 Microstructure and heat treatment

MAR M509 is generally used in the as-cast condition and the microstructure is typically composed of dendrites of the FCC (γCo) solid solution and interdendritic network of "Chinese script" MC carbides. In addition, there are interdendritic eutectics consisting of mixtures of the γCo solid solution and carbides. The carbides in these eutectics may be $M_{23}C_6$, M_6C or M_7C_3, depending on the alloy composition(47). The M_6C and M_7C_3 phases convert into $M_{23}C_6$ and/or MC on heating. Two forms of eutectic are evident: a coarser eutectic consisting of $M_{23}C_6$ particles in a matrix of γCo, and a finer eutectic consisting of γCo particles in an $M_{23}C_6$ matrix(59,62,63). Above 1040°C the solubility of $M_{23}C_6$ and MC increase with increasing temperature with MC being more stable than $M_{23}C_6$. Carbides provide the major strengthening mechanism and all mechanical properties are influenced by the shape, size, distribution, and stability of the carbides(2,59,62,64). Woulds and Cass(59) consider the $M_{23}C_6$ carbide to be $(Cr_{0.77}Co_{0.17}W_{0.03}(Ni,Ta)_{0.03})_{23}C_6$.which can be represented approximately by the formula $(Cr_{18}Co_4WTa)C_6$. The investigation by V Biss(63) gave the MC carbide as $(Ta_{11}Co_4Cr_3ZrTi)C_{20}$

and the $M_{23}C_6$ eutectics as $(Cr_{15}Co_6WNi)C_6$ for the coarse eutectic and $(Cr_{11}Co_9Ni_2W)C_6$ for the fine eutectic.

If not used in the as-cast condition, the component heat treatment is generally limited to solutioning and ageing to control the precipitation of the $M_{23}C_6$ carbides. Solutioning for 4 hours at 1275°C dissolves most of the as-cast $M_{23}C_6$ grain boundary carbides and some intragranular carbides. Solutioning generally increases ductility and this treatment is often useful for improving alloy weldability. Ageing after solution heat treatment for 24 hours at 925°C produces $M_{23}C_6$ and MC in a number of forms including agglomerated carbides, fine semi coherent precipitates and Widmanstatten plates on the {111} planes of the matrix. This heat treatment improves tensile strength but reduces tensile ductility compared to that of as-cast material.

2.12.3 Mould reactivity

Mould reactivity or Intercarbidic Oxidation (ICO) is a problem with MAR M509 particularly in thick sections (Figure 2.20). 'ICO' is evident as particles of ZrO_2 close to the surface of the casting. It is generally believed that the higher the mould preheat temperature and the higher the superheat, the greater the extent of the 'ICO'(60). Casting in air also leads to far greater 'ICO', for this reason MAR M509 is cast under vacuum. Even then the components may have to be surface ground to remove the 'ICO' affected layer.

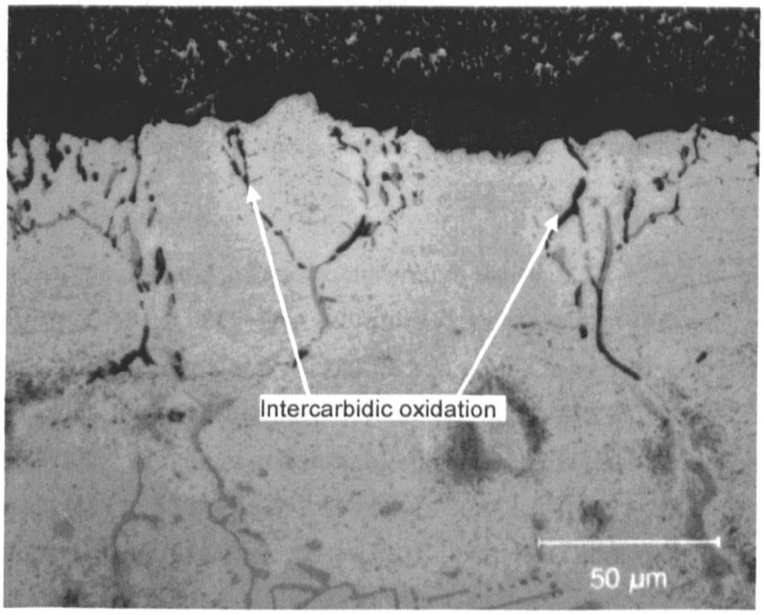

Figure 2.20 Photomicrograph of intercarbidic oxidation at surface of MAR M509 casting.

Some of the explanations for 'ICO' are:

- With the mould in contact with the metal, zirconium and oxygen diffuse into the MC carbides and tantalum diffuses from the carbide into the surrounding matrix(65).

- Zirconium in the molten alloy reacts with less stable oxides in the mould face coat such as silica. The reaction product is zirconia in the casting surface. Since the solubility of zirconium is low in both nickel and cobalt-based superalloys, the bulk of the zirconium is located in the grain boundaries(66).

There are similar mould reaction problems with other alloys that contain highly reactive elements such as hafnium, yttrium and lanthanum.

'ICO' is thought to be detrimental to the performance of a component since the oxidised carbide could act as a crack initiator at the grain boundaries, and because it can lead to poor coatability for both diffusion and overlay coatings. It is considered that cobalt-based superalloys with high zirconium contents always have to be vacuum cast to minimise 'ICO'. However, cobalt-based superalloys are air cast due to cost considerations and 'ICO' affected areas are then mechanically removed by belt sander.

To minimise 'ICO', the composition of MAR M509 has been modified reducing zirconium content from 0.4-0.6% to 0.05% in alloy ECY768.

2.12.4 Thermal ageing

Morrow et al(47) reported that samples aged for 1,000 hours at 815°C showed coalescence and coarsening of the interdendritic and eutectic carbides with precipitation of secondary phases in the γCo dendrites in areas adjacent to the interdendritic eutectics. The second phase precipitates were considered to be $M_{23}C_6$, M_6C, M_7C_3 or a combination of these. The precipitates were often observed in directional patterns characteristic of Widmanstatten carbide precipitation or preferential nucleation of carbides on stacking faults in the γCo solid solution.

Drapier et al(62) investigated the microstructural stability of MAR M509 in samples aged at temperatures from 800 to 1200°C. Thin foil transmission electron microscopy showed, after 100 hours at 800°C the presence of fine (100-250 A) tantalum carbides on the {111} planes of the matrix. With longer times the carbides coarsened, and after 250 hours the carbides were of the order 125 to 300Å with semi coherent $M_{23}C_6$ carbides evident on the {111} planes with dimensions typically 200 to 500Å. After 1,000 hours semi coherent and non coherent tantalum carbides were apparent with isolated coarse $M_{23}C_6$ particles. The microstructure of samples aged at 900°C and 1000°C were essentially similar with the secondary carbides increasing in size with both time and temperature. The tantalum carbide in the 500 hours 1000°C sample had typical dimensions 300Å to 1000Å. Stress enhanced the precipitation reaction and favoured the loss of coherency of the precipitate particles. The precipitation reactions were noted up to 1100°C where after prolonged exposure the $M_{23}C_6$ carbide went into solution and the MC carbides coalesced. At 1200°C all the carbides, except the tantalum carbides which coalesced, were in solution. A similar investigation on samples aged at 815°C for 1,000 hours(63) showed the presence of fine tantalum carbide precipitates along matrix crystallographic planes (Figure 2.21). Woulds and Cass(59) report that M_7C_3 is formed in large castings with slow cooling rates. The carbide is usually contiguous to MC with an almost total absence of the $M_{23}C_6$ - γ matrix eutectics.

Of interest is the report by Morral et al(67) which identifies the phases in MAR M509 as MC, $M_{23}C_6$ and a (CoCrW) unidentified phase. Beltran et al(64) considered MAR M509 to have a high degree of phase stability and did not detect Laves, σ or μ that form in other superalloys during long-term high temperature exposure in any of his samples.

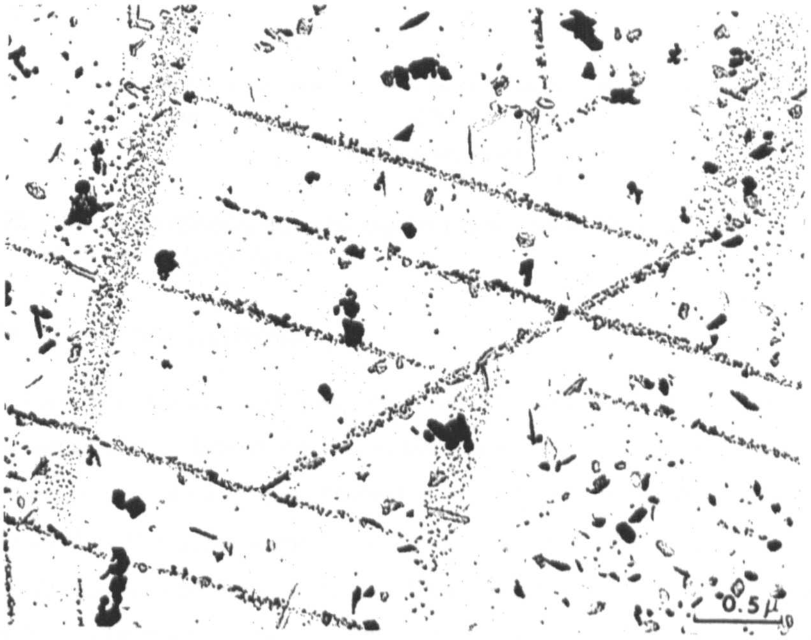

Figure 2.21 TEM extraction replica showing fine tantalum carbide on matrix planes in MAR M509(63).

The age hardening response of as-cast MAR M509 during ageing at various temperatures is shown in Figure 2.22(62). Drapier et al(62) considered the initial increase in hardness over the first 10 hour period to be the result of the precipitation of fine semi-coherent carbides. The decrease evident in the 900°C and 950°C hardness, after ~4500 hours, is considered to be the result of significant carbide coarsening. The trend evident at 1100°C, where the hardness decreases appreciably after a slight increase is likely to be the result of carbide coalescence and carbide solutioning.

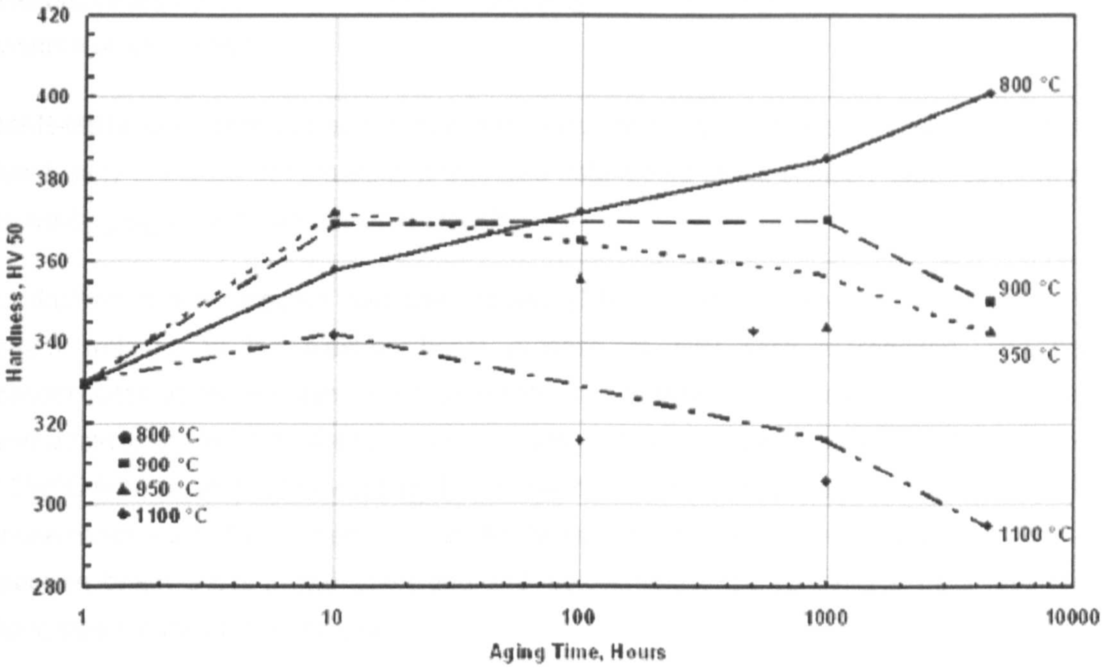

Figure 2.22 Plot of hardness against ageing time for MAR M509 taken from Drapier et al using Ungraph(62).

2.12.5 Oxidation and hot corrosion

Most cobalt-based superalloys are less oxidation resistant than the aluminium containing nickel based superalloys. Cobalt-based superalloys rely on Cr_2O_3 scale formation for oxidation resistance, this oxide is less stable and protective than the Al_2O_3 scale that forms on high strength nickel based superalloys(5). The alloy chemistry of MAR M509 was designed to ensure that no protective coating was required for oxidation and corrosion resistance during service under both static and cyclic loading conditions(68). The general matrix oxidation of MAR M509 is consistent with simple Co-Cr binary alloys where a layered oxide structure forms with Cr_2O_3 at the oxide-alloy interface and CoO at the air-oxide interface(69,70). Cobalt-based superalloys are, however, more hot corrosion resistant than nickel based superalloys and are thus useful for industrial and marine turbine applications(30).

2.12.6 Rejuvenation and repair

The weldability of MAR M509 is considered satisfactory with care. Chase and Beltran(43) found hot cracking in the HAZ to be the main problem with gas tungsten arc welds. The hot cracking was primarily associated with carbide precipitation. The pseudo-eutectic $M_{23}C_6$ carbides undergo remelting in the fusion zone during welding. Solidification, diffusion, nucleation and growth produces carbides with a higher surface area to volume ratio in the HAZ, which enhances brittle crack propagation. The Chinese script tantalum rich MC carbide in MAR M509 plays little or no role in weld hot cracking as it is considered stable to the melting point of MAR M509. Since the MC carbide does not go into solution, the post weld heat treatment is ineffective in terms of altering MC morphology or distribution.

Recommended precautions to limit hot cracking are minimising both the heat input and the volume of weld metal.

MAR-M918 was identified as the best filler alloy for the gas tungsten arc process that was least likely to induce hot cracking. It was also determined that a solution heat treatment prior to welding significantly reduces hot-cracking.

In addition to the tungsten inert gas process (TIG), Chase and Beltran(43) studied electron beam welding. In the electron beam process no filler alloy is required. The highly concentrated electron beam heat source produces a smaller molten volume, less shrinkage and a narrower HAZ than the tungsten inert gas process. The base material was solutioned at 1230°C for 4 hours prior to welding. The as-welded material properties show similar trends to those observed in TIG welded material. All the tests carried out on the tungsten inert gas and electron beam welds in the as-welded and welded/solutioned specimens were reported to have failed in the parent material.

2.13 NiCoCrAlY Coating

Overlay coatings of the NiCoCrAlY type are used extensively for their oxidation resistance in hot section components in gas turbine engines. The addition of cobalt significantly improves coating ductility over the NiCrAlY and CoCrAlY coatings(4). Commercial NiCoCrAlY coatings are based on the γ FCC and β (NiCo)Al phases but they may in addition contain phases such as γ', αCr and σ (CrCo)(40).

Baufeld et al(42) describe thermo-mechanical fatigue testing of a NiCoCrAlYRe bond coat with a 7 wt.% Y_2O_3 stabilised ZrO_2 top coat on a MAR M509 substrate. No microstructural analysis of the coating is reported other than to comment on the failure of the bond coat which was facilitated by a very brittle chromium-carbide phase, which formed at high temperatures at the interface between the MAR M509 and the bond coat. Czech et al(71) report the microstructure of the aged NiCoCrAlYRe bond coat as γ-(Ni,Cr) matrix with grains of β- NiAl, α-Cr and σ-(Co,Cr).

Quadakkers(40) notes that in coatings which possess a high chromium activity, precipitation of fine carbides can occur throughout the coating or as a near continuous band at the coating/substrate interface. The carbides form as a result of the affinity of chromium for carbon which diffuses from the substrate into the coating. In addition γ' stabilising elements such as tantalum and titanium have been found to diffuse from the substrate through the coating. After long time's tantalum can form brittle intermetallic compounds at the coating/TGO interface and titanium can promote chromia formation, thereby hampering the protective alumina scale.

Rehfeldt et al⁽⁷²⁾ confirmed by selected area electron diffraction the presence of β, γ′ and a high chromium phase in an as sprayed NiCoCrAlY coating. Although the lattice structure of the high chromium phase could not be determined uniquely it was considered that the high chromium content (~60 at.%) pointed to σ phase. EDS results from the SEM and TEM are detailed in Table 2.9.

	Ni	Cr	Co	Al	Si	Hf	Y
Nominal bulk composition	42.11	16.51	18.0	22.46	0.54	0.04	0.34
β in bond coat *	45	8	14	31	1	1	
β in bond coat **	41	12	15	29	1		2
γ′ in bond coat *	36	26	24	12	1	1	
γ′ in bond coat **	37	23	24	14	1		1
γ′ single phase alloy**	34	27	26	11	1		1
Cr rich phase in bond	16	68	9	5	2		

*measured by TEM/EDS
** measured by SEM/EDS

Table 2.9 Composition of the bond coat phases identified in a NiCoCrAlY coating in the as sprayed condition⁽⁷²⁾ (at.%).

Hasegawa and Kagawa⁽⁷³⁾ investigated the changes in the microstructure of a NiCoCrAlY bond coat following heat treatment at 1150°C for up to 100 hours. The initial microstructure of the bond coat was considered to be a fine mixture of β and γ′. EDS measurements of the phases are detailed in Table 2.10.

Ageing time (h)	Phase	Ni	Co	Cr	Al
0	As-sprayed BC	43.6	18.2	16.8	21.4
10	Bright (γ/γ′)	44.1	21.1	20.4	14.4
50	Bright (γ)	50.0	17.5	17.6	14.9
100	Bright (γ)	52.8	16.5	18.4	12.3
10	Dark (β)	47.7	9.4	5.3	37.6
50	Dark (β)	49.0	8.7	5.6	36.7

Table 2.10 EDS composition of an as sprayed NiCoCrAlY and the EDS composition of bright and dark phases after ageing⁽⁷³⁾ (wt.%).

Measurements of the width of the outer (Zone I_a) and inner (Zone I_b) denuded zones and the central β and γ′ layer (Zone II) were taken and plotted (Figure 2.23). The results show that after 100 hours the central β and γ′ layer had disappeared. The authors suggest that as the total thickness of Zone I and Zone II are almost the same ($h_{zoneI}{}^{a}+h_{zoneI}{}^{b}+h_{zoneII}$ ~100 μm) the thickness of the bond coat layer is independent of heat exposure time t_h.

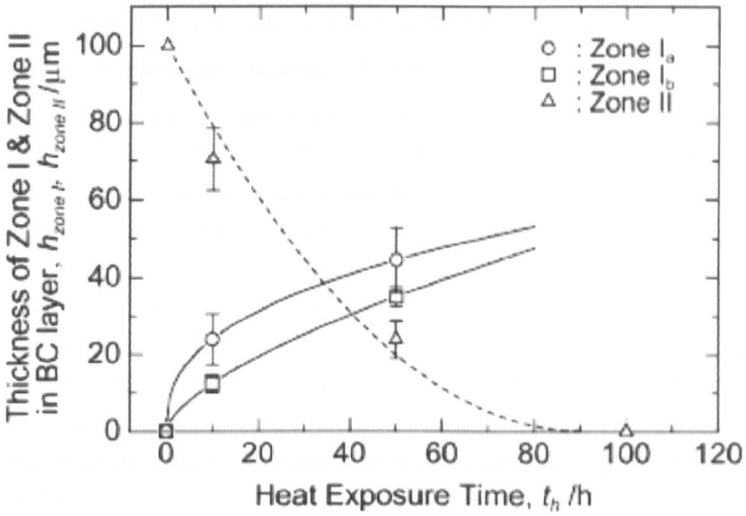

Figure 2.23 Thickness of Zones I and II in the bond coat layer as a function of heat exposure time(73).

Amdry 997 is a NiCoCrAlY coating with 3.5-4.5 wt.% tantalum. The addition of tantalum to a NiCoCrAlY coatings is reported to act as a solid solution strengthener for γ and γ´, reduce interdiffusion of nickel, improve oxidation and hot corrosion resistance and reduce the thermal expansion coefficient(74). Researchers have also suggested that tantalum ties up titanium and carbon diffusing from the substrate into the overlay coating, preventing these elements from decreasing the oxidation resistance of the coating(75).

There are no reports dealing with Amdry 997 on a MAR M509 substrate however a small number of reports dealing with Amdry 997 have been identified. Frances et al(76) carried out oxidation studies of an Amdry 997 coating on cast Amdry 997 plates. Cast Amdry 997 plates were used to avoid interdiffusion between the substrate and coating. The coated samples were given an homogenisation heat treatment of 48 hours at 1100°C in argon followed by ageing for 800 hours at 850°C. The coating phases were identified by EDS as γ, γ´, β, σ and M_5Y. The EDS compositions from the report are detailed in Table 2.11.

wt.%	Ni	Co	Cr	Al	Ta	Y
Amdry 997	40.2-48.3	22-24	18-21	7.5-9.5	3.5-4.5	0.7-0.8
γ	38.9	28.4	24.8	4	3.9	
γ´	9.4	12.9	6.1	8.9	12.7	
β	58.5	13.9	6.2	20.6	0.8	
σ	13.8	29	55.6	0.6	1	
M_5Y	58.1	8.1	2.7	5.8		25.3

Table 2.11 EDS composition of phases in Amdry 997 coating aged for 800 hours at 850°C(76) (wt.%).

Wells[9] identified the initial coating phases in Amdry 997 as γ and β phase plus white spots the composition of the phases are detailed in Table 2.12.

	Ni	Co	Cr	Al	Ta	W	Y	O	Hf
γ	36.2	26.7	24.3	5.6	3.7	1.8			
β	54.7	15.3	7.1	18.7		1.0			
white	44.8	12.3	5.0	6.9	17.5	7.4	2.4	1.0	2.3

Table 2.12 EDS composition of coating phases in as deposited Amdry 997 coating[9] (wt.%).

Di Martino[77] investigated the microstructural changes that occurred as a result of thermal exposure of Amdry 997on a DCT6 substrate. In the as-received condition, the coating microstructure was considered to comprise γ domains containing finely dispersed γ' and β phase (Table 2.13).

	Ni	Co	Cr	Al	Ta	Ti
γ/γ'	63.5-64.4	10.5-12.1	4.0-5.2	7.5-9.0	7.8-9.7	0.5-1.6
β	59.4-60.7	11.6-13.3	4.0-5.5	15.3-20.0	1.7-4.5	

Table 2.13 EDS analysis of as sprayed coating phases in Amdry 997 coating on DCT6 substrate[77] (wt.%).

The effects of ageing time and temperature on the bulk microstructure of the coating is summarised in Table 2.14.

Ageing temperature	Ageing time	Bulk coating microstructure
850°C	200-10,000 hrs	γ, γ' and β (transformation of β to γ' visible after 2,000 hours)
950°C	200-10,000 hrs	γ, γ' and β (β not identified after 5,000 hours)
1000°C	1,000 hr	γ and γ' (a small volume fraction of β was evident in centre of coating)
1050°C	200-10,000 hrs	Coarse γ' and small fraction of β in γ matrix. (β no longer evident after 2,000 hours, bulk of coating γ after 10,000 hours) Tantalum and titanium rich carbides and yttrium rich precipitates evident in coating after 10,000 hours.

Table 2.14 Bulk coating microstructural changes in Amdry 997 on DCT6 substrate as a result of ageing between 850-1050°C for times up to 10,000 hours[77].

2.14 Summary

This chapter has reviewed a number of different aspects of materials used for gas turbine engines, primarily for power generation. Cobalt-based superalloys used in gas turbines are normally characterised by a cobalt-chromium FCC matrix containing second phases, which are principally carbides. Components can be used in the as-cast, forged or heat treated condition. The heat treatment generally consists of a solution treatment followed by ageing to precipitate fine carbides. The primary carbides are metastable and subsequent ageing or service at high temperatures will result in secondary carbide precipitation and carbide degeneration. The strength of a cobalt superalloy is derived from both solid solution and precipitation strengthening. Primary carbides inhibit grain boundary sliding, whereas fine secondary carbides pin dislocations. The weldability of cobalt-based superalloys is considered to be generally good.

Three specific superalloys used for these applications have been discussed in detail, particularly with respect to the formation of second phases during service. The carbides formed in the three superalloys reviewed are:

FSX 414 - Primary carbides are Cr rich $M_{23}C_6$ eutectic carbides with secondary $M_{23}C_6$ carbides forming during heat treatment and service.

NP 222 - Primary carbides are Ta, Ti, Nb rich MC carbides with Cr rich $M_{23}C_6$ carbides forming on the grain boundaries during heat treatment.

MAR M509 - Primary carbides are Ta rich MC carbides and Cr rich $M_{23}C_6$ eutectic carbides with secondary $M_{23}C_6$ carbides forming during heat treatment and service.

In service the components may be subject to high temperature oxidation, corrosion and erosion as a result of the working environment. In aggressive environments the components may be coated with high temperature oxidation and corrosion resistant coatings. As the turbine inlet temperatures rise, to gain improvements in efficiency, the use of thermal barrier coatings has become necessary to limit the temperature of the components. The application and type of coatings oxidation/corrosion resistance have been discussed with particular emphasis on NiCoCrAlY overlay coatings.

Microstructural changes as a function of temperature and time in service will form a large part of the experimental work within this thesis and the results are discussed in the context of predicting the remaining service life of components in subsequent chapters.

3 Experimental Methods

This investigation covers the characterisation of two cobalt-based superalloys, FSX 414, MAR M509 and a high cobalt (19 wt.%) nickel superalloy NP 222. In addition the effects of a NiCoCrAlTaY coating on the MAR M509 superalloy have been investigated. This chapter discusses the materials investigated, the test techniques employed and the analytical methods employed.

The techniques used to analyse the samples include Vickers hardness testing, optical microscopy, scanning electron microscopy (SEM), energy dispersive spectroscopy (EDS), wavelength dispersive spectroscopy (WDS) and X-ray diffraction (XRD). In addition, a focused ion beam field emission gun scanning electron microscope (FIB FEGSEM) has been used to produce thin foils for transmission electron microscopy (TEM) and parallel electron energy loss spectroscopy (PEELS). Thermodynamic equilibrium calculations were carried out for all of the materials by means of the JMatPro software package developed by Thermotech(1).

3.1 Materials

3.1.1 Superalloys

The chemical compositions of the three sets of samples used in the present study are shown in Table 3.1. The superalloys were vacuum melted and cast into plates 50 mm wide, 100 mm long and 6 mm thick. Casting conditions were controlled to give a grain size equivalent to that found in cast vanes. The FSX 414 and NP 222 plates were given standard solution and precipitation heat treatment described in Table 3.2. After heat treatment the FSX 414 and NP 222 plates and the as-cast MAR M509 plates were aged at 800, 850, 900, 950, 1000 and 1050°C for times up to 25,000 hours in air.

Sections were cut from the aged plates for metallographic preparation (optical and SEM), hardness measurements and carbide extraction. The optical and SEM cobalt-based samples were electrolytically etched in 10% hydrochloric acid in methanol and the nickel based samples in a solution of 1% citric acid, 1% ammonium sulphate in water. Etching the cobalt-based superalloys in 10% hydrochloric acid in methanol dissolves the matrix leaving the carbides and secondary phases in relief. Etching the nickel based NP 222 in 1% citric acid, 1% ammonium sulphate dissolves the matrix leaving the γ', carbides and secondary phases in relief.

	FSX 414	MAR M509	NP 222
C	0.24	0.6	0.09
Si	0.78	0.07	0.03
Mn	0.54	0.01	<0.01
P	0.006	0.005	<0.005
S	0.005	0.002	<0.001
Cr	30.0	23.7	22.4
Mo	0.14	0.05	0.01
Ni	10.4	9.96	balance
Al	0.01	0.18	1.22
Co	balance	balance	19.0
Nb	-	0.03	0.82
Ti	-	0.21	2.37
Ta	-	3.62	0.97
V	-	0.01	0.01
W	7.2	6.97	2.06
Fe	0.72	0.3	0.03
B	0.011	<0.001	0.007
Zr	<0.01	0.33	0.02

Table 3.1 Chemical composition of cast plate samples FSX 414, NP 222 and MAR M509 (XRF), wt.%.

Alloy	Standard heat treatment
FSX 414	Solution: 1150°C ±10°C in vacuum for 4 hours. Argon gas fan quench Precipitation: 980°C ± 10°C in vacuum for 4 hrs. Argon gas fan quench
NP 222	Solution: 1150°C ± 10°C in vacuum for 4 hours. Argon gas fan quench Precipitation: 800°C ± 5°C in vacuum for 8 hours. Argon gas fan quench

Table 3.2 FSX 414 and NP 222 plate solution and precipitation heat treatments prior to ageing.

3.1.2 Coated samples

The coating trials were carried out on cast plates of MAR M509 with and without inter-carbidic oxidation (Figure 3.1). Inter-carbidic oxidation is covered in Chapter 2.12.3.

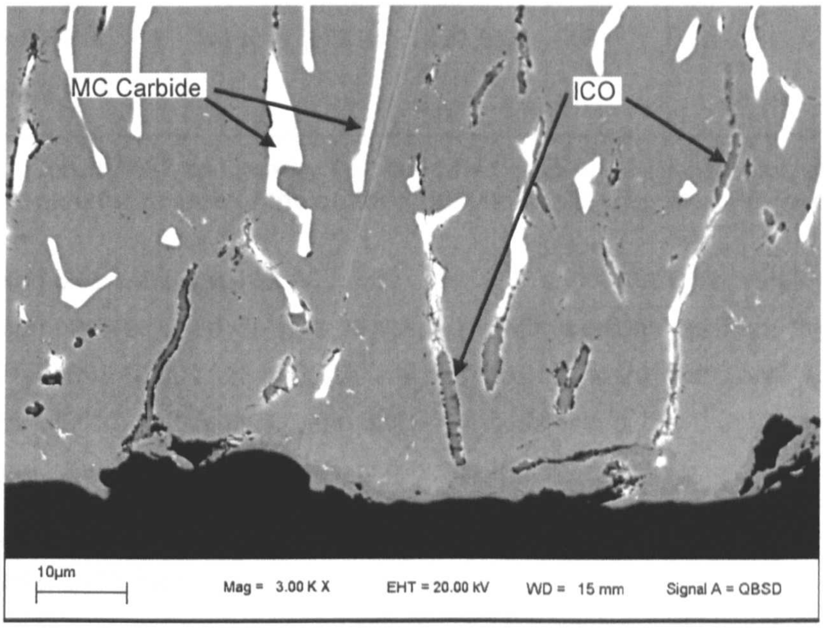

Figure 3.1 SEM BSE micrograph showing 'ICO' adjacent to the outer surface of the MAR M509 cast sample.

The 100 mm long 50 mm wide plates were cut to produce 40 mm square 6 mm thick samples. Before coating half of the samples were surface ground removing 0.5 mm of material from all surfaces removing all traces of 'ICO' from the samples. Coating of the samples was carried out by a commercial coating company to an existing coating specification. Both sets of samples were coated with a three layer system of low pressure plasma spray (LPPS) MCrAlY bond coat, LPPS MCrAlY key coat and APS thermal barrier coating (TBC). The alloy for the bond coat was Amdry 997 (NiCoCrAlTaY), the key coat Amdry 962 (NiCrAlY) and the TBC, Sulzer Metco 204 B-NS 8 wt.% yttria stabilized zirconia. The specified composition of the Amdry 997 and Amdry 962 alloys are given in Table 3.3.

The bond coat thickness was specified as 225 ± 25 μm, the key coat thickness as 15-30 μm and the TBC thickness as 200 ± 50 μm. On completion of the bond coat and key coat, and prior to air plasma spraying (APS) of the ceramic TBC, the parts were heat treated in vacuum at 1000 ± 10°C for 4 hours followed by an argon gas fan quench to ambient temp at 40-50°C/min.

Wt.%	Ni	Cr	Co	Al	Ta	Y
Amdry 997	47.6	20	23	8.4	4	0.6
Amdry 962	Bal	21-23		9-11		0.8-1.0
Amdry 997 as deposited EDS	44.5	19.7	22.9	7.8	4.6	0.5

Table 3.3 Amdry 997 and Amdry 962 specified coating compositions, and EDS measurements of the coating bulk analysis prior to ageing (wt.%).

The coated samples were aged at 800, 850, 900, 950 and 1000°C for times up to 25,000 hours. One sample was used at each temperature with sections cut from the samples at 1,000, 2,000, 5,000, 10,000, 15,000, 20,000 and 25,000 hours. Additional samples were taken from the 1000°C sample at 500 and 3,000 hours. Ageing of the 1000°C sample stopped at 15,000 hours when the entire sample had been used.

For the purpose of the metallurgical investigation the coating was broadly split into the following areas (Figure 3.2):

Outer denuded layer - forms on the outer edge of the coating local to the thermally grown oxide, no γ' or β.

Bulk – central section of coating with γ' and/or β present.

Inner layer – local to interface with increased levels of γ' and or αCr when compared to the bulk.

Inner denuded layer - forms local to the interface with no γ' or β present.

Interface - junction between bond coat and MAR M509 substrate.

Interdiffusion layer – local to the interface in the MAR M509 where microstructural changes have occurred.

It should be noted that the inner layer and the inner denuded layer exist at the same position at different times of the coating life (mutually exclusive).

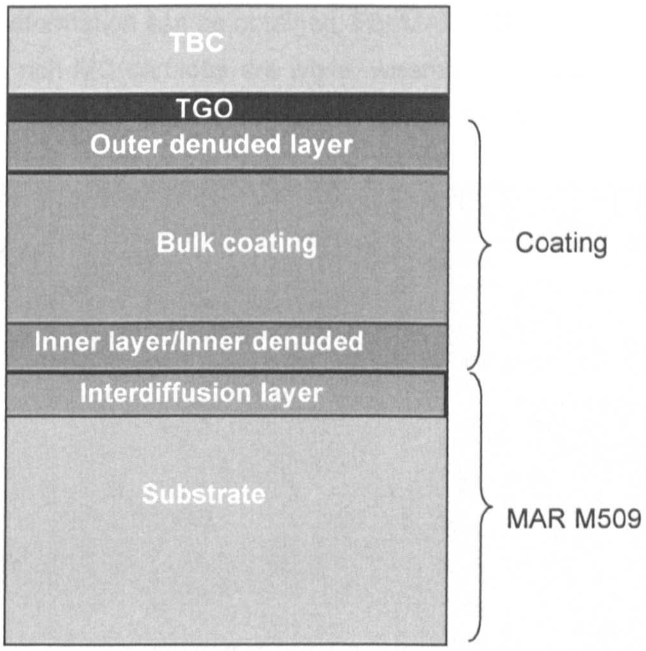

Figure 3.2 Schematic diagram illustrating the positions of the layers formed in the coating and the interdiffusion layer with the substrate.

3.2 Optical Microscopy

Following preparation and etching the samples were examined on an Olympus BX60M optical microscope. Optical microscopy allows a rapid assessment of the quality of sample preparation and any microstructural changes in the samples. Optical images were taken on a Reichert MeF-3 microscope with an attached digital camera.

3.3 Scanning Electron Microscopy (SEM)

Samples were examined on a Leo 1455 VP SEM equipped with a fixed backscattered electron detector at accelerating voltages of 15-20kV. The SEM is fitted with Oxford Instruments EDS and WDS systems for measuring chemical composition.

Images in the SEM were viewed either in secondary electron (SE) or backscatter (BSE) modes. Secondary electrons have low energies (< 50 eV) and are created from the near surface of the sample. Secondary electrons are therefore sensitive to topography, giving good resolution and depth of field, see for example Figure 3.3.

Backscattered electrons, with energies greater than 50 eV, are produced within the interaction volume beneath the incident beam illustrated in Figure 3.4. The major advantage of backscattered electrons is that the intensity of the signal is proportional to the atomic number of the elements from which it is derived, which results in higher atomic number elements appearing brighter than lower atomic number elements. The image from the backscatter detector shows little if any topographical information. However, the backscatter detector can have four quadrants so that if two are switched off then a mixed image showing topographical and compositional information can be obtained. For MAR M509 using the backscatter imaging mode the tantalum rich MC carbides are white, whereas the chromium rich $M_{23}C_6$ carbides and the γ matrix are grey due to the difference in atomic number contrast (Figure 3.5).

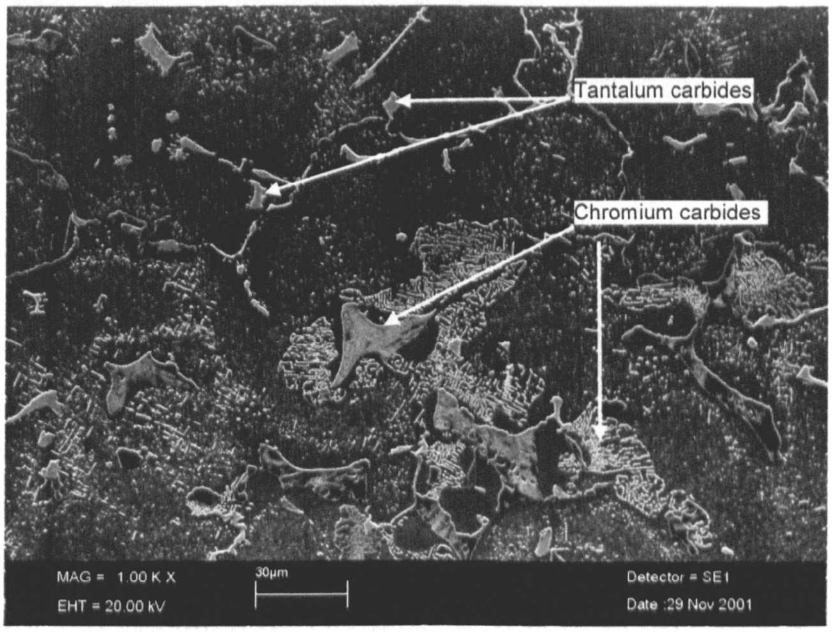

Figure 3.3 SEM SE image of MAR M509 showing tantalum rich and chromium rich carbides.

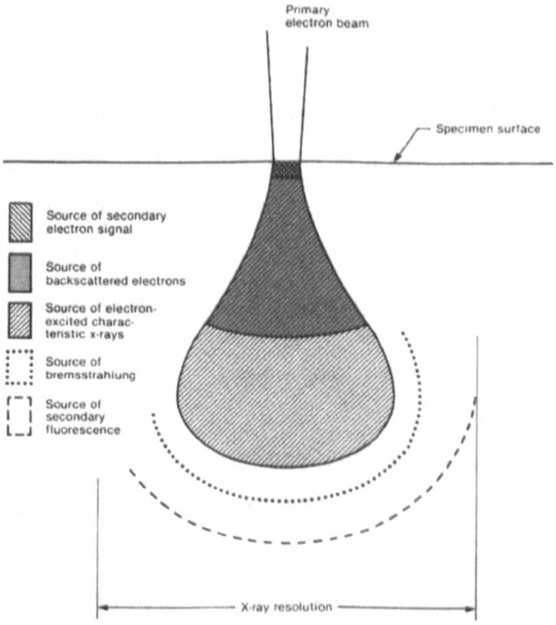

Figure 3.4 Illustration of interaction volume for different electron-specimen interactions(78).

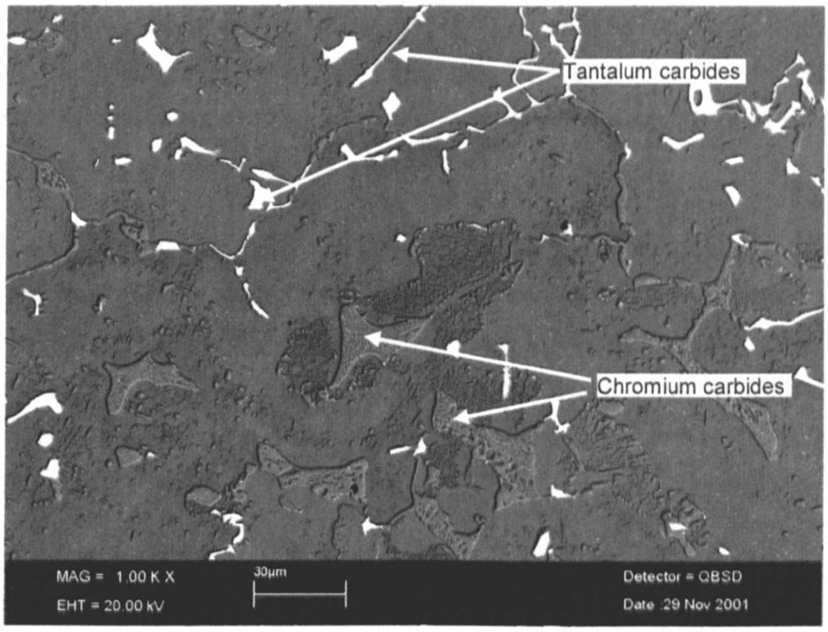

Figure 3.5 SEM BSE image of MAR M509 showing tantalum rich carbides (white) and chromium rich carbide (grey).

3.4 Energy and Wavelength Dispersive Spectroscopy (EDS and WDS)

Both EDS and WDS use the characteristic X-rays generated from a sample bombarded with electrons to identify the elemental constituents in the sample. By determining the energies or wavelengths of the X-rays emitted, the elements present in the sample can be identified (qualitative analysis). The rate at which the characteristic X-rays are detected is used to measure the amounts of elements present (quantitative analysis). Both EDS and WDS collect X-rays to identify individual elemental components in a sample but with different approaches. In EDS data are collected for all energies and are displayed as a histogram of counts versus X-ray energy. In WDS separation of the characteristic X-rays emitted by the specimen according to their wavelengths is based upon diffraction according to Braggs law

$$\lambda = 2d\sin\theta$$

By using suitable diffraction crystals, the constituent wavelengths of the characteristic spectrum emitted by the specimen can be split and detected at different spectrometer positions. The main advantages of WDS are better peak resolution and peak separation with an increased peak to background ratio. The combination of better resolution and the ability to deal with higher count rates allows WDS to detect elements at typically an order of magnitude lower concentration than EDS. The improved resolution of WDS allows lines to be resolved that are obscured by peak overlaps in the EDS spectrum. Analysis by WDS is slow and is therefore used only for elements whose peaks overlap or where increased accuracy is required.

The current work has been carried out using an Oxford Link Pentafet ISIS system and Microspec WDS-400 attached to a Leo 1455 VP SEM operating Oxford INCA Energy+ software. The INCA Energy+ software combines the outputs of the EDS and WDS spectrometers to provide a single analysis.

Analysis was carried out at a gun voltage of 15 – 20 kV with cobalt as the quantitative optimization standard. The quantitative calibration is used to establish spectrometer gain and effective beam current. Elements were entered into the program using the standardless analysis option. Unless stated the totals are normalised to 100%. The normalisation is carried out by altering the effective value of the beam current internally so that the sum of apparent concentrations totals 100%.

Both EDS and WDS allow the determination of the composition of phases and particles that are larger than the interaction volume. If the size of the particle is comparable to or smaller than the beam spot size or thinner than the interaction volume, the composition obtained will contain contributions from the surrounding phases. Only phases with a surface width >2μm were analysed. A number of phases in the samples were smaller than 2μm, in these cases the composition is considered to be indicative only and were further investigated by TEM.

For each EDS/WDS analysis given in the current work a minimum of 10 phases with a similar elemental signature were analysed and the results averaged.

The EDS detector attached to the Leo 1455 VP SEM has a beryllium window which precludes the quantitative analysis of oxygen. However if oxygen is present it will be detected and will show as an oxygen peak on the EDS trace.

It is considered that WDS can detect carbon but requires additional carbon standards to give a quantitative result. For the purpose of this investigation any carbon analysis is considered to be indicative only.

3.5 Identification of phases

Three microscopes were used for identifying phases: an FEI Nova Nano Lab 600 dual beam (FEG-SEM/FIB) system, a Jeol 200FX TEM fitted with Oxford INCA X sight and a Philips Tecnai F20 FEG TEM with an Oxford LINK ISIS 300 EDS system and a GATAN DigiPEELS spectrometer.

3.5.1 TEM sample preparation (FEG SEM/FIB)

Within this research, early attempts to produce TEM samples by carbon extraction replicas and perforated electropolished thin foils proved problematic due to the large carbides present in the cobalt superalloys. However, specimens were prepared for TEM directly from the bulk SEM samples by focused ion beam (FIB) milling using a FEI Nova Nano Lab 600 dual beam

(FEG-SEM/FIB) system. The FEI Nova Nano Lab 600 system, using the "lift out" technique, provides a rapid method of manufacturing electron transparent cross sections from a specific site of interest.

The sequence of operation to produce a thin foil for the TEM is shown in Figure 3.6. The first part of the sequence is carried out automatically after the area of interest has been defined. A platinum layer ~1 µm wide is deposited across the area of interest to mark the area and to protect the underlying surface from subsequent ion beam milling. Trenches are cut either side of the platinum line (Figure 3.6 (a)). The sample is tilted (7°) and the bottom and sides of the specimen are cut (Figure 3.6 (b)) leaving a small ligament on either side. The rest of the sequence is carried out under manual control. A tungsten extraction needle (Omniprobe micromanipulator) is FIB micro welded with platinum to the sample (Figure 3.6 (c)). The sample is cut away (Figure 3.6 (d)), manipulated to and micro welded to a TEM grid. The extraction needle is cut away from the specimen (Figure 3.6 (e)) and further thinning is carried out by FIB milling at successively smaller beam currents to enable the production of a uniform thin section (Figure 3.6 (d)). The maximum apparent thickness of the lift out specimen in the FIB SEM is considered to be 100 nm.

The milling conditions used to produce the samples after lift out are

Initial thinning – beam current 1 nA - sample ~750 nm thick

Second stage polishing – beam current 0.5 nA – sample thickness reduced to ~500 nm.

Final polishing – beam current 0.1 nA – sample thickness reduced to ~250 nm.

The initial stage of polishing is carried out on both sides of the sample at an angle 1.2° either side of straight down (straight down is 52°). The final stage of polishing is carried out at 1° either side of straight down. All ion milling is carried out at 30 kV.

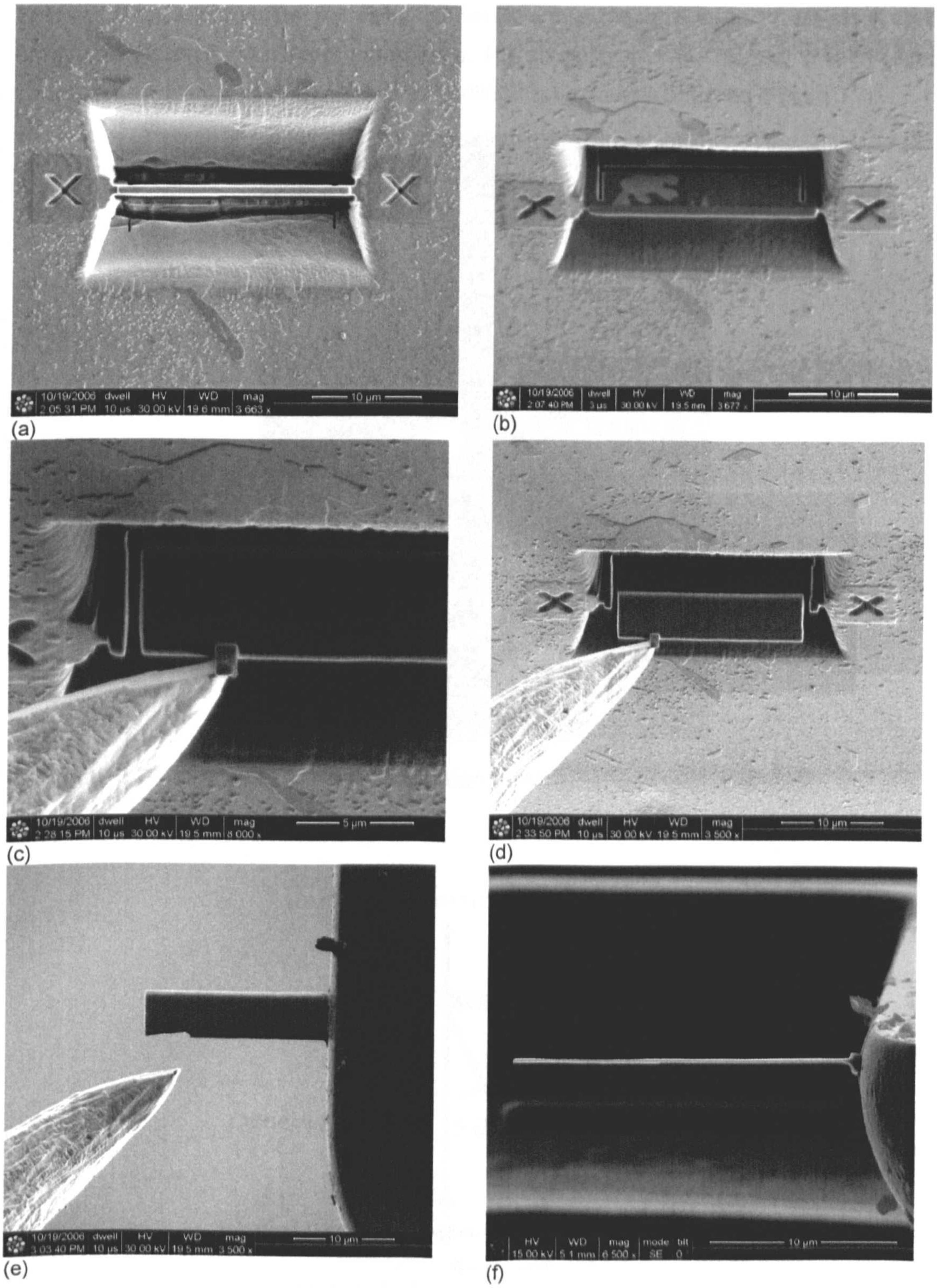

Figure 3.6 **FIB SEM sequence illustrating (a) (b) initial milling, (c) (d) lift out and (d) thin foil attached to a TEM grid and (e) final thinning of thin foil.**

3.6 Transmission Electron Microscopy (TEM)

Selected area electron diffraction using thin foils is one of the most reliable methods available for the identification of unknown precipitates. The precipitates of interest are chosen using a selected area aperture and a corresponding diffraction pattern is obtained (Figure 3.7).

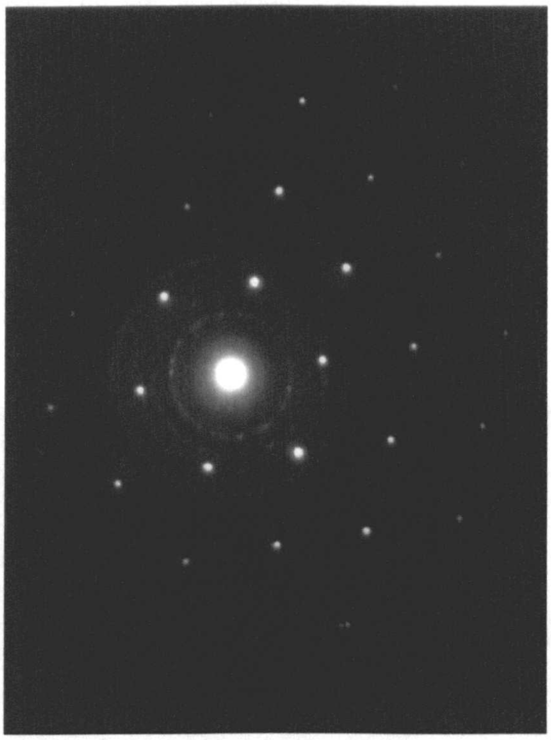

Figure 3.7 TEM selected area diffraction pattern.

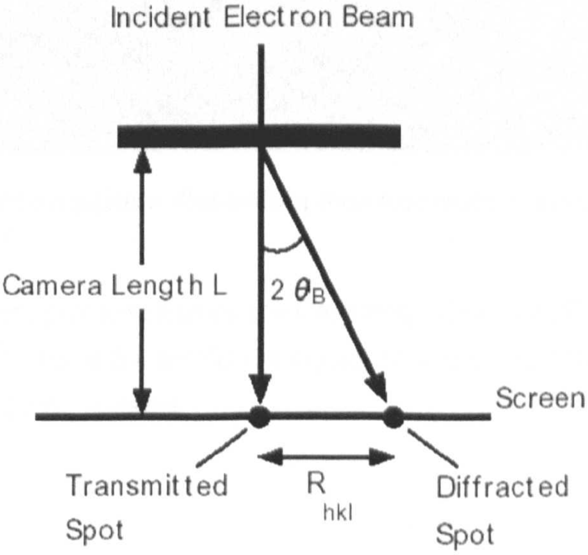

Figure 3.8 Schematic diagram of the geometry of diffraction in transmission electron microscopy.

In electron diffraction the distance measured between two different spots on a pattern R_{hkl} (Figure 3.8) is related to the spacing d_{hkl} for the planes of Bragg indices hkl by;

$$R_{hkl}d_{hkl} = L\lambda = \text{camera constant}$$

Where L is the camera length and λ is the wavelength associated with the electrons for a given accelerating voltage. The camera length used for this work was 100 mm and the wavelength 0.025 Å at 200kV.

Two electron diffraction patterns were obtained at different specimen positions from each of the phases under examination. Figure 3.9 shows a selected area diffraction pattern. The spot electron diffraction patterns were indexed by selecting a base plane of spots, measuring the distance between spots (R_1) on this plane and then measuring the position of two further spots (R_2 and R_3) and their angle with the base plane (θ_{1-2} and θ_{1-3}).

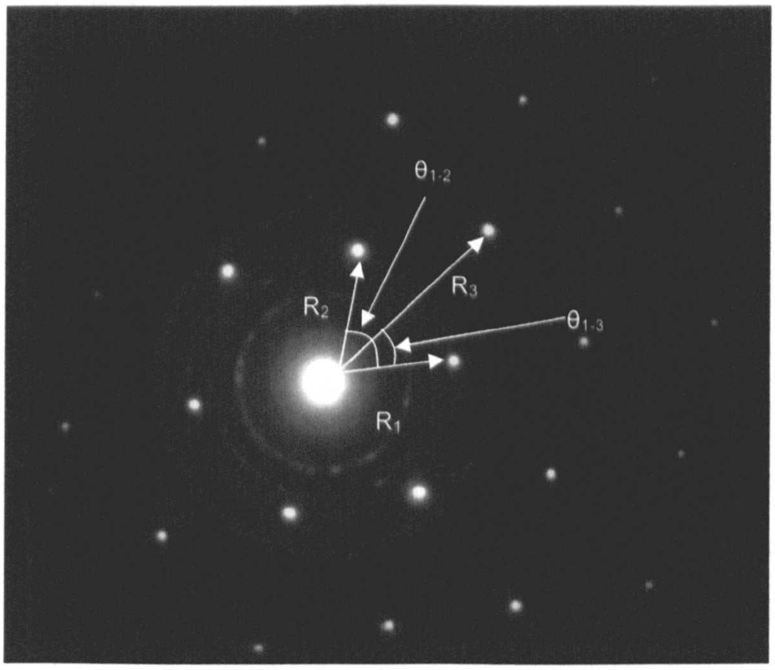

Figure 3.9 Diffraction pattern illustrating measurement of spot distances and angles.

The measurements were processed using the Cambridge University Practical Crystallography software Version 1.6(79). Table 3.4 details the crystal structure and lattice parameters used to index the electron diffraction patterns.

Phase	Basic crystal structure	Lattice parameter Å		PDF card
		a_o	c_o (b_o)	
Al_2O_3	Hexagonal	5.544	9.024	26-31
Al_2O_3 α	Hexagonal	4.758	12.991	10-173
Al_2O_3 β	Hexagonal	5.64	22.65	10-414
Al_2O_3 γ	Cubic	7.9		10-425
Al_2O_3 δ	Tetragonal	7.943	23.5	16-394
AlNi	Cubic	2.887		20-19
$AlNi_3$	Cubic	3.561		9-97
γ′	FCC	3.561 - 3.568		(4)
Al_3Ni	Orthorhombic	6.598	4.802	2-416
Al_3Ni_2	Hexagonal	4.036	4.9	14-648
$AlNi_2Ti$	Cubic	5.85		19-36
Ni_3Ti (η)	Hexagonal	5.093	8.276	5-723
η	Hexagonal	5.09-5.12	8.31-8.35	(80)
Ni_3Al	Tetragonal	3.78	3.28	21-8
Ni_3(AlTi)	Cubic	3.575		18-872
Co_2W	Hexagonal	4.73	7.70	(67)
Co_3W	Hexagonal	5.13	4.128	2-1298
Co_7W_6 (μ)	Hexagonal	4.751	25.67	2-1091
CrCo	Tetragonal	8.81	4.56	9-52
NiCoCr (σ)	Tetragonal	8.85	4.59	21-1271
Laves	Hexagonal	4.75 – 4.95	7.70-8.15	(4,80)
$Co_3W_6C_4$	Hexagonal	7.826	7.826	6-616
Co_3W_3C	FCC	11.112		27-1125
Co_6W_6C	FCC	10.897		23-939
Cr (α)	Cubic	2.8839		6-694
TaC	Cubic	4.4555		19-1292
(TiTaNb)C	FCC	4.3-4.7		(4,80)
$(CoCrNi)_{23}C_6$	Cubic	10.64		11-545
$Cr_{23}C_6$	Cubic	10.638		14-407
$M_{23}C_6$	FCC	10-5-10.8		(4,80)
M_6C	FCC	10.85 – 11.75		(4)
Cr_7C_3	Hex (trig)	13.98	4.523	11-55 0
Cr_7C_3	Orthoganal	7.02	4.53 (12.15)	36-1482
M_7C_3	Hexagonal	13.982	4.506	(4)
Cr_3C_2	Orthorhombic	11.46	2.821	14-406
Cr_2C	Hexagonal	2.79	4.46	14-519
Zr	Hexagonal	3.232	5.147	5-665

Phase	Basic crystal structure	Lattice parameter Å		PDF card
		a_o	c_o (b_o)	
Zr	Hexagonal	5.039	3.136	26-1399
ZrO	FCC	4.62		20-684
ZrO_2	Cubic	5.09		27-997
ZrO_2	Tetragonal	3.64	5.27	24-1164
ZrO_2	Tetragonal	5.12	5.25	17-923
ZrO_2	Hexagonal	3.643	9.05	37-31
ZrO_2	Monoclinic	5.1477	5.3156	13-307
$ZrO_{0.35}$	Hexagonal	5.6295	5.1975	17-385
ZrO_3	Rhombohedral	5.563	31.185	22-1025
Y_2O_3	BCC	10.604		25-1200
Y_2O_3	Hexagonal	3.81	6.08	20-1412
$YO_{1.458}$	Monoclinic	14.009	8.791 (3.5) 96.76°	39-1063
YAl	Cubic	3.754		20-66
Al_3Y	Hexagonal	6.26	4.58	30-50
Al2Y	FCC	7.86		29-103
YAl_3	Rhombohedral	6.20	21.13	20-67
YAl_3	Cubic	4.32		20-70
Y_3Al_2	Tetragonal	8.24	7.65	20-73
Y_5Al_3	Hexagonal	8.84	6.5	39-775

Table 3.4 Details of crystal structure and lattice parameters tested to index electron diffraction patterns.

3.6.1 Parallel Electron Energy Loss Spectrometry (PEELS)

In order to detect the presence of carbon, particularly in the samples containing chromium rich precipitates, the thin foils were examined in a Philips Tecnai F20 FEG TEM with a super-twin objective lens (operated at 200 kV). Attached to the microscope are an Oxford LINK ISIS 300 EDS system and a GATAN DigiPEELS spectrometer. The PEELS system measures the electron energy losses which occur when electrons are reflected or scattered from a solid. The measurement of energy loss in the TEM is limited to thin foils where an electron will undergo a single inelastic collision. The GATAN DigiPEELS spectrometer is in the bottom of the FEG TEM column below the viewing screen. The spectrometer produces a spectrum of the energy distribution in the transmitted electrons relative to the primary beam energy. Most of the electrons in the spectrum are found in the initial zero loss peak and in loss peaks involving interactions with valency or conduction electrons, up to ~50 eV loss. Beyond this is a smoothly falling background which has superimposed on it the ionisation edge of atoms whose x-ray absorption energies are reached (Figure 3.10). These are the peaks used for analysis. Information on chemical bonding, molecular structure and dielectric constant may be obtained from a study of energy loss curves. The resolution of fine structure depends on the design of the spectrometer and on the energy spread of the primary electron beam. The technique has been found to be most useful when applied to steels to determine the presence of the light elements C, N, O and B which are difficult to detect by EDS.

Details of the peak positions are detailed in the EELS atlas(81). The peaks of interest in this investigation are as follows;

Carbon = 283.8 eV

Chromium = 574 eV

Nickel = 854 eV

Cobalt = 779 eV

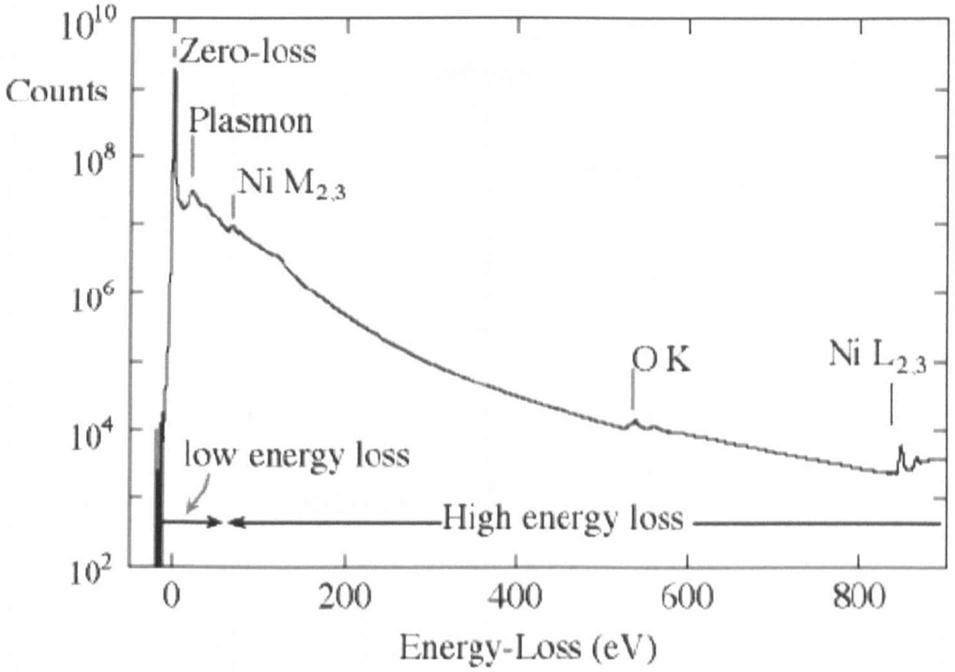

Figure 3.10 Schematic diagram of PEELS output illustrating the zero loss and plasmon peaks and the nickel and oxygen ionisation edges.

3.7 X-Ray Diffraction (XRD)

To measure the type and volume fraction of carbides present in the samples, the carbides were separated from the matrix by a bulk electrolytic extraction method. The electrolyte used was 10% hydrochloric acid, 1% tartaric acid in methanol. The technique dissolves the γ matrix in the cobalt-based superalloys and in the case of NP 222 the γ matrix and the γ' phase. After 3 hours of extraction the electrolyte was centrifuged to separate the extract and the electrolyte. The samples before and after extraction and the dried extract were weighed to an accuracy of ± 5 µg.

The extract was deposited on a silicon wafer and placed in a Siemens D500 diffractometer with a copper tube at 40 kV and 40 mA. The samples were scanned between 20° and 120° 2θ at an angle step interval of 0.02° and a step time of 7 seconds.

Analysis of the resultant trace was carried out using Diffrac^{plus} software and the Powder Diffraction File. The Diffrac^{plus} software allows measurement of the net area under a peak. This technique was used on the MAR M509 XRD traces to obtain a ratio between the amounts of MC and $M_{23}C_6$ carbides. Prior to measuring the net area, the background and the $K_{\alpha 2}$ peaks were stripped from the trace. Peak areas were measured for the TaC peaks (111) and (200) and the $Cr_{23}C_6$ peaks (420) and (511) (Figure 3.11). Additional measurements of the peak heights were taken from the same peaks to provide a second measure of the MC and $M_{23}C_6$ carbide ratio.

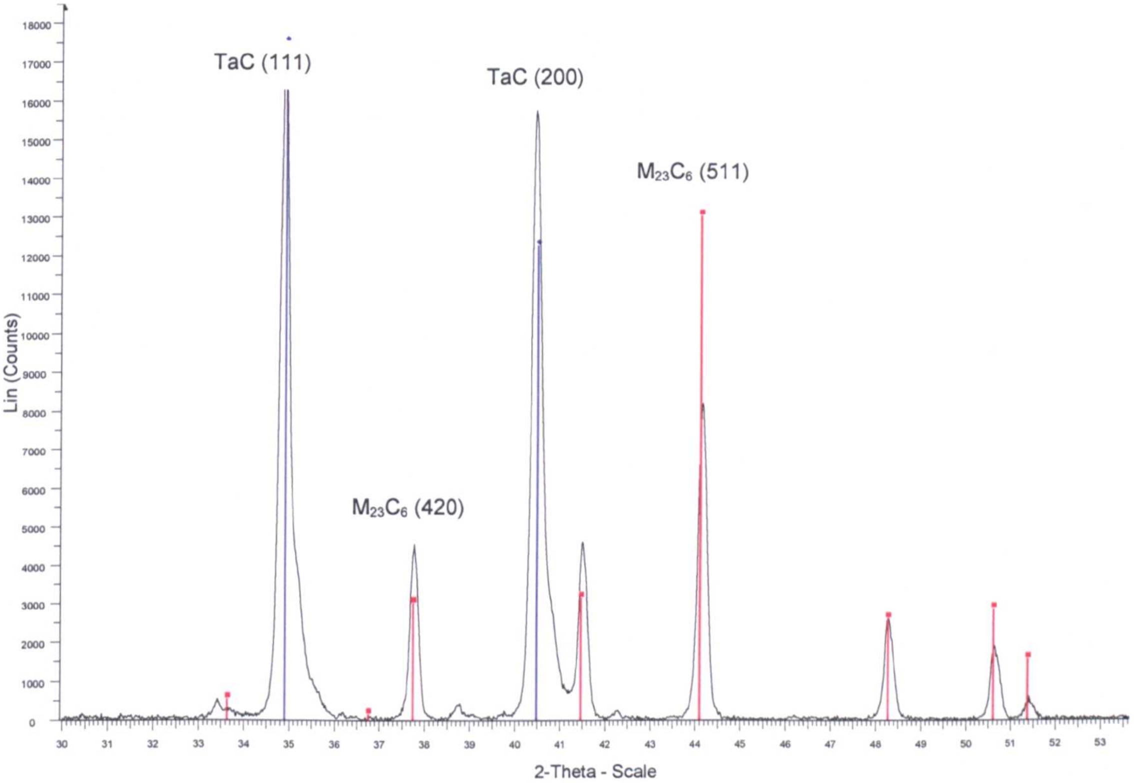

Figure 3.11 MAR M509 XRD trace illustrating peaks used for MC:$M_{23}C_6$ assessment.

The TaC (111) and (200) peaks are the largest peaks with intensities on the PDF files of 100 and 80% respectively. It was noted that on a number of the traces examined the (200) peak was higher than the (111) peak possibly as a result of the carbides acicular shape. The $Cr_{23}C_6$ peaks (420) and (511) are identified in the PDF file as the 80 and 100% intensity peaks respectively and are in the same area of the trace as the TaC peaks.

3.8 Image Analysis

Image analysis was carried out using Leica QWin image analysis software. The QWin software takes an image and digitises it into picture elements or 'pixels'. At each pixel the brightness of the image is sampled and it is this digitised representation that is analysed.

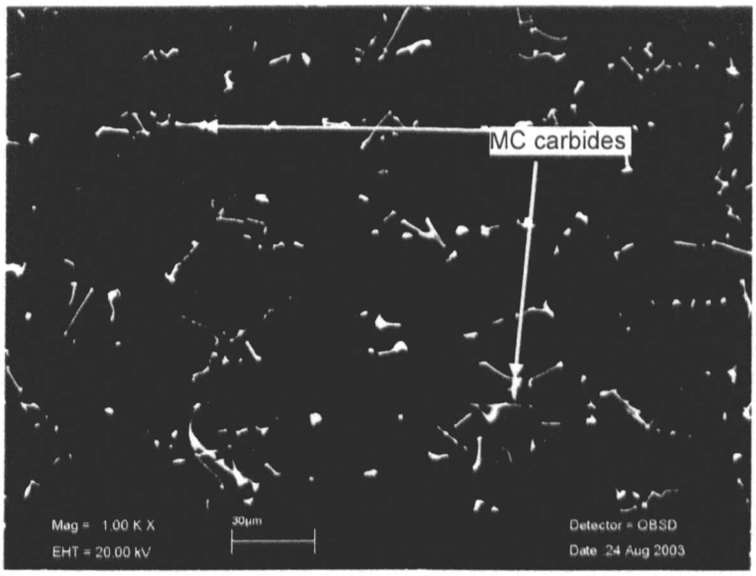

Figure 3.12 SEM BSE image of MAR M509 MC carbide used for image analysis (1,000 hrs 1000°C).

Image analysis was carried out on the MC carbides in the MAR M509 as-cast samples. In the backscatter imaging mode the MC carbide is white as a result of the high atomic number of the elements within the carbide; the matrix and the $M_{23}C_6$ carbides are dark grey in comparison (Figure 3.12). Twenty images were taken from each sample at a magnification of 500 in backscatter mode. At this magnification approximately 100 carbides were evident on each image. No software image manipulation was applied. Each image was analysed, and the results were then averaged and plotted against temperature.

A number of trials were carried out to increase the contrast between the $M_{23}C_6$ carbides (MAR M509 and FSX 414) and the matrix to allow image analysis. However, the results were inconclusive. One of the major problems with the $M_{23}C_6$ carbides is the high level of segregation of the fine carbides. Low magnification images would have been required to average out the high and low areas of fine $M_{23}C_6$ carbides. However, at low magnification the resolution would have precluded measurement of a large number of the fine carbides.

3.9 Thermodynamic Equilibrium Calculations

3.9.1 JMatPro

The software used for the current investigation is JMatPro (Java-based Material Properties software) described as a multi platform software programme developed to predict material properties for a wide range of multi-component alloy types(1). The software allows calculations for stable and metastable phase equilibrium; solidification behaviour and properties; thermo-physical and physical properties; phase transformations; chemical properties; and mechanical properties for nickel and iron based superalloys. The approach adopted in the development of the programme was to augment the thermodynamic calculation by incorporating various theoretical models and property databases that make a quantitative calculation for the materials property within a larger software structure(1). The thermodynamic calculations utilise core minimisation routines developed for the PMLFKT software programme by Lukas(82) and recently extended by Kattner et al(83) to multi component alloys.

The JMatPro(1) software package allows the determination of the phases present and their composition within the alloy microstructure at thermodynamic equilibrium as a function of temperature. The software is easy to use with a main input window from which the material base type is identified and the composition of the alloy is entered. For the current programme the nickel database was used with the alloy compositions identified in Table 3.1 and 3.3. The start and finish temperatures for the step temperature calculation and the step size are identified and unless otherwise stated all phases are allowed to exist. The output is described as a temperature step plot identifying the phases (wt.%) present over the temperature range chosen, see for example Figure 3.13.

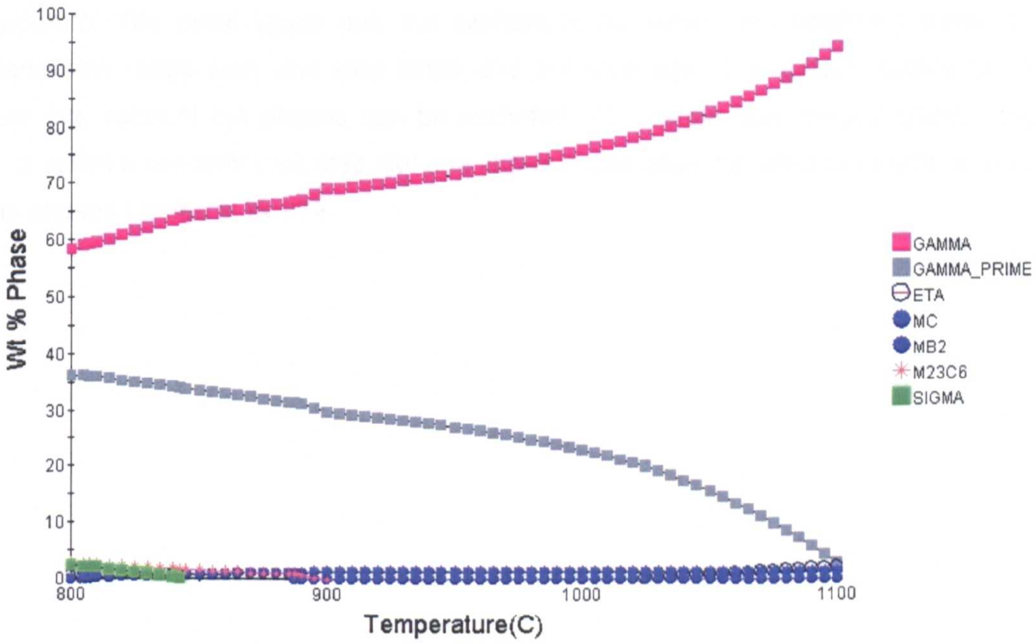

Figure 3.13 Example of a thermodynamic calculation, temperature step plot for alloy IN 939 generated in JMatPro.

In addition the composition of the phases can be displayed (Figure 3.14) by choosing the phase from a pop up menu.

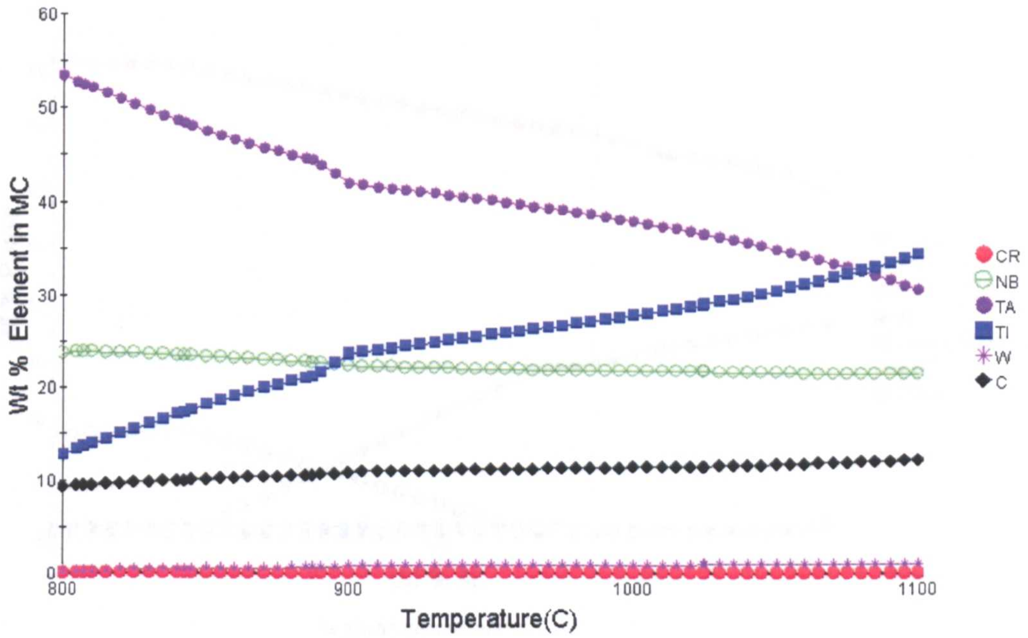

Figure 3.14 Example of a composition profile for MC carbide in alloy IN 939 generated in JMatPro.

An additional calculation is the concentration stepping calculation which allows the concentration of a single element to be varied across a concentration range at a single temperature. The initial inputs are, the element to be varied, the balancing element, the concentration range start and stop limits and the step size. The default setting takes all phases into account but phases can be excluded. The output from the calculation, Figure 3.15, is called a concentration step plot and shows in this case the effect of varying aluminium on the phases formed in IN 939.

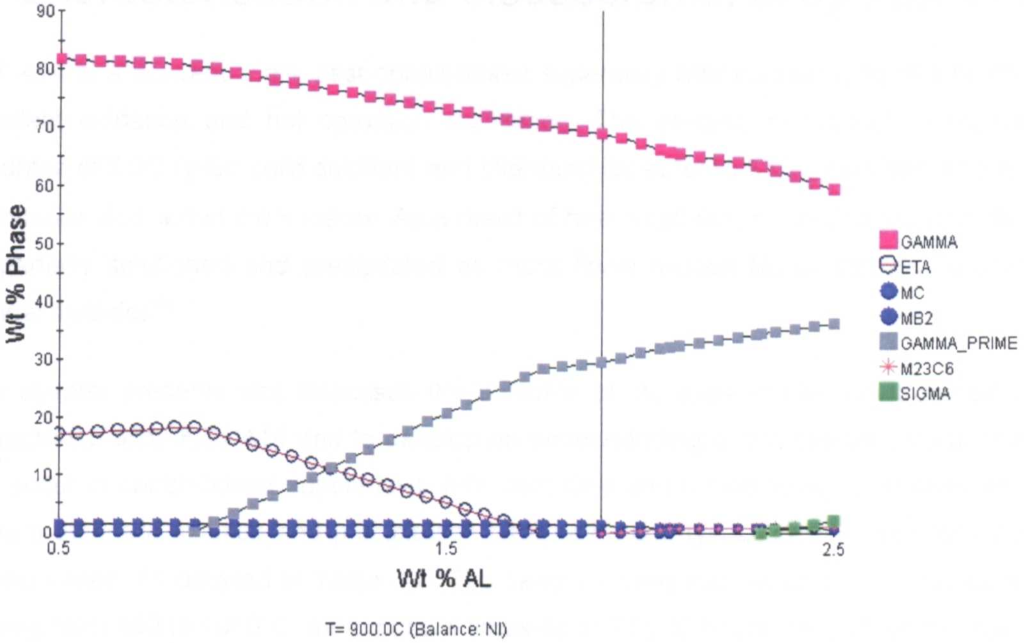

Figure 3.15 Example of a concentration step plot at 900°C, changing aluminium balancing with nickel for alloy IN 939, generated in JMatPro.

The software used was version 4.0 in which the materials database includes cobalt but is not optimised for cobalt-based superalloys. The current programme has used the nickel based materials database. The full database contains the elements:

- Ni, Al, Co, Cr, Fe, Hf, Mo, Mn, Nb, Re, Ru, Si, Ta, Ti, W, Zr, B, C, N with data for the following phases.
- Liquid, γ, γ′, NiAl, Ni$_3$Nb, γ′′, η, Ni$_4$Mo, δ-NiMo, α(Cr,Mo,W), Laves, σ, μ, R, P, M(C,N), M$_{23}$(BC)$_6$, M$_6$C, M$_7$(BC)$_3$, M$_2$N, M$_3$B, (FeNi)$_2$B, (Cr,Mo)$_2$B, M$_3$B$_2$, MB, Cr$_5$B$_3$, TiB$_2$, Ni$_3$Si, Ni$_5$Si, Cr$_3$Si, Cr$_3$Ni$_5$Si$_2$.

4 Characterisation and discussion of alloy FSX 414

FSX 414 is a conventionally cast cobalt-based superalloy with modest rupture strength and excellent oxidation and hot corrosion resistance. The as-cast microstructure consists of dendrites of FCC (γ-Co solid solution) and interdendritic eutectic $M_{23}C_6$ carbides, at the grain boundaries and within the γ matrix. As a result of heat treatment or service the carbides can be partially solutioned and precipitated as more finely divided $M_{23}C_6$ carbides around the original carbides(5).

This chapter presents and discusses the outcome of the experimental work carried out to characterise alloy FSX 414 and to develop an understanding of the microstructural changes that occur in cobalt-based superalloys, with both time and temperature. Cast samples were given a standard solution and precipitation heat treatment, typical of that used for industrial turbine vanes, as detailed in Table 3.2. The samples were then aged in air at temperatures ranging from 850 to 1050°C, for exposure times up to 25,000 hours, as detailed in Chapter 3. The chemical composition of FSX 414 used in this study is given in Table 3.1.

A detailed microstructural characterisation was carried out by means of optical and scanning electron microscopy. Additional thin foils were produced by FIB SEM for electron diffraction in a TEM in order to conclusively identify the unknown phases. The results of thermodynamic equilibrium calculations performed using JMatPro are presented, followed by the results from EDS, XRD and hardness measurements.

4.1 Microstructural Observations

The identification of the phases was initially based on EDS chemical composition measurements and comparison with representative compositions found in the literature.

The microstructure following the standard heat treatment is shown in Figure 4.1. The original dendritic pattern is evident with primary $M_{23}C_6$ eutectics and fine secondary $M_{23}C_6$ carbide outlining the original dendritic structure. Large areas of the γ matrix are optically devoid of precipitates.

The primary eutectic carbide appears in three forms as shown in Figure 4.2; fine eutectic; coarse eutectic; and an open eutectic.

The secondary $M_{23}C_6$ carbides vary in size with fine carbides typically 0.1 μm in diameter interspersed with coarse cubic and rod shaped carbides ~5 μm long as shown in Figure 4.2. Grain boundaries may be evident at a number of positions. At higher magnification precipitate free zones (PFZ) are evident around the primary carbides.

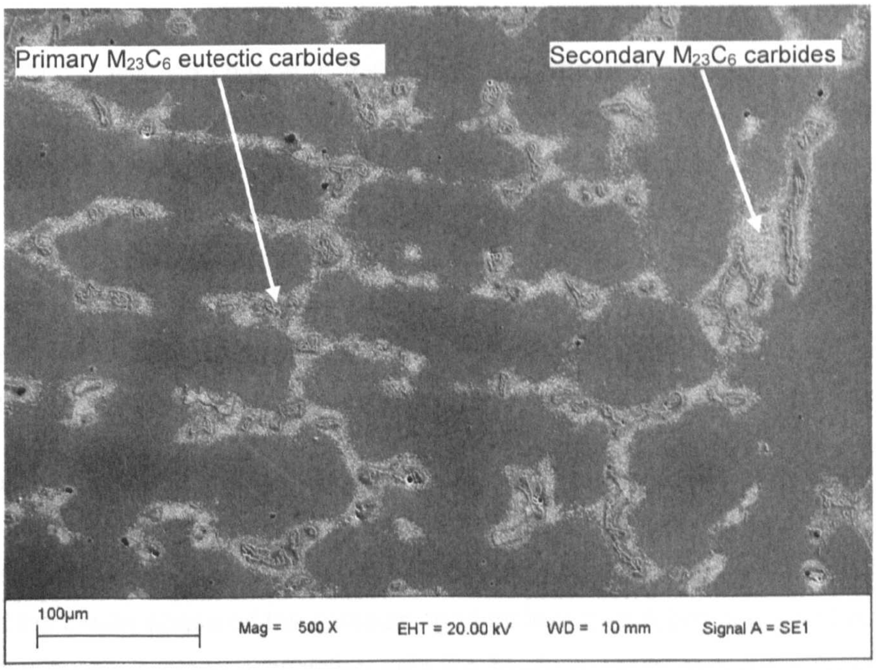

Figure 4.1 FSX 414 SEM SE image showing dendritic structure of the samples after a solution and precipitation heat treatment showing dendritic pattern of primary eutectic and secondary $M_{23}C_6$ carbides.

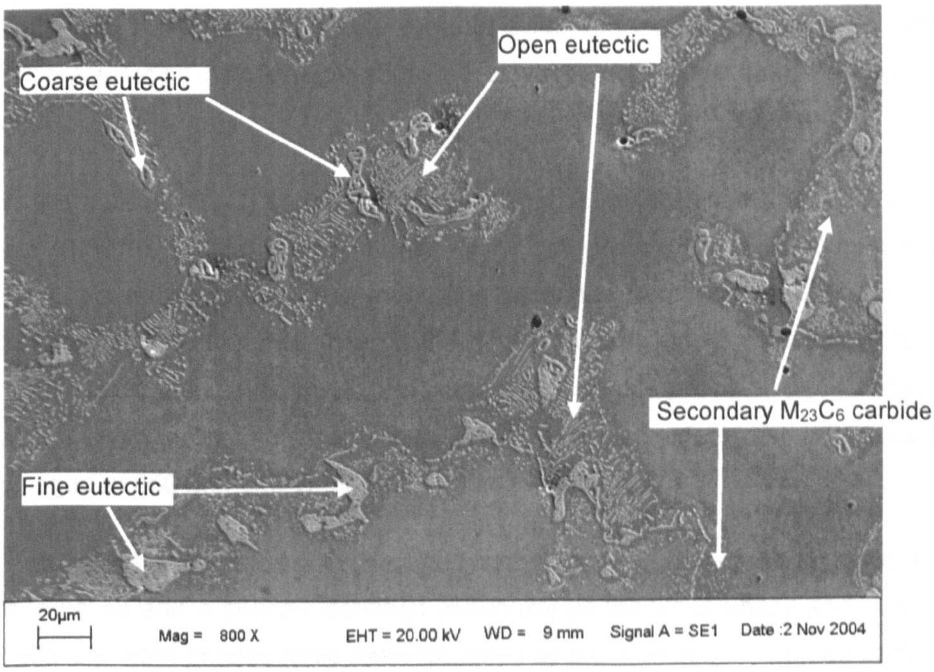

Figure 4.2 FSX 414 SEM SE image showing structure of primary coarse, fine and open $M_{23}C_6$ eutectic carbides and small secondary $M_{23}C_6$ carbides.

The samples aged at 850°C, 900°C and 950°C show similar microstructures to the initial heat treatment sample, with no change in the primary eutectic or secondary carbides, however, there are additional secondary carbides in the previously precipitate free γ matrix (Figure 4.3). With increasing time and temperature the secondary carbides coarsen. However, 0.1 µm secondary carbides are still evident after 25,000 hours at these temperatures. At 1000°C and 1050°C the $M_{23}C_6$ carbide eutectics start to coalesce into large blocky carbides with a reduced level of secondary carbides evident. The 1050°C 10,000 and 15,000 hours samples show extensive oxidation, through the full 6mm thickness of the 15,000 hour sample, with visual changes in the coalesced carbides evident both optically and in the SEM (Figure 4.4).

In SEM backscatter mode a large blocky ~10 µm (light grey) phase is evident in association with the $M_{23}C_6$ eutectic carbides in all of the 850°C and 900°C samples at times greater than 5,000 hours (Figure 4.5). The samples at 950°C and above show no evidence of this phase. The lack of the blocky phase on the samples aged for less than 5,000 hours and the presence of the blocky phase in close association with the $M_{23}C_6$ eutectic carbides suggests that the blocky phase has initiated on the $M_{23}C_6$ carbides during ageing. In addition to the blocky phase, the backscatter image of the 850°C and 900°C (Figure 4.5) and to a lesser extent the 950°C samples, show small particles of a white phase in backscatter mode, again associated with the $M_{23}C_6$ carbides. The white phase was not evident in the initial sample, following the solution and precipitation heat treatment, but is evident in the aged samples from 1,000 - 25,000 hours.

In summary the eutectic $M_{23}C_6$ carbides show some evidence of consolidation, at the higher 1000°C and 1050°C ageing temperatures. With increasing time and temperature the secondary $M_{23}C_6$ carbides coarsen. However, fine secondary $M_{23}C_6$ carbides are still evident in the 25,000 hour 1050°C samples. The 1050°C 15,000 hours sample is oxidised through the full 6mm sample thickness. Of interest is the presence of a white phase, in backscatter mode, in all samples aged at temperatures less than 950°C. A large blocky phase is also evident in the samples aged at 850 and 900°C for 5,000 hours and above.

The optical and SEM observations for the aged samples are summarised in Table 4.1. The table refers to Laves and σ phases identified previously as the white phase and large blocky phase respectively. Both phases have been identified by electron diffraction (see section 4.4). Representative SEM micrographs of the 1,000, 5,000, 15,000 and 25,000 hour samples are contained in Figure 4.6 - 4.10 and show more clearly the changes in the microstructure with time and temperature.

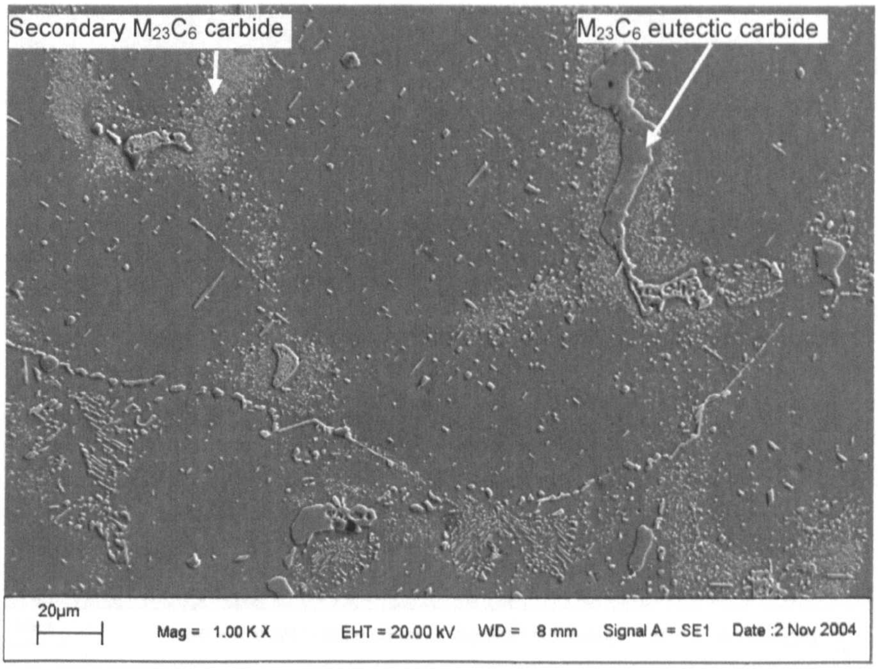

Figure 4.3 SEM SE image showing primary eutectic and secondary $M_{23}C_6$ carbides in FSX 414 matrix (10,000 hrs 900°C).

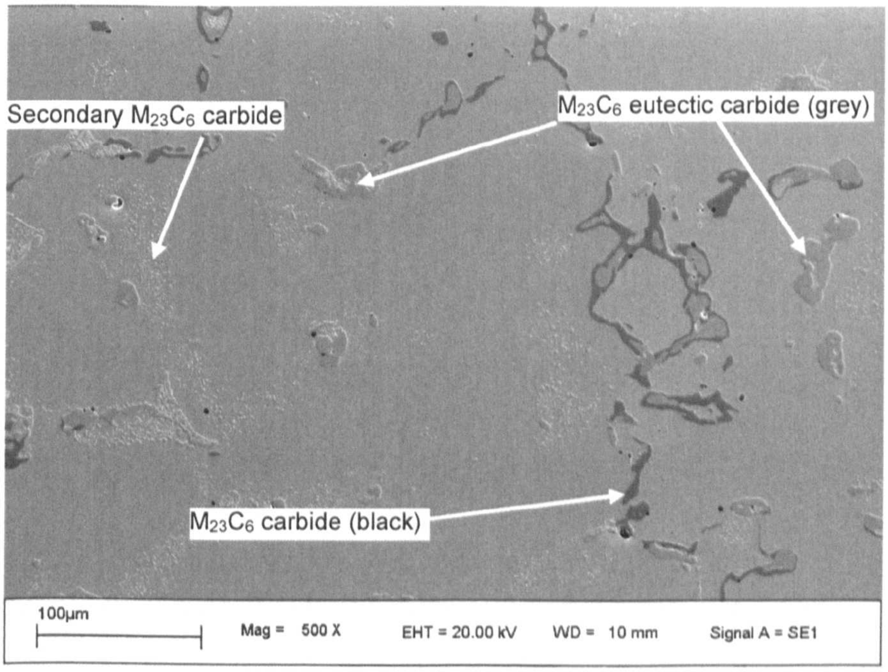

Figure 4.4 FSX 414 SEM SE image showing blocky coalesced $M_{23}C_6$ carbide (grey) low tungsten black (10,000 hrs 1050°C).

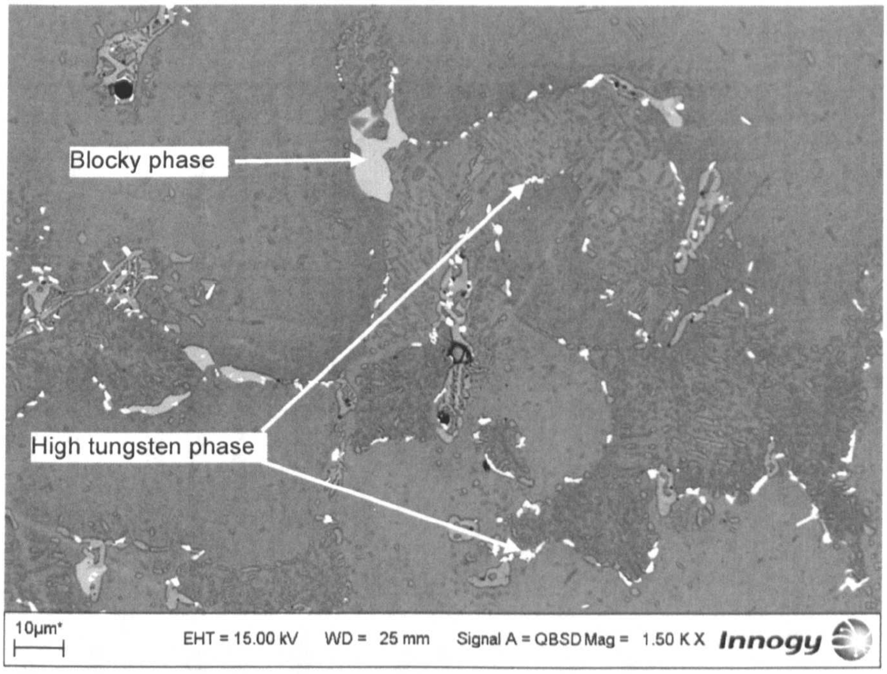

Figure 4.5 **SEM SE image of FSX 414 showing high tungsten and blocky phases in sample aged at 900°C for 10,000 hrs.**

	1,000 hrs	2,000 hrs	5,000 hrs	10,000 hrs	15,000 hrs	20,000 hrs	25,000 hrs
850°C	Eutectic $M_{23}C_6$ Secondary $M_{23}C_6$ Laves phase in $M_{23}C_6$	Eutectic $M_{23}C_6$ Secondary $M_{23}C_6$ Laves phase in $M_{23}C_6$	Eutectic $M_{23}C_6$ Secondary $M_{23}C_6$ Laves phase in $M_{23}C_6$ Blocky σ particles	Eutectic $M_{23}C_6$ Secondary $M_{23}C_6$ Laves phase in $M_{23}C_6$ Blocky σ particles	Eutectic $M_{23}C_6$ Secondary $M_{23}C_6$ Laves phase in $M_{23}C_6$ Blocky σ particles	Eutectic $M_{23}C_6$ Secondary $M_{23}C_6$ Laves phase in $M_{23}C_6$ Blocky σ particles	Eutectic $M_{23}C_6$ Secondary $M_{23}C_6$ Laves phase in $M_{23}C_6$ Blocky σ particles
900°C	Eutectic $M_{23}C_6$ Secondary $M_{23}C_6$ Laves phase in $M_{23}C_6$	Eutectic $M_{23}C_6$ Secondary $M_{23}C_6$ Laves phase in $M_{23}C_6$	Eutectic $M_{23}C_6$ Secondary $M_{23}C_6$ Laves phase in $M_{23}C_6$ Blocky σ particles	Eutectic $M_{23}C_6$ Secondary $M_{23}C_6$ Laves phase in $M_{23}C_6$ <Blocky σ particles	Eutectic $M_{23}C_6$ Secondary $M_{23}C_6$ Laves phase in $M_{23}C_6$ <Blocky σ particles	Eutectic $M_{23}C_6$ Secondary $M_{23}C_6$ Laves phase in $M_{23}C_6$ <<Blocky σ particles	Eutectic $M_{23}C_6$ Secondary $M_{23}C_6$ Laves phase in $M_{23}C_6$ <<Blocky σ particles
950°C	Eutectic $M_{23}C_6$ Secondary $M_{23}C_6$ < Laves phase in $M_{23}C_6$	Eutectic $M_{23}C_6$ Secondary $M_{23}C_6$ < Laves phase in $M_{23}C_6$	Eutectic $M_{23}C_6$ Secondary $M_{23}C_6$ < Laves phase in $M_{23}C_6$	Eutectic $M_{23}C_6$ Secondary $M_{23}C_6$ < Laves phase in $M_{23}C_6$	Eutectic $M_{23}C_6$ Secondary $M_{23}C_6$ < Laves phase in $M_{23}C_6$	Eutectic $M_{23}C_6$ Secondary $M_{23}C_6$ << Laves phase in $M_{23}C_6$	Eutectic $M_{23}C_6$ Secondary $M_{23}C_6$ << Laves phase in $M_{23}C_6$
1000°C	Eutectic $M_{23}C_6$ Secondary $M_{23}C_6$	Eutectic $M_{23}C_6$ Secondary $M_{23}C_6$	Eutectic $M_{23}C_6$ Secondary $M_{23}C_6$	Eutectic $M_{23}C_6$ Secondary $M_{23}C_6$	Eutectic $M_{23}C_6$ Secondary $M_{23}C_6$	Eutectic $M_{23}C_6$ Secondary $M_{23}C_6$	Eutectic $M_{23}C_6$ Secondary $M_{23}C_6$
1050°C	Eutectic $M_{23}C_6$ Secondary $M_{23}C_6$	Eutectic $M_{23}C_6$ Secondary $M_{23}C_6$	Eutectic $M_{23}C_6$ Secondary $M_{23}C_6$	Oxidised carbides	Oxidised carbides		

< low levels
<< very low levels

Table 4.1 FSX 414 Optical and SEM observations of the aged samples. (Note that the γCo matrix has not been included).

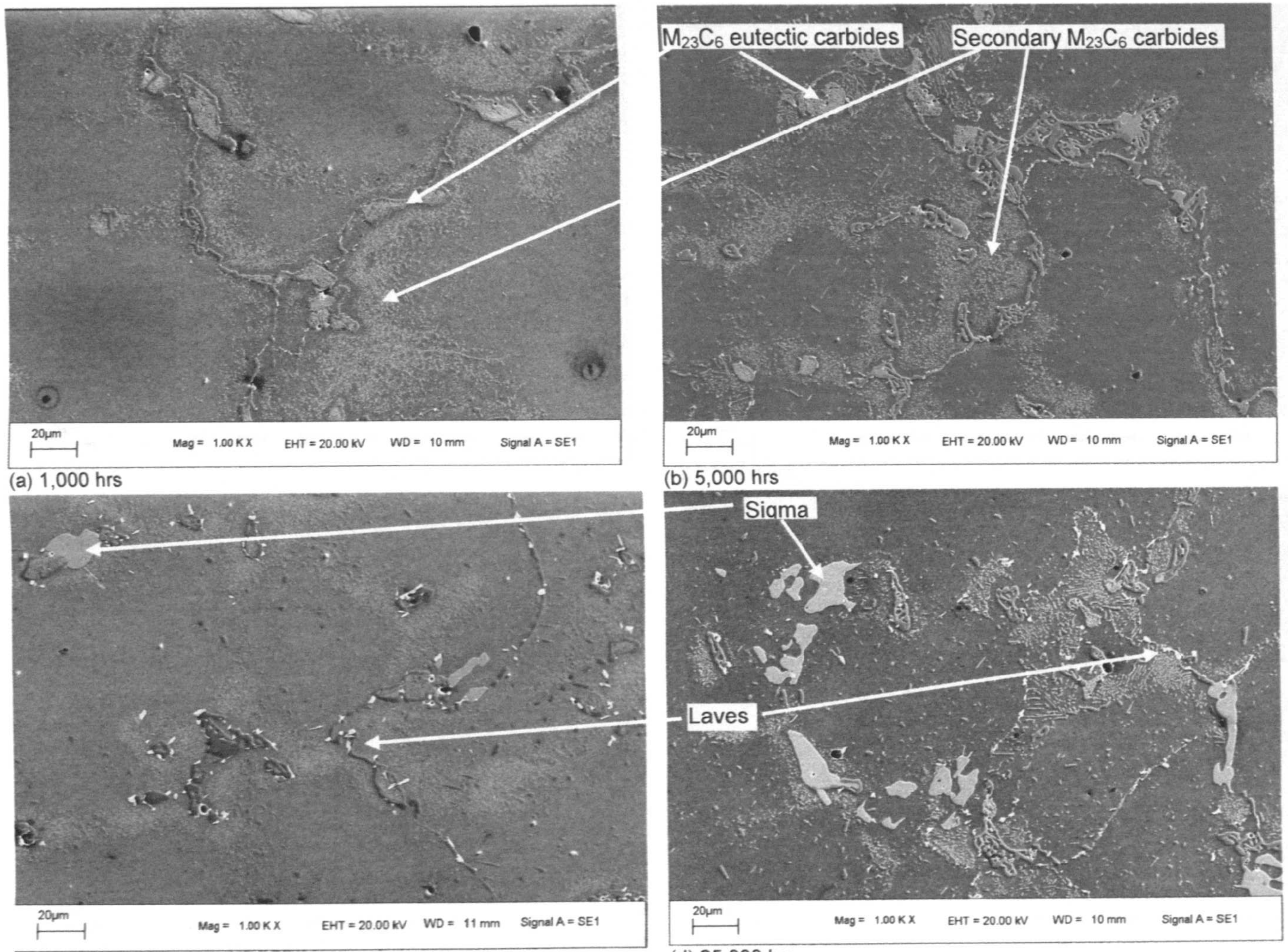

(a) 1,000 hrs

(b) 5,000 hrs

(c) 15,000 hrs

(d) 25,000 hrs

Figure 4.6 SEM SE images of FSX 414 of samples aged at 850°C for (a) 1,000, (b) 5,000, (c) 15,000 and (d) 25,000 hours respectively.

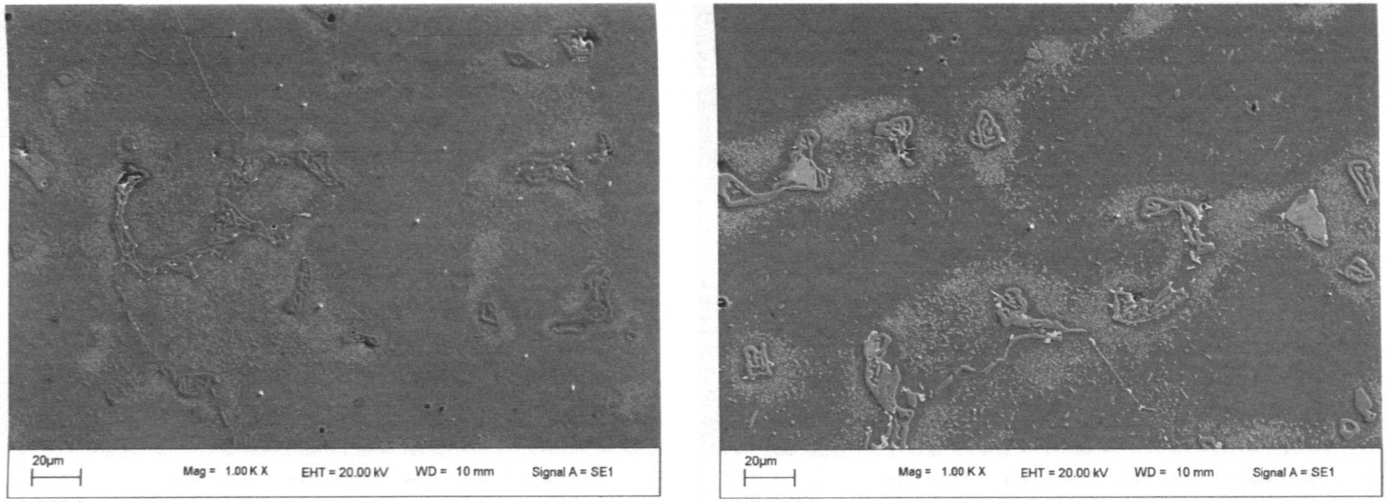

(a) 1,000 hrs

(b) 5,000 hrs

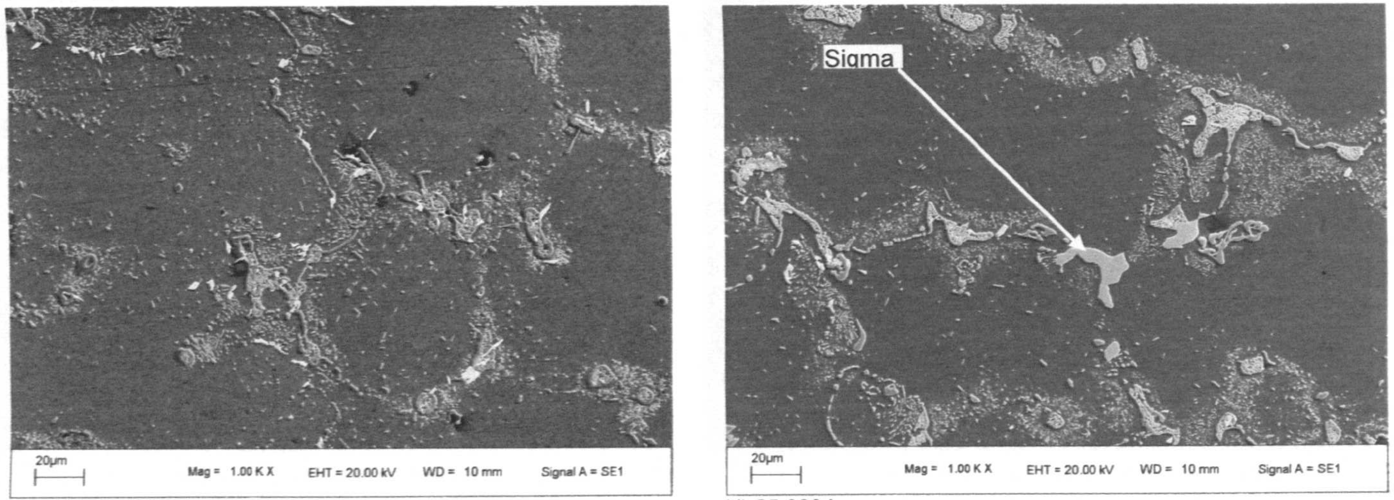

(c) 15,000 hrs

(d) 25,000 hrs

Figure 4.7 SEM SE images of FSX 414 samples aged at 900°C for (a) 1,000, (b) 5,000, (c) 15,000 and (d) 25,000 hours respectively.

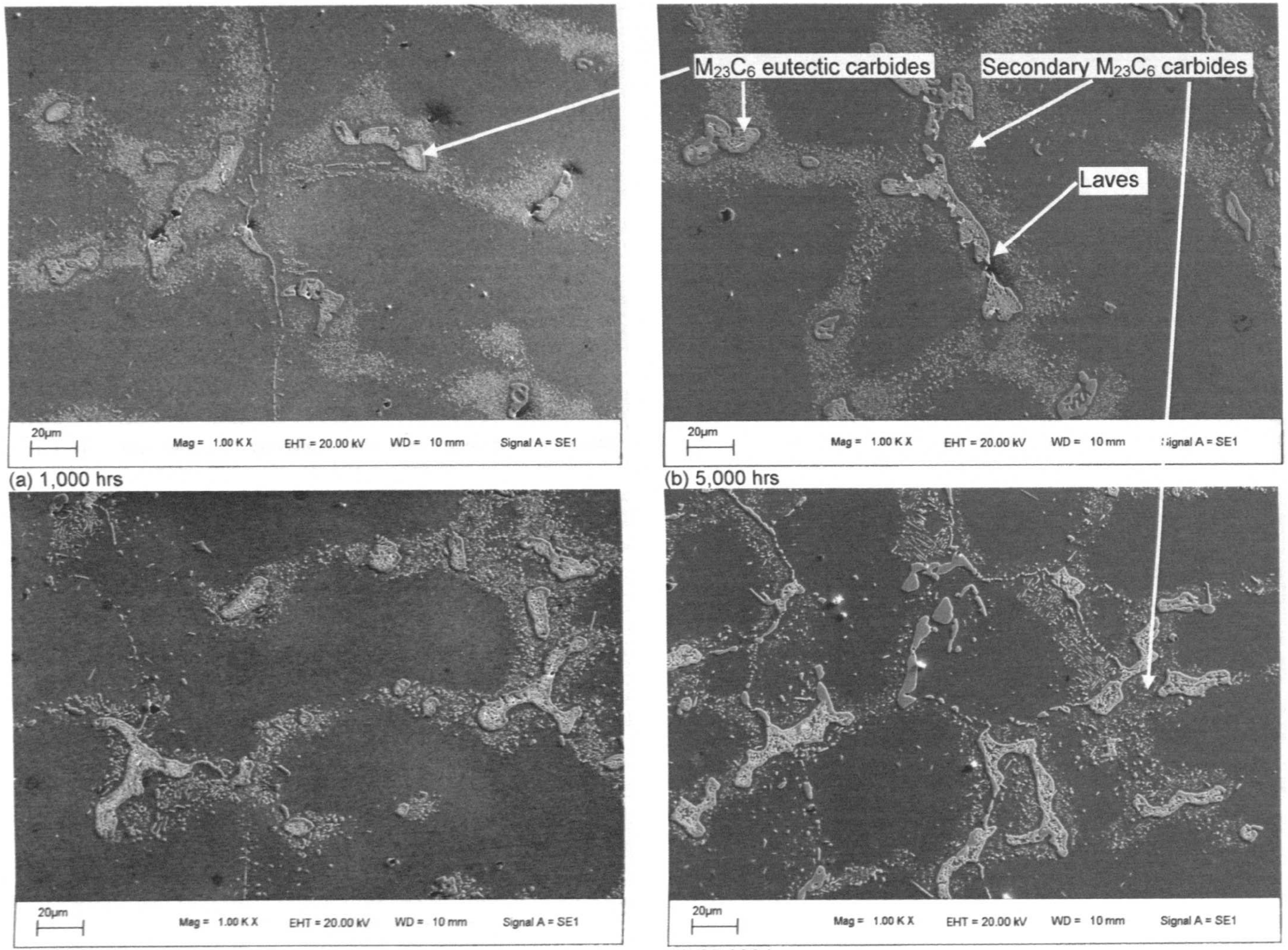

(a) 1,000 hrs

(b) 5,000 hrs

(c) 15,000 hrs

(d) 25,000 hrs

Figure 4.8 SEM SE images of FSX 414 samples aged at 950°C for (a) 1,000, (b) 5,000, (c) 15,000 and (d) 25,000 hours respectively.

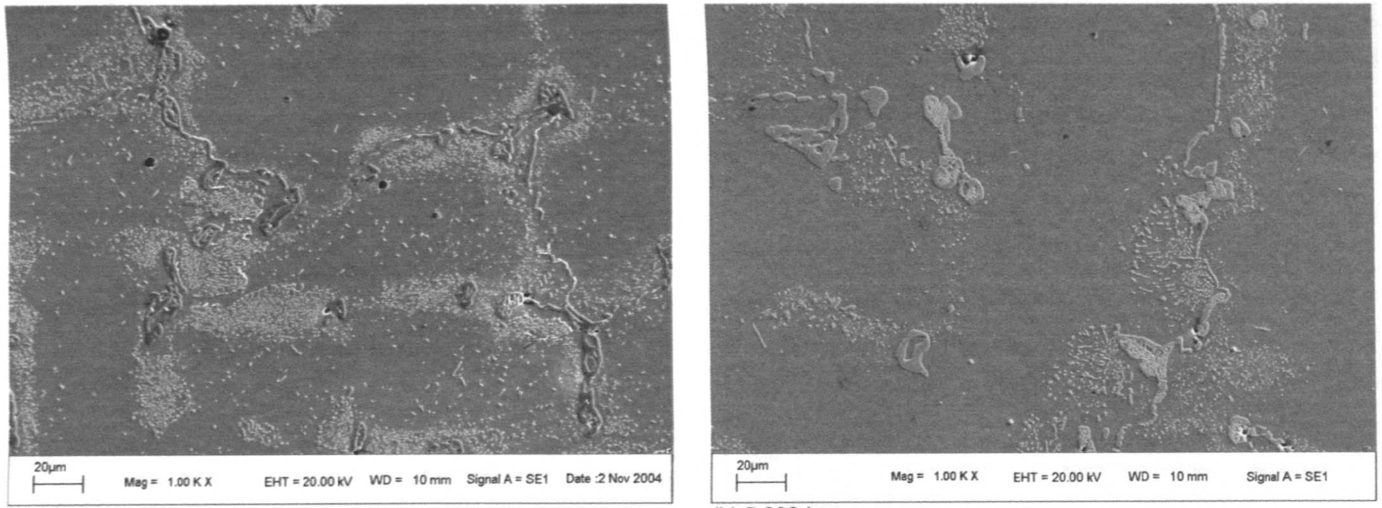

(a) 1,000 hrs

(b) 5,000 hrs

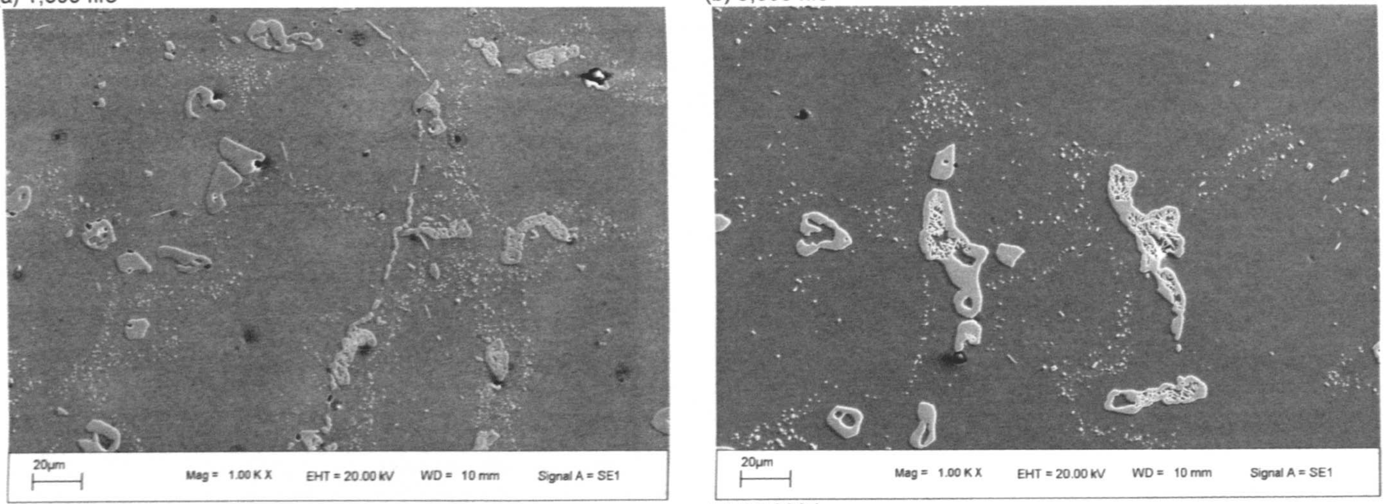

(c) 15,000 hrs

(d) 25,000 hrs

Figure 4.9 **SEM SE images of FSX 414 samples aged at 1000°C for (a) 1,000, (b) 5,000, (c) 15,000 and (d) 25,000 hours respectively.**

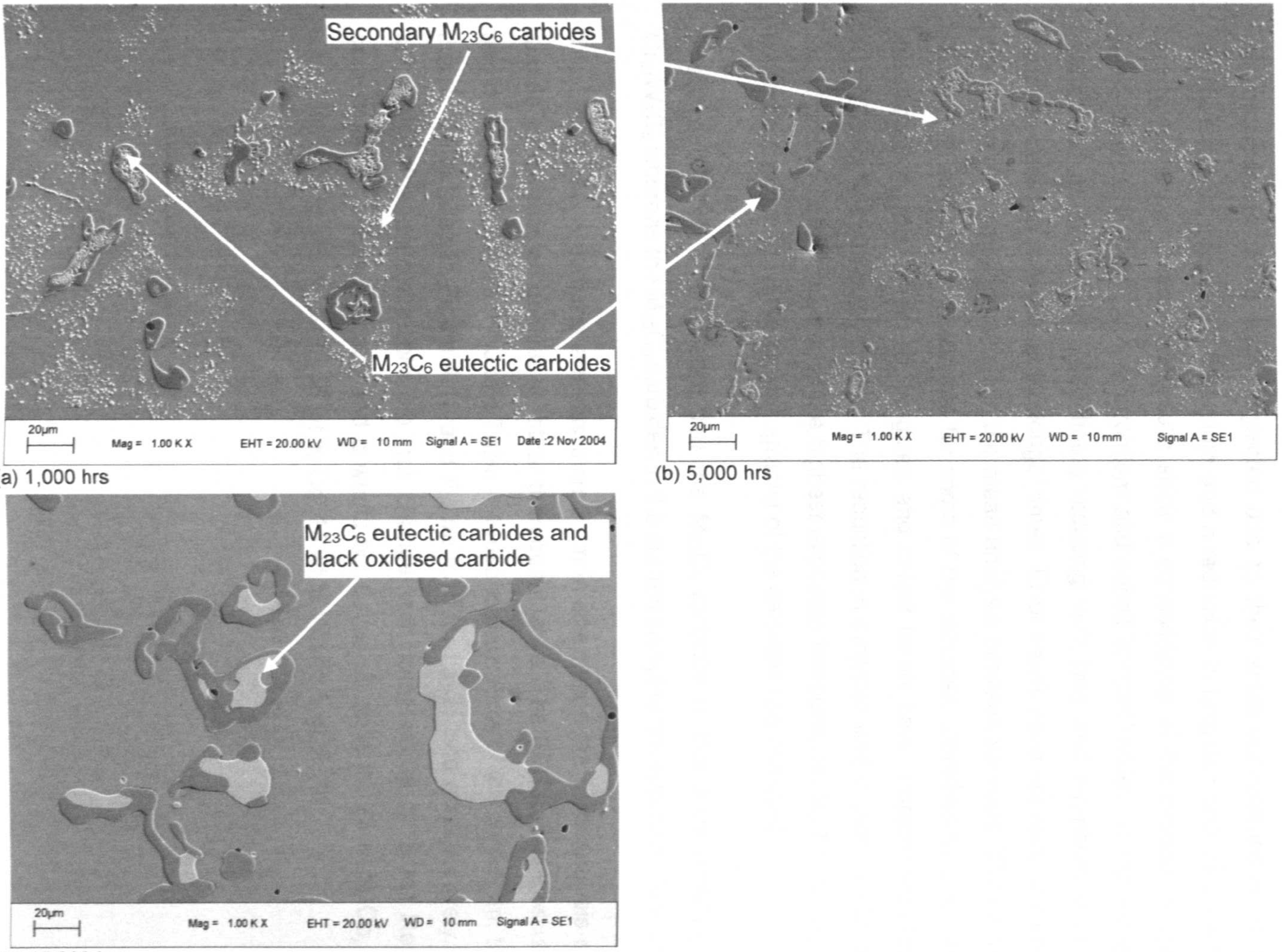

(a) 1,000 hrs

(b) 5,000 hrs

(c) 15,000 hrs

Figure 4.10 SEM SE images of FSX 414 samples aged at 1050°C for (a) 1,000 (b) 5,000 and (c) 15,000 hours respectively.

4.2 Phase Composition (EDS)

SEM EDS analysis of the coarse $M_{23}C_6$ carbides and secondary phases are detailed in Table 4.2 – 4.4 respectively. The results are the mean values of ten spot analyses taken from phases with a similar elemental signature from each sample, the analyses are normalised to 100 wt.%. Figure 4.11 shows plots of chromium, tungsten and cobalt from Table 4.2. Nickel and molybdenum have been neglected due to their small concentrations. In general the results show an increase in chromium and a reduction in tungsten and cobalt with both time and temperature. Overall the results show a consolidation of the carbide analysis with the initial ~5 wt.% variation in the chromium and cobalt content evident in the samples at 850-950°C and at 1,000 and 5,000 hours reducing with time and temperature to a ~2 wt.% variation between samples at the longer times. Error bands have not been shown in the plots due to the very small variations in the mean analysis between samples. The carbide analysis (Table 4.2) at 1050°C shows that for some of the carbides, identified as black in Table 4.2, the chromium has increased, tungsten and cobalt levels have dropped significantly in the 10,000 and 15,000 hour samples. The reduction in tungsten and cobalt may be the result of the oxidation of the carbides at the highest exposure temperature. No further work has been carried out to confirm if the crystallography of the carbides has changed.

Foster and Sims(44) considered that the $M_{23}C_6$ carbides in this alloy probably existed as $Cr_{21}W_2C_6$ whereas the $M_{23}C_6$ carbides in the current samples are approximately $Cr_{18}Co_3W_2C_6$.

The Laves phase particles are less than 2 µm in size hence the EDS analysis of the phase should be considered qualitative rather than quantitative. The EDS analysis results for Laves and σ are shown in Table 4.3 and Table 4.4 respectively. Plots of the chromium, tungsten and cobalt are detailed in Figure 4.12 and Figure 4.13 for Laves and σ respectively. The results show that the concentrations do not change with temperature or time. Representative compositions for Laves phase and σ would be, Laves 55 wt.% W, 25 wt.% Co, 14 wt.% Cr and 3 wt.% Ni, σ 43 wt.% Cr, 36 wt.% Co, 15 wt.% W and 5 wt.% Ni.

Time hrs	Temp °C	Cr	Co	Ni	Mo	W
1,000	850	66.6	12.6	1.9	0.5	18.5
	900	66.6	12.6	2.2	0.5	18.1
	950	68.6	10.8	1.9	0.5	18.2
	1000	70.9	9.4	1.8	0.4	17.5
	1050	71.4	9.6	1.8	0.4	16.8
5,000	850	67.3	12.2	2.1	0.5	17.9
	900	68.0	11.5	2.1	0. 6	18.0
	950	70.0	8.7	1.8	0.5	18.1
	1000	71.7	9.1	1.8	0.4	17.1
	1050	71.9	9.4	1.8	0.4	16.4
10,000	850	68.2	11.6	2.1	0.5	17.7
	900	69.3	10.7	1.8	0.6	17.7
	950	71.1	8.0	1.7	0.4	17.7
	1000	72.4	8.7	1.8	0.4	16.8
	1050	72.7	9.5	1.7	0.4	16.3
Black	1050	93.4	1.6	0.3		4.6
15,000	850	68.9	10.5	1.9	1.0	17.6
	900	70.3	9.0	1.9	1.3	17.6
	950	71.7	7.9	1.9	1.1	17.4
	1000	72.3	8.8	1.7	0.4	16.8
	1050	71.9	9.9	1.9	0.4	15.8
Black	1050	93.7	1.6	0.3	0.1	4.4
20,000	850	70.2	9.0	1.9	1.4	17.5
	900	71.5	8.6	1.7	0.9	17.4
	950	72.5	8.1	1.7	0.3	17.4
	1000	72.6	8.5	1.6	0.4	16.9
25,000	850	70.8	9.1	1.8	0.6	17.7
	900	71.2	9.0	2.0	0.5	17.3
	950	72.1	7.9	1.8	1.2	17.0
	1000	72.4	8.6	1.7	0.5	16.8

Table 4.2 FSX 414 SEM EDS mean analysis of primary $M_{23}C_6$ carbide eutectic (normalised to 100 wt.%).

(a) Chromium

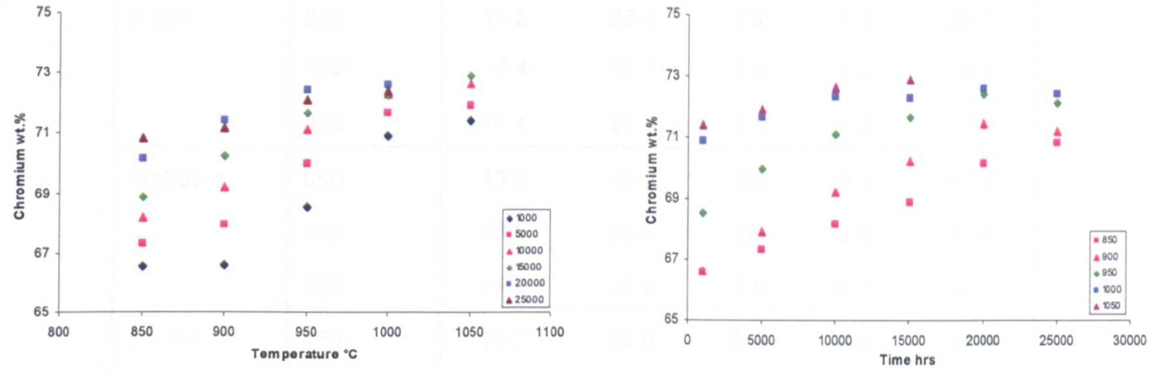

(b) Tungsten

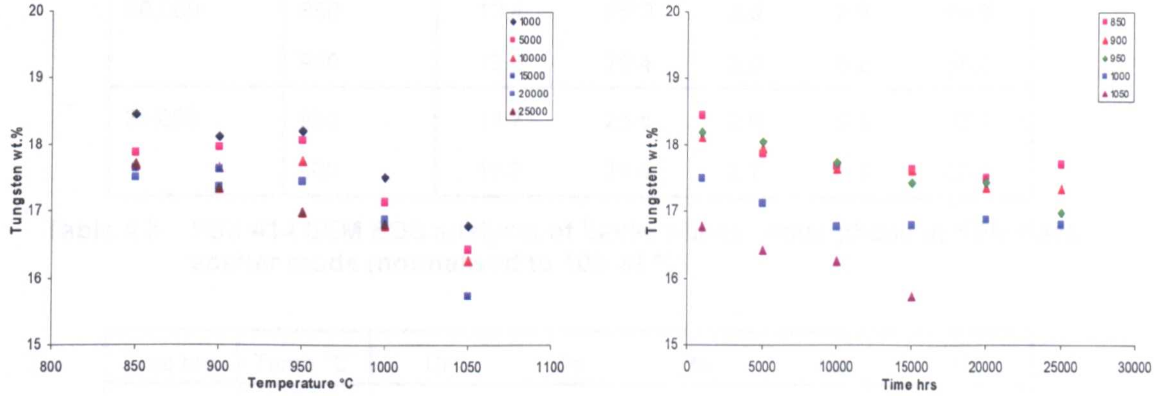

(c) Cobalt

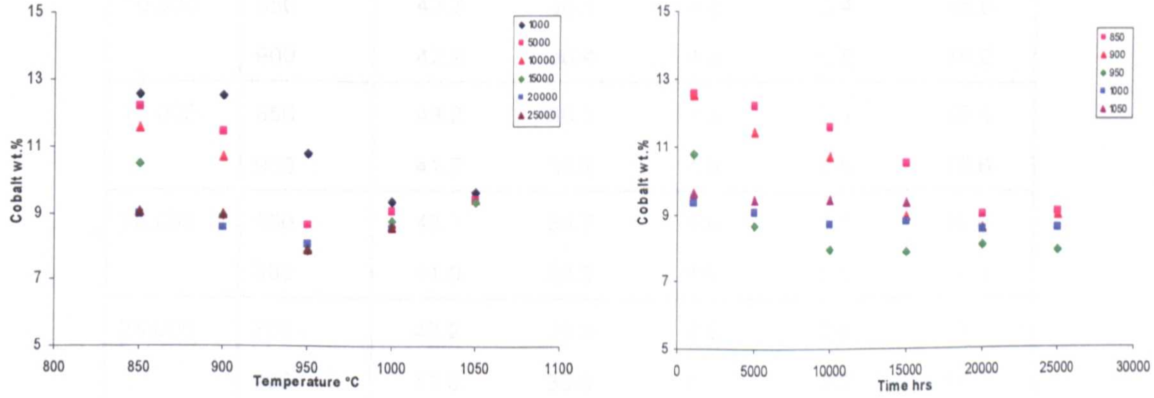

Figure 4.11 FSX 414 $M_{23}C_6$ carbide analysis (a) chromium (b) tungsten and (c) cobalt respectively plotted as a function of temperature and time (wt.%).

Time hrs	Temp °C	Cr	Co	Ni	Mo	W
5,000	850	14.5	25.8	3.2	0.4	56.1
	900	14.4	25.7	2.9	0.2	56.9
	950	14.4	25.4	2.8	0.2	57.4
10,000	850	13.9	25.9	3.0	0.4	56.9
	900	13.5	25.8	2.9	0.2	57.6
	950	14.2	25.4	2.8	0.3	57.2
15,000	850	13.7	25.6	2. 9	0.3	57.5
	900	13.6	25.2	2.9	1.8	56.5
	950	13.7	25.2	2.9	1.5	56.7
20,000	850	13.4	25.0	2.9	2.0	56.8
	900	13.6	25.4	2.9	0.2	58.0
25,000	850	13.7	25.5	2.9	0.3	57.7
	900	13.2	25.4	2.7	0.3	58.5

Table 4.3 FSX 414 SEM EDS analysis of Laves phase, white phase in SEM back scatter mode (normalised to 100 wt.%).

Time hrs	Temp °C	Cr	Co	Ni	Mo	W
5,000	850	44.0	36.2	5.0	0.4	14.4
	900	43.0	36.0	4.9	0.4	15.7
10,000	850	43.7	36.1	4.8	0.4	15.0
	900	42.2	36.4	4.9	0.5	16.0
15,000	850	43.2	36.1	4.9	0.4	15.4
	900	41.7	36.2	4.9	0.6	16.6
20,000	850	42.7	35.7	4.9	1.1	15.6
	900	41.0	36.3	4.9	0.3	17.6
25,000	850	43.2	36.3	4.8	0.4	15.3
	900	41.0	36.3	4.7	0.5	17.5

Table 4.4 FSX 414 SEM EDS analysis of σ phase, blocky light grey phase in SEM backscatter mode (normalised to 100 wt.%).

4.3 Thermodynamic Equilibrium Predictions

This section presents thermodynamic equilibrium predictions for alloy FSX 414 carried out using JMatPro software. FSX 414 is a cobalt-based superalloy, JMatPro does not have a cobalt-based superalloy database therefore all of the following thermodynamic predictions are based upon the nickel superalloy database. The sample composition in Table 3.1 has been used for all JMatPro calculations.

In this programme of work the JMatPro software has been used to predict the equilibrium phases that would form over a specified range of temperatures. In using this software it has been assumed that no phase transformations occur on cooling. To validate this assumption FSX 414 samples aged at 850°C and 1050°C for 12,000 hours were water quenched. These samples were compared with samples cooled in still air. Optically there was no variation between the air cooled and water quenched samples. Examination of the samples in the SEM confirmed that all the secondary phases found previously were evident in both samples. EDS analysis showed no significant changes in the chemical analysis of the carbides or secondary phases between the quenched samples and those slowly cooled.

The JMatPro software allows the exclusion of phases from the calculations. The initial calculations were carried out with all phases included. At equilibrium the JMatPro software predicts gamma, $M_{23}C_6$ carbide, σ and μ and a very small amount of MC carbide to be the equilibrium phases. Indexing of diffraction patterns (Chapter 4.4) confirmed the two phases, other than the $M_{23}C_6$ carbides, found in the FSX 414 samples were σ phase (light grey) and Laves phase (white phase). Removing μ phase from the JMatPro calculation and allowing the calculation down to 700°C, Laves phase is predicted (0.6 wt.%) at 700°C. Small changes in gamma, $M_{23}C_6$ and σ were also observed. Laves phase is not predicted above 725°C or at 700°C with μ allowed in the calculation. In the aged samples Laves phase is evident at 850°, 900°C and to a lesser degree at 950°C with σ evident at 850°C and 900°C (Table 4.1).

The predicted changes in the mass of the phases are: γ increasing from 89 wt.% at 850°C to 95 wt.% at 900°C and remains constant at this level to 1100°C, $M_{23}C_6$ carbide reduces from approximately ~4.8 wt.% at 850°C to ~4.4 wt.% at 1050°C and σ phase reduces from ~5 wt.% at 850°C to 0 wt.% at 900°C (Figure 4.14).

JMatPro predicts small changes in the composition of $M_{23}C_6$ as a function of temperature. With increasing temperature JMatPro predicts chromium reduces from 72 wt.% to 67 wt.%, tungsten increases from 11 wt.% to 13 wt.% and cobalt increases from 10 wt.% to 12 wt.% over the 850-1050°C temperature range. Carbon remains constant at 4.9 wt.%. JMatPro indicates that σ and Laves phase should have relatively constant compositions over the short temperature range they are predicted to exist.

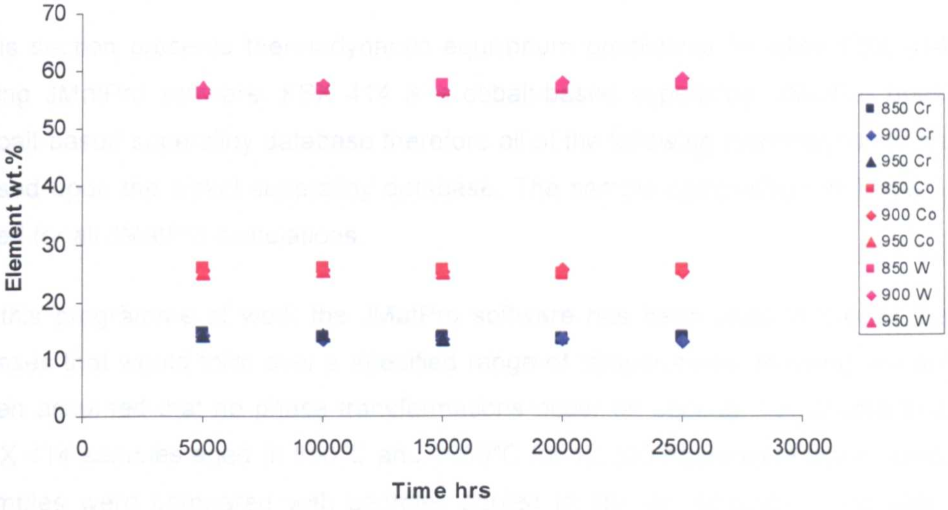

Figure 4.12 **FSX 414 Laves phase EDS analysis plots of chromium, cobalt and tungsten respectively plotted as a function of time (wt.%).**

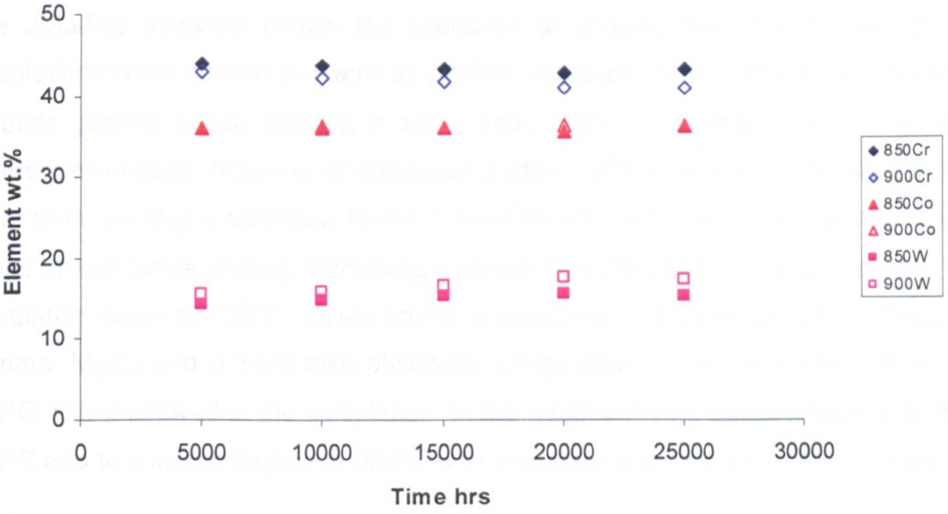

Figure 4.13 **FSX 414 σ phase EDS analysis plots of chromium, cobalt and tungsten respectively plotted as a function of time (wt.%).**

4.3 Thermodynamic Equilibrium Predictions

This section presents thermodynamic equilibrium predictions for alloy FSX 414 carried out using JMatPro software. FSX 414 is a cobalt-based superalloy, JMatPro does not have a cobalt-based superalloy database therefore all of the following thermodynamic predictions are based upon the nickel superalloy database. The sample composition in Table 3.1 has been used for all JMatPro calculations.

In this programme of work the JMatPro software has been used to predict the equilibrium phases that would form over a specified range of temperatures. In using this software it has been assumed that no phase transformations occur on cooling. To validate this assumption FSX 414 samples aged at 850°C and 1050°C for 12,000 hours were water quenched. These samples were compared with samples cooled in still air. Optically there was no variation between the air cooled and water quenched samples. Examination of the samples in the SEM confirmed that all the secondary phases found previously were evident in both samples. EDS analysis showed no significant changes in the chemical analysis of the carbides or secondary phases between the quenched samples and those slowly cooled.

The JMatPro software allows the exclusion of phases from the calculations. The initial calculations were carried out with all phases included. At equilibrium the JMatPro software predicts gamma, $M_{23}C_6$ carbide, σ and μ and a very small amount of MC carbide to be the equilibrium phases. Indexing of diffraction patterns (Chapter 4.4) confirmed the two phases, other than the $M_{23}C_6$ carbides, found in the FSX 414 samples were σ phase (light grey) and Laves phase (white phase). Removing μ phase from the JMatPro calculation and allowing the calculation down to 700°C, Laves phase is predicted (0.6 wt.%) at 700°C. Small changes in gamma, $M_{23}C_6$ and σ were also observed. Laves phase is not predicted above 725°C or at 700°C with μ allowed in the calculation. In the aged samples Laves phase is evident at 850°, 900°C and to a lesser degree at 950°C with σ evident at 850°C and 900°C (Table 4.1).

The predicted changes in the mass of the phases are: γ increasing from 89 wt.% at 850°C to 95 wt.% at 900°C and remains constant at this level to 1100°C, $M_{23}C_6$ carbide reduces from approximately ~4.8 wt.% at 850°C to ~4.4 wt.% at 1050°C and σ phase reduces from ~5 wt.% at 850°C to 0 wt.% at 900°C (Figure 4.14).

JMatPro predicts small changes in the composition of $M_{23}C_6$ as a function of temperature. With increasing temperature JMatPro predicts chromium reduces from 72 wt.% to 67 wt.%, tungsten increases from 11 wt.% to 13 wt.% and cobalt increases from 10 wt.% to 12 wt.% over the 850-1050°C temperature range. Carbon remains constant at 4.9 wt.%. JMatPro indicates that σ and Laves phase should have relatively constant compositions over the short temperature range they are predicted to exist.

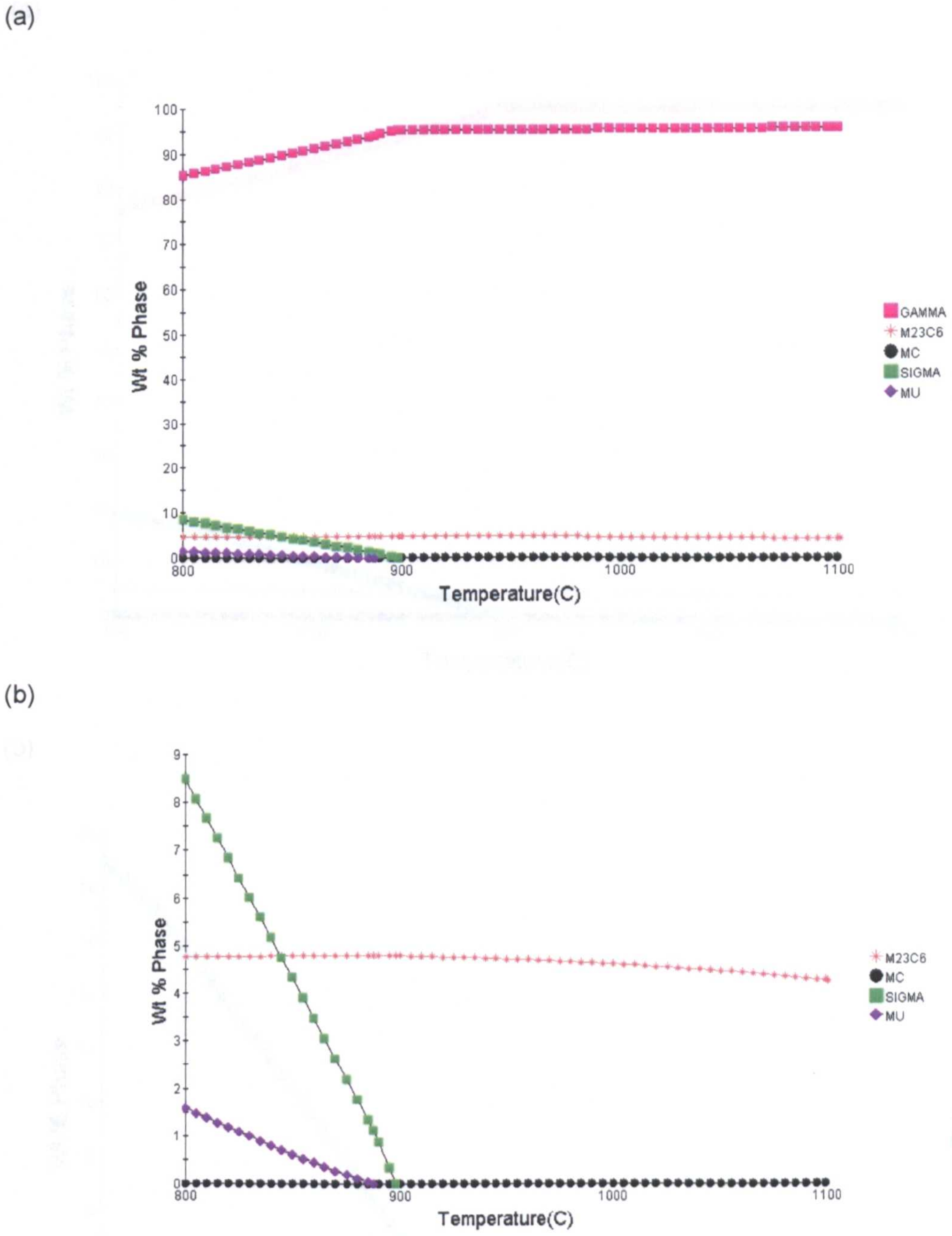

Figure 4.14 FSX 414 JMatPro prediction of (a) equilibrium phases (b) rescaled.

(a)

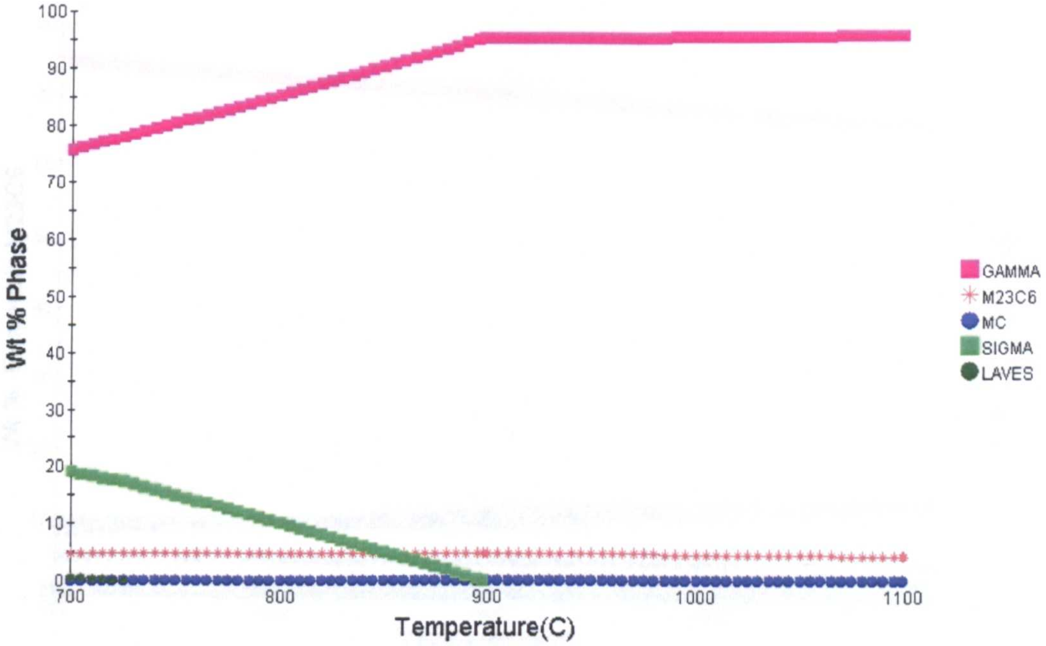

(b)

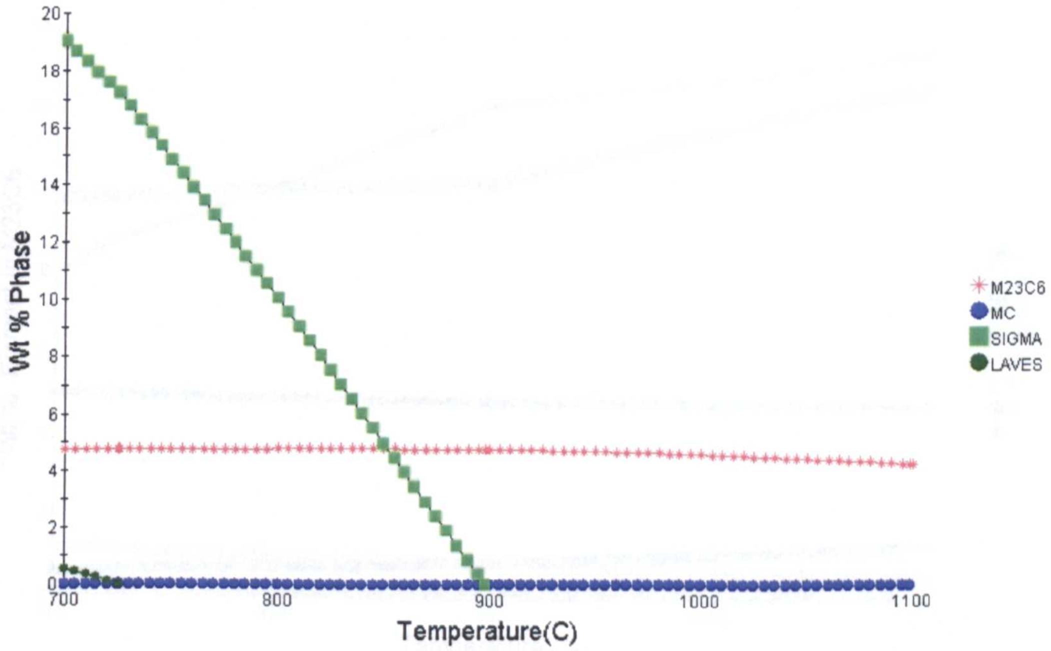

Figure 4.15 FSX 414 JMatPro prediction of (a) equilibrium phases with μ excluded from calculation (b) rescaled.

(a)

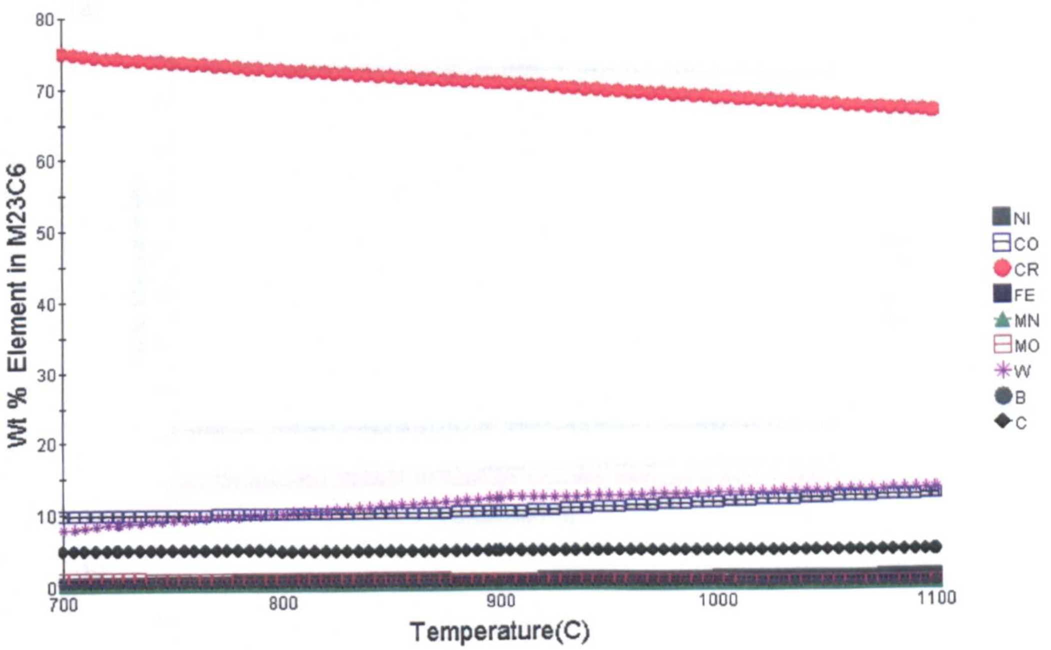

(b)

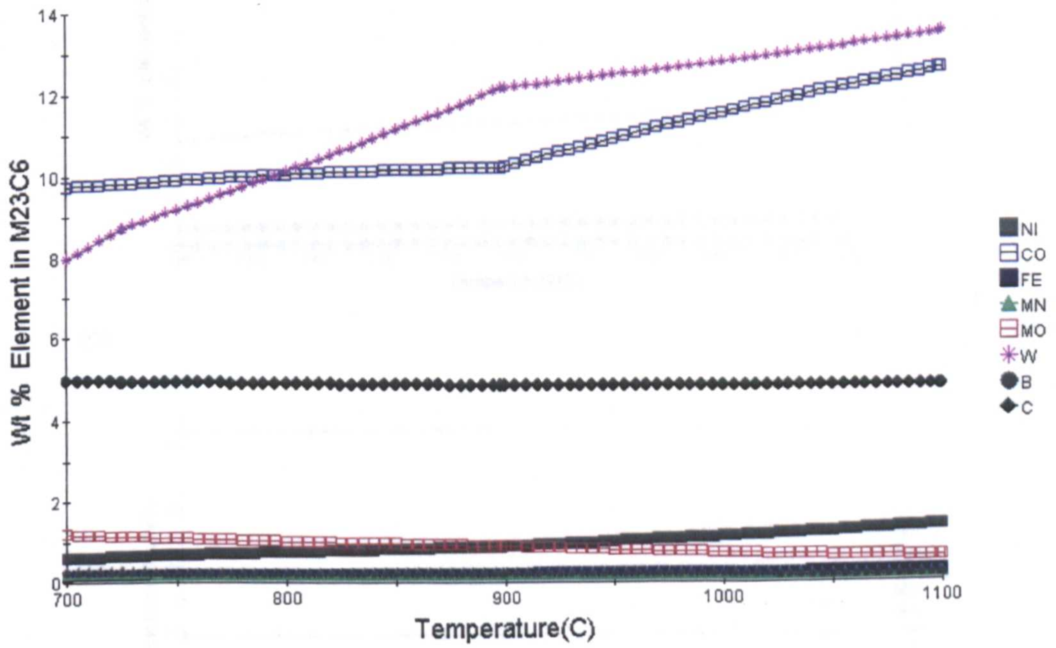

Figure 4.16 FSX 414 JMatPro predictions of (a) $M_{23}C_6$ carbide composition (b) rescaled.

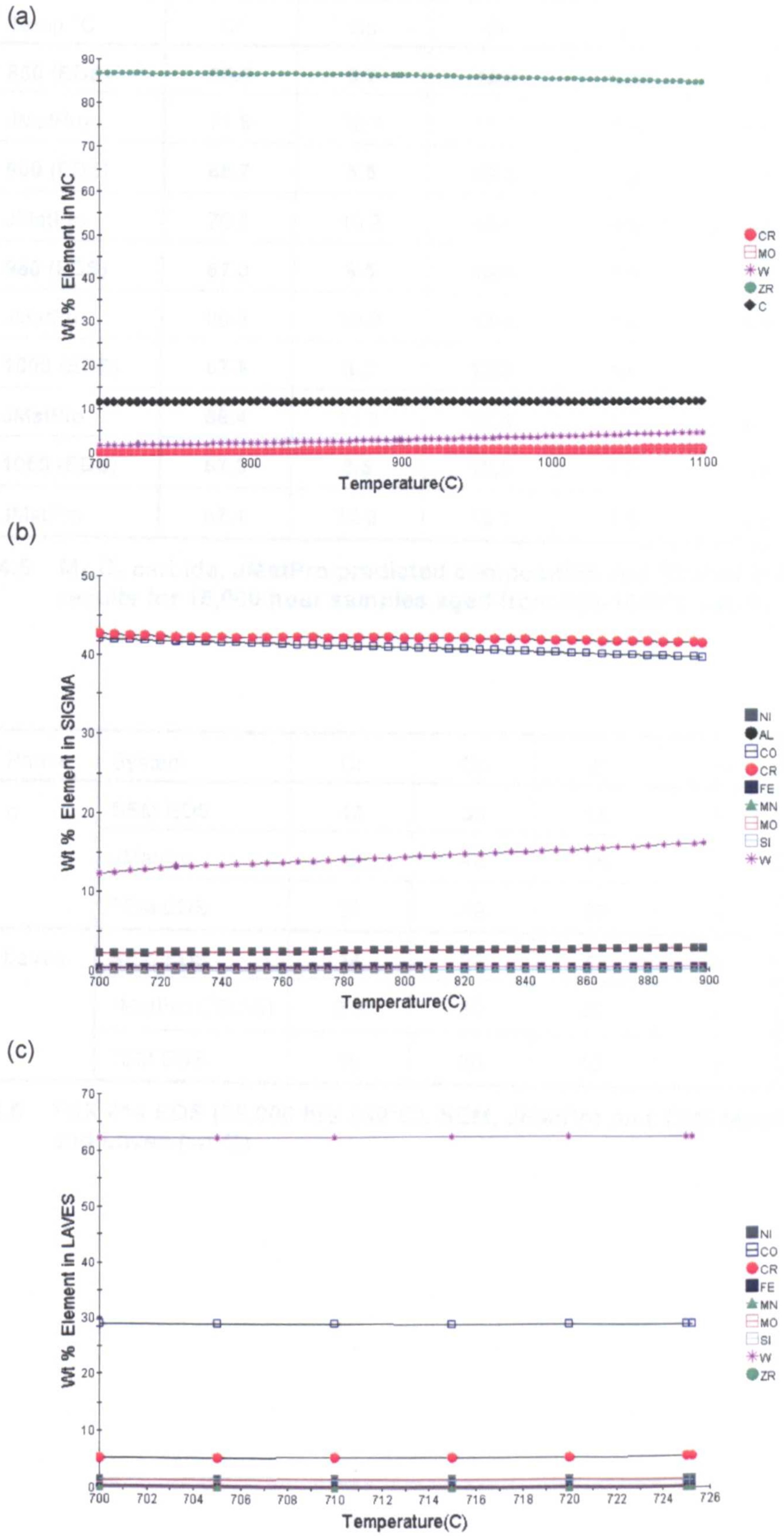

Figure 4.17 **FSX 414 JMatPro composition predictions of (a) MC carbide (b) σ and (c) Laves phase.**

Temp °C	Cr	Co	W	Ni	C
850 (EDS)	**65.0**	**9.7**	**16.9**	**1.6**	**6.7**
JMatPro	71.8	10.1	11.1	0.8	4.9
900 (EDS)	**66.7**	**8.5**	**16.3**	**1.8**	**6.7**
JMatPro	70.5	10.2	12.1	0.9	4.9
950 (EDS)	**67.0**	**8.5**	**16.4**	**1.8**	**6.6**
JMatPro	69.3	10.9	12.4	1.0	4.9
1000 (EDS)	**67.8**	**8.2**	**15.3**	**1.6**	**7.1**
JMatPro	68.4	11.5	12.8	1.1	4.8
1050 (EDS)	**67.3**	**8.5**	**15.3**	**1.7**	**7.2**
JMatPro	67.4	12.2	13.1	1.3	4.8

Table 4.5 $M_{23}C_6$ carbide, JMatPro predicted composition and SEM EDS FSX 414 results for 15,000 hour samples aged from 850-1050°C (wt.%).

Phase	System	Cr	Co	W	Ni
σ	**SEM EDS**	**43**	**36**	**15**	**5**
	JMatPro	42	40	15	3
	TEM EDS	37	39	20	4
Laves	**SEM EDS**	**14**	**26**	**58**	**3**
	JMatPro (700°C)	5.3	30	62	2
	TEM EDS	19	26	52	3

Table 4.6 FSX 414 EDS (25,000 hrs 850°C), SEM, JMatPro and TEM results for σ and Laves (wt.%).

4.4 Unknown Phase Identification (Electron diffraction)

Figure 4.18 and 4.19 show thin foil samples removed from the 10,000 hour 850°C sample by FIB SEM. The figures show a TEM image of the thin foil sample and the corresponding selected area electron diffraction patterns for both phases. The electron diffraction patterns were indexed using the Cambridge University Practical Crystallography software Version 1.6(79). The phases investigated were γ, μ, η, σ, Laves MC, M_6C and $M_{23}C_6$. Indexing of the patterns confirmed the white phase as Laves phase (Co_2W, hexagonal lattice, parameter a_o 4.75Å c_o 7.9Å) and the blocky phase as σ (CrCo, tetragonal, lattice parameter a_o 8.81 Å, c_o 4.56 Å).

The chemical compositions of the phases were determined in the TEM by EDS and are compared with the SEM EDS results in Table 4.6. There are variations in the measured compositions for both phases. The larger variations ~6 wt.% are in the chromium and tungsten concentrations. There is no systematic variation other than when the chromium is low the tungsten is high and vica versa. The σ TEM EDS values show lower chromium and higher tungsten than the SEM EDS values whereas the Laves phase TEM EDS chromium is higher and the tungsten lower than the SEM EDS values. The lower SEM EDS chromium value for Laves phase was unexpected as the Laves phase is associated with the chromium rich $M_{23}C_6$ carbide and it was expected that as a result of the small size of the Laves phase the electron beam would overlap on to chromium rich $M_{23}C_6$ carbide resulting in higher chromium values. It should be noted that the SEM EDS result are the mean value from ten spot analyses whereas the TEM EDS result is the mean of two analyses. The variations in composition evident in Table 4.6 are probably less the result of the equipment more an indication of the variation in the composition of the phases found in the samples.

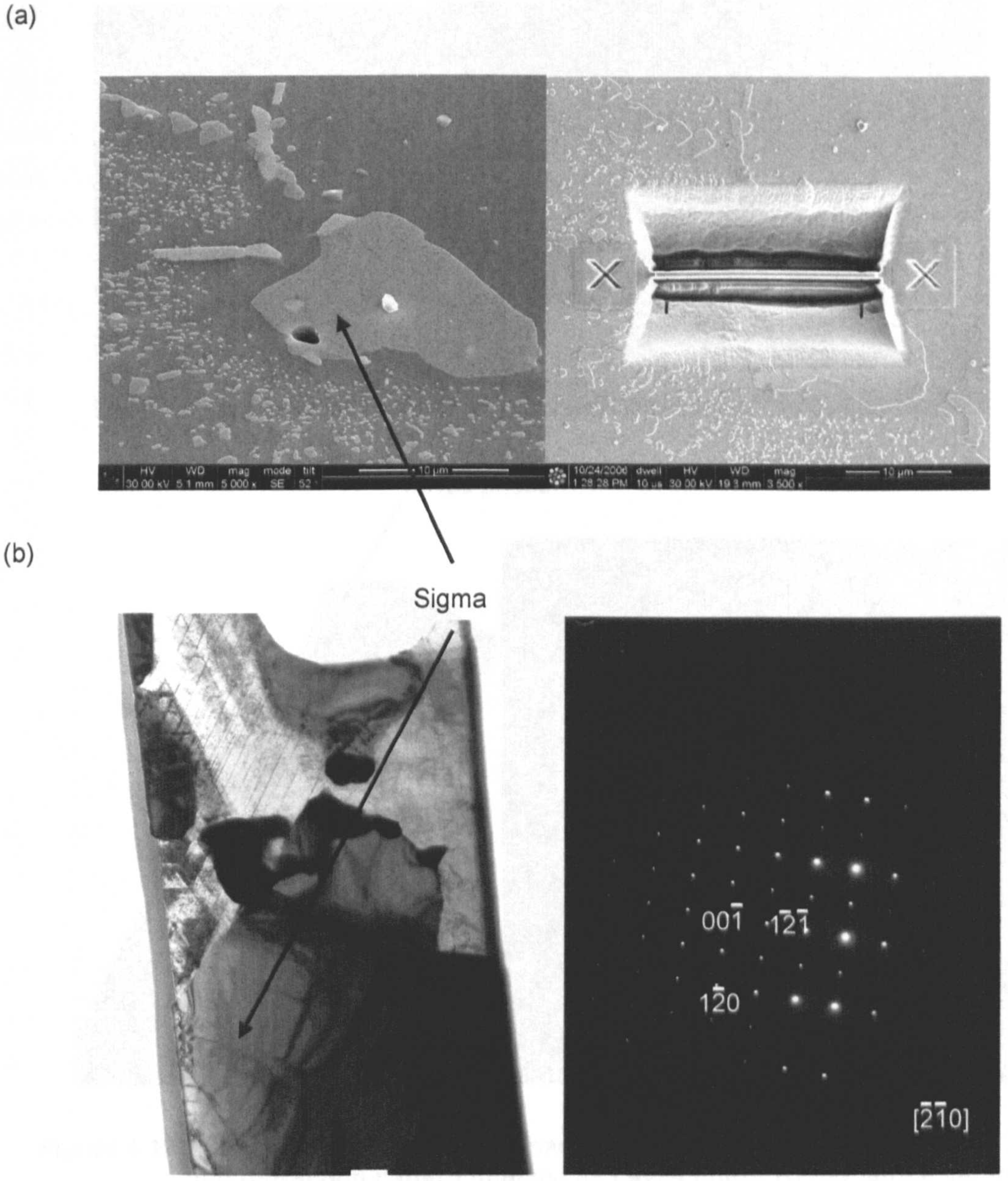

Figure 4.18 FSX 414 (a) FIB SEM image, sample position (b) TEM image of thin foil and diffraction pattern indexed as σ (CrCo tetragonal lattice parameter a_o 8.81Å, c_o 4.56Å).

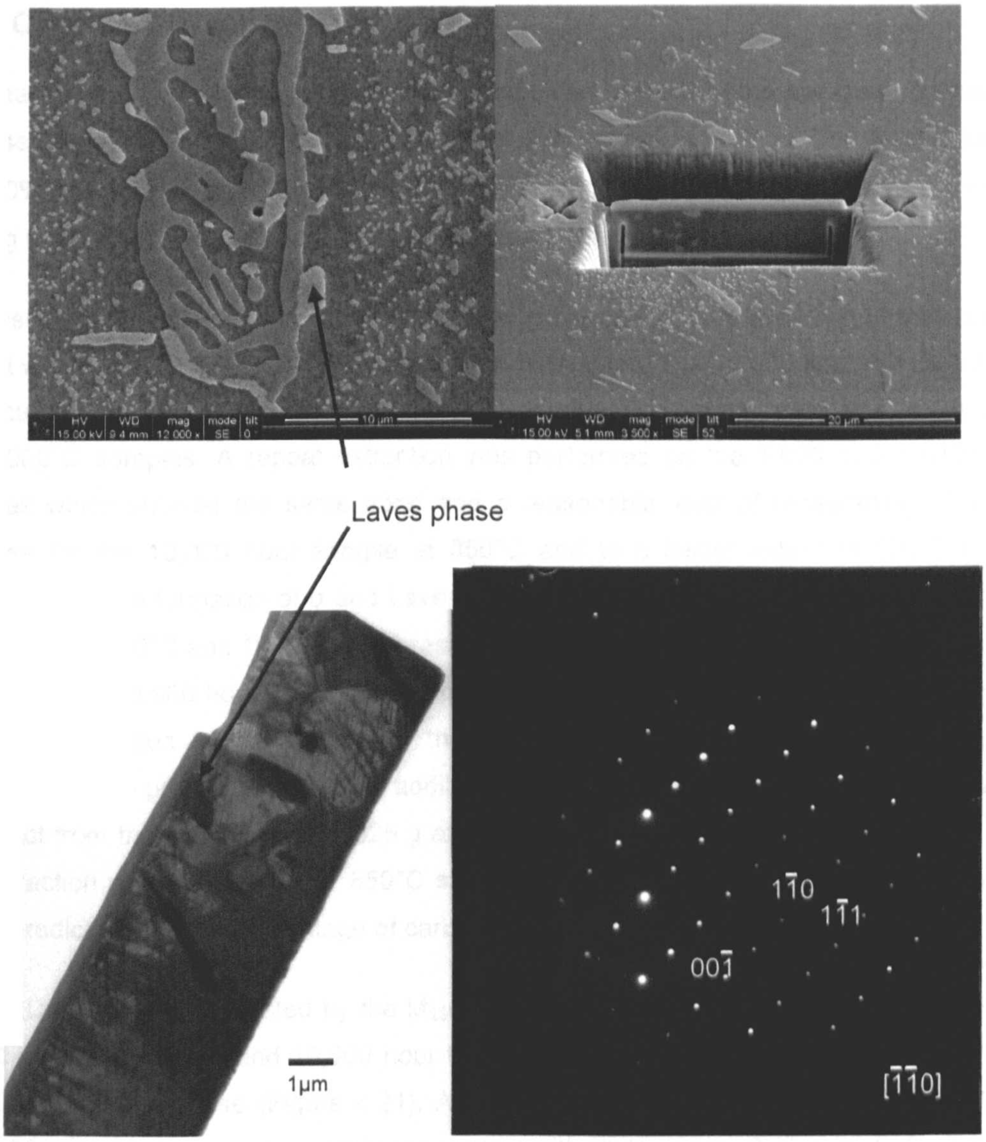

Figure 4.19 FSX 414 (a) FIB SEM image sample position (b) TEM image of thin foil and diffraction pattern indexed as Laves phase (Co_2W lattice parameter a_o 4.75Å c_o 7.9Å).

4.5 Carbide extract and XRD

To measure the type and volume fraction of carbides present in the samples, the carbides were separated from the matrix by a bulk electrolytic extraction method. The electrolyte used was 10% hydrochloric acid, 1% tartaric acid in methanol. The technique dissolves the γ matrix leaving the carbides as sediment. For further details see Chapter 3.7.

The results of the carbide extraction are detailed in Figure 4.20 and show a relatively constant extract weight for the 1,000, 2,000 and 5,000 hour samples. The 10,000 hour samples show a significant increase in the 850°C and 1050°C samples with smaller increases in the 900°C and 1000°C samples. A repeat extraction was performed on the 5,000 and 10,000 hours samples which showed the same trend and a reasonable level of repeatability. The large increase for the 10,000 hour sample at 850°C and to a lesser extent at 900°C may be attributable to the formation of σ and Laves phase (Figure 4.21). The increase in the carbide extraction at 1000°C and 1050°C is the result of the pickup of chromium nitrides evident in the trace from the 10,000 hour 1050°C sample (Figure 4.22). The use of the weight of extract to show any changes in the volume of the $M_{23}C_6$ carbide with time or temperature was prevented by the presence of the two additional phases (Laves and σ). The maximum weight of extract from the samples was 0.025 g after a three hour extraction. The total extract for X-ray diffraction of the 10,000 hour 850°C sample gave ~5.4 wt.%. The figures from JMatPro would predict the weight percentage of carbide and second phases as ~10 wt.% at 850°C.

The XRD traces are dominated by the $M_{23}C_6$ carbide phase. Additional peaks evident on the 850°C and 900°C 5,000 and 10,000 hour traces are in reasonable agreement with σ (CoCr) and Laves (Co_2W) phase (Figure 4.21). Additional peaks evident on the 5,000 and 10,000 hour 1050°C traces are in reasonable agreement with Cr_2N and Cr_2C (Figure 4.22). The peak positions for Cr_2N and Cr_2C are very similar and it is considered that the peaks are actually from Cr_2N particles which have formed within the oxidised layer and have not been removed prior to the extraction process. μ phase did not fit with the data. Details of the phases identified from the XRD traces are given in Table 4.7.

(a)

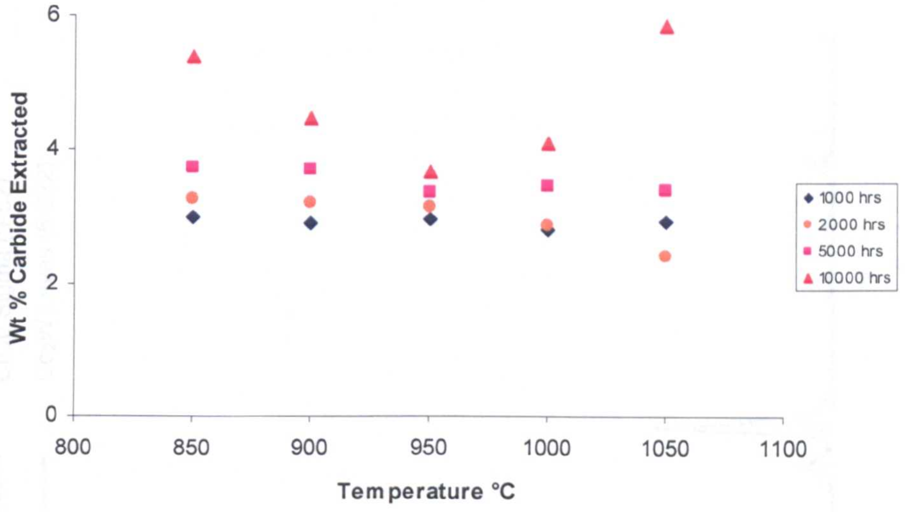

(b)

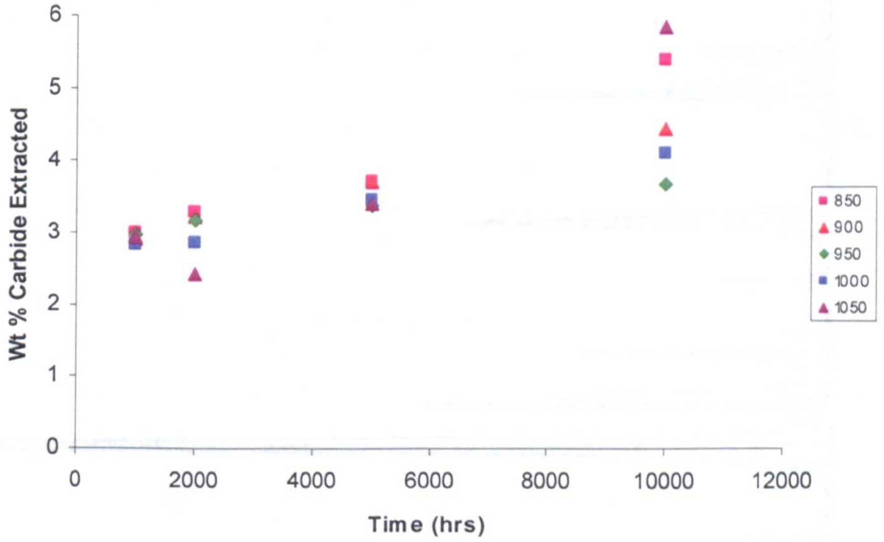

Figure 4.20 **FSX 414 weight of carbide extracted for all samples plotted as a function of (a) temperature and (b) time (wt.%).**

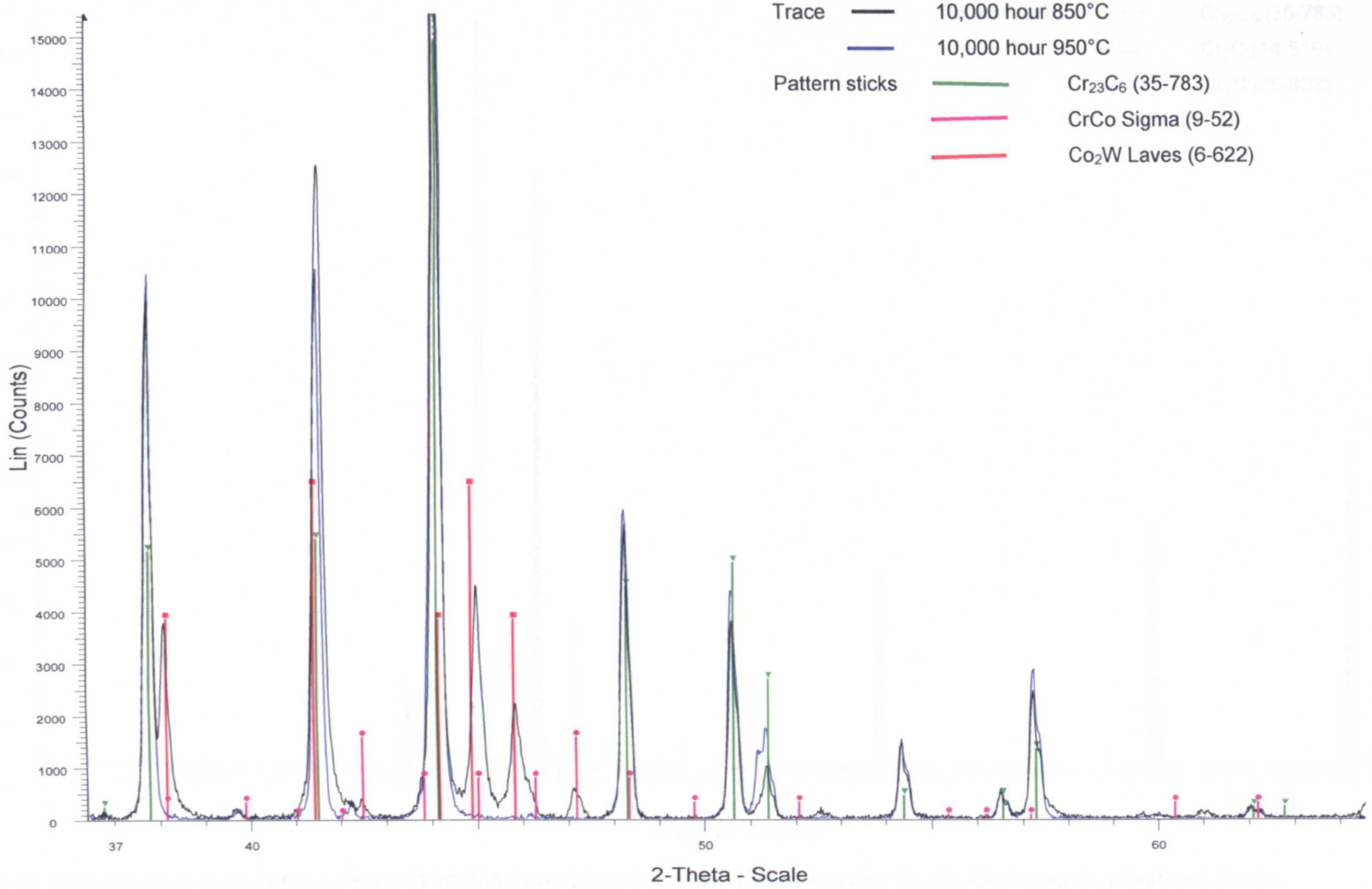

Figure 4.21 XRD trace from FSX 414 10,000 hour 850°C and 950°C sample extract showing $M_{23}C_6$, σ and Laves pattern sticks.

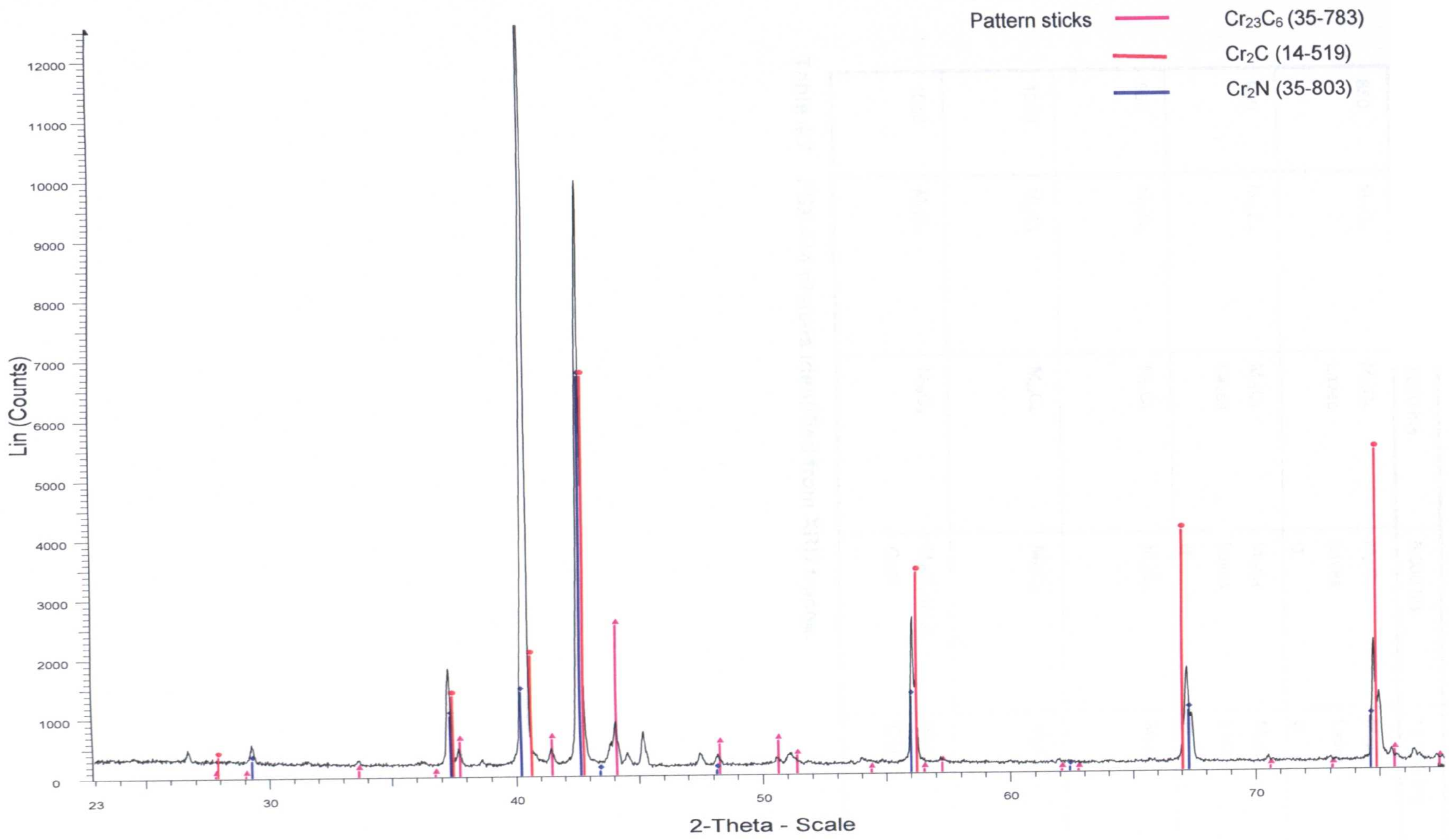

Figure 4.22 XRD trace of extract from FSX 414 10,000 hour 1050°C sample trace showing $M_{23}C_6$, Cr_2C and Cr_2N pattern sticks.

Temp °C	1,000 hrs	2,000 hrs	5,000 hrs	10,000 hrs
850	$M_{23}C_6$	$M_{23}C_6$ Laves	$M_{23}C_6$ Laves σ	$M_{23}C_6$ Laves σ
900	$M_{23}C_6$	$M_{23}C_6$ Laves	$M_{23}C_6$ Laves σ	$M_{23}C_6$ Laves σ
950	$M_{23}C_6$	$M_{23}C_6$	$M_{23}C_6$	$M_{23}C_6$
1000	$M_{23}C_6$	$M_{23}C_6$	$M_{23}C_6$	$M_{23}C_6$
1050	$M_{23}C_6$	$M_{23}C_6$	$M_{23}C_6$ small Cr_2N	$M_{23}C_6$ Cr_2N

Table 4.7 FSX 414 phases identified from XRD traces.

4.6 Hardness

Hardness measurements would, if there were significant changes in the hardness as a result of ageing, be the ideal method for predicting temperature or time of components taken out of service. The results Figure 4.23 (a) for temperature show a drop in hardness of ~30 Hv_{20} as the ageing temperature increases from 850°C to 950°C. There is no significant change in hardness between 950°C and 1050°C. The results do not show any systematic changes with ageing time The results plotted against time Figure 4.23 (b) show a consistent drop in hardness with ageing temperature (850-1000°C) at each time interval and a dip in hardness from 1,000 to 10,000 hours recovering to approximately the original hardness at 25,000 hours. All of the samples are following a similar trend which would suggest that the formation of σ and Laves (850°C, 900°C and to a lesser extent 950°C) has no significant effect on hardness. The only other microstructural changes are the precipitation of the secondary $M_{23}C_6$ carbides, the subsequent coarsening of the secondary carbides and the coalescence of the primary eutectic $M_{23}C_6$ carbides. It is not possible from the information collected in this investigation to confirm if the precipitation and coalescence of the carbides are responsible for the changes in hardness. However, the γ matrix micro-hardness results, Figure 4.24, show only a slight drop in hardness with temperature and no evidence of a hardness dip with time. Micro-hardness measurements of the σ phase in the 15,000 hour 850°C sample show hardness from 900 to 1300 $Hv_{0.05}$, significantly harder than the matrix.

The small variations in both macro and micro-hardness with both time and temperature would preclude hardness as a time temperature indicator.

(a)

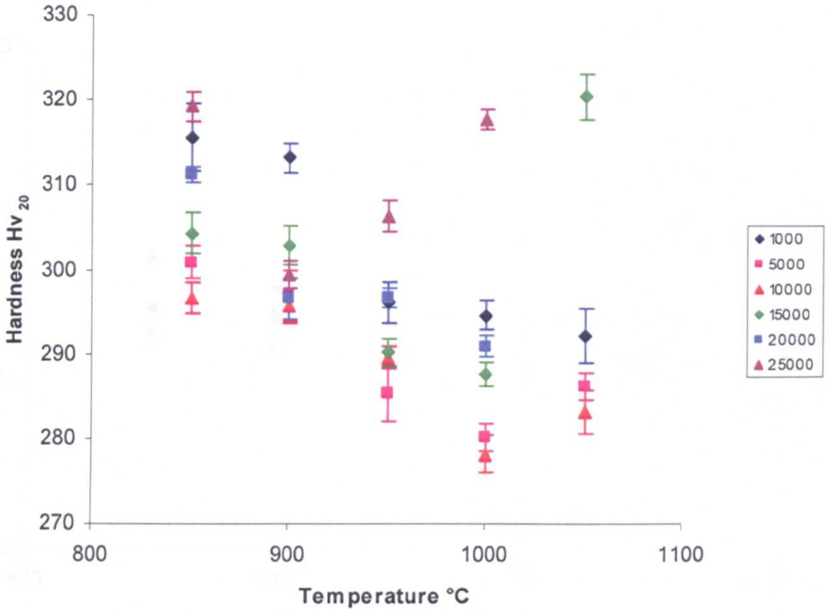

(b)

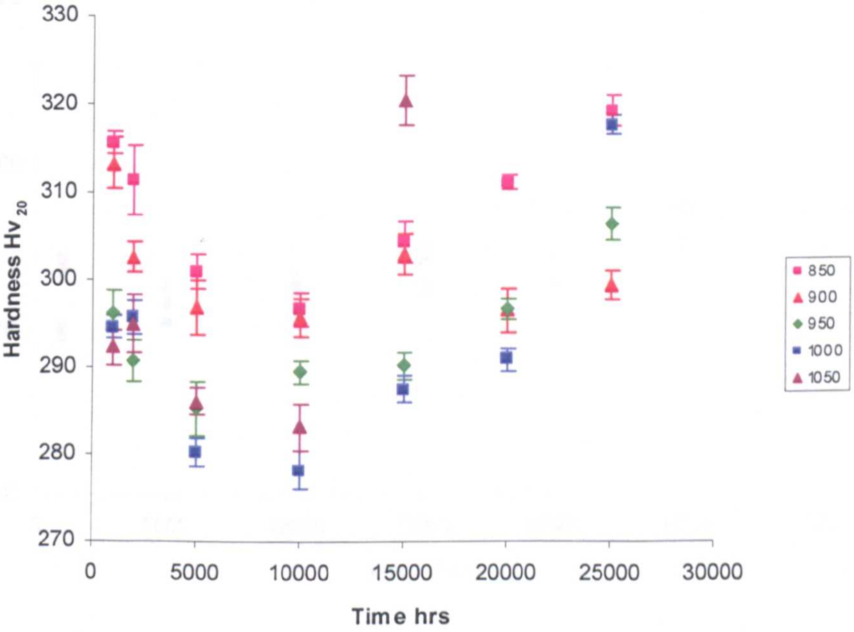

Figure 4.23 **FSX 414 hardness values (error bars - standard error of mean) plotted as a function of (a) temperature and (b) time.**

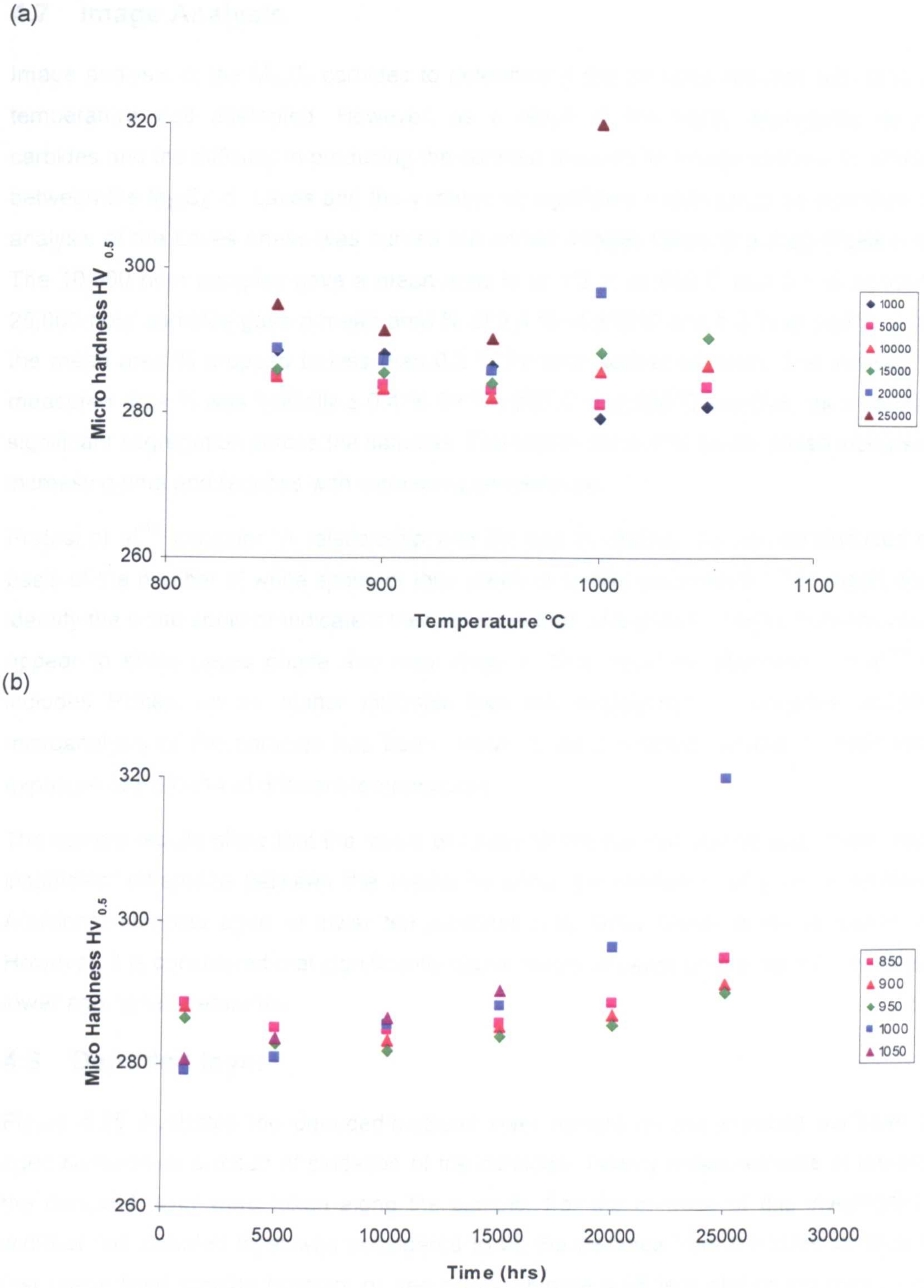

Figure 4.24 FSX 414 micro-hardness measured in γ matrix plotted as a function of (a) temperature and (b) time.

4.7 Image Analysis

Image analysis of the $M_{23}C_6$ carbides to determine if the carbides reduced with time and or temperature was attempted. However, as a result of the highly segregated secondary carbides and the difficulty in producing the contrast required for image analysis to differentiate between the $M_{23}C_6$, σ, Laves and the γ matrix no significant trends could be identified. Image analysis of the Laves phase was carried out on ten images taken at a magnification of 250. The 10,000 hour samples gave a mean area % of 1.3 % at 850°C and 0.7 % at 900°C the 25,000 hour samples gave a mean area % of 2.4 % at 850°C and 1.3 % at 900°C. At 950°C the mean area % dropped to less than 0.2 % for both sets of samples. The variation in the measured area % was typically ± 0.4 % for the 850°C and 900°C samples, as a result of the significant segregation across the samples. The results show that Laves phase increases with increasing time and reduces with increasing temperature.

Pratesi et al(49) consider "A relationship with life and or residual life can be deduced on the basis of the number of white spots, or their areas or similar parameters." The report does not identify the white spots or indicate if there is more than one phase. Images from the report do appear to show Laves phase and may show σ. The report by Mezzedimi et al(45) which includes Pratesi as an author indicates that the segregation of tungsten carbide and microanalysis of the particles has been shown to be a method capable of estimating the exposure of FSX 414 at different temperatures.

The current results show that the levels of Laves phase are low and as such there would be insufficient difference between the results to allow the prediction of time or temperature. Additional samples aged at lower temperatures may show higher levels of Laves phase. However, it is considered that significantly higher levels of Laves phase would not be found at lower ageing temperatures.

4.8 Denuded layer

Figure 4.25 illustrates the denuded/oxidised layer formed on the exposed surfaces of the aged samples as a result of oxidation of the carbides. Twenty measurements of the width of the denuded layer were taken along the sample. For the purpose of this investigation the width of the denuded layer was considered to be the distance from the outer surface to the first un-oxidised carbide (primary or secondary). Figure 4.26 is a plot of the mean width of denuded/oxidised layer against temperature and time with standard error of mean as error bars. The plots show a correlation with time which would allow the prediction of an operating temperature for an uncoated vane with a known operating time. The error bars show that the width of the denuded layer is relatively constant around the samples. Figure 4.27 is a plot of the mean width of the denuded layer against time^{½} showing a reasonable linear relationship between time and the width of the denuded layer. However, the samples were held at a constant temperature with a very small number of cooling events. It was evident from the oxide scale in the furnace that spalling of the oxide occurred at temperature. In addition, violent spalling of the oxide occurred on cooling the samples to room temperature. Further work would be required to determine the effects of thermal cycling and composition on the width of the denuded layer.

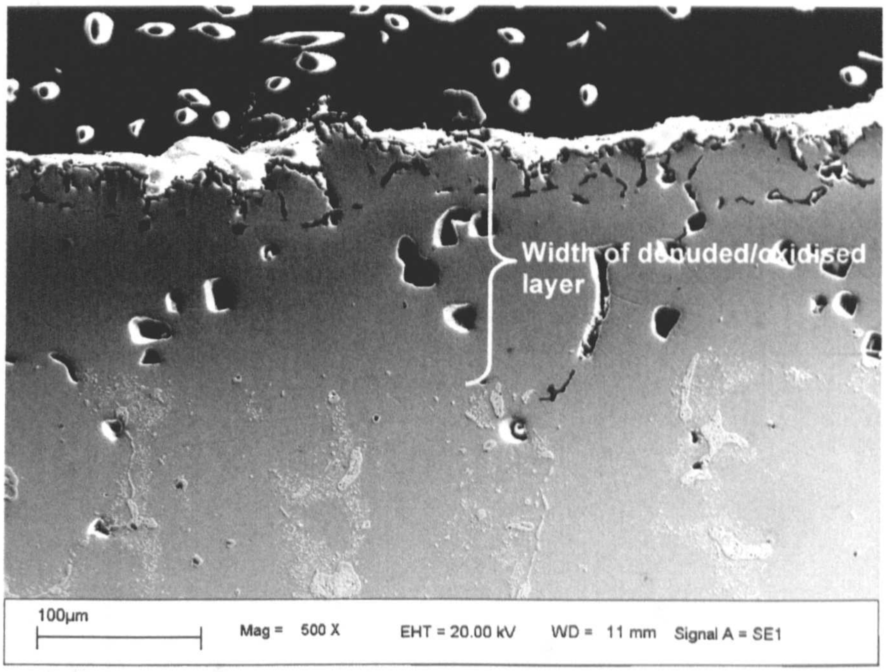

Figure 4.25 SEM SE image of FSX 414 showing denuded/oxidised layer on 15,000 hour 900°C sample.

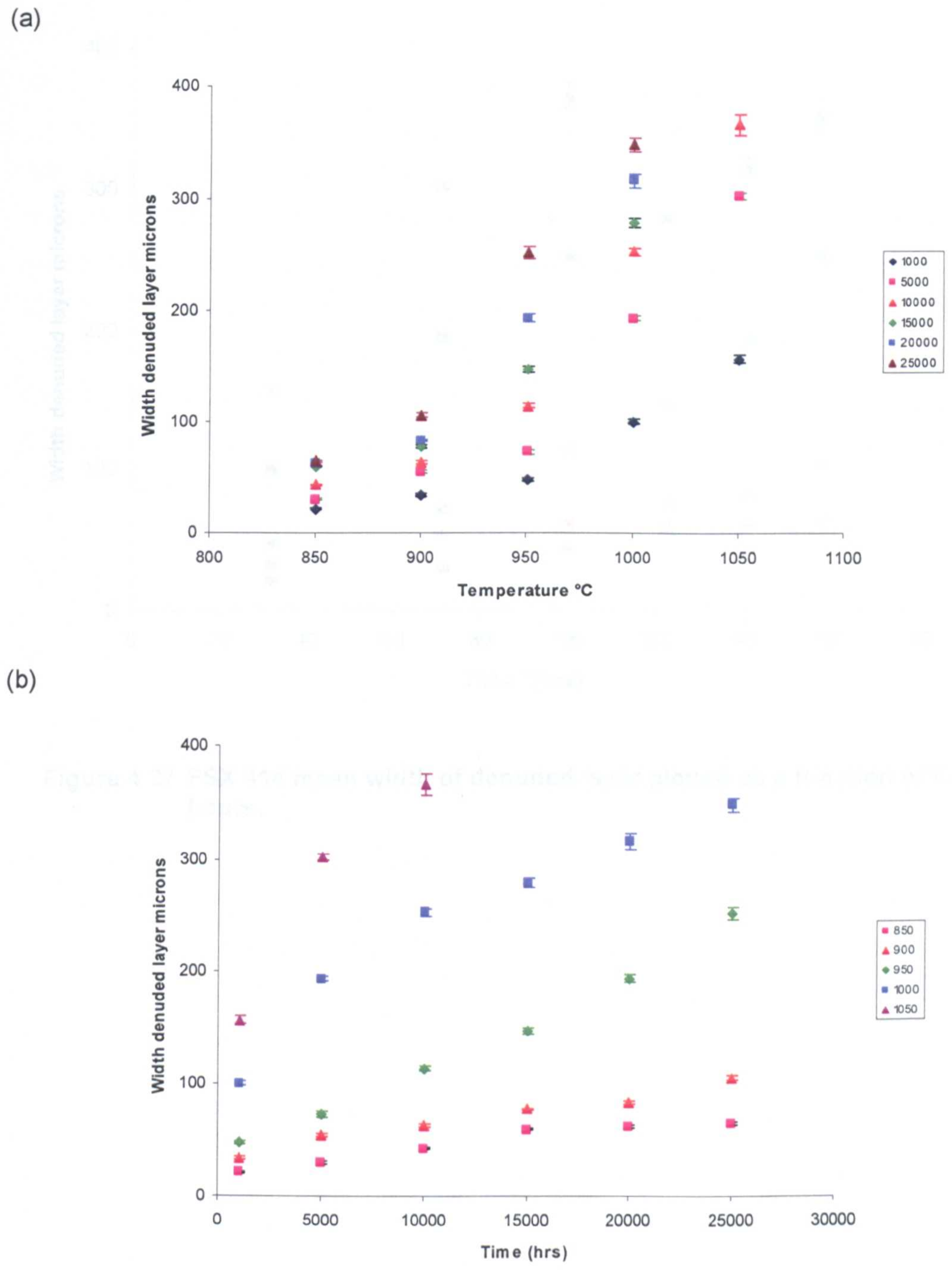

Figure 4.26 **FSX 414 mean width of denuded layer measured on the exposed surface of the samples (error bars are standard error of mean) plotted as a function of (a) temperature and (b) time.**

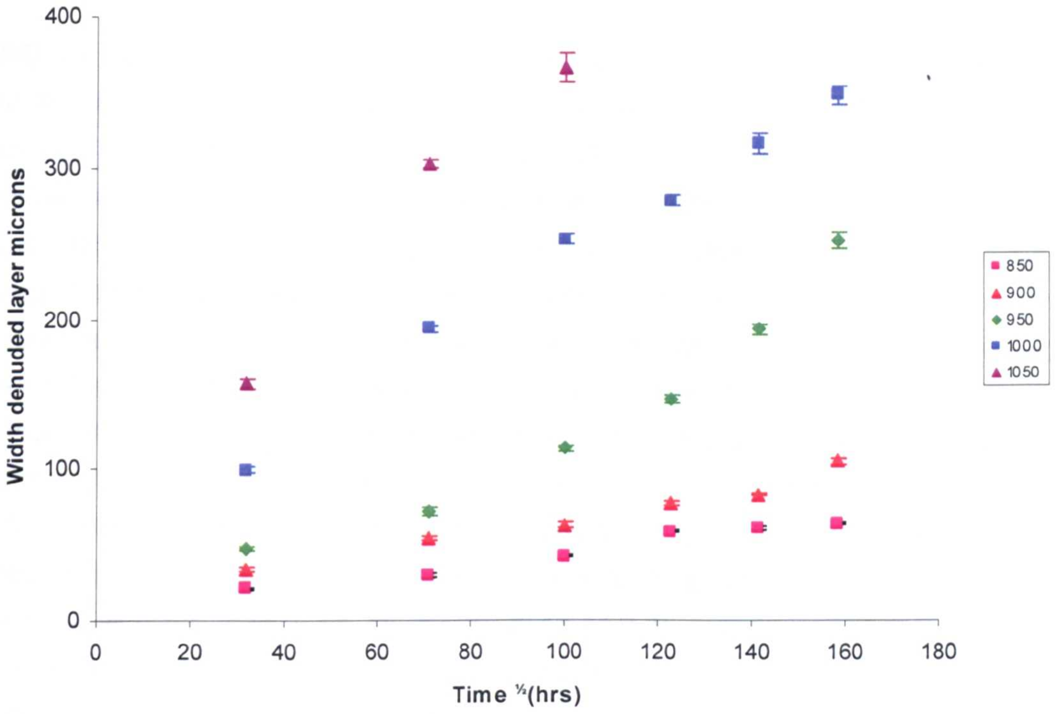

Figure 4.27 FSX 414 mean width of denuded layer plotted as a function of time^{½} hours.

4.9 Summary

XRD and EDS have confirmed that the carbides present in the aged samples of FSX 414 are primary chromium rich $M_{23}C_6$ eutectic carbides and secondary $M_{23}C_6$ carbides. The chromium rich $M_{23}C_6$ eutectic carbides contain tungsten, cobalt and nickel and can be expressed as approximately $Cr_{80}Co_{11}W_7Ni_2$ (where the subscript describes the concentration in at.%). The EDS levels of chromium in the carbides were similar to the JMatPro predictions. However, the tungsten and cobalt levels were at variance with the JMatPro prediction by 25% and 20% respectively. Two additional phases were evident in the samples aged at temperatures less than 950°C; a large blocky phase and a high tungsten phase both associated with the coarse eutectic $M_{23}C_6$ carbides. The phases were identified as σ and Laves phase respectively by electron diffraction. JMatPro predicts σ and Laves phase to be present at lower temperatures with predicted compositions similar to those determined by EDS. The composition of Laves phase and σ determined by EDS is: Laves 55 wt.% W, 25 wt.% Co, 14 wt.% Cr and 3 wt.% Ni and σ 43 wt.% Cr, 36 wt.% Co, 15 wt.% W and 5 wt.% Ni. σ and Laves phase could be used to indicate qualitatively the operating temperatures and service time experienced. With σ evident the samples had a metallurgical operating temperature of less than 900°C for times greater than 5,000 hours. The presence of Laves phase without σ would indicate a sample operating at less than 950°C for between 1,000 and 25,000 hours. Further work would be required to determine the effect of alloy composition on the formation of Laves and σ phase in FSX 414.

Image analysis of the carbides was inconclusive due to the large variation in the size of the primary and secondary carbides. However, it is considered that image analysis of the secondary $M_{23}C_6$ carbides may provide a correlation with time and temperature. Image analysis of the Laves phase did show an increase with increasing time and a reduction with increasing temperature. However, the low levels of Laves in the aged samples would prohibit the use of this phase for the prediction of time and or temperature in practice.

The use of the weight of extract removed to indicate any changes in the amount of $M_{23}C_6$ carbide with time or temperature was precluded by the presence of the two additional phases (σ and Laves phase). The small variations in both macro hardness and the micro-hardness of the matrix also preclude hardness as a time/temperature indicator. The width of the denuded layer evident on the exposed surfaces of the sample could be used to indicate a metallurgical operating temperature on uncoated samples. However, further work is required to determine the effect of temperature cycling and composition on the denuded layer formation.

5 Characterisation and discussion of alloy NP 222

NP 222 is a conventionally cast γ′ (~20%) strengthened nickel based superalloy with a high level, ~19 wt.%, of cobalt. The alloy exhibits a primary tantalum, titanium, niobium rich MC carbide and a chromium rich grain boundary $M_{23}C_6$ carbide(55).

This chapter presents and discusses the outcome of the experimental work carried out to characterise alloy NP 222 and to develop an understanding of the microstructural changes that occur, with both time and temperature, for life prediction, refurbishment and failure investigations. Cast samples were given a solution and precipitation heat treatment (Table 3.2), typical of that used for industrial turbine vanes, and were subsequently aged in air at temperatures ranging from 800 to 1050°C, for exposure times up to 25,000 hours.

A detailed microstructural characterisation was carried out by means of optical and scanning electron microscopy (SEM). Thin foils containing the unknown phases, identified in the SEM, were produced by FIB SEM for electron diffraction in a transmission electron microscope (TEM). The results of thermodynamic equilibrium calculations performed using JMatPro are presented followed by the results from EDS, XRD and hardness measurements.

5.1 Microstructural Observations

The identification of the phases was initially based on EDS chemical composition measurements and comparison with representative compositions found in the literature. In SEM backscatter mode the MC carbides show white, the $M_{23}C_6$ carbides as black and the γ′ precipitates as grey due to the difference in the atomic contrast (Figure 5.1 and 5.2).

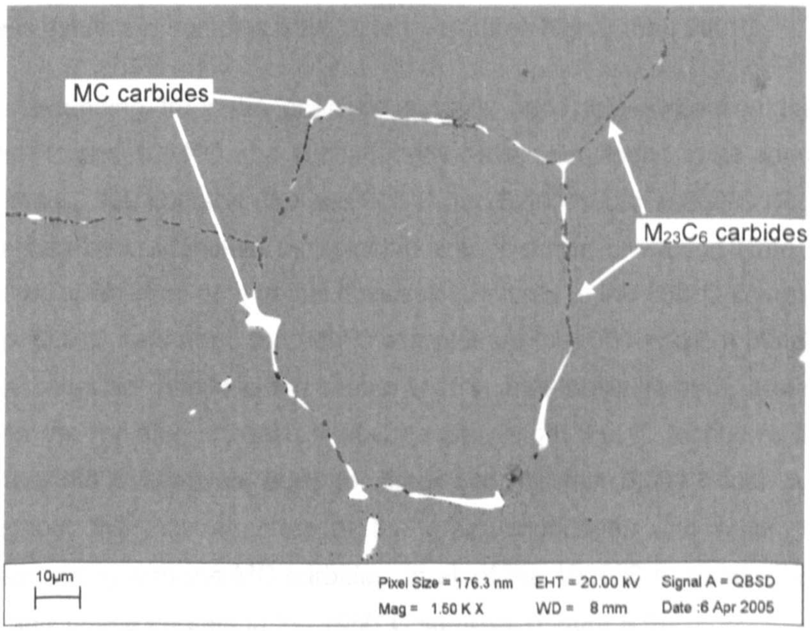

Figure 5.1 SEM BSE image of NP 222 showing grain boundary MC and $M_{23}C_6$ carbides (1,000 hrs 800°C).

The microstructure of the samples after the standard heat treatment, prior to ageing consists of a γ matrix, γ′ precipitates, grain boundary and intergranular MC carbides. $M_{23}C_6$ carbides could not be resolved on the grain boundaries (Figure 5.2).

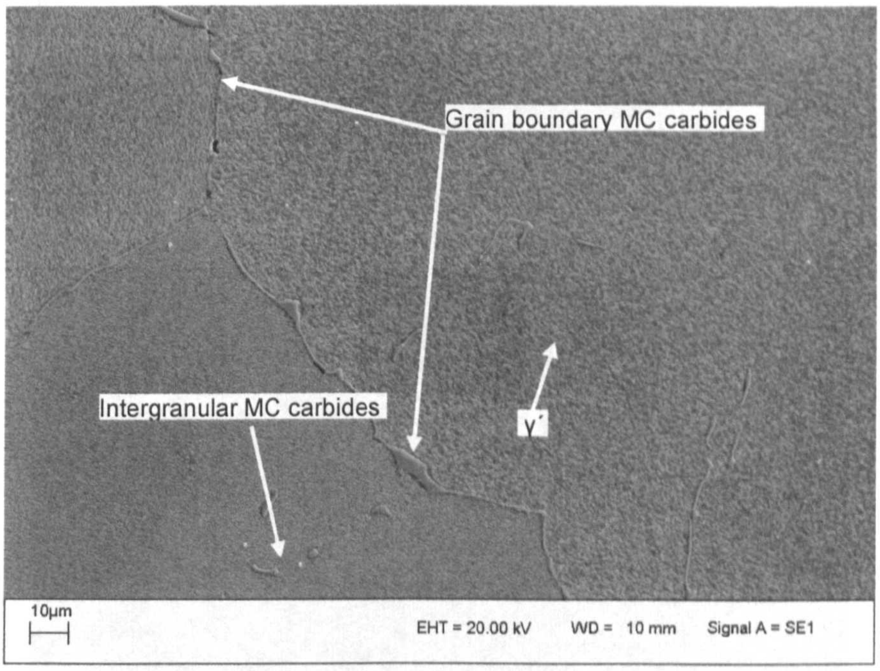

Figure 5.2 SEM SE image of NP 222 microstructure following standard solution and precipitation heat treatment showing γ′, grain boundary and MC carbides.

γ′ is evident in all samples aged from 800 to 950°C and coarsens with both temperature and time. Grain boundary $M_{23}C_6$ carbides are evident in the 800, 850 and 900°C samples. Samples aged at 900°C for times greater than 10,000 hours show no $M_{23}C_6$ carbides. No $M_{23}C_6$ carbide is evident in samples aged at temperatures higher than 950°C.

Fine platelets extending from the grain boundaries were first evident in the 1,000 hour samples at 950°C and 1000°C and subsequently have been found in all samples aged for times greater than 2,000 hours at 850 and 900°C and 5,000 hours at 800°C (Figure 5.3). The platelet phase has been identified by selected area electron diffraction (Chapter 5.4) as η phase and will be referred to as η in this discussion. Initially in the 850°C samples, the 900°C samples up to 10,000 hours and the 950°C samples up to 5,000 hours η platelets extended from the grain boundary and into the matrix with γ′ free areas forming around the plates (Figure 5.3). As the η plates increase in volume and length the γ′ decreases in volume and coarsens. In the 950°C samples, aged for times greater than 5,000 hours, η platelets are evident throughout the microstructure at the grain boundaries and within the matrix. η platelets remain, along with the MC carbides, in all of the 1000°C samples (Figure 5.8). MC carbide is the only phase present in the 1050°C samples (Figure 5.9).

The SEM and optical observations for the aged samples are summarised in (Table 5.1). Representative SEM micrographs of the 1,000, 5,000, 15,000 and 25,000 hour samples are presented in Figure 5.4 - 5.9 and show more clearly the changes in the microstructure with time and temperature.

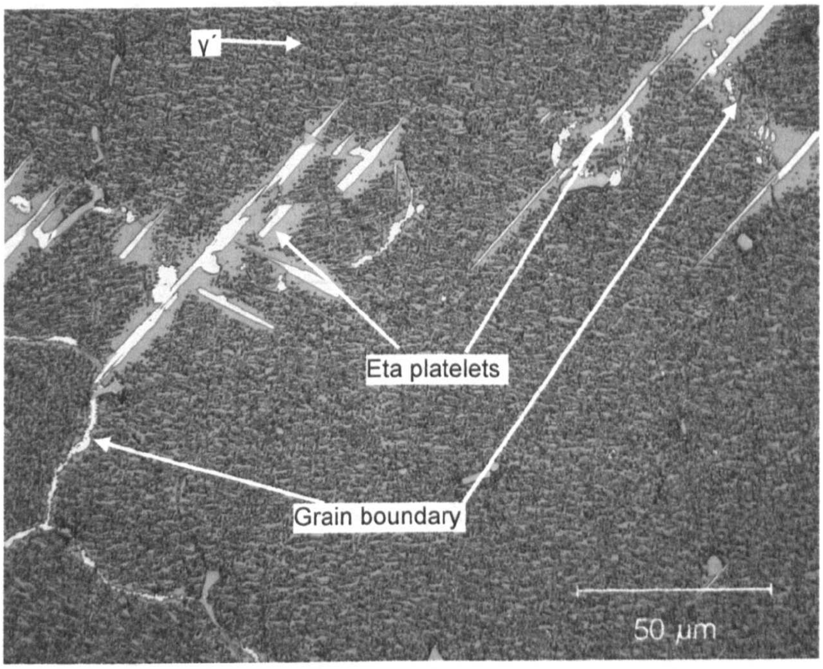

Figure 5.3 Optical micrograph of NP 222 showing η needles growing from the grain boundary with gamma free areas (10,000 hours at 850°C).

	1,000 hrs	2,000 hrs	5,000 hrs	10,000 hrs	15,000 hrs	20,000 hrs	25,000 hrs
800°C	MC $M_{23}C_6$ (GB+M) γ'	MC $M_{23}C_6$ (GB+M) γ'	MC $M_{23}C_6$ (GB+M) γ' $<< \eta$	MC $M_{23}C_6$ (GB+M) γ' $<\eta$	MC $M_{23}C_6$ (GB+M) γ' η	MC $M_{23}C_6$ (GB+M) γ' η	MC $M_{23}C_6$ (GB+M) γ' η
850°C	MC $M_{23}C_6$ (GB + M) γ'	MC $M_{23}C_6$ (GB+M) γ' $<< \eta$	MC $M_{23}C_6$ (GB+M) γ' $< \eta$	MC $M_{23}C_6$ (GB+M) γ' η	MC $M_{23}C_6$ (GB+M) γ' η	MC $M_{23}C_6$ (GB+M) γ' η	MC $M_{23}C_6$ (GB+M) γ' η
900°C	MC $M_{23}C_6$ (GB) $< \gamma'$	MC $M_{23}C_6$ (GB) $< \gamma'$ $<< \eta$	MC $<M_{23}C_6$ (GB) $<\gamma'$ $< \eta$	MC $<<M_{23}C_6$ (GB) $< \gamma'$ η	MC γ' η	MC γ' η	MC γ' η
950°C	MC $<\gamma'$ $<< \eta$	MC $<<\gamma'$ $< \eta'$	MC $<<\gamma'$ η	MC $<<\gamma'$ η	MC $<<\gamma'$ η	MC $<<\gamma'$ η	MC $<<\gamma'$ η
1000°C	MC $<< \eta$	MC $<< \eta$	MC $<< \eta$	MC $<< \eta$	MC $<< \eta$	MC $<< \eta$	MC $<< \eta$
1050°C	MC	MC	MC	MC	MC	No sample	No sample

GB Grain boundary
M Matrix

< low levels
<< very low levels

Table 5.1 NP 222 phases identified in aged samples by optical and SEM observations (γ matrix not included).

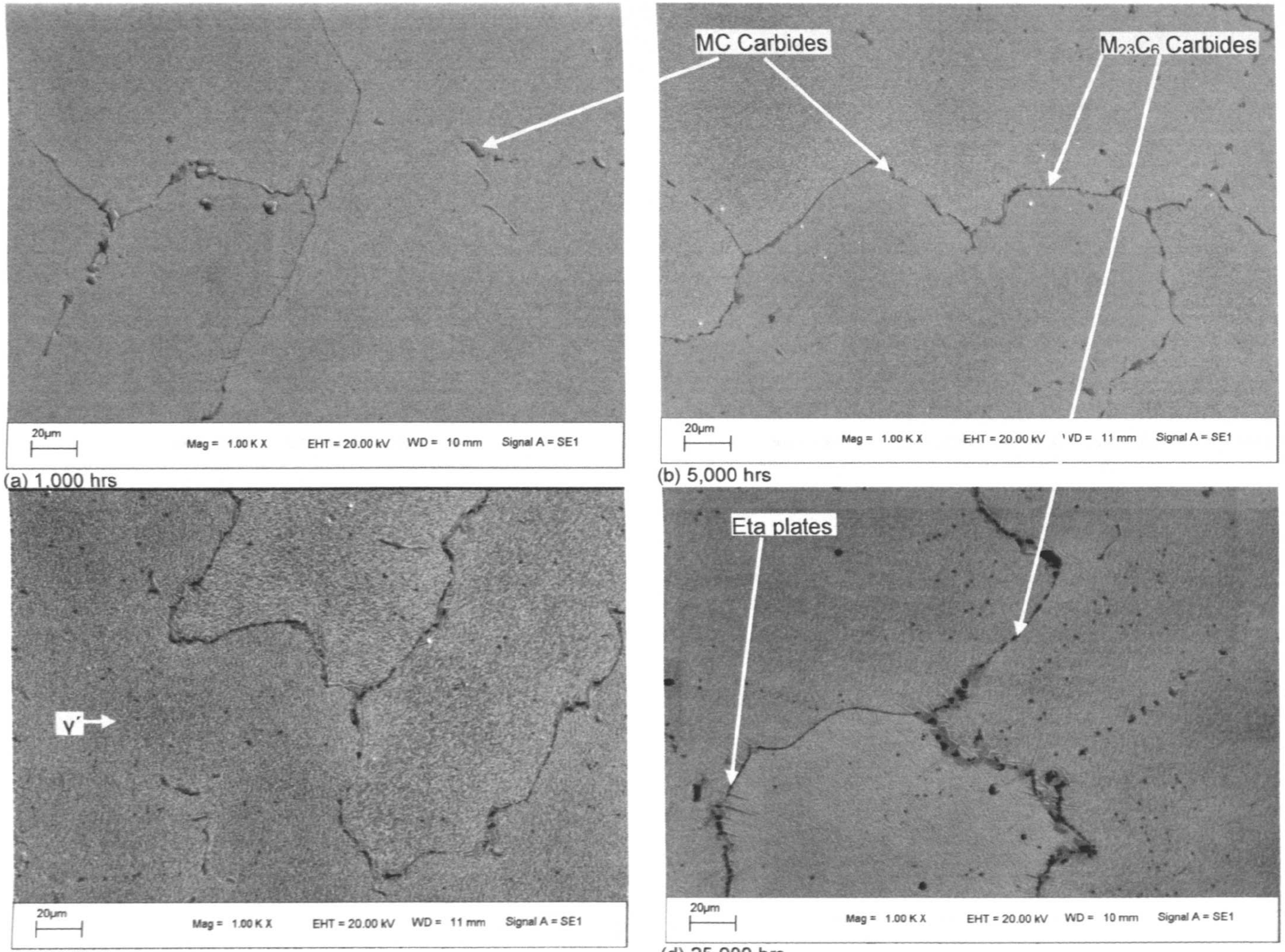

(a) 1,000 hrs

(b) 5,000 hrs

(c) 15,000 hrs

(d) 25,000 hrs

Figure 5.4 SEM SE images of NP 222 samples aged at 800°C for (a) 1,000 (b) 5,000, (c) 15,000 and (d) 25,000 hours respectively.

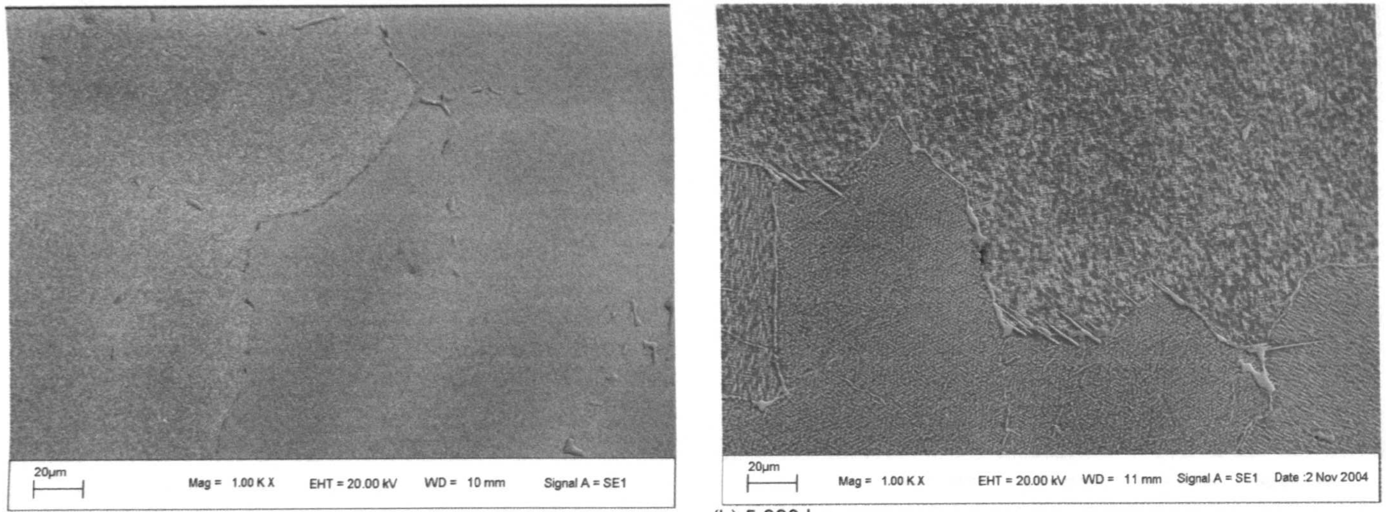

(a) 1,000 hrs (b) 5,000 hrs

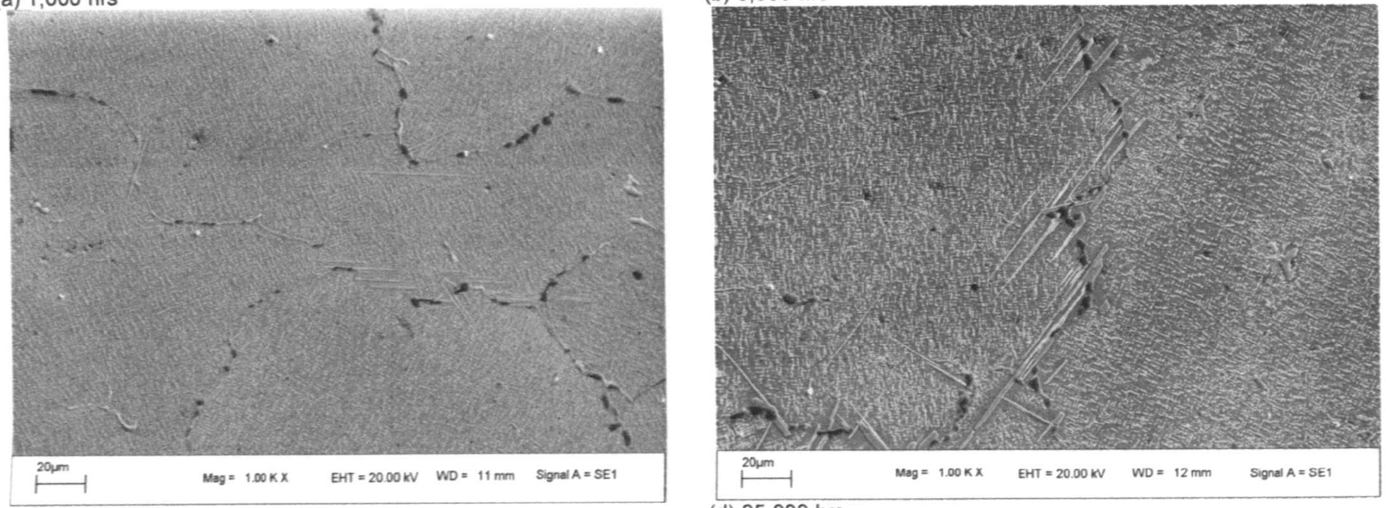

(c) 15,000 hrs (d) 25,000 hrs

Figure 5.5 SEM SE images of NP 222 samples aged at 850°C for (a) 1,000 (b) 5,000, (c) 15,000 and (d) 25,000 hours respectively.

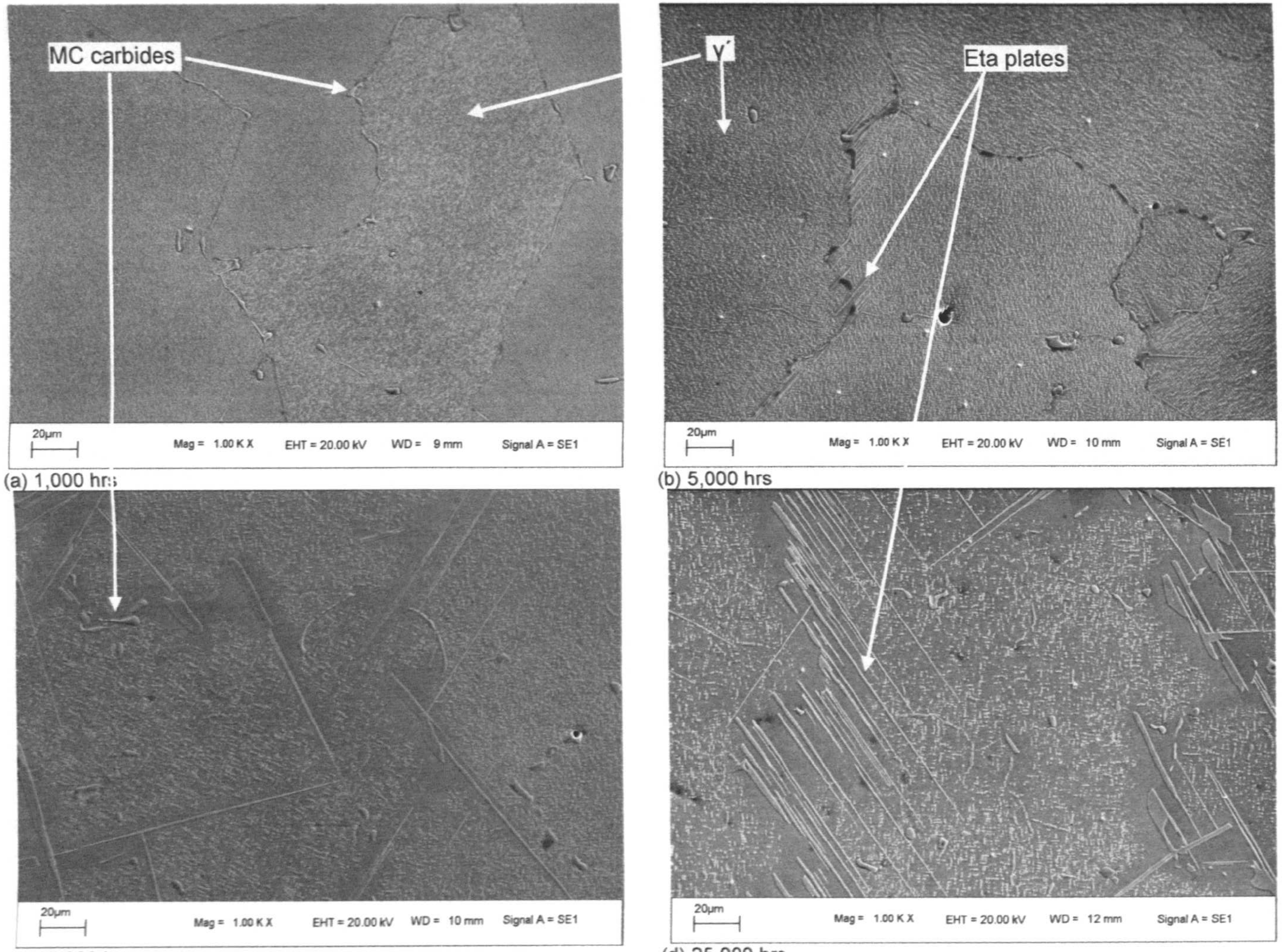

(a) 1,000 hrs

(b) 5,000 hrs

(c) 15,000 hrs

(d) 25,000 hrs

Figure 5.6 SEM SE images of NP 222 samples aged at 900°C for (a) 1,000 (b) 5,000, (c) 15,000 and (d) 25,000 hours respectively.

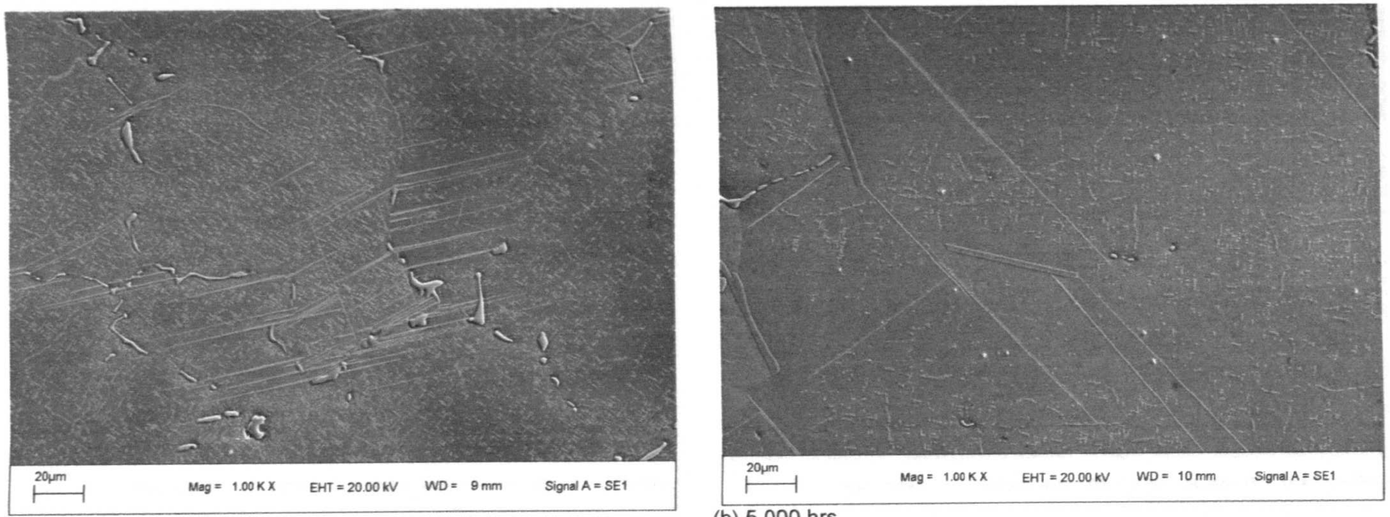

(a) 1,000 hrs

(b) 5,000 hrs

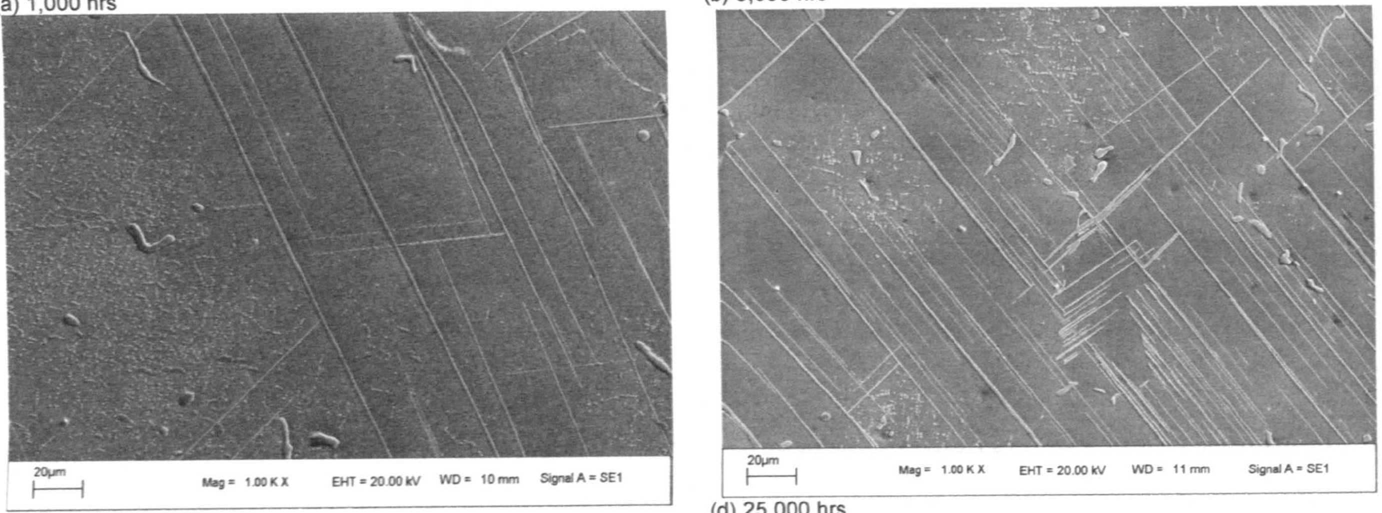

(c) 15,000 hrs

(d) 25,000 hrs

Figure 5.7 SEM SE images of NP 222 samples aged at 950°C for (a) 1,000 (b) 5,000, (c) 15,000 and (d) 25,000 hours respectively.

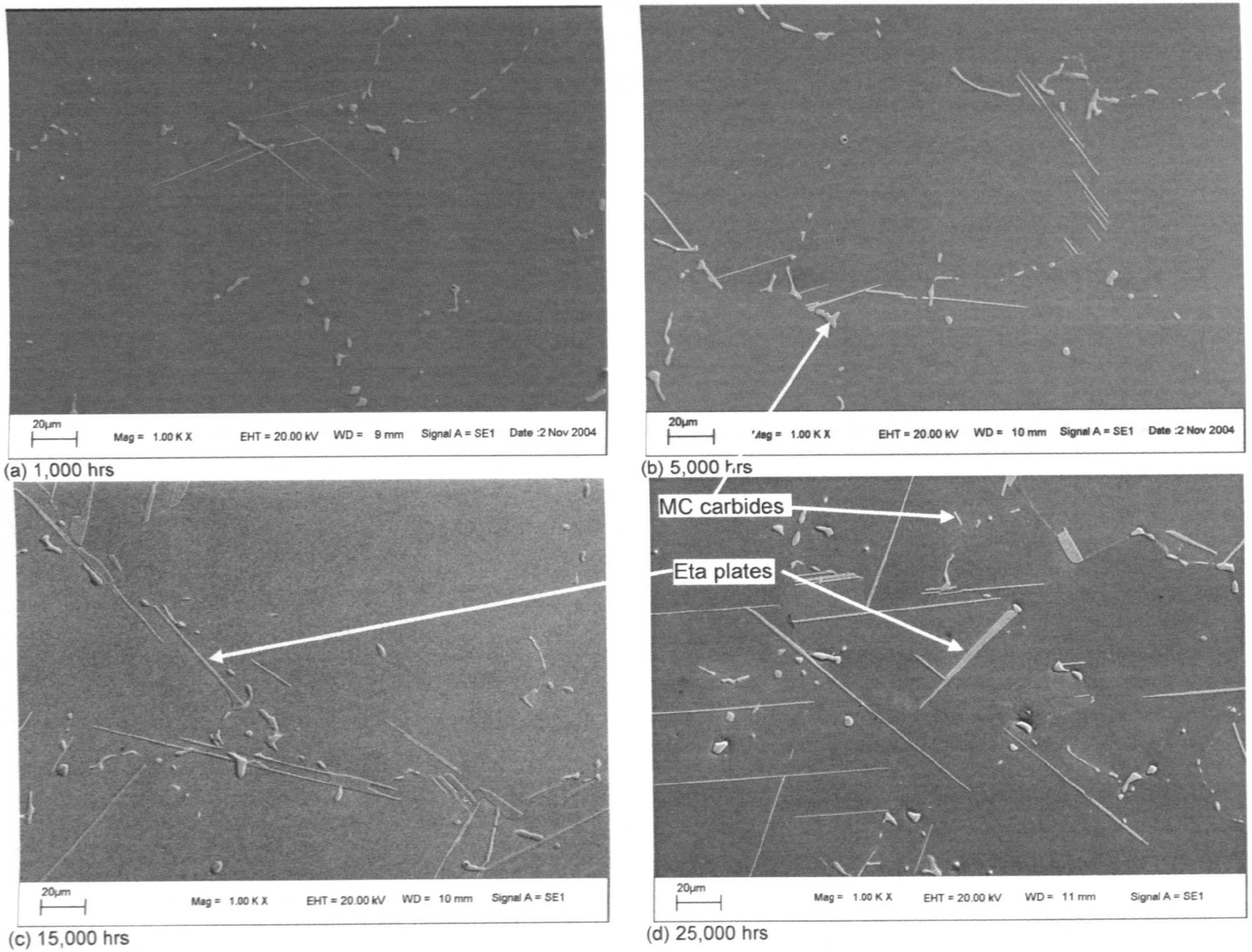

(a) 1,000 hrs

(b) 5,000 hrs

(c) 15,000 hrs

(d) 25,000 hrs

Figure 5.8 **SEM SE images of NP 222 samples aged at 1000°C for (a) 1,000 (b) 5,000, (c) 15,000 and (d) 25,000 hours respectively.**

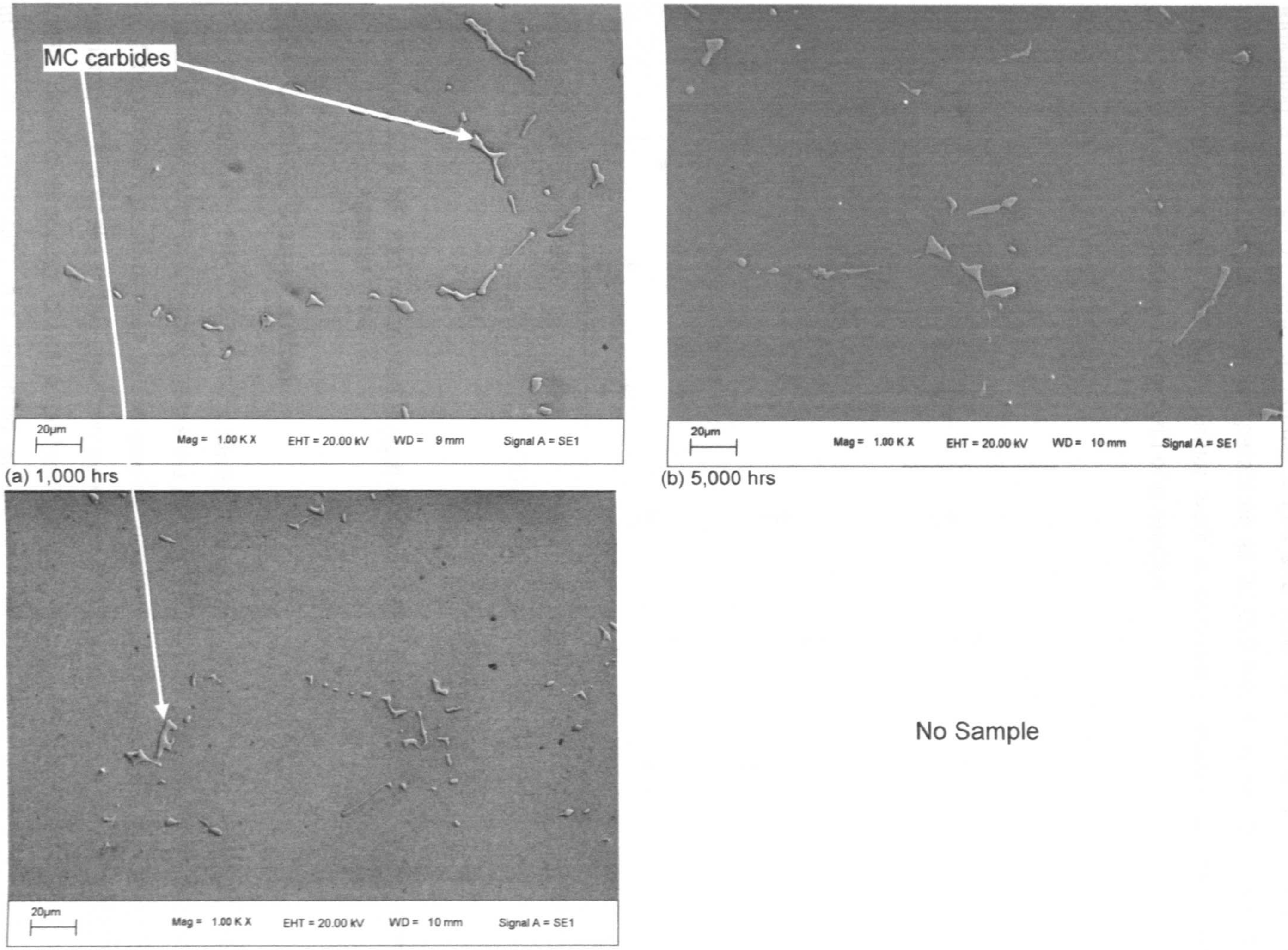

(a) 1,000 hrs

(b) 5,000 hrs

(c) 15,000hrs

No Sample

Figure 5.9 SEM SE images of NP 222 samples aged at 1050°C for (a) 1,000 (b) 5,000 and (c) 15,000 hours respectively.

Figure 5.10 is a plot of grain boundary initiated η needle length against time for the 800 – 950°C samples. Measurement of the needle length was carried out on a light microscope with an in eyepiece graticule. Thirty individual needle lengths were measured along the centre line of each sample. Only needles which had initiated at the grain boundaries were measured, needles which crossed grain boundaries or other needles were excluded. The results show a series of curves indicating a correlation between needle length and time. Of interest is that the results show a maximum needle length for all temperatures at 20,000 hours. Although there is a correlation between needle length and time, further work is required to determine the effect of the alloy composition on the initiation and growth of η needles.

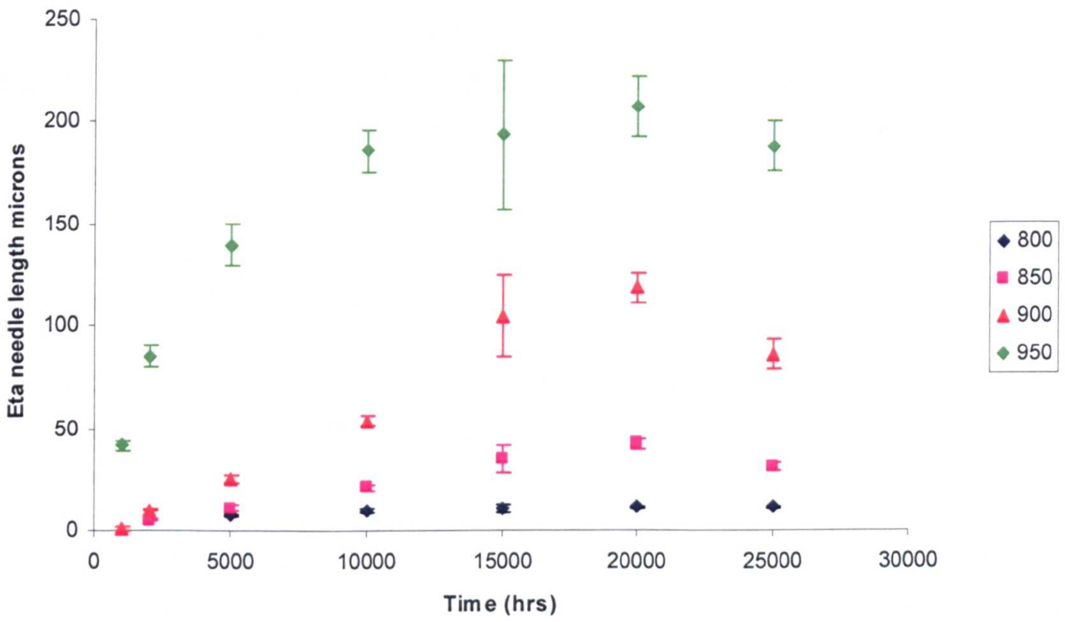

Figure 5.10 NP 222 measured length of grain boundary initiated η needles plotted against time.

5.2 Carbide Composition

The MC carbide in NP 222 contains tantalum and tungsten which produce overlapping peaks in the EDS data. With overlapping peaks the EDS software determines the quantity of each element by fitting known peak profiles to the overlap region. The accuracy of the fitting depends on the similarity of the peaks in the unknown spectrum to those of the profiles in the EDS database. In WDS peak overlapping is not a problem as the X-rays are separated using diffraction and individual wavelengths are detected at different spectrometer positions. The INCA Energy+ software used for the analysis of the MC carbides combines the outputs of the EDS and WDS spectrometers to provide a single analysis.

The EDS/WDS analysis results for the MC carbide are summarised in Table 5.2, tantalum and tungsten values were obtained by WDS. The results show similar levels of tantalum, titanium and niobium (~31 wt.%) with tungsten at ~3 wt.%. An earlier analysis of the carbides by EDS alone gave a tungsten levels of ~7 wt.%. Plots of the mean MC carbide analysis for tantalum, titanium, niobium and tungsten are contained in Figure 5.11. The temperature plots show none of the large changes in the MC carbide composition predicted by JMatPro (Chapter 5.3) for tantalum and titanium. The time plots show small reductions in tantalum and tungsten and a small increase in titanium.

JMatPro predicts the equilibrium composition as a function of temperature. The MC carbides have formed in the cast alloy at high temperatures and are therefore most likely to have a composition close to the high temperature prediction of ~30 wt.% of tantalum, titanium and niobium. The predictions indicate that as equilibrium is approached at lower temperatures carbides would become richer in tantalum at the expense of titanium. The EDS/WDS results show the reverse of this (Table 5.3).

The EDS/WDS results show no significant changes in the MC carbide composition that would allow the prediction of time or temperature.

The limitations imposed by the spot size precluded the quantitative EDS measurement of γ' and $M_{23}C_6$ carbides. However, EDS was used to confirm the presence of $M_{23}C_6$ carbides in the samples where the η phase peaks dominated the XRD traces (Chapter 5.5).

From the EDS measurements the metallic component of the MC carbide can be expressed as approximately $Ti_{48}Nb_{26}Ta_{16}W_3Cr_3Ni_3Co$ (where the subscript describes the concentration in at.%).

Time	Temp °C	Ti[a]	Cr[a]	Co[a]	Ni[a]	Nb[a]	Ta[b]	W[b]
1,000	800	30.1	1.7	0.9	2.1	30.4	31.5	3.4
	850	30.1	1.7	0.9	2.2	31.0	30.9	3.4
	900	29.9	1.7	0.9	2.7	31.5	29.7	3.5
	950	29.2	1.8	1.1	3.0	31.7	29.8	3.6
	1000	29.2	1.5	1.0	2.6	31.6	30.8	3.4
	1050	29.0	1.3	0.8	2.2	31.1	32.1	3.6
5,000	800	29.5	1.2	0.9	2.2	30.4	32.6	3.3
	850	28.6	1.3	0.7	2.3	30.6	33.4	3.3
	900	28.3	1.6	0.9	2.3	30.3	33.4	3.4
	950	29.1	1.6	0.9	2.2	30.7	32.2	3.5
	1000	29.4	1.7	1.0	2.2	31.9	30.6	3.4
	1050	29.7	1.3	0.8	2.2	32.0	30.7	3.4
10,000	800	29.3	1.3	0.8	2.1	30.9	32.5	3.4
	850	28.5	1.2	0.8	2.2	30.7	33.2	3.5
	900	28.9	1.2	0.8	2.1	30.5	33.2	3.4
	950	29.5	1.4	0.8	2.1	30.5	32.4	3.4
	1000	29.4	1.5	0.9	2.2	31.5	31.2	3.4
	1050	28.3	1.4	0.9	2.2	30.3	33.6	3.4
15,000	800	30.0	1.8	0. 9	2.7	32.5	28.7	3.5
	850	29.4	1.6	0.9	2.8	33.0	28.6	3.6
	900	29.5	1.5	0.8	2.4	32.9	29.6	3.4
	950	29.4	1.3	0.8	2.1	32.8	30.3	3.5
	1000	29.3	1.6	0.9	2.2	32.6	29.9	3.6
	1050	29.4	1.4	0.9	2.4	32.2	30.4	3.4
20,000	800	30.2	1.8	1.0	3.2	32.1	28.5	3.2
	850	30.1	1.6	1.2	3.1	33.0	27.7	3.3
	900	30.1	1.7	1.0	2.8	33.6	27.7	3.2
	950	30.2	1.7	1.0	2.8	32.4	28.7	3.2
	1000	30.3	1.5	0.8	2.3	32.3	29.5	3.4
25,000	800	31.0	1.6	1.3	3.2	31.8	27.9	3.2
	850	31.0	2.0	1.2	3.8	33.1	26.1	2.9
	900	30.6	2.3	1.3	3.6	32.5	26.5	3.2
	950	30.7	2.1	1.3	3.7	32.5	26.7	3.1
	1000	30.8	2.0	1.3	3.1	31.2	28.5	3.2

[a] EDS analysis
[b] WDS analysis

Table 5.2 **NP 222 EDS/WDS results for MC carbide (wt.%). Tantalum and tungsten determined by WDS remaining elements by EDS (normalised to 100 wt.%).**

(a) Tantalum

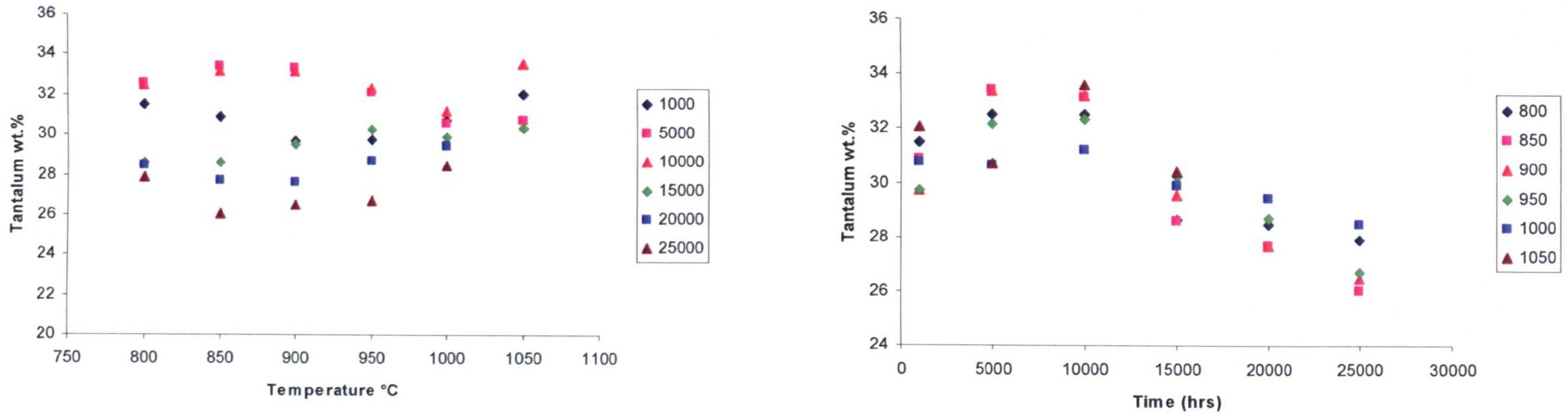

(b) Titanium

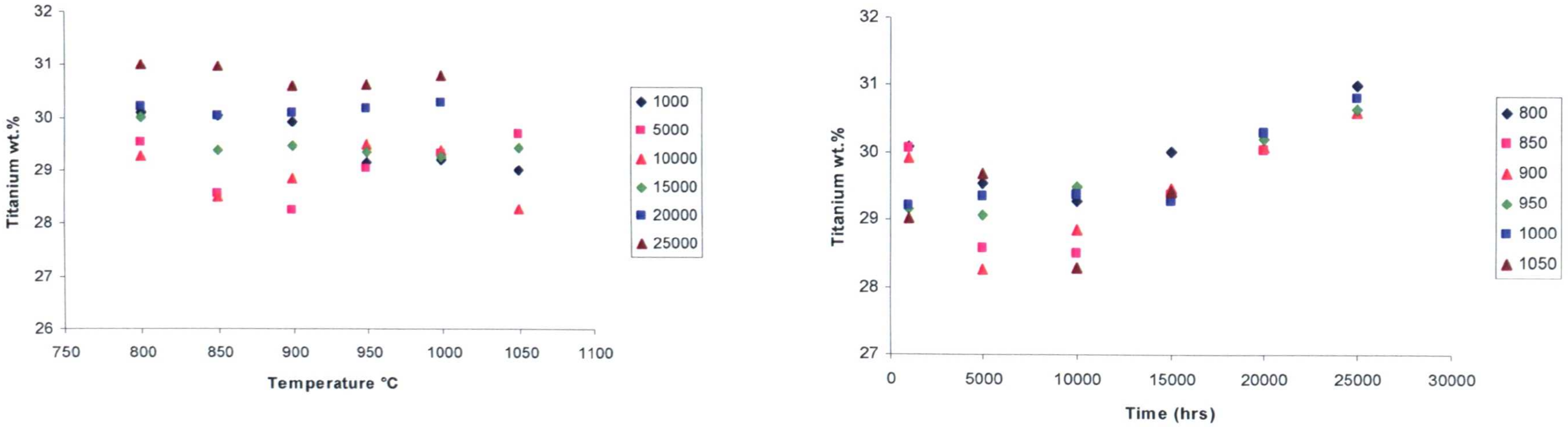

(c) Niobium

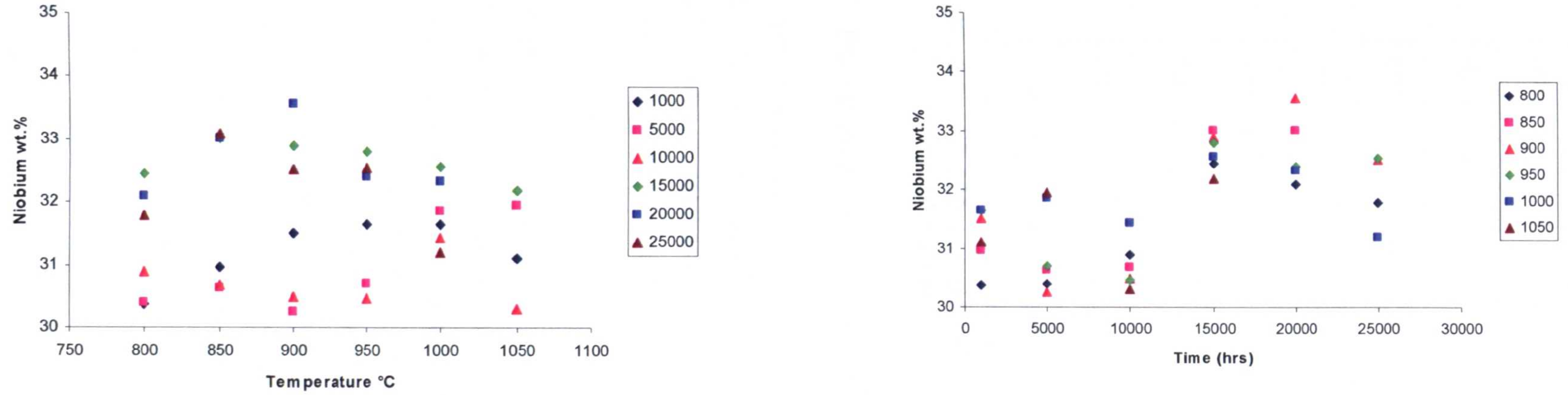

(d) Tungsten

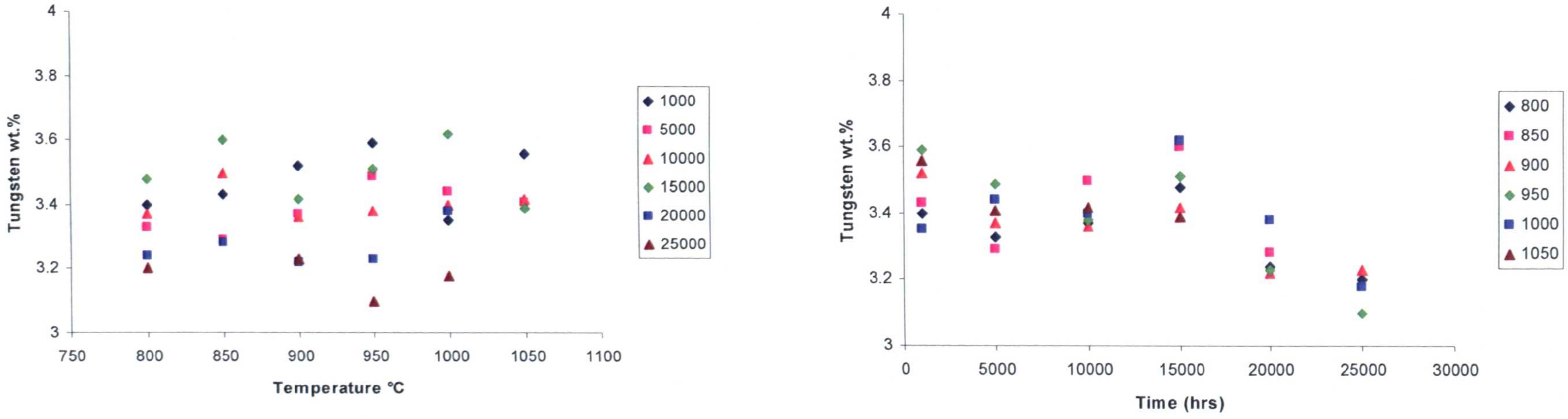

Figure 5.11 NP 222 MC carbide EDS/WDS analysis (wt.%) (a) tantalum, (b) titanium, (c) niobium and (d) tungsten respectively plotted with temperature and time.

wt.%	Ti	Cr	Co	Ni	Nb	Ta	Al	Zr	W
MC carbide									
EDS	28.5	1.5	0.8	2.4	30.7	33.4			3.6
JMatPro	20.7	0.2			27.4	38.1		2.0	0.7
η phase									
EDS (SEM)	11.7	1.9	8.5	66.1	3.4	5.9	2.5		
EDS (TEM)	12.6	1.8	9.8	64.4	4.5	4.1	2.5		
JMatPro	14.3	0.3	12.3	64.0	5.6	1.9	1.5		

Table 5.3 NP 222 comparison of EDS and JMatPro results for MC carbide and η phase (10,000 hrs 850°C).

5.3 Thermodynamic Equilibrium Predictions

This section presents thermodynamic equilibrium predictions for alloy NP 222 carried out using JMatPro software. NP 222 is a nickel based superalloy and as such JMatPro using the nickel based superalloy database should provide a close approximation of the phases present at equilibrium. The JMatPro calculations are based on the composition of the samples detailed in Table 3.1.

The JMatPro software is used to predict the equilibrium phases that would form under equilibrium conditions at the sample ageing temperatures. To compare the JMatPro predictions with the aged sample it is essential that no phase transformations occur on cooling. To confirm that no phase changes occur on cooling from the ageing temperature NP 222 samples aged at 850°C and 1050°C for 12,000 hours were water quenched. These samples were compared with a samples cooled in still air. Optically there was no variation between the air cooled and water quenched samples. Examination of the samples in the SEM confirmed that all the secondary phases found previously were evident in both samples. EDS analysis showed no significant changes in the chemical analysis of the carbides or secondary phases between the quenched samples and those slowly cooled.

The JMatPro software predicts ~80 wt.% γ at 800°C increasing to ~99 wt.% γ at 1040°C with ~19 wt.% γ' at 800°C reducing to zero at ~1000°C (Figure 5.12). This is in agreement with the aged samples which show a consistent reduction in the levels of γ' from 800°C through to 950°C with no γ' evident at 1000°C. η is predicted by JMatPro to reduce from ~1.1 wt.% at 800°C to ~0.4 wt.% at

850°C. The reduction in η between 800 and 850°C is followed by an increase to ~4 wt.% at 1000°C and a sharp drop with η no longer present at temperatures above 1040°C (Figure 5.12). The aged samples show η evident in the microstructure from 800 - 900°C peaking at ~950°C. Only small amounts of η are present at 1000°C and no η is evident at 1050°C. There is no evidence in the samples to indicate the predicted reduction in η between 800 and 850°C.

At 800°C the software predicts a low ~0.5 wt.% level of MC carbide and ~0.9 wt.% of $M_{23}C_6$ carbide with the $M_{23}C_6$ carbide no longer evident at temperatures higher than 840°C. As the $M_{23}C_6$ carbide reduces, the MC carbide content increases, peaking at ~0.9 wt.% at 840°C dropping slightly to 1050°C (Figure 5.12). Visually the primary MC carbide in the 800°C and the 850°C aged samples are similar with lower levels of $M_{23}C_6$ than MC. $M_{23}C_6$ carbides were evident in the 900°C samples up to 10,000 hours.

The MC carbides are predicted to be rich in tantalum, titanium and niobium. The JMatPro predictions show significant changes in the MC carbide analysis with tantalum reducing from ~46 wt.% at 800°C to ~30 wt.% at 1050°C. This change is mirrored by an increase in titanium from ~11% at 800°C to ~29% wt.% at 1040°C, remaining constant to 1100°C. Niobium is predicted to stay relatively constant at ~29 wt.% with tungsten at less than 1 wt.% and zirconium reducing over the temperature range from ~4 wt.% to 1 wt.% (Figure 5.13 (a)). The $M_{23}C_6$ carbide is a chromium rich carbide predicted to contain ~ 88 wt.% chromium with 4.5 wt.% carbon and low levels of cobalt (~4 wt.%), nickel (~2.5 wt.%) and tungsten (< 1 wt.%) the JMatPro predictions show no change in composition with temperature (Figure 5.13(b)). The MC carbide EDS results do not show the large changes predicted by JMatPro in tantalum and titanium. The EDS results show niobium is relatively constant with approximately 3 wt.% tungsten and no zirconium.

The JMatPro predictions for η show a relatively constant composition of ~65 wt.% nickel, ~14 wt.% titanium, ~5 wt.% niobium with a small increase in cobalt content from 10.5 to 13 wt.% from 800 to 1040°C (Figure 5.13 (c)). United States Patent 4,810,467(54) is a patent covering a nickel based superalloy with a preferred melt chemistry range in which the current samples fall (Table 5.4). The document discusses the formation of undesirable phases such as η as a result of elemental segregation in large slowly cooled investment castings or during subsequent sustained high temperature service and that a carefully balanced mix of alloying elements must be maintained to avoid the formation of such phases. This suggests that the alloy specification was optimised to preclude the formation of η phase. However, JMatPro predicts η would be present above 800°C with the sample analysis of 2.37 wt.% titanium. This has been confirmed with the current samples. If the JMatPro calculations are repeated with a reduced titanium composition to the bottom of the specified range of 2.2 wt.% JMatPro still predicts the formation of η as an equilibrium phase forming at 880°C (Figure 5.14). Niobium and tantalum are considered to substitute for titanium in η(2). By reducing the levels of niobium and tantalum individually to the lower specified limits no significant changes were noted in the temperature at which η was predicted. However, by reducing the titanium and niobium concentrations to the lower limit specified, with nickel as the balancing element JMatPro predicts η will not be present below 916°C (Figure 5.15). In both cases the predictions show slightly lower levels of η over a reduced range of temperature. The predicted temperatures at which η would be present are considered to be above the normal operating temperatures for stage 2 and stage 3 vanes. The predictions would suggest that η would not be formed in NP 222 vanes, with titanium and niobium levels at the bottom end of the specified composition range, under normal operating conditions.

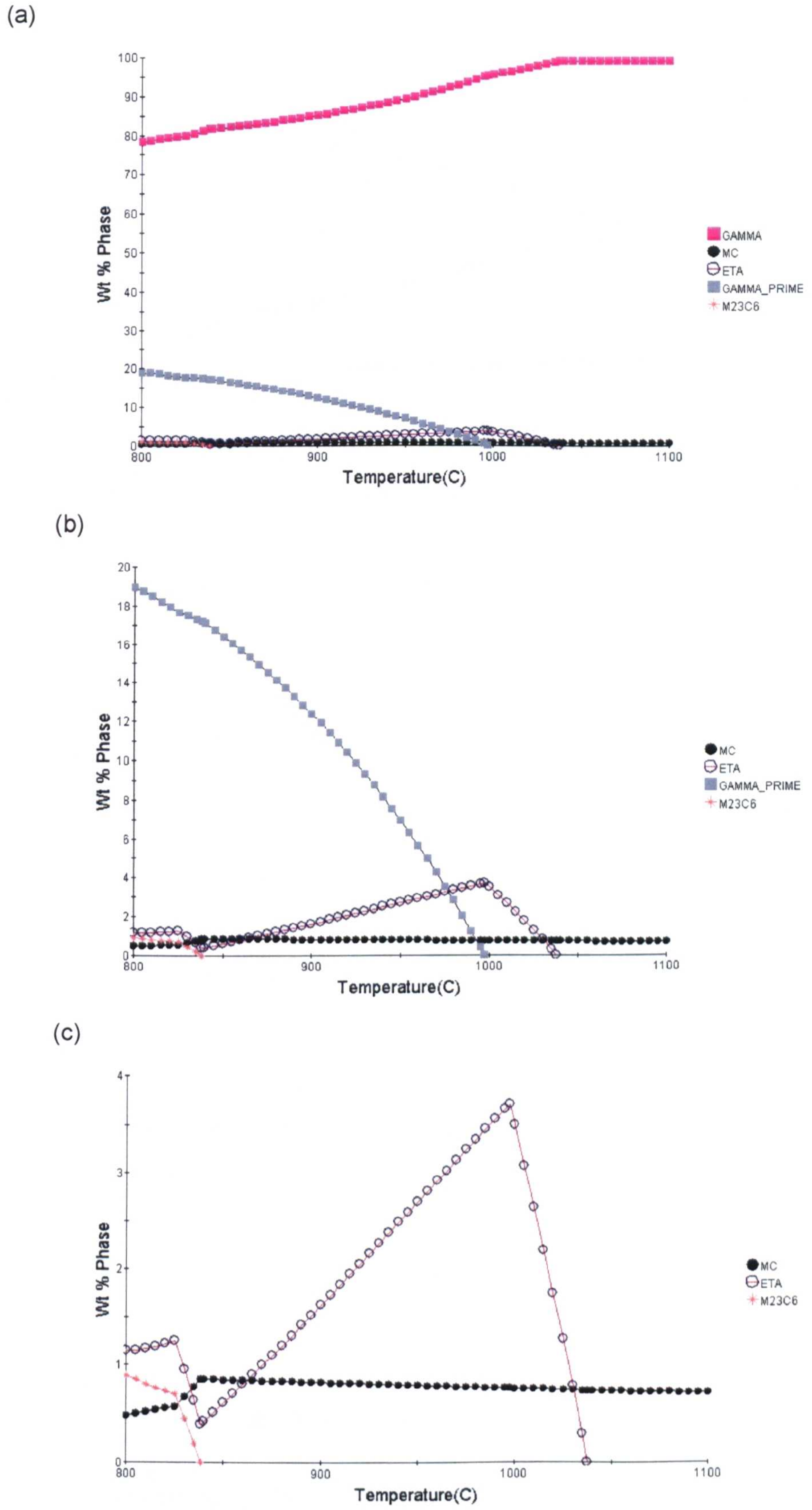

Figure 5.12 **NP 222 JMatPro thermodynamic predictions illustrating (a) predicted equilibrium phases (b) and (c) rescaled.**

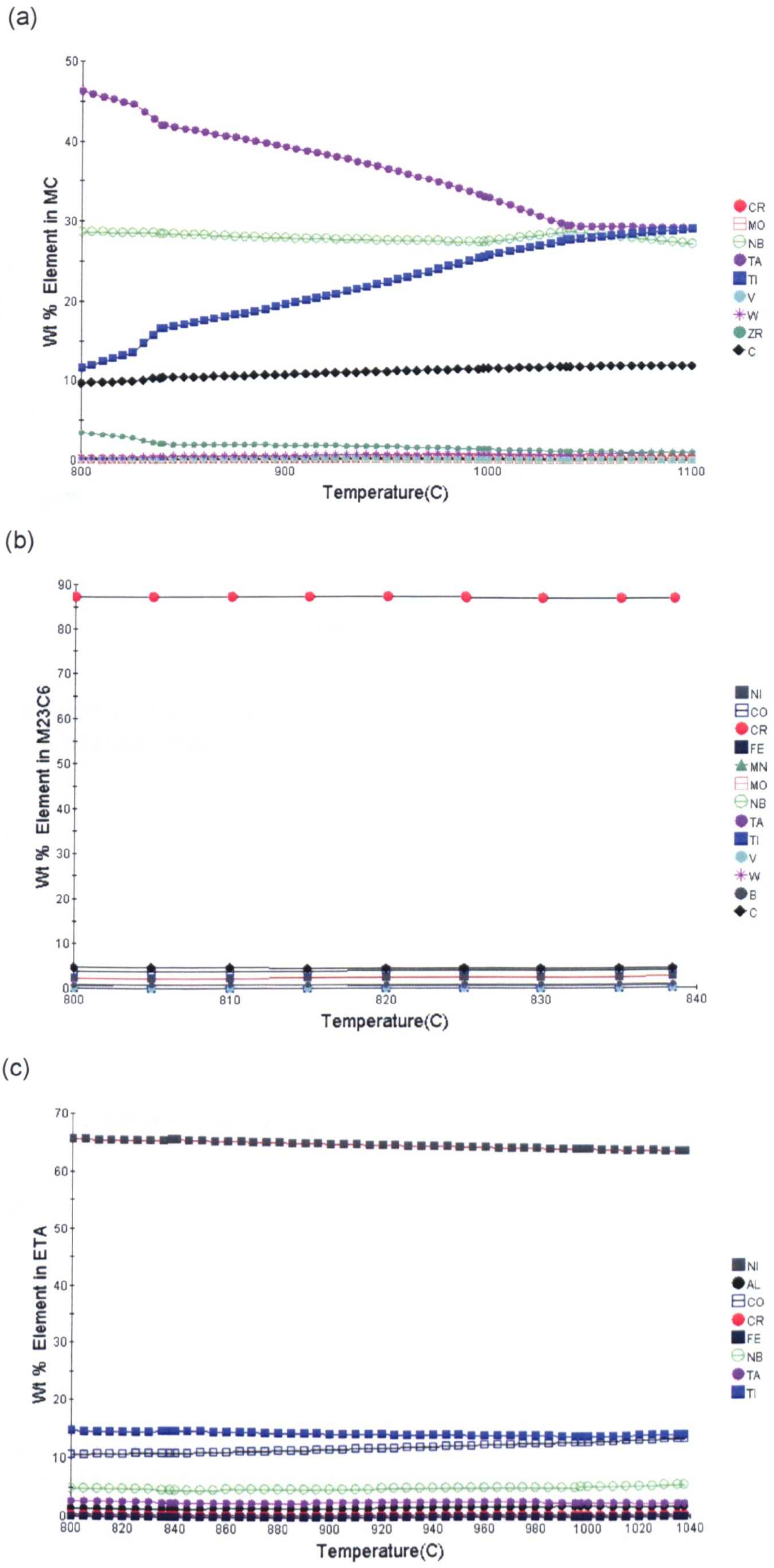

Figure 5.13 NP 222 JMatPro thermodynamic predictions illustrating the predicted chemical composition of the (a) MC, (b) $M_{23}C_6$ and (c) eta phases.

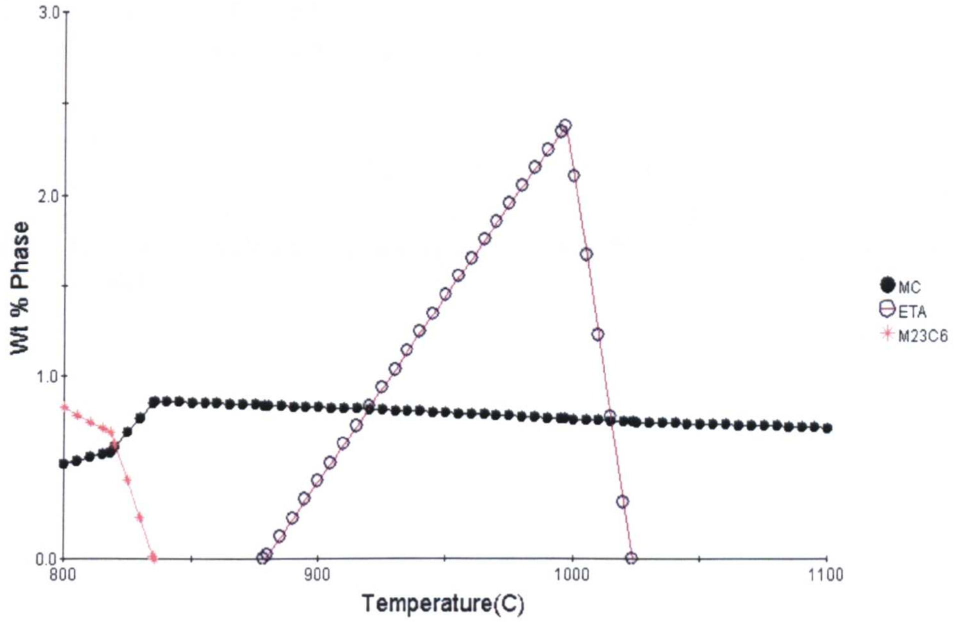

Figure 5.14 JMatPro thermodynamic predictions for η with 2.2 wt.% titanium (balance of nickel altered).

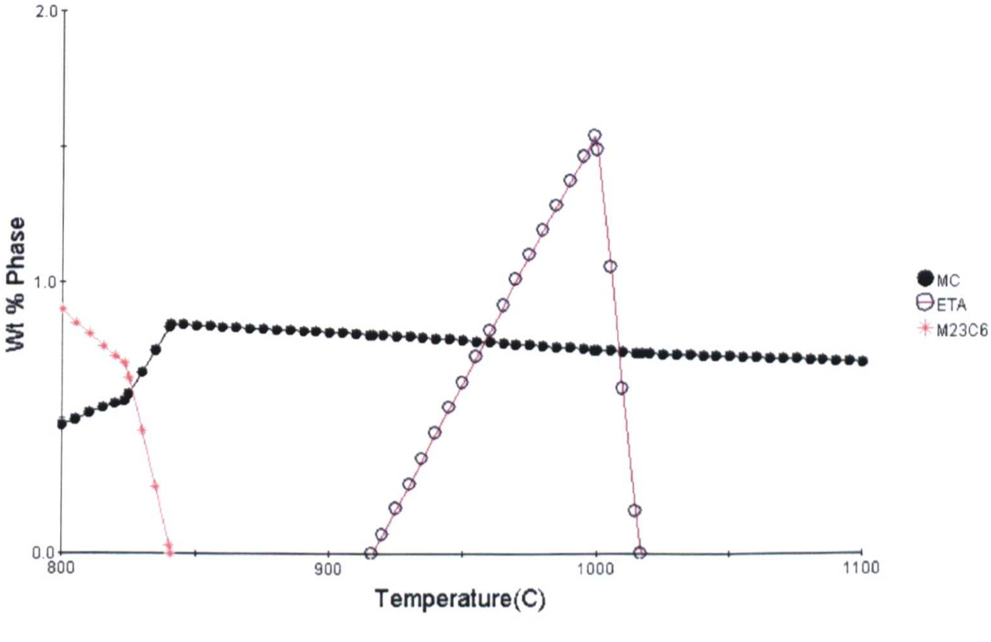

Figure 5.15 NP 222 JMatPro thermodynamic predictions for η with 2.2 wt.% titanium and 0.7 wt.% niobium (balance of nickel altered).

	Ni	Co	Cr	W	Al	Ti	Nb	Ta	B	Zr	C
Patent 4,810,467^(54) Preferred melt chemistry	Bal	18.8 19.5	22.2 22.8	1.8 2.2	1.1 1.3	2.2 2.4	0.7 0.9	0.9 1.1	0.005 0.015	0.005 0.02	0.08 0.12
Sample analysis	Bal	19	22.4	2.06	1.22	2.37	0.82	0.97	0.007	0.02	0.09

Table 5.4 Comparison United States Patent 4,810,467(54) and NP 222 sample XRF analysis.

5.4 Unknown Phase Identification (Electron Diffraction)

A thin foil sample containing the grain boundary needle phase was removed from the 900°C 5,000 hour sample by FIB SEM (Figure 5.16 (a)). Figure 5.16 (b) illustrates a TEM image of the thin foil sample and a corresponding selected area electron diffraction pattern from the needle phase (Figure 5.16 (c)). The pattern was indexed using the Cambridge University Practical Crystallography software Version 1.6(79). The phases investigated were γ, γ´, μ, η, σ, MC, M_6C and $M_{23}C_6$ Indexing of the pattern confirmed the needles formed in the sample are η phase. The chemical composition of the needles determined by EDS in the TEM is detailed in Table 5.3. The results show a reasonable agreement between the SEM and TEM EDS results with JMatPro predicting lower levels of chromium, tantalum and aluminium than the EDS results.

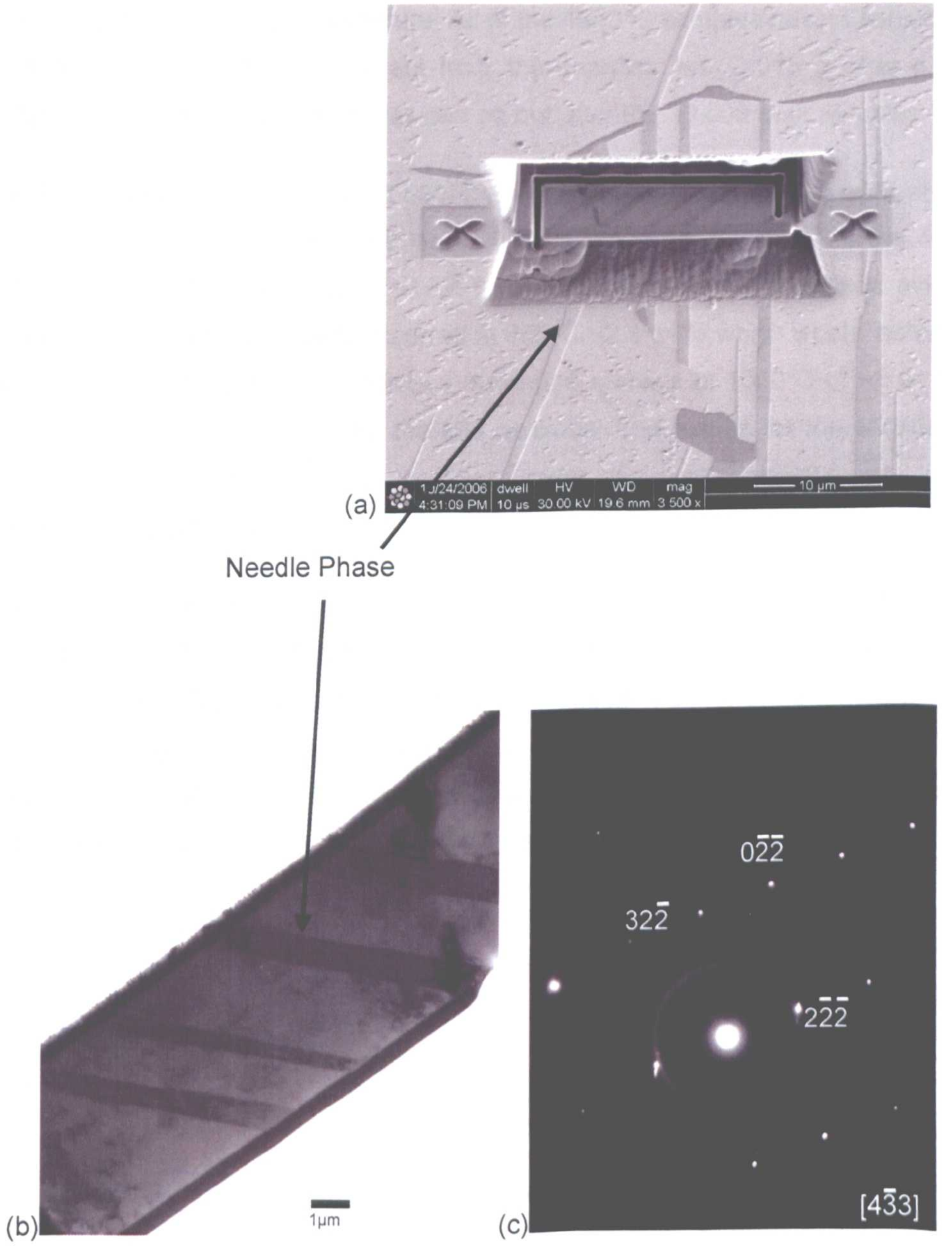

Figure 5.16 NP 222 (a) FIB SEM image of foil prior to removal, (b) TEM image showing thin foil sample illustrating needle like phases and (c) corresponding selected area electron diffraction pattern from needles.

5.5 Carbide extraction and XRD

To measure the type and volume fraction of carbides present in the samples, the carbides were separated from the matrix by a bulk electrolytic extraction method. The electrolyte used was 10% HCl, 1% tartaric acid in methanol. The technique dissolves the γ matrix and the γ' phase in NP 222 leaving the carbides and η phase as a sediment. For further details see Chapter 3.7.

The 1,000 and 2,000 hour samples show a steady reduction in extract from ~1.6 wt.% at 800°C to ~1 wt.% at 1050°C. This is consistent with the optical/SEM results with MC and $M_{23}C_6$ carbides extracted at 800°C and only MC carbide extracted at 1050°C. The increase in extract evident from 800 - 950°C for 5,000 and 10,000 hours is as a result of the increase in the levels of η phase being extracted along with the carbides. The decrease evident in the 1000°C samples is considered the result of the reduction in η at this temperature. All of the 1050°C samples have a consistent 1 wt.% of extract. The maximum weight of extract from the samples was 0.015 g after a three hour extraction. No further carbide extraction was carried out after the 10,000 hour samples.

JMatPro predicts a total carbide content at 800°C of ~1.4 wt% reducing to ~0.8 wt.% at 1050°C. At 800°C the total extract for XRD was 1.6 wt.%, with MC and $M_{23}C_6$ carbides the only phases evident in this sample. This reduced to ~1 wt.% at 1050 with only MC carbide evident in the sample. The maximum extract for XRD occurred at 950°C ~2.4 wt.% which would include both MC and η phase (Figure 5.19). JMatPro predicts a maximum η levels at 1000°C of ~4 wt.% to which should be added a further ~0.8 wt.% for the MC carbides. The results for the carbides are very similar to the JMatPro predictions. However, lower levels of η were extracted from the samples than were predicted by JMatPro.

The phases identified from the XRD traces are a tantalum, titanium, and niobium rich MC carbide, a chromium rich $M_{23}C_6$ carbide (Figure 5.17) and η phase (Figure 5.18). The peaks of the MC carbide fall between the TiC, TaC and NbC (not shown) pattern sticks shown in Figure 5.17. The presence of the very large η peak at 44° (2-theta) (Figure 5.18) reduces the $M_{23}C_6$ carbide peaks to minor blips on the XRD trace. However, it would be possible to scan over a limited angle to detect the presence of $M_{23}C_6$ peaks and avoid the large η peak. Table 5.5 identifies the phases detected by XRD.

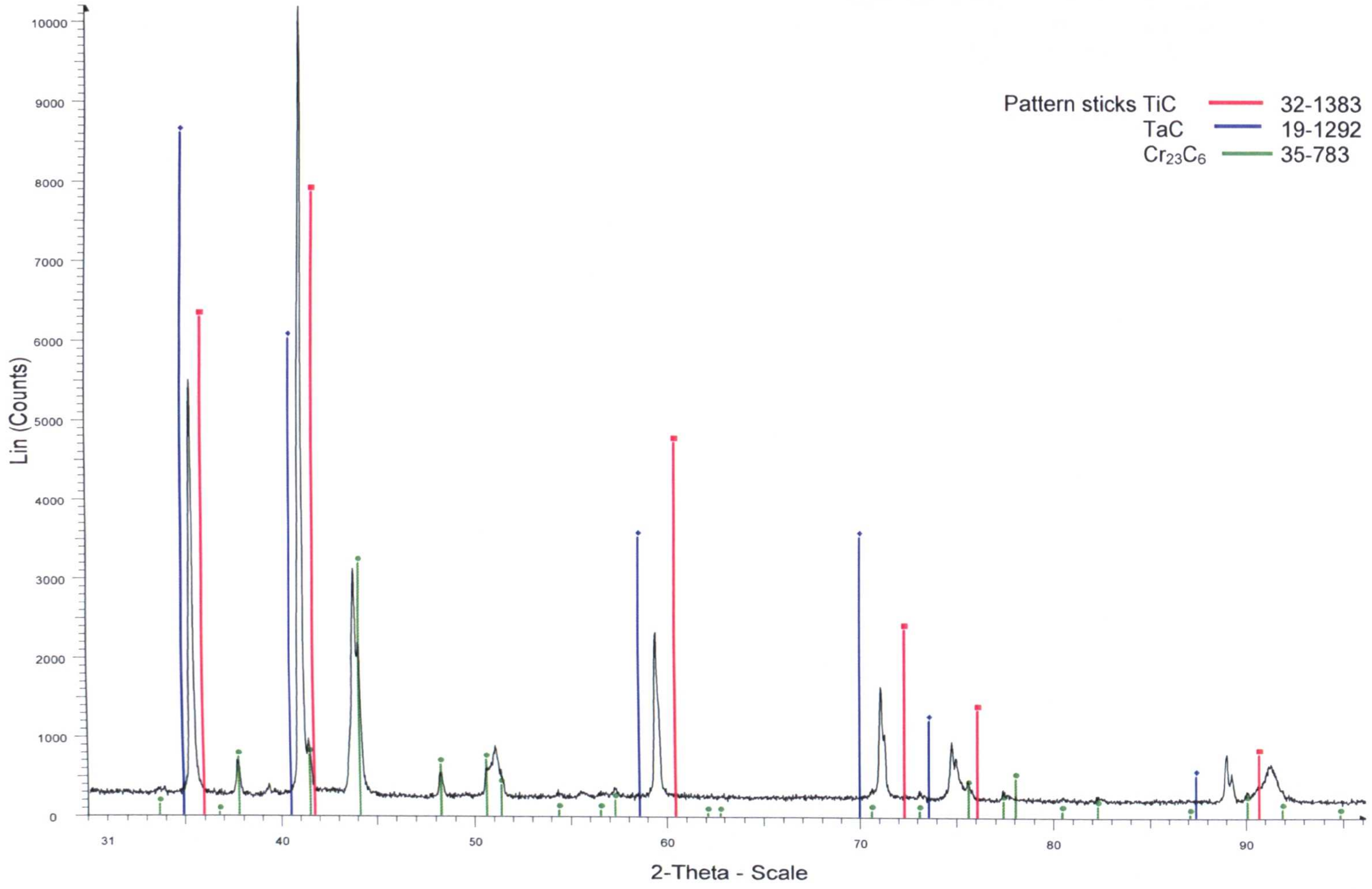

Figure 5.17 XRD trace of extract from NP 222 1,000 hrs 800°C sample showing MC (TaC, TiC) carbide and $M_{23}C_6$ carbide pattern sticks.

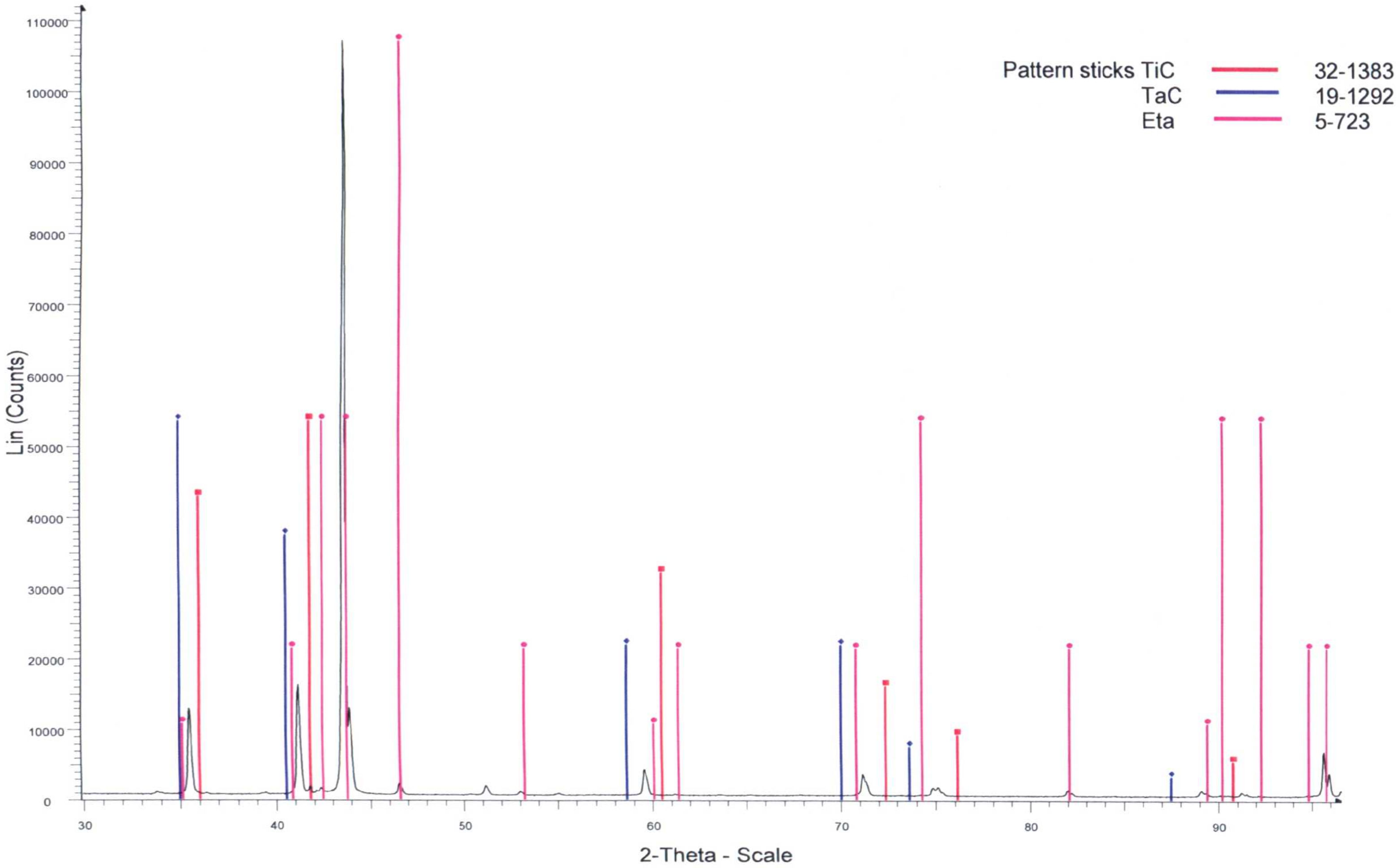

Figure 5.18 XRD trace of extract from NP 222 sample aged at 950°C for 5,000 hrs showing MC (TaC and TiC) carbide and η pattern sticks.

	1,000 hrs	2,000 hrs	5,000 hrs	10,000 hrs
800°C	MC $M_{23}C_6$	MC $M_{23}C_6$	MC $M_{23}C_6$	MC $M_{23}C_6$ η
850°C	MC $M_{23}C_6$	MC $M_{23}C_6$	MC $M_{23}C_6$	MC $M_{23}C_6$ η
900°C	MC $M_{23}C_6$	MC $M_{23}C_6$	MC $<M_{23}C_6$ η	MC η
950°C	MC η	MC η	MC η	MC η
1000°C	MC η	MC <<η	MC <<η	MC <<η
1050°C	MC	MC	MC	MC

< low levels

<< very low levels

Table 5.5 NP 222 phases identified from XRD traces for samples aged up to 10,000 hours.

(a)

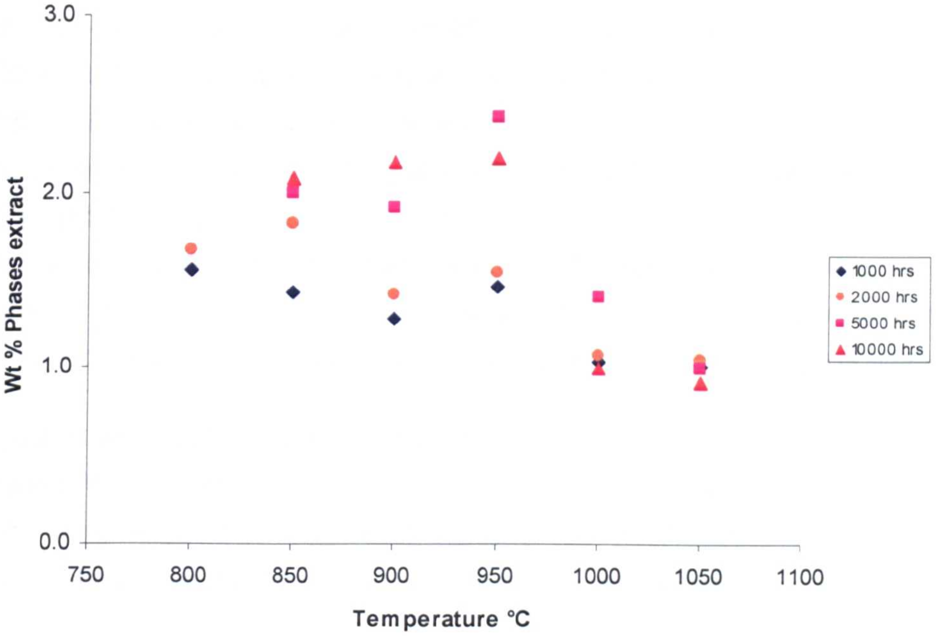

(b)

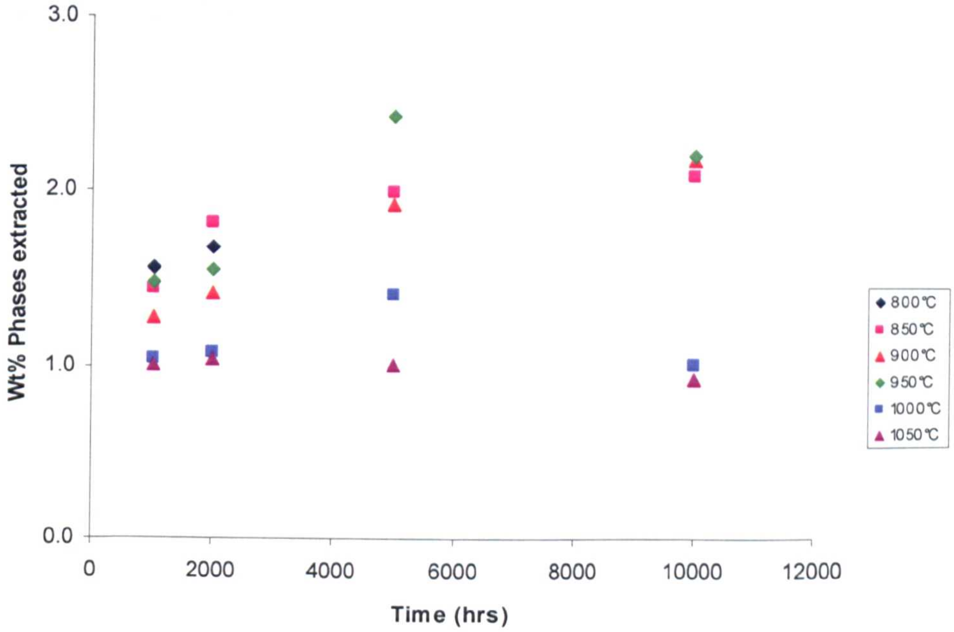

Figure 5.19 **NP 222 wt.% of phases extracted for XRD plotted as a function of (a) temperature and (b) time.**

5.6 Hardness

The mean hardness levels and error bars of the standard error of mean are shown in Figure 5.20. The 800 - 950°C results show a reduction in hardness with both time and temperature. The 1000°C and 1050°C samples show a decrease in hardness with time and an increase with temperature. The mean hardness drops from 300 - 350 Hv_{20} at 800°C to 210-240 Hv_{20} at 950°C with an increase to ~270-310 Hv_{20} at 1000°C and 1050°C. The decrease in hardness between 850°C and 950°C occurs as γ' coarsens the levels of γ' reduce and η levels increase. A drop in hardness of 60 points could be used to predict operating temperature. However, any prediction of operating temperature from hardness would result in a broad temperature prediction. The hardness changes with time are small and would preclude the prediction of operating time.

At 1000°C and 1050°C the microstructure is, other than a small number of η platelets, matrix and carbides. What is difficult to explain is the increase in hardness of the gamma matrix over this temperature range other than the possibility of solid solution hardening or, having taken γ' into solution, the precipitation of very fine, unresolved, γ' on cooling.

The micro-hardness results, Figure 5.21, show similar hardness levels and a similar trend with both time and temperature. The micro-hardness indentations were placed in γ/γ' for the 800-900°C samples and the γ matrix for the 950-1050°C samples. The similarity in the results between the macro and micro-hardness would suggest that the low levels of carbide in NP 222 have little or no effect on the overall hardness.

(a)

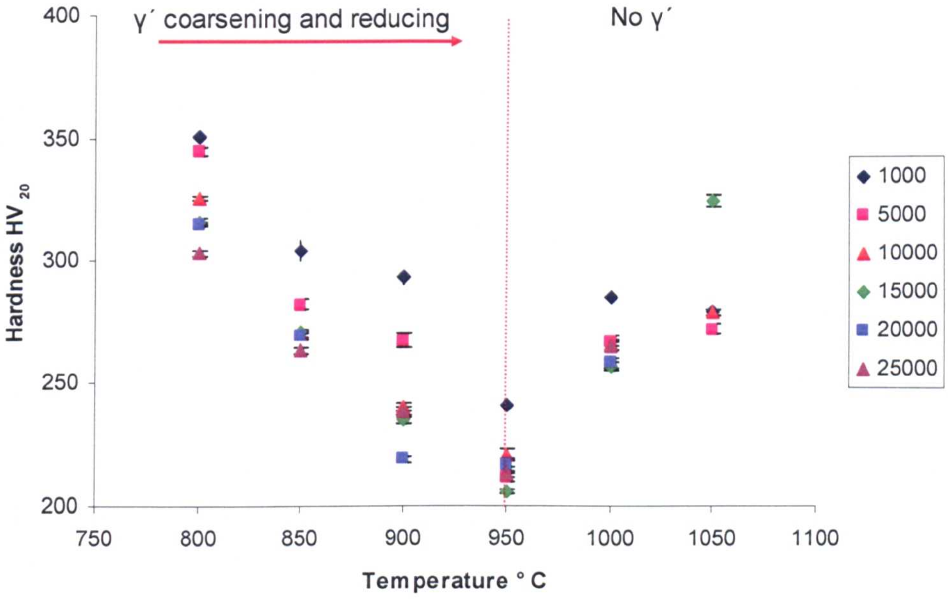

(b)

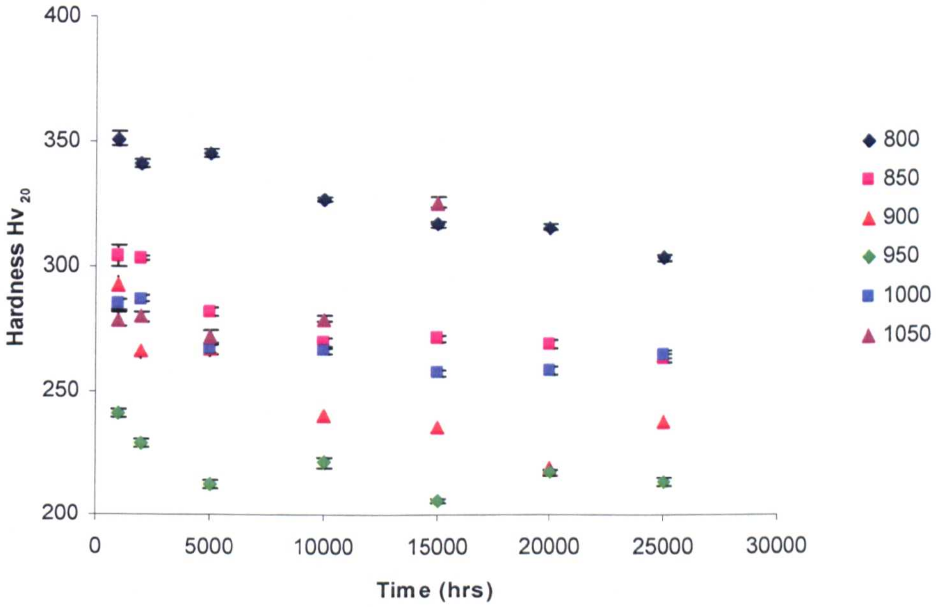

Figure 5.20 NP 222 hardness results (error bars – standard error of mean) plotted as a function of (a) temperature and (b) time.

(a)

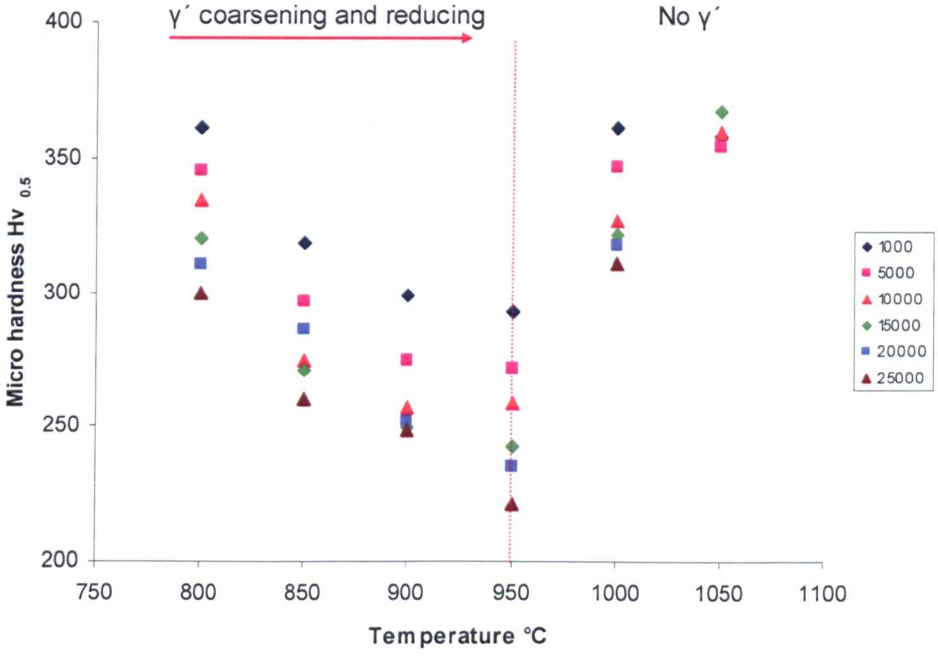

(b)

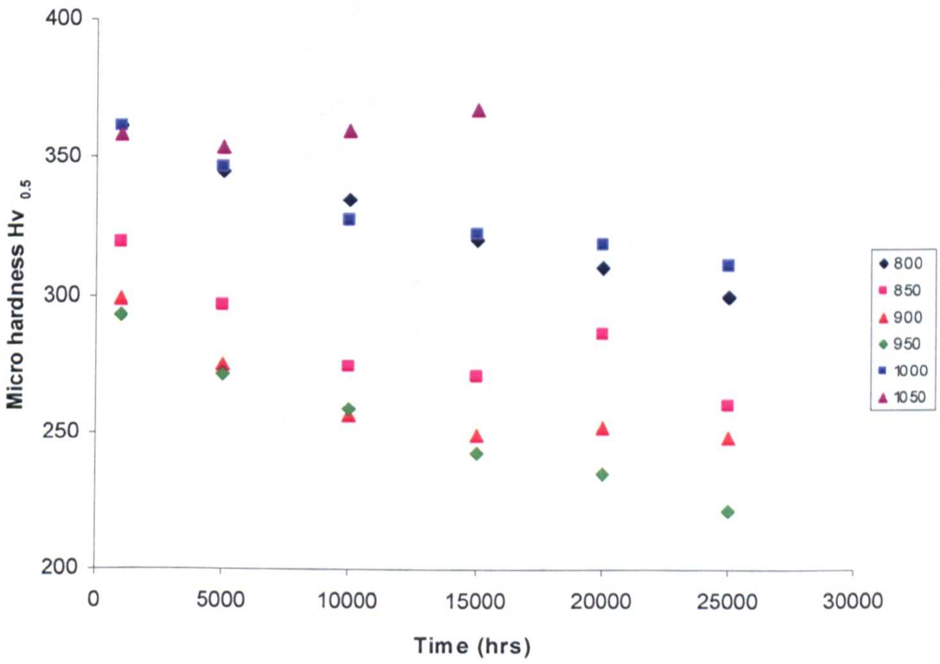

Figure 5.21 NP 222 micro-hardness results, 800/900°C in γ/γ´, 950/1050°C in γ plotted as a function of (a) temperature and (b) time.

5.7 Denuded Layer

Figure 5.22 is a micrograph of the denuded/oxidised layer evident on the exposed surfaces of the samples as a result of the loss of gamma prime and oxidation of the carbides. Measurements of the width of the denuded layer are plotted in Figure 5.23. The plotted results are the mean of 20 measurements taken along the sample. For the purpose of this investigation the width of the layer is considered to extend from the outer surface of the sample to the first gamma prime particle. In the samples denuded of gamma prime the width of the denuded layer was considered to be the distance from the outer surface to the first un-oxidised carbide. Figure 5.23 shows a good correlation with time^{½} which would allow the prediction of an operating temperature for an uncoated vane with a known operating history. However, the samples were held at a constant temperature with a very small of number cooling events. It was evident from the oxide scale in the furnace that spalling of the oxide occurred at temperature. In addition, violent spalling of the oxide occurred on cooling the samples to room temperature. Further work would be required to determine the effects of thermal cycling and composition on the width of the denuded layer.

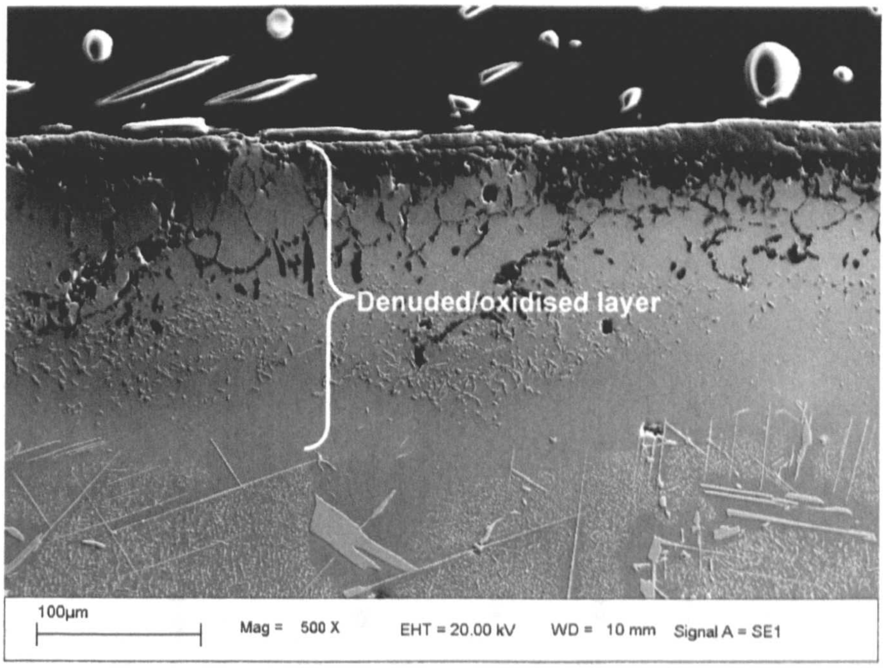

Figure 5.22 SEM SE image of NP 222 sample aged at 900°C for 15,000 hours showing denuded/oxidised layer.

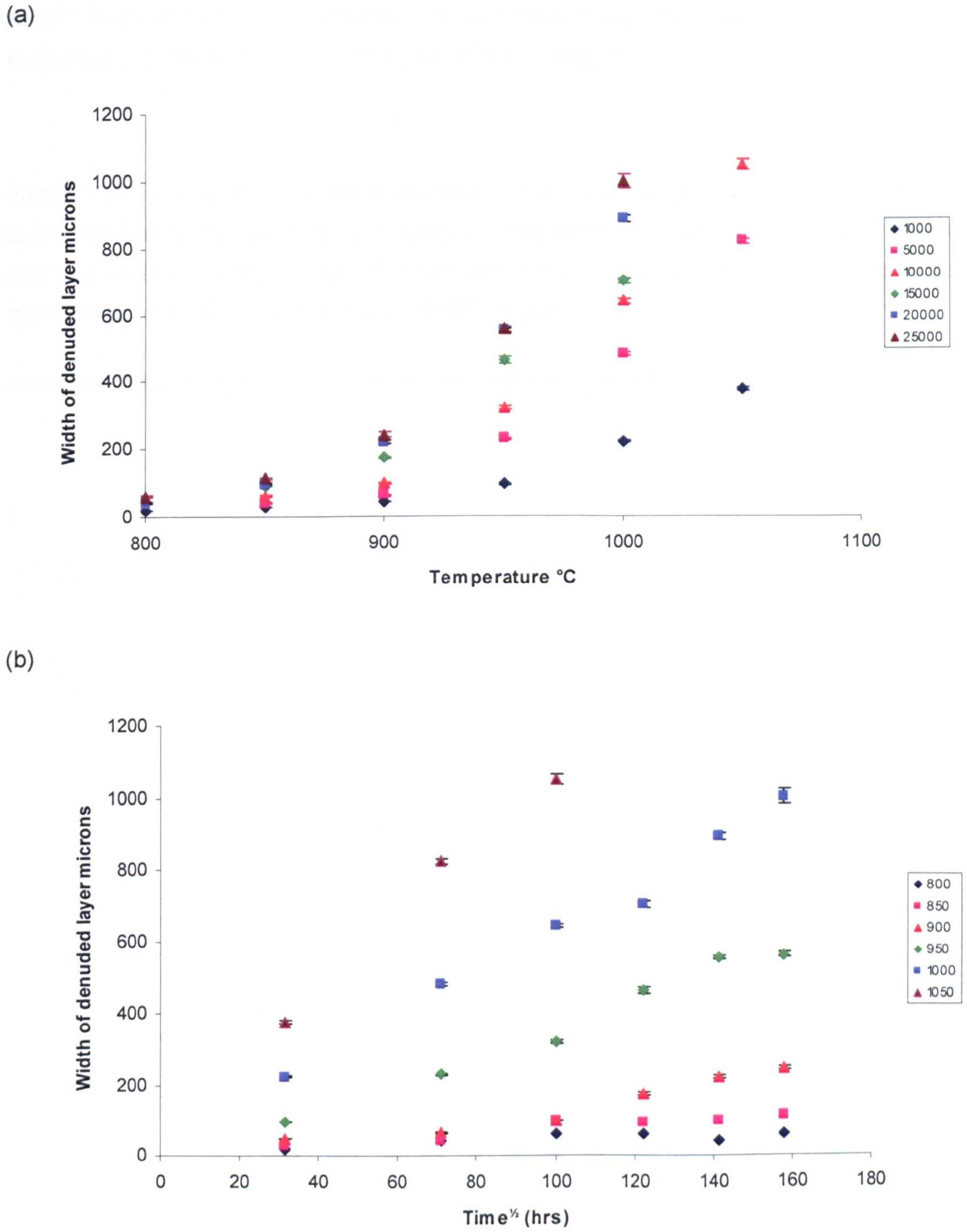

Figure 5.23 NP 222 width of denuded/oxidised layer plotted as a function of (a) temperature and (b) time.

5.8 Image Analysis

Sims(2) indicates that the dominant carbide reaction in many nickel based superalloys is believed to be the formation of $M_{23}C_6$ carbide by the following reaction:

$$MC + \gamma \rightarrow M_{23}C_6 + \gamma'$$

Image analysis of the MC carbide to determine if there are changes with time or temperature was attempted with limited success. In backscatter imaging the titanium rich η phase is only slightly less intense than the MC carbide. Further work is required to eliminate or reduce the intensity of the η phase to allow image analysis of the MC carbide.

No measurement of gamma prime coarsening has been carried out on these samples.

5.9 Summary

XRD and EDS/WDS confirmed the presence of MC (Ta, Ti, Nb) carbide and a chromium rich $M_{23}C_6$ carbide. The $M_{23}C_6$ carbide is evident in the samples aged at temperatures less than 900°C. Due to the small size of the $M_{23}C_6$ carbide, EDS measurements in the SEM were considered qualitative and were only used to confirm the presence of the carbide. The $M_{23}C_6$ carbide is evident in all the samples aged at 800°C and 850°C, and the 900°C samples aged for times less than 10,000 hours. η phase was evident in all samples aged in the range 800 - 1000°C for times greater than 5,000 hours. γ' reduced and coarsened with both time and temperature and was not evident in any of the samples aged at 1000°C and 1050°C. The changes in microstructure could be used as a temperature indicator with $M_{23}C_6$ carbide indicating a temperature below 900°C. The presence of γ' also indicates temperatures of less than 950°C, and the absence of γ' indicating temperatures in excess of 1000°C. The presence of η in the microstructure with no γ' would indicate a temperature between 1000°C and 1050°C.

The EDS/WDS analysis results for the MC carbide in the aged samples show similar levels of tantalum, titanium and niobium ~31 wt.% with tungsten at ~3 wt.%. The metallic component of the MC carbide can be expressed as approximately $Ti_{48}Nb_{26}Ta_{16}W_3Cr_3Ni_3Co$ (where the subscript describes the concentration in at.%). EDS/WDS analysis of the MC carbide showed none of the changes in composition predicted by JMatPro with ageing temperature. No predictions of service time or temperature could be made with the small changes in composition found in the MC carbide.

JMatPro has been used to study the effect of varying the alloy composition of NP 222 on the formation of η. The predictions would suggest that η would not be formed in NP 222 vanes, with titanium and niobium levels at the bottom end of the specified composition range below 900°C. The predicted temperatures at which η would be present are considered to be above the normal operating temperatures for stage 2 and 3 vanes. Therefore the presence of η in a NP 222 vane is likely to indicate a fault condition.

The reduction in the measured mean hardness between 800°C and 950°C could provide a coarse prediction of operating temperature but would require verification that the microstructure incorporated γ'. Correlations are also evident for η needle length and the γ' denuded/oxidised layer formed on the exposed surfaces of the sample. Further work would be required to understand the effects of composition on η needle growth and composition and thermal cycling on the formation of denudation zones on free surfaces.

6 Characterisation and discussion of alloy MAR M509

MAR M509 is a high carbon, high strength, vacuum cast cobalt-based superalloy which is generally used in the as-cast condition. The microstructure is typically composed of dendrites of the FCC (γ-Co) solid solution and an interdendritic network of "Chinese script" MC carbides and interdendritic eutectic $M_{23}C_6$ carbides consisting of mixtures of the γCo solid solution and carbide.

This chapter presents and discusses the outcome of the experimental work carried out to characterise alloy MAR M509 and to develop an understanding of the microstructural changes that occur, with both time and temperature, for life prediction, refurbishment and failure investigations. Cast samples were aged at temperatures ranging from 850 to 1050°C, for times up to 25,000 hours, as detailed in Chapter 3. The chemical composition of the samples is given in Table 3.1. The results of thermodynamic equilibrium calculations are also presented and compared with experimental data.

6.1 Microstructural Observations

The identification of the phases within the microstructure was initially based on EDS chemical composition measurements and a comparison with representative compositions found in the literature. In SEM backscatter mode the MC carbides are white, whereas the $M_{23}C_6$ carbides are grey due to the difference in the atomic contrast.

The microstructure of the as-cast MAR M509 samples consists of primary MC and $M_{23}C_6$ eutectic carbides. The primary carbides are interlinked in some areas by thin ribbons of MC and $M_{23}C_6$ carbides (Figure 6.1). Large areas of the γ matrix are optically devoid of precipitates. Thin layers of $M_{23}C_6$ carbide are evident on a number of the MC carbides. Two types of $M_{23}C_6$ eutectics are evident: a fine enclosed eutectic and a coarse open eutectic (Figure 6.2). Backscatter SEM images also indicate the presence of a white phase typically less than 5μm in diameter predominantly within the coarse $M_{23}C_6$ eutectics (Figure 6.3). The phase has been identified by electron diffraction (Chapter 6.5) as M_6C and therefore will be referred to as M_6C in the following discussions.

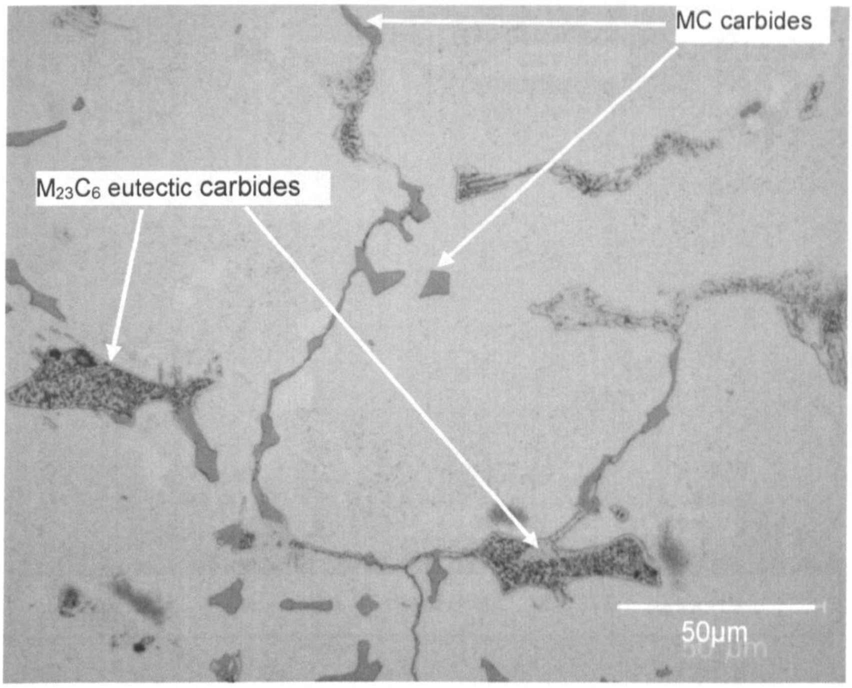

Figure 6.1 **MAR M509 optical micrograph, as-cast microstructure showing MC and $M_{23}C_6$ eutectic carbides.**

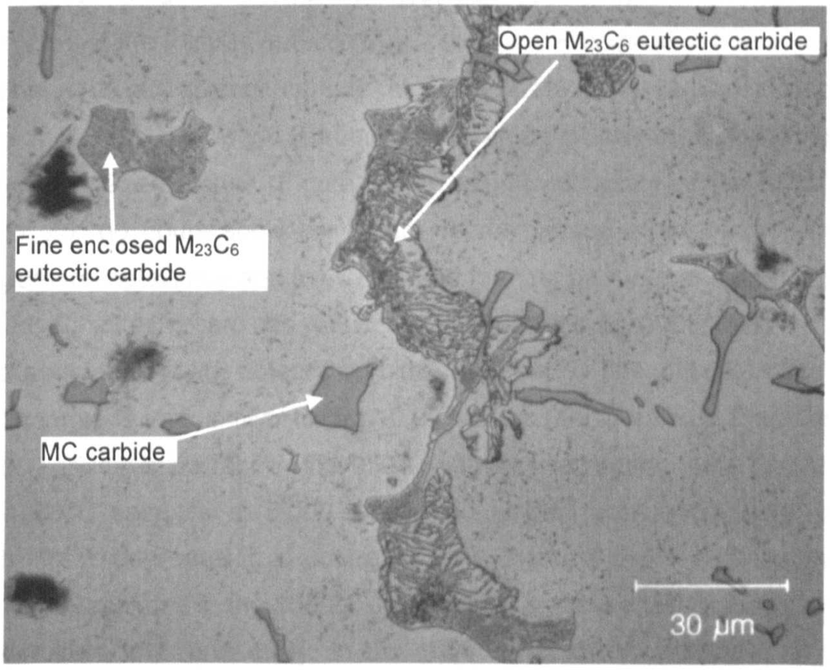

Figure 6.2 **MAR M509 optical micrograph showing open eutectic $M_{23}C_6$, fine enclosed $M_{23}C_6$ eutectic carbides and MC carbide in as-cast microstructure.**

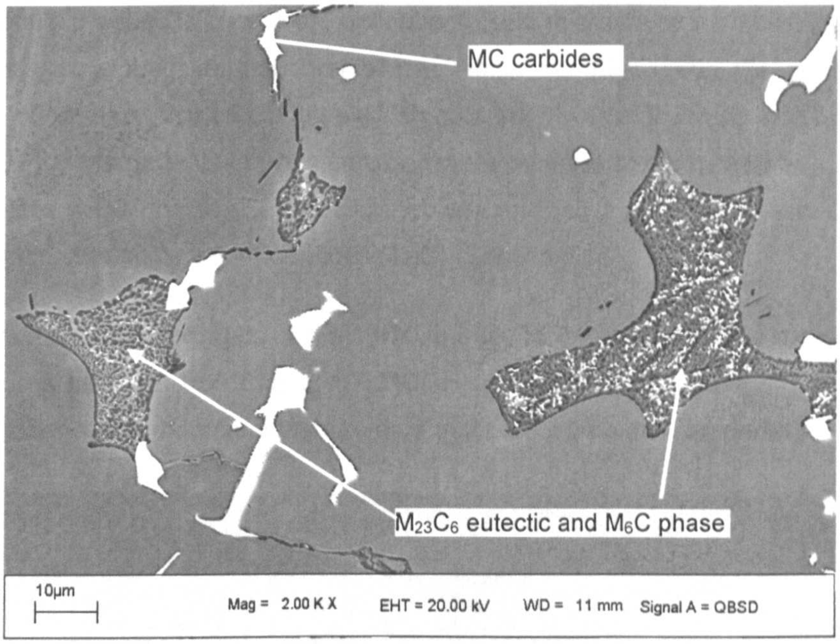

Figure 6.3 SEM BSE image of MAR M509 as-cast microstructure showing M_6C carbide in the $M_{23}C_6$ eutectic carbides.

The 1,000 hours 850°C sample shows fine $M_{23}C_6$ carbides throughout the matrix with a higher concentration around the primary eutectic $M_{23}C_6$ carbides. Precipitation free zones are evident around the primary $M_{23}C_6$ eutectic carbide. M_6C is evident in the $M_{23}C_6$ eutectic carbides. A "cross hatched" pattern is evident in some of the areas of fine $M_{23}C_6$ carbides suggesting precipitation on preferred planes (Figure 6.4). The microstructure of the 850°C and 900°C samples up to 25,000 hours show only slight microstructural changes with the fine $M_{23}C_6$ carbides agglomerating slightly and $M_{23}C_6$ carbide forming on more of the MC carbides. M_6C phase in the $M_{23}C_6$ eutectic carbides reduces with increasing ageing time and a tantalum rich phase precipitates in the $M_{23}C_6$ eutectic carbides and matrix. The microstructure of the 1,000 hours 950°C sample is very similar to the 10,000 hours 900°C sample. Degeneration of the $M_{23}C_6$ eutectic carbide is evident in the 950°C samples for ageing time greater than 5,000 hours. The 1000°C samples at 5,000 hours and longer times show large blocky $M_{23}C_6$ carbides with little if any eutectic structure evident (Figure 6.5). In SEM backscatter mode ~25% of the $M_{23}C_6$ carbides in the 1050°C 10,000 hour sample show as black rather than the grey $M_{23}C_6$ carbides seen previously. In the 1050°C 15,000 hour sample all of the $M_{23}C_6$ carbides are black with black needles evident throughout the cross section (Figure 6.6). EDS analyses (chapter 6.2) of the needles show high levels of aluminium and nitrogen. For the purpose of this report the needles will be considered to be nitride needles. The MC carbides do not appear optically to have changed with time and temperature. However, the MC carbide in the 1050°C 15,000 hour sample, in the optical microscope had the appearance of a cored structure (Figure 6.7).

Table 6.1 details the results of both the optical and SEM microstructural investigation. Of note are the loss of the tungsten rich precipitates within the $M_{23}C_6$ eutectic carbide and the precipitation of tantalum rich precipitates within both the $M_{23}C_6$ eutectic carbide and the matrix (Figure 6.8). Fine matrix tantalum rich carbides were reported by both Drapier(62) and Biss(84). The precipitates within the $M_{23}C_6$ eutectic carbides and the matrix have been confirmed by electron diffraction to be tantalum carbides (TaC) (Section 6.5).

Representative SEM micrographs of the 1,000, 5,000, 15,000 and 25,000 hour samples aged at temperatures between 850°C and 1050°C are contained in Figure 6.9-6.13 and clearly illustrate the changes in the microstructure as a function of time and temperature.

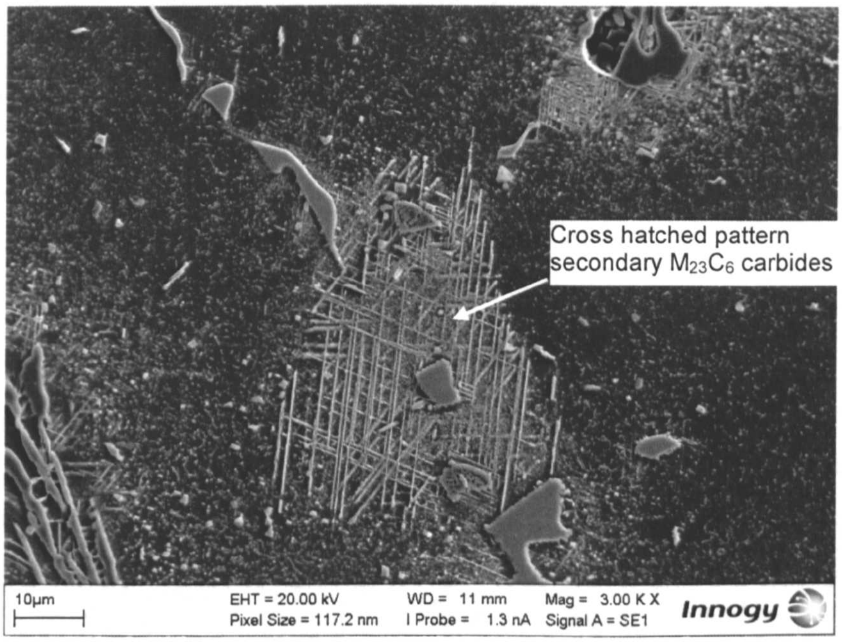

Figure 6.4 MAR M509 SEM SE image showing "cross hatch" pattern of fine $M_{23}C_6$ carbide in 850°C 1,000 hrs sample.

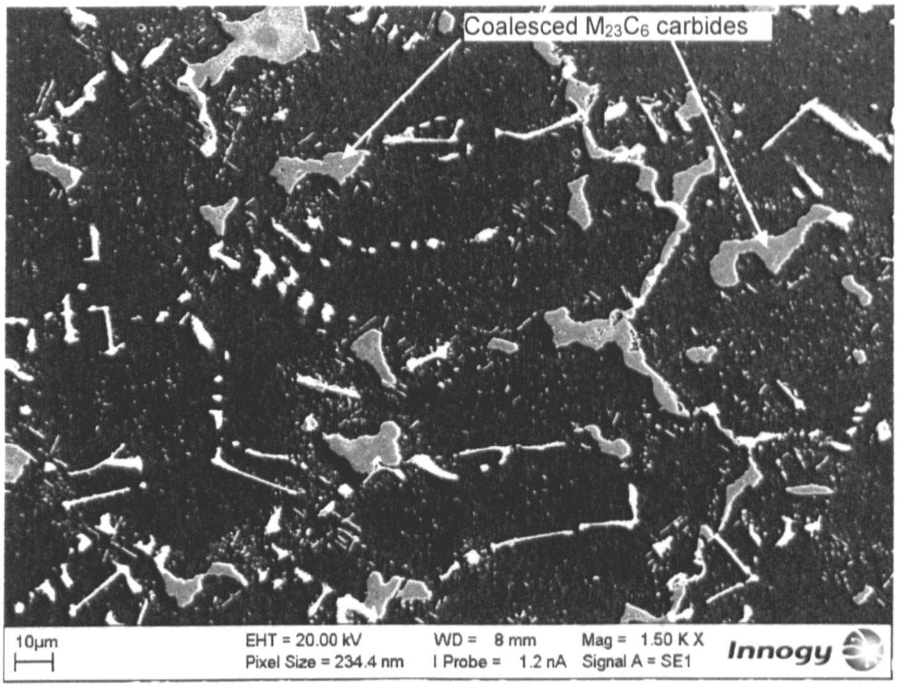

Figure 6.5 **MAR M509 SEM SE image showing coalesced $M_{23}C_6$ carbides in 1000°C 15,000 hour sample.**

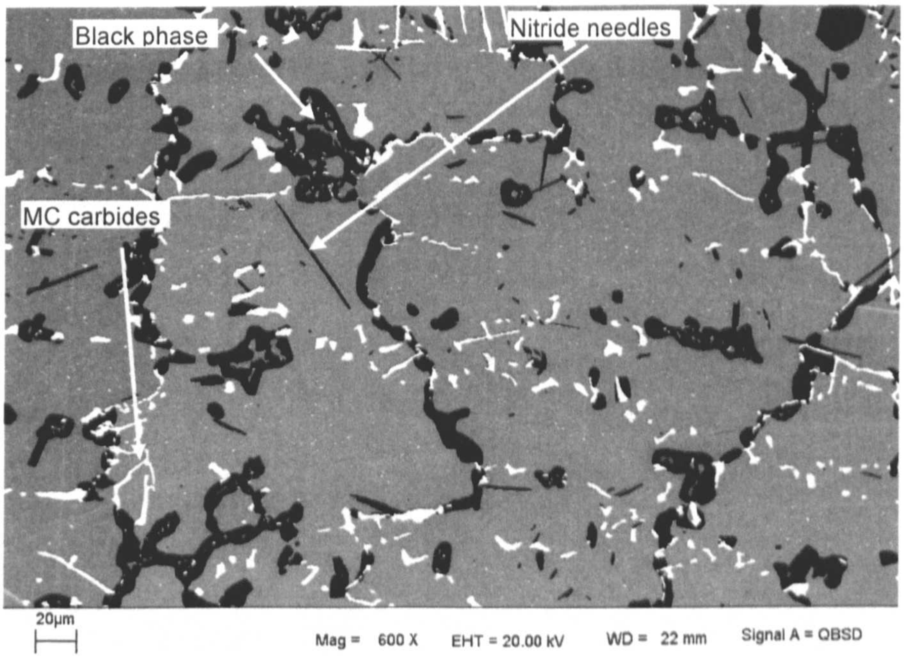

Figure 6.6 **MAR M509 SEM BSE image of black phase and nitride needles in 1050°C 15,000 hour sample.**

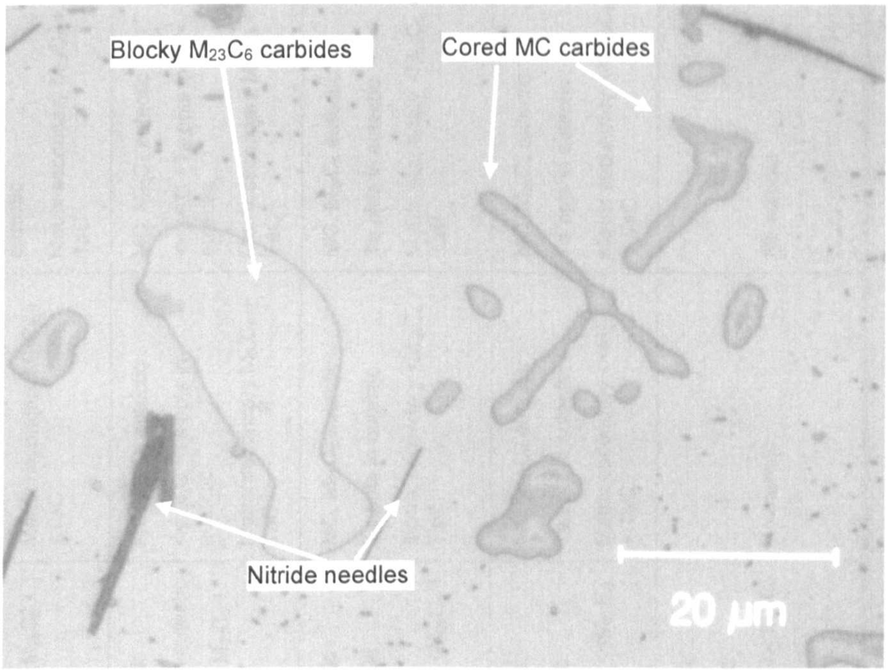

Figure 6.7 **MAR M509 optical micrograph illustrating cored MC carbides, blocky $M_{23}C_6$ carbides and nitride needles in 1050°C 15,000 hour sample.**

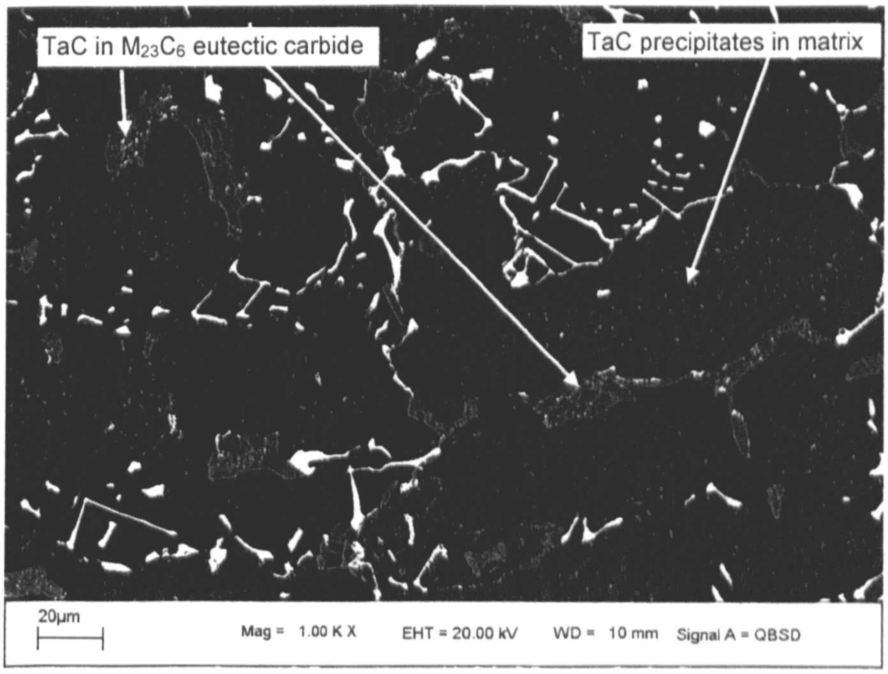

Figure 6.8 **MAR M509 SEM BSE image of tantalum carbide in $M_{23}C_6$ carbide and matrix 1000°C 15,000 hour sample.**

	1,000 hrs	5,000 hrs	10,000 hrs	15,000 hrs	20, 000 hrs	25,000 hrs
850°C	MC, $M_{23}C_6$ eutectic M_6C ppts in $M_{23}C_6$ eutectic Matrix secondary $M_{23}C_6$ + <TaC	MC, $M_{23}C_6$ eutectic M_6C +Ta ppts in eutectic Matrix secondary $M_{23}C_6$ + <TaC	MC, $M_{23}C_6$ eutectic M_6C +Ta ppts in eutectic Matrix secondary $M_{23}C_6$ + <TaC	MC, $M_{23}C_6$ eutectic M_6C +Ta ppts in eutectic Matrix secondary $M_{23}C_6$ + <TaC	MC, $M_{23}C_6$ eutectic < M_6C +Ta ppts in eutectic Matrix secondary $M_{23}C_6$ + <TaC	MC, $M_{23}C_6$ eutectic << M_6C +Ta ppts in eutectic Matrix secondary $M_{23}C_6$ + TaC
900°C	MC, $M_{23}C_6$ eutectic M_6C +Ta ppts in eutectic Matrix secondary $M_{23}C_6$ +<TaC	MC, $M_{23}C_6$ eutectic M_6C +Ta ppts in eutectic Matrix secondary $M_{23}C_6$ + <TaC	MC, $M_{23}C_6$ eutectic M_6C +Ta ppts in eutectic Matrix secondary $M_{23}C_6$ + <TaC	MC, $M_{23}C_6$ eutectic < M_6C +Ta ppts in eutectic Matrix secondary $M_{23}C_6$ + TaC	MC, $M_{23}C_6$ eutectic << M_6C +Ta ppts in eutectic Matrix secondary $M_{23}C_6$ + TaC	MC, $M_{23}C_6$ eutectic << M_6C +Ta ppts in eutectic Matrix secondary $M_{23}C_6$ + TaC
950°C	MC, $M_{23}C_6$ eutectic < M_6C +Ta ppts in eutectic Matrix secondary $M_{23}C_6$ + <TaC	MC, $M_{23}C_6$ eutectic << M_6C +Ta ppts in eutectic Matrix secondary $M_{23}C_6$ + TaC	MC, $M_{23}C_6$ eutectic << M_6C +Ta ppts in eutectic Matrix secondary $M_{23}C_6$ + TaC	MC, $M_{23}C_6$ eutectic << M_6C +Ta ppts in eutectic Matrix secondary <$M_{23}C_6$ + TaC	MC, $M_{23}C_6$ eutectic Ta ppts in eutectic Matrix secondary <$M_{23}C_6$ + TaC	MC, $M_{23}C_6$ eutectic Ta ppts in eutectic Matrix secondary <$M_{23}C_6$ + TaC
1000°C	MC, $M_{23}C_6$ eutectic Ta ppts in eutectic Matrix secondary <$M_{23}C_6$ + TaC	MC, $M_{23}C_6$ eutectic Ta ppts in eutectic Matrix secondary <<$M_{23}C_6$ + TaC	MC, $M_{23}C_6$ eutectic Ta ppts in eutectic Matrix secondary <<$M_{23}C_6$ + TaC	MC, $M_{23}C_6$ eutectic Ta ppts in eutectic Matrix secondary <<$M_{23}C_6$ + TaC	MC, $M_{23}C_6$ eutectic Ta ppts in eutectic Matrix secondary <<$M_{23}C_6$ + TaC	MC, $M_{23}C_6$ eutectic Ta ppts in eutectic Matrix secondary <<$M_{23}C_6$ + TaC
1050°C	MC, $M_{23}C_6$ eutectic Ta ppts in eutectic Matrix secondary << $M_{23}C_6$ + TaC	MC. $M_{23}C_6$ eutectic Ta ppts in eutectic Matrix secondary << $M_{23}C_6$ + TaC Nitride Needles	MC, $M_{23}C_6$ eutectic Ta ppts in eutectic Matrix secondary << $M_{23}C_6$ + TaC Nitride needles	MC, $M_{23}C_6$ eutectic Ta ppts in eutectic Matrix secondary << $M_{23}C_6$ + TaC Nitride needles	No sample	No sample

< low levels
<< very low levels

Table 6.1 MAR M509 phases identified in aged samples by optical and SEM observations (γ matrix not included).

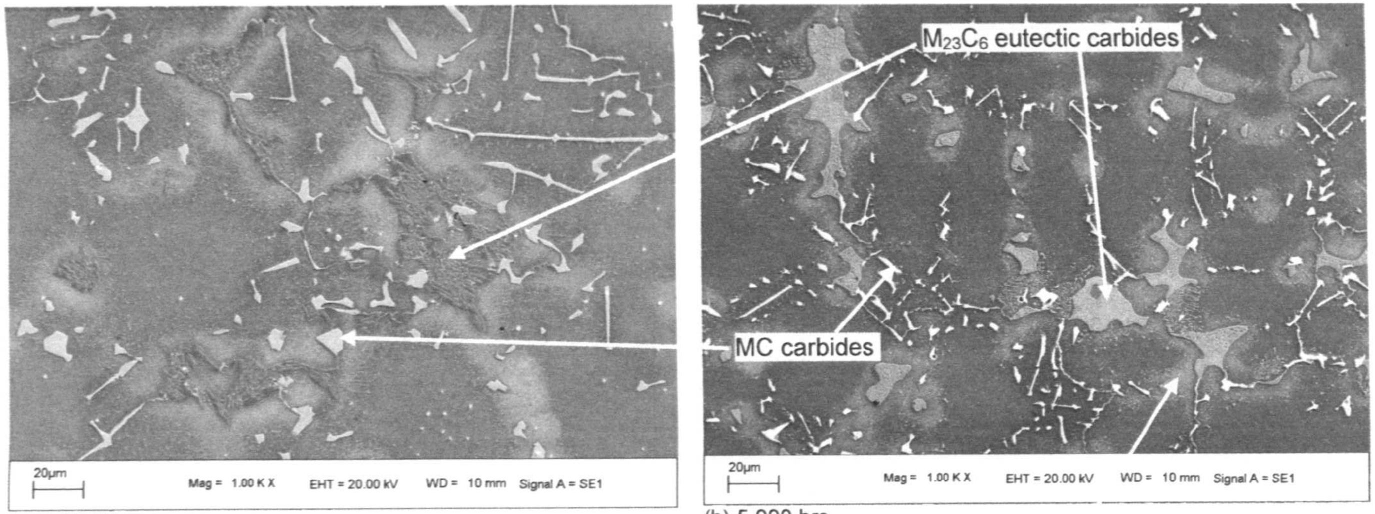

(a) 1,000 hrs

(b) 5,000 hrs

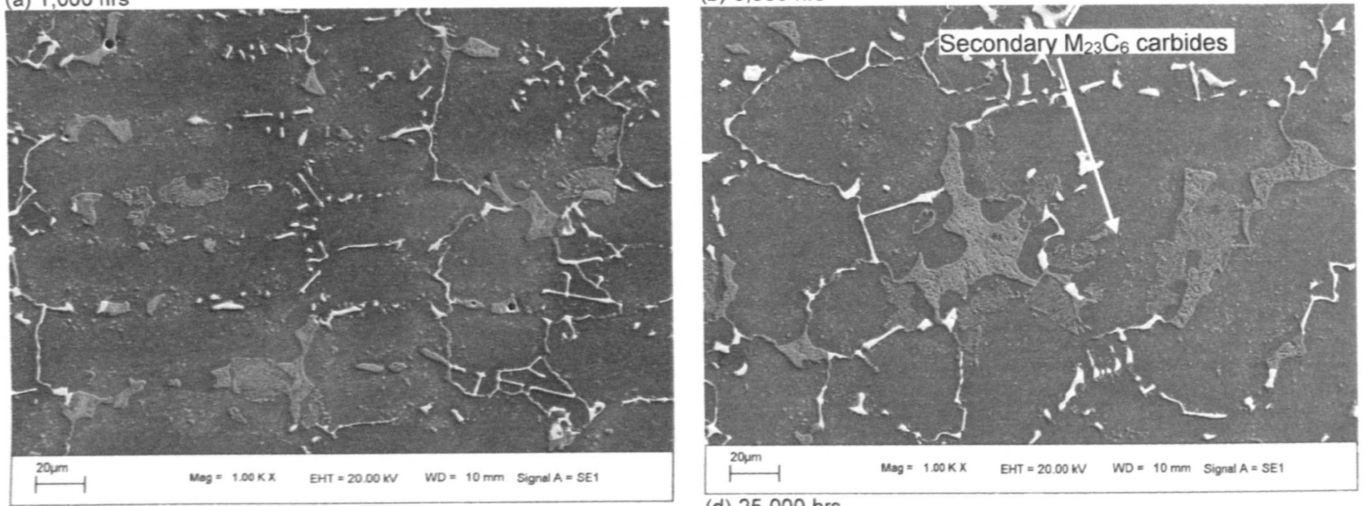

(c) 15,000 hrs

(d) 25,000 hrs

Figure 6.9 SEM SE images of MAR M509 samples aged at 850°C for (a) 1,000, (b) 5,000, (c) 15,000 and (d) 25,000 hours respectively.

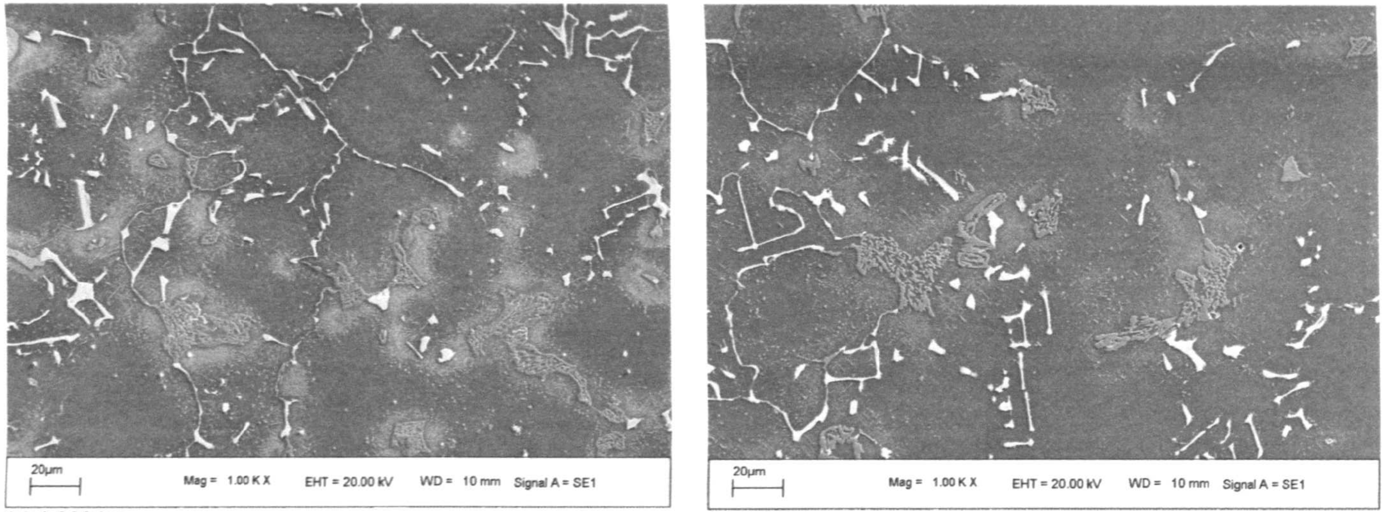

(a) 1,000 hrs

(b) 5,000 hrs

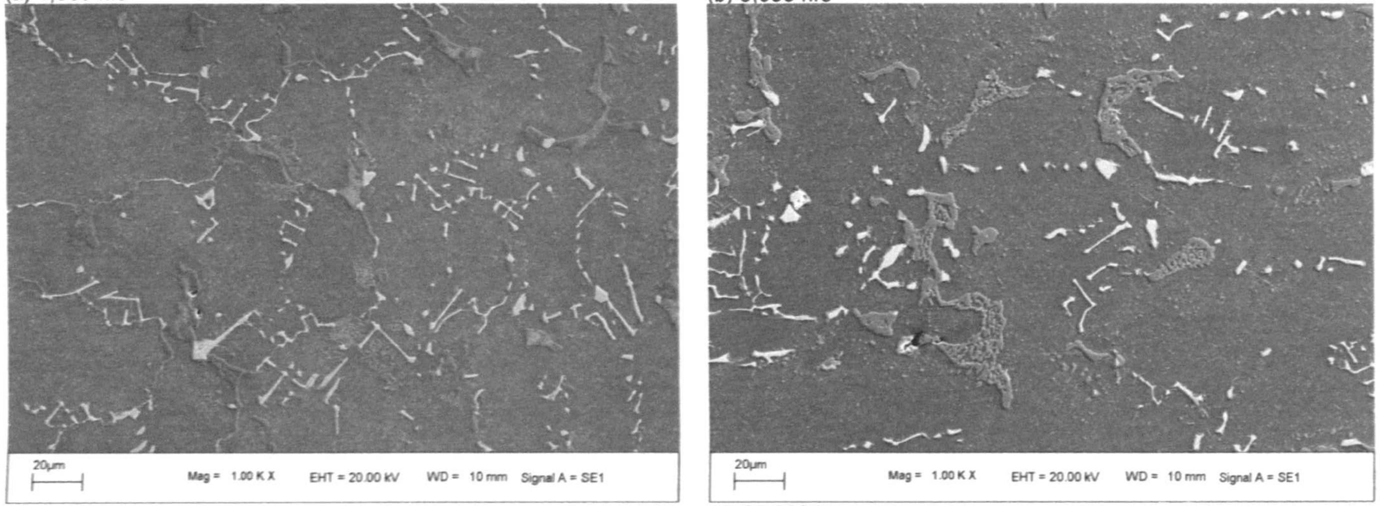

(c) 15,000 hrs

(d) 25,000 hrs

Figure 6.10 SEM SE images of MAR M509 samples aged at 900°C for (a) 1,000, (b) 5,000, (c) 15,000 and (d) 25,000 hours respectively.

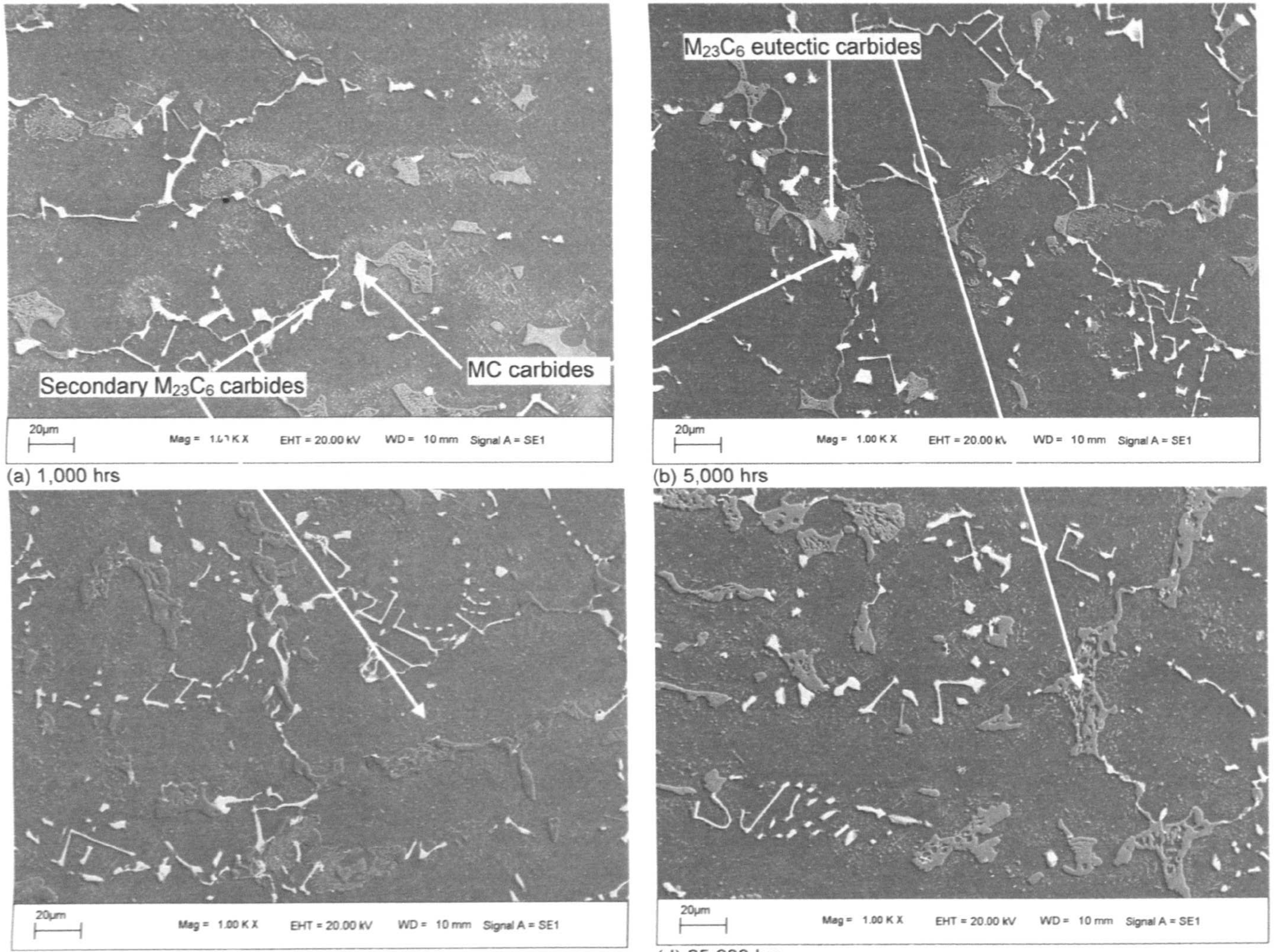

(a) 1,000 hrs
(b) 5,000 hrs
(c) 15,000 hrs
(d) 25,000 hrs

Figure 6.11 SEM SE images of MAR M509 samples aged at 950°C for (a) 1,000, (b) 5,000, (c) 15,000 and (d) 25,000 hours respectively.

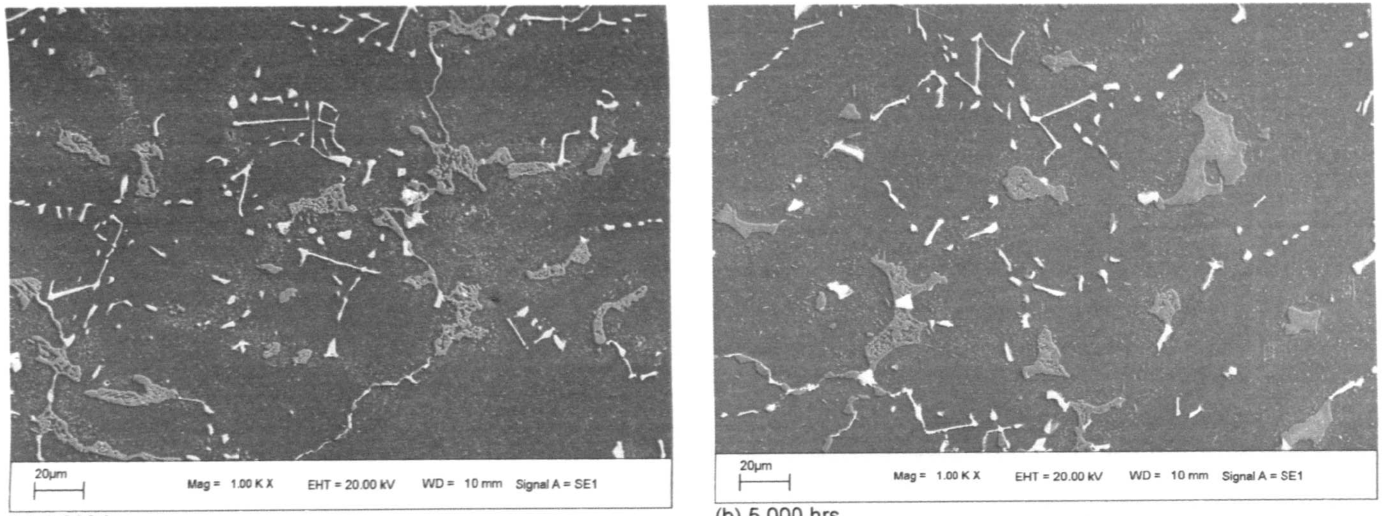

(a) 1,000 hrs

(b) 5,000 hrs

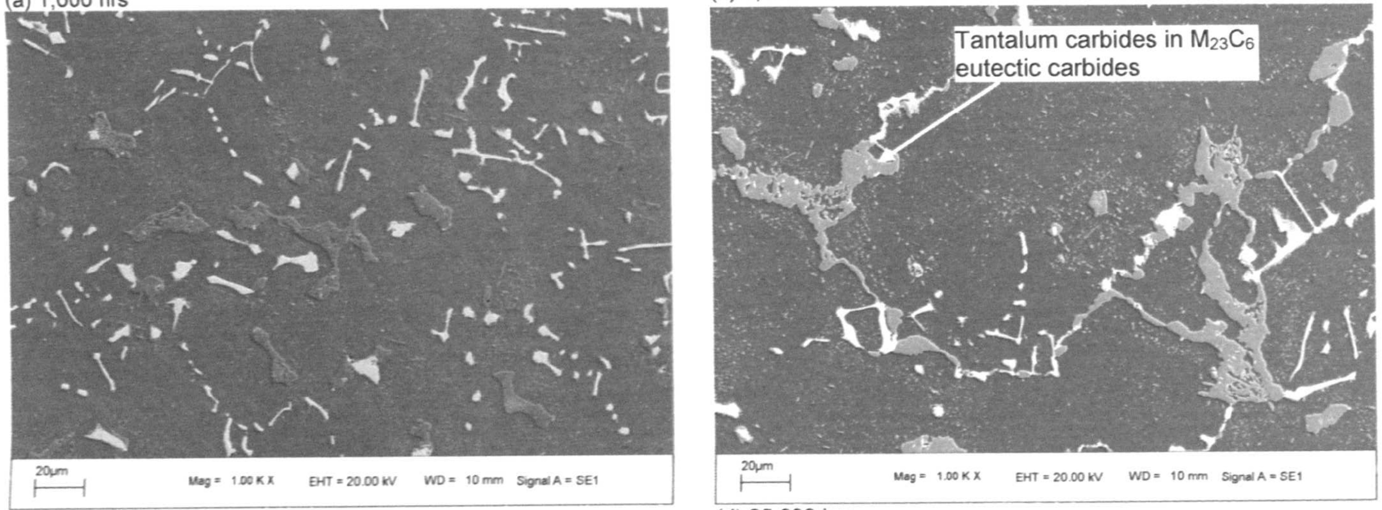

Tantalum carbides in $M_{23}C_6$ eutectic carbides

(c) 15,000 hrs

(d) 25,000 hrs

Figure 6.12 SEM SE images of MAR M509 samples aged at 1000°C for (a) 1,000, (b) 5,000, (c) 15,000 and (d) 25,000 hours respectively.

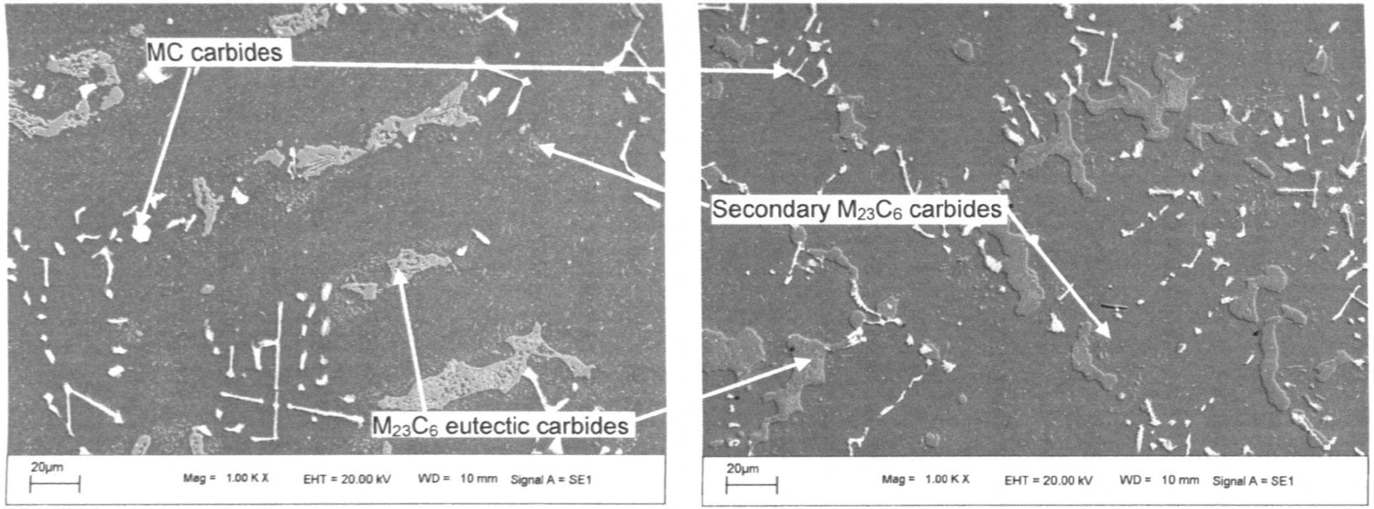

(a) 1,000 hrs

(b) 5,000 hrs

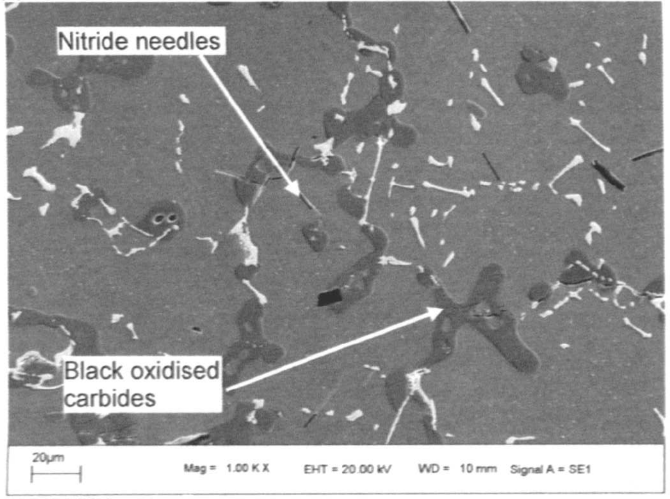

(c) 15,000 hrs

No Sample

Figure 6.13 SEM SE images of MAR M509 samples aged at 1050°C for (a) 1,000, (b) 5,000 and (c) 15,000 hours respectively.

6.2 Energy/Wavelength Dispersive Spectroscopy

The MC carbide in MAR M509 contains tantalum, tungsten and zirconium which produce overlapping peaks in the EDS data. With overlapping peaks the EDS software determines the quantity of each element by fitting known peak profiles to the overlap region. The accuracy of the fitting depends on the similarity of the peaks in the unknown spectrum to those of the profiles in the EDS database. In WDS peak overlapping is not a problem as the X-rays are separated using diffraction and individual wavelengths are detected at different spectrometer positions. The INCA Energy+ software used for the analysis of the MC carbides combines the outputs of the EDS and WDS spectrometers to provide a single analysis.

The results of the EDS/WDS analysis of the MC and EDS analysis of the $M_{23}C_6$ carbides from the aged samples are detailed in Table 6.2 and Table 6.3 respectively. The compositions are mean values from ten phases with a similar elemental signature.

The elemental plots for the MC and $M_{23}C_6$ carbides are shown in Figure 6.14 and Figure 6.15 respectively. The MC carbide tantalum, titanium, tungsten and zirconium results show minor variations in composition with no significant variations with time or temperature. The $M_{23}C_6$ carbide chromium, cobalt and tungsten plots show a consolidation of the carbide composition with both time and temperature. This shows that the changes in the carbide analysis are too small to be used to predict either time or temperature. From the EDS measurements the metallic component of the MC carbides can be expressed as approximately $Ta_{53}Zr_{16}Ti_{12}Cr_8Co_8W_3$ (where the subscript describes the concentration in at.%). The metallic component of the $M_{23}C_6$ carbides can be expressed as approximately $Cr_{82}Co_{10}W_5Ni_3$ (where the subscript describes the concentration in at.%).

The EDS analysis of the black phase (Table 6.3) evident in the 10,000 and 15,000 hour 1050°C samples shows reduced levels of tungsten and cobalt possibly as a result of oxidation. EDS analysis of the black needles evident in the 15,000 hour 1050°C samples show high levels of aluminium and nitrogen. The needle phase is considered to be aluminium nitride needles. This phase was not identified in the XRD traces (chapter 6.4). Etching of the samples in 10% HCl in methanol etched away the nitride needles.

Time hrs	Temp °C	Ti(a)	Cr(a)	Co(a)	Ni(a)	Zr(b)	Ta(b)	W(b)
1,000	850	4.7	1.7	2.7	0.5	11.3	75.9	3.3
	900	4.6	2.0	2.8	0.5	11.6	74.6	3.8
	950	5.0	1.8	2.6	0.5	12.0	74.8	3.4
	1000	4.6	2.2	2.9	0.5	11.4	74.2	4.1
	1050	4.6	1.9	2.7	0.5	11.8	75.0	3.6
5,000	850	4.6	2.3	2.9	0. 6	12.1	73.1	4.4
	900	4.7	1.8	2.5	0.5	12.5	74.4	3. 6
	950	4.7	2.3	2.9	0.6	11.6	74.0	3.9
	1000	4.7	1.9	2.6	0.5	11.9	75.0	3.6
	1050	4.9	2.7	3.1	0.6	12.5	71.9	4.4
10,000	850	4.3	2.9	4.1	0.7	11.0	73.0	4.0
	900	4.5	1.9	2.7	0.5	11.6	75.4	3.4
	950	4.7	1.7	2.4	0.4	11.5	76.0	3.4
	1000	4.6	2.3	3.0	0.5	11.9	73.5	4.4
	1050	4.9	2.0	2.6	0.5	12.6	73.9	3.6
15,000	850	4.5	2.3	3.0	0.6	11.6	73.6	4.4
	900	4.5	2.6	3.3	0.6	11.2	73.1	4.6
	950	4.5	2.0	2.8	0.5	11.0	75.3	3.9
	1000	4.3	1.8	2.5	0.5	10.5	76.5	3.9
	1050	4.2	1.6	2.0	0.4	11.2	77.2	3.4
20,000	850	4.6	2.0	2.6	0.5	11.3	74.9	4.0
	900	4.6	1.8	2.5	0.5	11.5	75.6	3.5
	950	4.6	2.1	2.7	0.5	12.0	74.1	4.0
	1000	4.5	1.8	2.2	0.4	12.0	75.7	3.5
25,000	850	5.1	2.1	2.9	0.6	12.7	73.3	3.4
	900	5.0	2.6	3.2	0.7	13.0	71.8	3.6
	950	4.9	2.5	3.2	0.6	11.8	73.1	4.0
	1000	5.1	2.3	2.9	0.5	12.6	73.0	3.6

(a) Determined by EDS (b) Determined by WDS

Table 6.2 EDS analysis of coarse MC carbide from aged MAR M509 samples (normalised to 100 wt.%).

(a) Tantalum

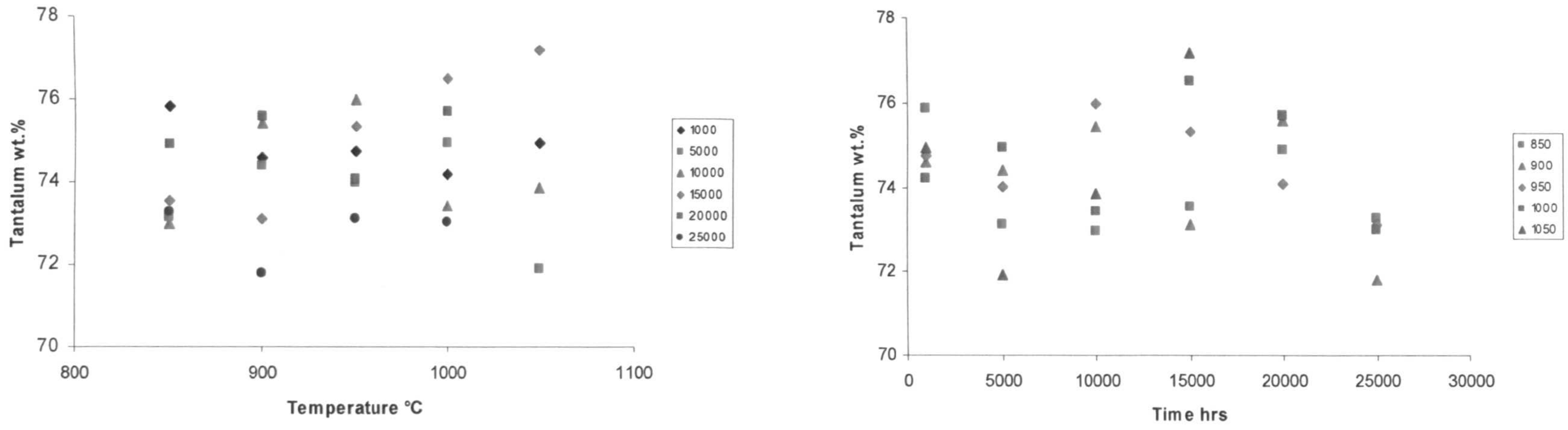

(b) Titanium

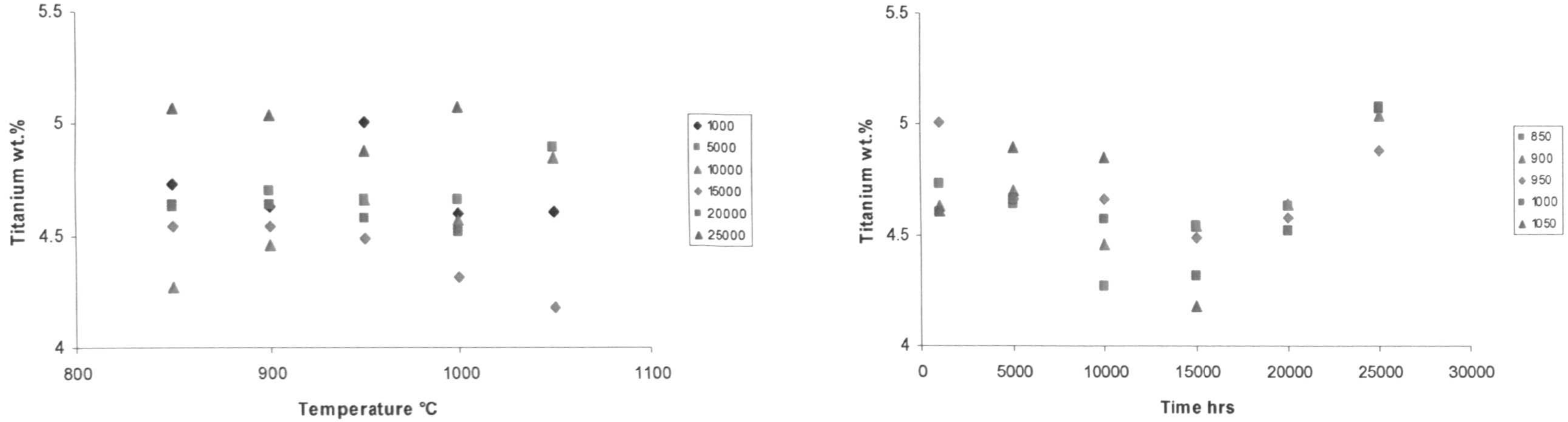

(a) Tungsten

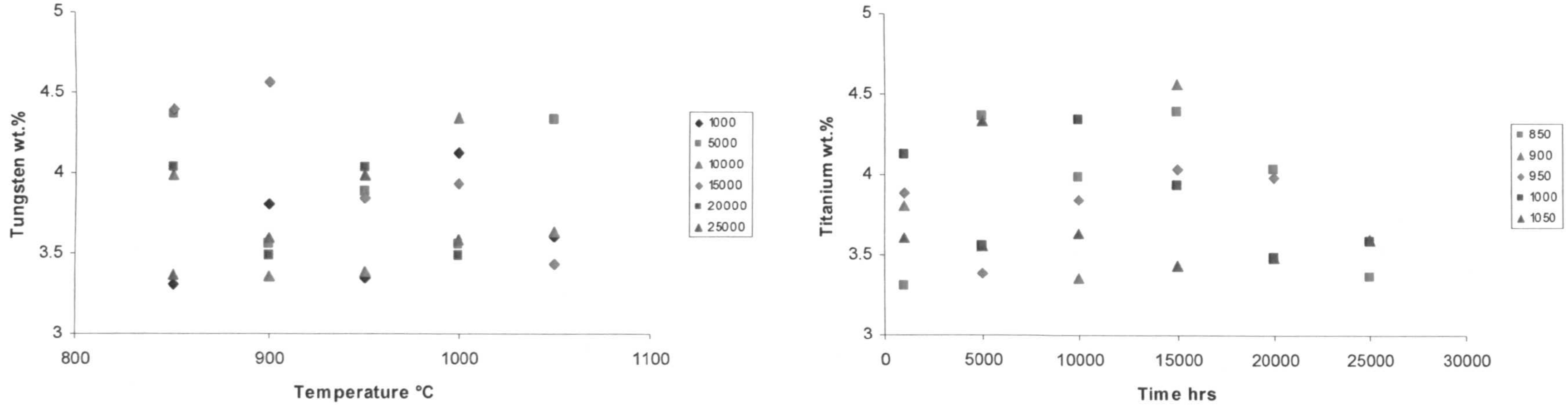

(d) Zirconium

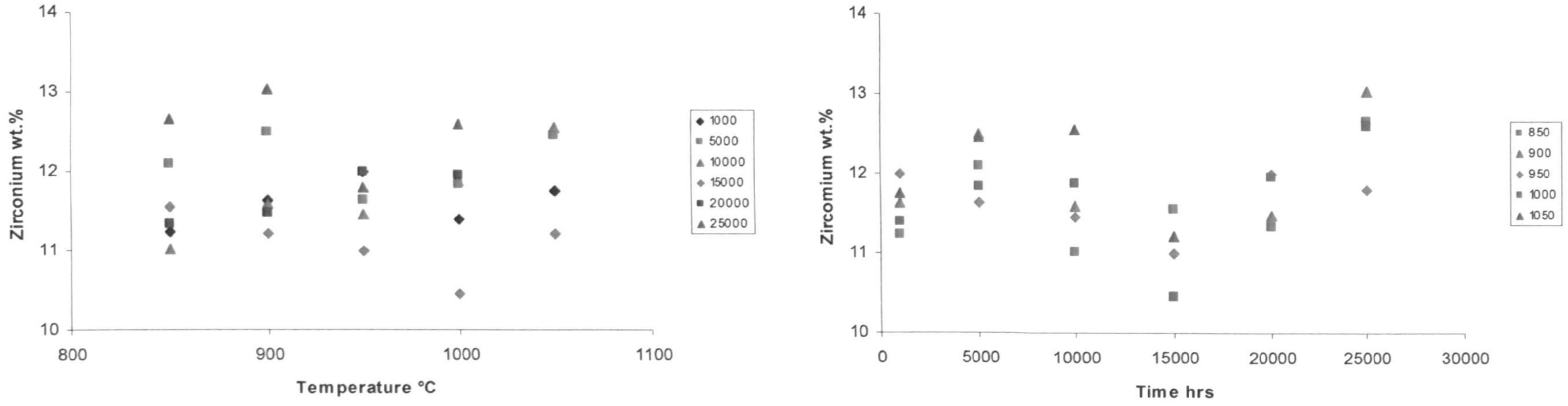

Figure 6.14 MC carbide analysis, MAR M509 aged samples (a) tantalum (b) titanium (c) tungsten and (d) zirconium respectively plotted with temperature and time (wt.%).

Time hrs	Temp °C	Cr	Co	Ni	Mo	W
1,000	850	76.7	11.1	1.4	0.3	10.6
	900	72.4	12.0	2.0	0.3	13.4
	950	68.8	12.7	2.2	0.3	16.0
	1000	69.7	12.6	1.9	0.2	15.5
	1050	69.1	13.7	1.9	0.2	15.1
5,000	850	66.2	16.6	3.0	0.3	13.9
	900	72.1	10.8	1.9	0.3	15.0
	950	69.5	12.2	2.0	0.3	16.1
	1000	69.7	12.7	1.8	0.2	15.5
	1050	67.9	15.0	1.9	0.3	14.9
10,000	850	65.0	15.1	4.8	0.3	14.8
	900	66.6	14.5	2.7	0.3	15.9
	950	69.6	12.2	2.0	0.2	16.0
	1000	69.2	13.1	1.9	0.3	15.5
	1050	66.8	15.9	2.0	0.3	15.0
Black	1050	91.1	2.6	0.3	0.2	5.9
15,000	850	70.7	10.7	2.0	0.3	16.2
	900	70.7	10.9	1.9	0.3	16.2
	950	70.3	11.5	1.9	0.3	16.0
	1000	69.7	12.5	1.8	0.3	15.6
	1050	68.6	12.8	1.9	0.2	16.5
Black	1050	89.3	2.5	0.3	0.2	7.7
20,000	850	71.4	10.4	1.9	0.3	16.0
	900	71.5	10.4	1.8	0.3	16.0
	950	70.9	11.4	1.8	0.3	15.6
	1000	70.1	12.6	1.9	0.3	15.3
25,000	850	70.5	10.7	2.1	0.3	16.5
	900	71.9	10.3	1.9	0.3	15.6
	950	71.2	11.3	1.8	0.2	15.5
	1000	70.2	12.5	1.9	0.2	15.2

Table 6.3 EDS analysis of coarse $M_{23}C_6$ carbide from aged MAR M509 samples (normalised to 100 wt.%).

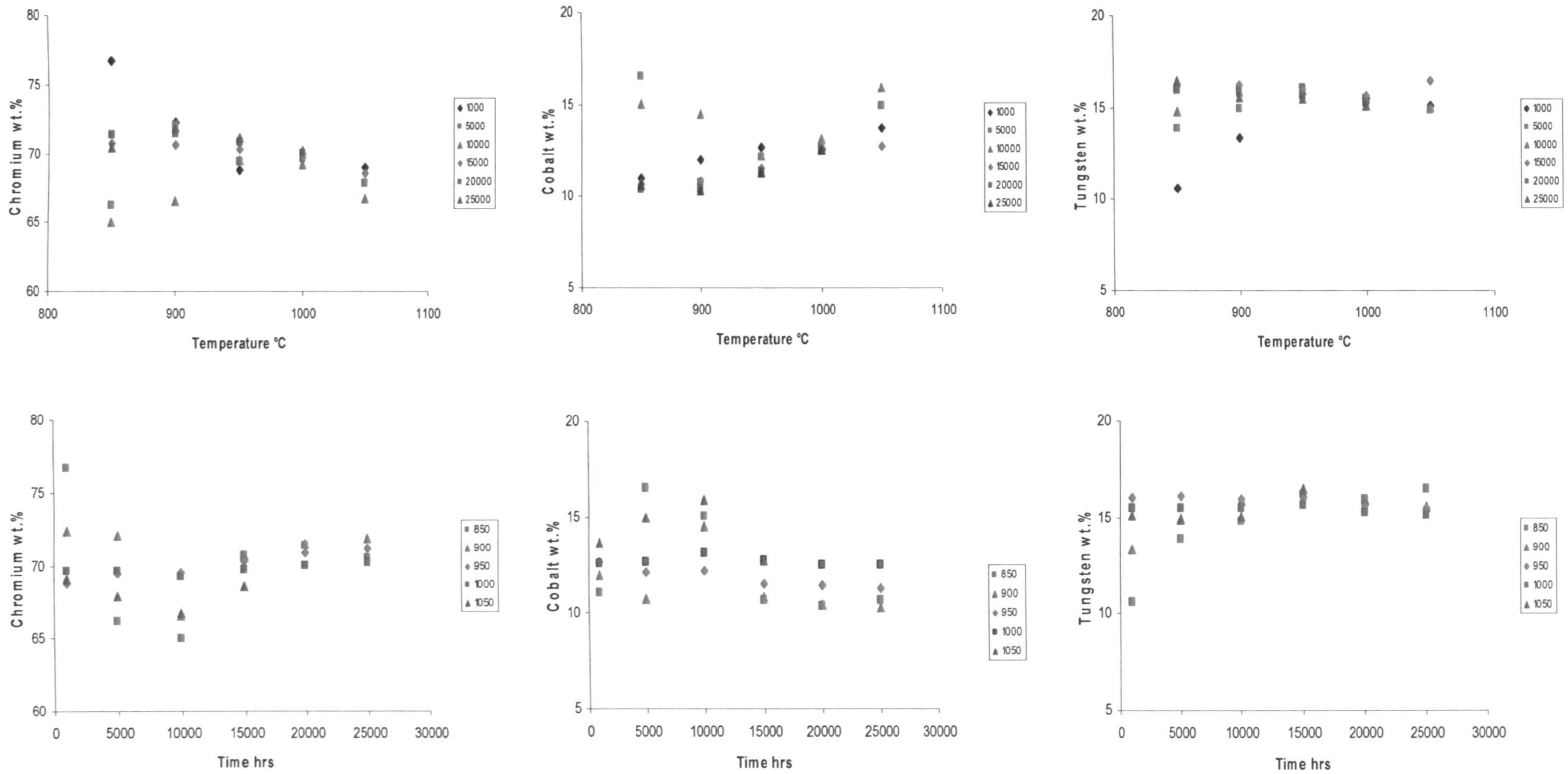

(a) Chromium

(b) Cobalt

(c) Tungsten

Figure 6.15 $M_{23}C_6$ analysis from MAR M509 aged sample (a)chromium (b) cobalt and (c) tungsten respectively plotted with both temperature and time (wt.%).

6.3 Thermodynamic Equilibrium Predictions

This section presents thermodynamic equilibrium predictions for alloy MAR M 509 carried out using JMatPro software. MAR M509 is a cobalt-based superalloy. JMatPro does not have a cobalt-based superalloy database therefore all of the following thermodynamic predictions are based upon the nickel based superalloy database. The JMatPro calculations are based on the composition of the samples detailed in Table 3.1.

The JMatPro software predicts the equilibrium phases that would form under equilibrium conditions. In this programme of work the JMatPro software has been used to predict the equilibrium phases that would form at specific ageing temperatures. In using this software it has been assumed that no phase transformations occur on cooling. To validate this assumption MAR M509 samples aged at 850°C and 1050°C for 12,000 hours were water quenched directly from the ageing temperature. These samples were compared with samples cooled in still air. Optically there was no variation between the air cooled and water quenched samples. Examination of the samples in the SEM confirmed that all the secondary phases found previously were evident in both samples. EDS analysis showed no significant changes in the chemical analysis of the carbides or secondary phases between the quenched samples and those slowly cooled.

JMatPro predicts three equilibrium phases γ, MC and $M_{23}C_6$. γ remains constant at ~91 wt.% across the temperature range. The MC carbide content increases from 4.6 to 4.7 wt.% between 850°C and 1050°C, the $M_{23}C_6$ carbide content drops from 4.9 to 4.0 wt.% over the same temperature interval (Figure 6.16). This would indicate a reduction in the carbide content from 9.5-8.7 wt.% over the 850-1050°C temperature range.

The JMatPro composition predictions for MC and $M_{23}C_6$ carbides show small variations over the temperature range from 850 to 1050°C. The predicted changes in the composition of the $M_{23}C_6$ carbide (Figure 6.17) are chromium reduces from 67 to 63 wt.%, cobalt increases from 14.3 to 17.8 wt.%, nickel increasing from 1.1 to 1.8 wt.% with tungsten and carbon constant at 12 wt.% and 5 wt.% respectively. The variations in the composition of the MC carbide (Figure 6.18) are tantalum reducing from 78 to 76 wt.%, tungsten increasing from 2.8 to 4.6 wt.% with zirconium, carbon and titanium remaining relatively level at 7.0 wt.%, 7.4 wt.% and 4 wt.% respectively. The equilibrium predictions have been derived using the nickel database, if the predictions are valid the changes in the carbide analysis with temperature are small and would not provide a robust method of predicting time or temperature for service exposed components.

Table 6.4 contains the JMatPro predictions for the MC and $M_{23}C_6$ carbides at 950°C and the WDS/EDS analysis for the MC and $M_{23}C_6$ carbides obtained from the 950°C 1,000 hour and 20,000 hours samples. For the MC carbide the WDS/EDS results and JMatPro predictions are similar, other than WDS for zirconium, which is almost double the JMatPro prediction. For the $M_{23}C_6$ carbide, again the analyses are similar other than the EDS tungsten level which is higher than the JMatPro prediction, and the EDS cobalt level which is lower than the JMatPro prediction. The 20,000 hour 950°C EDS analysis has been included to illustrate the effects of including carbon in the EDS analysis. As stated earlier carbon analysis by EDS should be considered qualitative rather than quantitative. The results show that the carbon levels from EDS and JMatPro are similar. For the MC carbide, other than for tantalum, including carbon brings the EDS analysis more in line with the JMatPro predictions. However, the tantalum EDS value is less than that predicted by JMatPro. The inclusion of carbon in the EDS composition reduces the EDS tantalum value and thus increases the variance between the measured and predicted values. For the $M_{23}C_6$ carbide, other than for cobalt, again the effect of including carbon is to bring the EDS analysis more in line with the JMatPro prediction. However, the EDS cobalt value is less than that predicted by JMatPro.

Drapier et al(62) and Beltran et al(64) used an electron microprobe to carry out carbide analysis on MC and $M_{23}C_6$ carbides in MAR M509. The results are included in Table 6.4. Beltran noted that the MC carbide analysis did not correspond to an idealised composition and gave the most probable cause as overlap of the electron beam on to the matrix due to the small carbide size. He did consider the $M_{23}C_6$ carbide analysis to be accurate. It should be noted that the Beltran and Drapier results were not normalised to 100 wt.%. The Drapier MC carbide results are similar to the current EDS and JMatPro predictions. His tungsten levels are more in line with the JMatPro predictions than the current EDS results. The Beltran MC carbide results do show high levels of cobalt which would confirm his assumption that the beam had included some of the matrix. The $M_{23}C_6$ carbide results of Drapier are similar, with lower tungsten levels than predicted by JMatPro and found by EDS in the current samples. The results of Beltran for $M_{23}C_6$ carbide show lower levels of chromium with higher levels of cobalt and nickel. These variations in the $M_{23}C_6$ carbide analysis may indicate the wide variations that could exist in the carbides possibly as a result of the casting conditions or variations in the bulk analysis within the MAR M509 specification.

The high tungsten phase evident in the as-cast sample reduces rapidly with time but residual particles are still found in the $M_{23}C_6$ eutectic carbides in the 25,000 hour, 850 and 900°C samples. No phases other than MC and $M_{23}C_6$ carbides are identified in the JMatPro equilibrium predictions. This would suggest the phase is not an equilibrium phase or has not been predicted as a consequence of using the nickel superalloy database.

JMatPro and the experimental results are very similar and both show that the carbides do not change significantly with time or temperature. Therefore there is no possibility of using the carbides in MAR M509 as time temperature indicators.

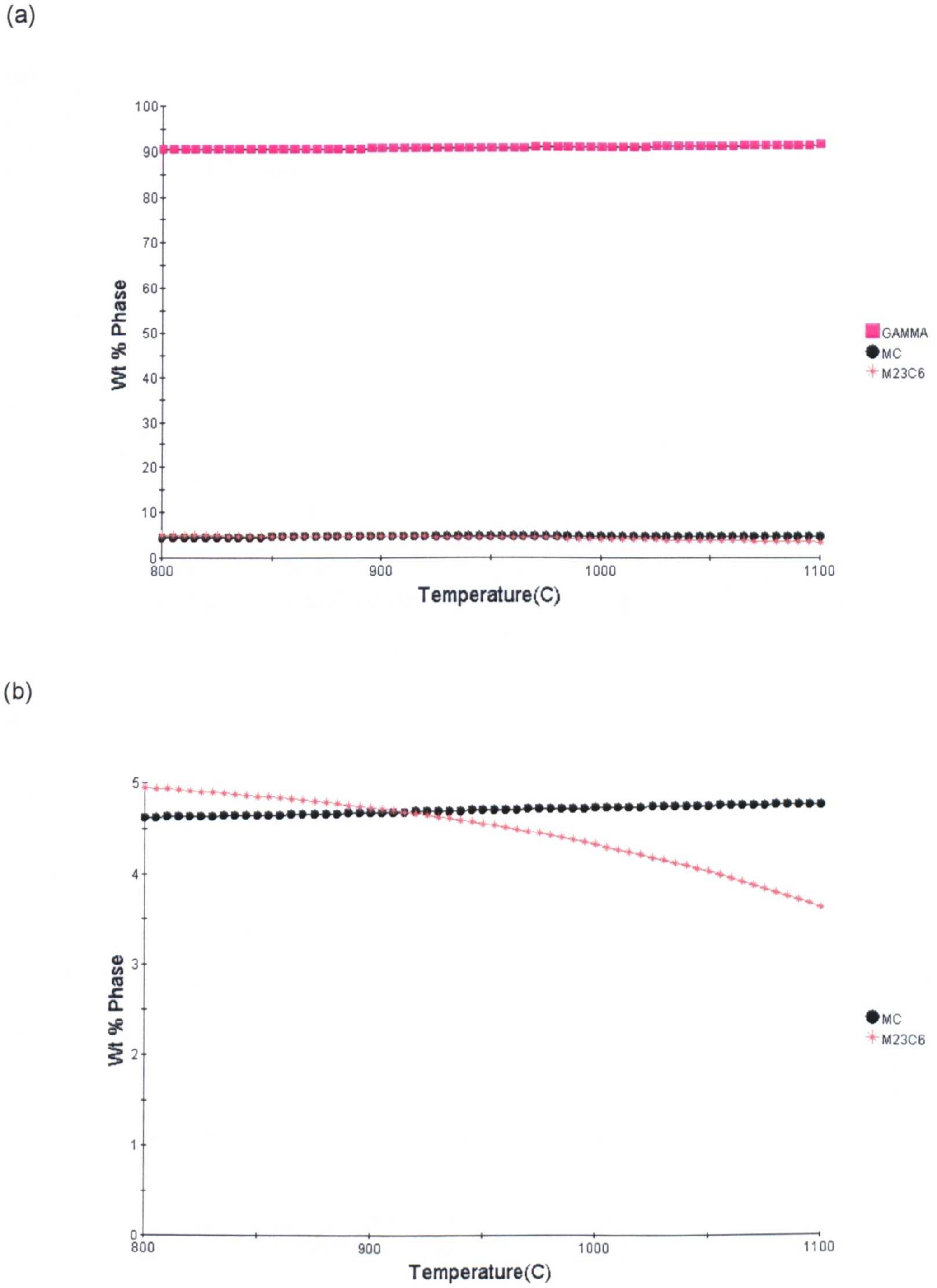

Figure 6.16 MAR M509 JMatPro predicted equilibrium phases (b) rescaled.

(a)

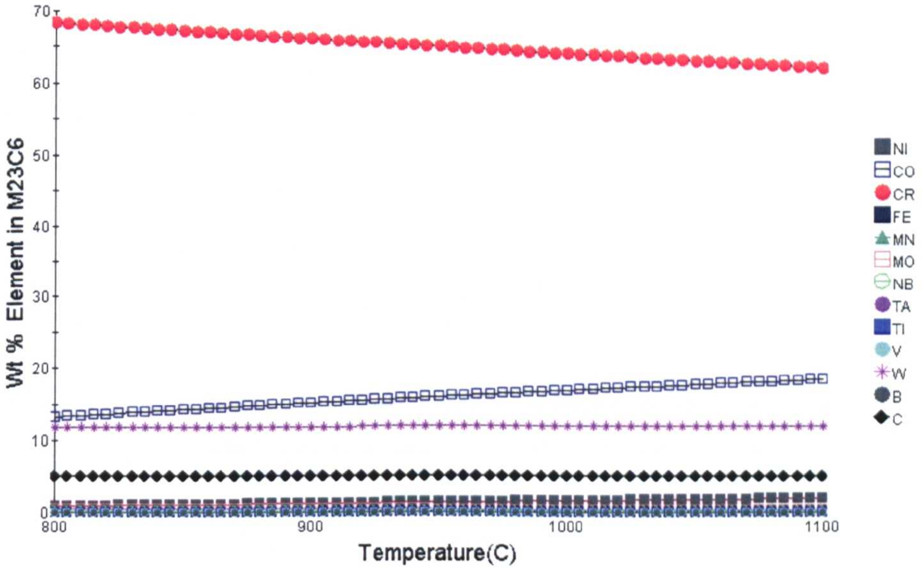

(b)

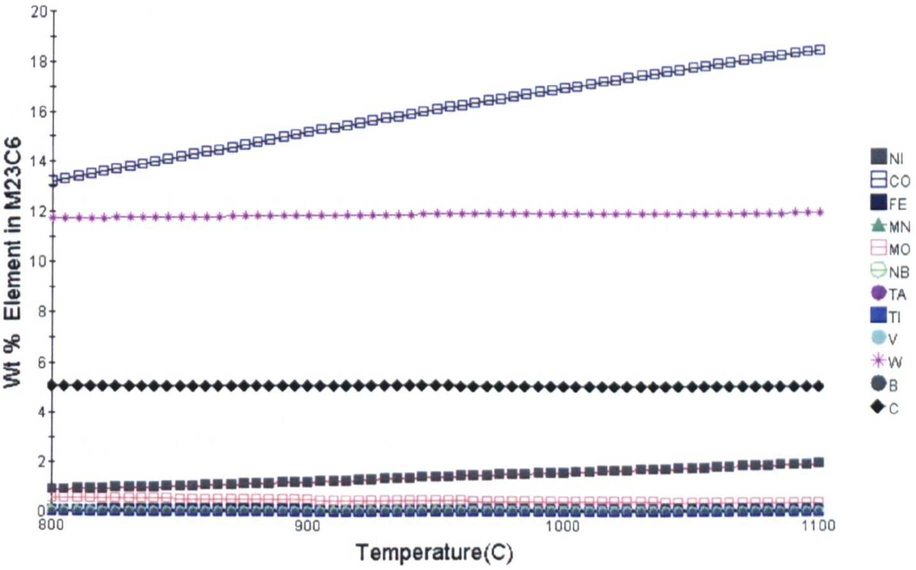

Figure 6.17 JMatPro analysis predicted for MAR M509 $M_{23}C_6$ carbide (b) rescaled.

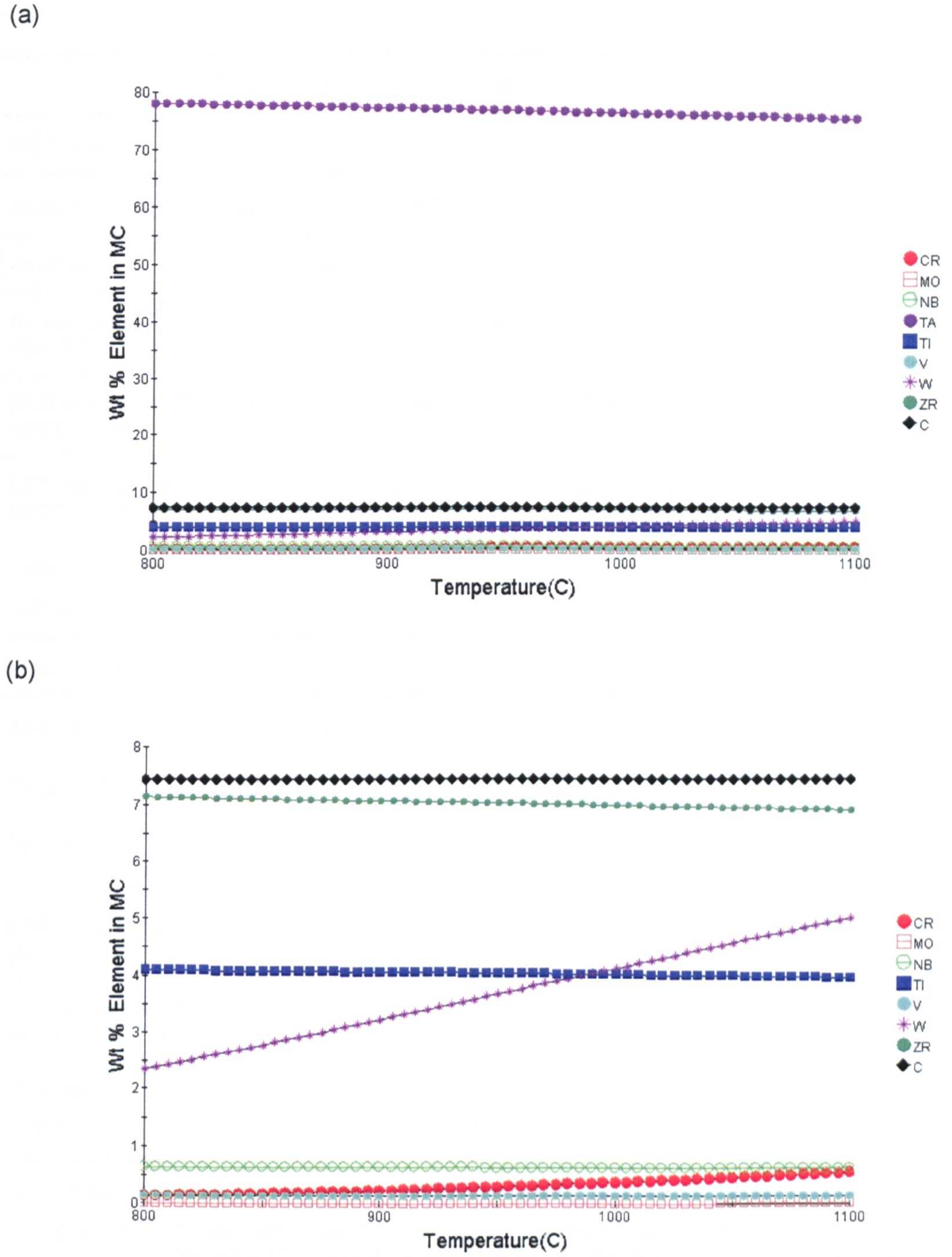

Figure 6.18 JMatPro analysis predicted for MAR M 509 MC carbide (b) rescaled.

	Ta	Zr	Ti	W	Cr	Co	Ni	Nb	C
MC Carbide									
As-cast(62)	70.2	9.8	4.2	2.2	0.8	1.9	0.2		
As-cast(64)	51	3	-	5	4	11	2		
As-cast aged 960°C 1571 hrs(64)	47	3	-	4	5	9	3		
EDS as-cast aged 950°C 1,000 hrs	74.8	12.4	5.0	3.4	1.8	2.6	0.5		
EDS as-cast aged 950°C 20,000 hrs	70.1	10.8	4.2	3.8	2.0	2.5	0.5		6.1
JMatPro 950°C	77	7	4.1	3.7	0.3			0.6	7.4
$M_{23}C_6$ Carbide									
As-cast(62)	1.0	0.1	0.1	9.1	65.3	16.3	1.7		
As-cast(64)	0.3	-		8	42	21	6		
As-cast aged 960°C 1571 hrs(64)	0.3			8	48	21	11		
EDS as-cast aged 950°C 1,000 hrs				16	69	12.7	2.2		
EDS as-cast aged 950°C 20,000 hrs				14	67	11.0	1.7		6.9
JMatPro 950°C				12	65	16.1	1.4		5.1

N.B It should be noted that the Drapier and Beltran results were not normalised to 100 wt.%

Table 6.4 Comparison of MC and $M_{23}C_6$ carbide analysis from Drapier(62), Beltran(64), aged MAR M509 sample WDS/EDS and JMatPro predictions (wt.%).

6.4 Carbide extraction and XRD

To measure the type and volume fraction of carbides present in the samples, the carbides were separated from the matrix by a bulk electrolytic extraction method. The electrolyte used was 10% HCl, 1% tartaric acid in methanol. The technique dissolves the γ matrix leaving the carbides as sediment. For further details see Chapter 3.7.

A series of extractions were carried out on sections from the MAR M509 950°C 2,000 hour test piece for 1, 2 and 3 hour periods to confirm that the carbides in the electrolyte were not attacked by the electrolyte during the three hour extraction periods. The weight percent of carbide extracted from the samples were 8.79, 8.68 and 8.66 wt.% for the 1, 2 and 3 hour extractions. This result is considered to show that the carbides are not attacked by the electrolyte during the 3 hour extraction.

For all of the samples the phases identified were MC and $M_{23}C_6$. In the 1050°C 5,000 and 10,000 hour samples in addition to the MC and $M_{23}C_6$, oxides of chromium, tantalum and titanium were identified. The maximum weight of extract from the samples was 0.07g after a three hour extraction. Additional small peaks on the XRD trace with counts less than 0.02% of the largest peak could not be assigned. Figure 6.20 is a plot of the weight percent of carbide extracted. For all temperatures there is an increase in the mass of the extract from 1,000 to 10,000 hours (from ~7 to 10 wt.%) followed by a drop in the weight extracted through to 25,000 hours. The increase may indicate the continuing precipitation of the secondary $M_{23}C_6$ carbides. It is not clear from the plot of temperature against time what the reason is for the drop in weight extracted for the 1,000 and 2,000 hour samples, the other samples remaining relatively constant.

The XRD traces have been used to show if the relative amounts of the MC and the $M_{23}C_6$ carbide are changing with ageing temperature or time. Two methods have been used to determine the relative amounts of the MC and $M_{23}C_6$ carbide from the XRD traces. Both methods compare the combined values from the MC (111) and (200) peaks with the $M_{23}C_6$ (420) and (511) peaks (Figure 6.19). The first technique utilises the peak area which may be affected by very fine precipitates causing peak broadening(85). The second method uses the peak heights or peak counts. Plots of the peak area (Figure 6.21) and peak height (Figure 6.22) show, in both cases a large drop in the relative amounts up to 5,000 hours followed by smaller changes up to 20,000 hours with a slight up turn at 25,000 hours. The precipitation of the secondary $M_{23}C_6$ carbides would account for the large drop between 1,000 and 5,000 hours. However, the measurements appear to show either that the precipitation of the TaC in the matrix and the eutectic is either very small and or the technique is unable to detect the increase in the TaC. It is also equally possible that there is a balance between the precipitation of the matrix and eutectic tantalum carbide and the solutioning of the original MC carbides.

JMatPro equilibrium predictions indicate that there should be a small increase in MC carbide with a drop in the $M_{23}C_6$ carbides with temperature (Figure 6.16b). Figure 6.23 illustrates the peak area results and includes the JMatPro predictions for MC and $M_{23}C_6$ carbides. The results from the XRD measurements do show a similar increase with temperature consistent with the JMatPro predictions.

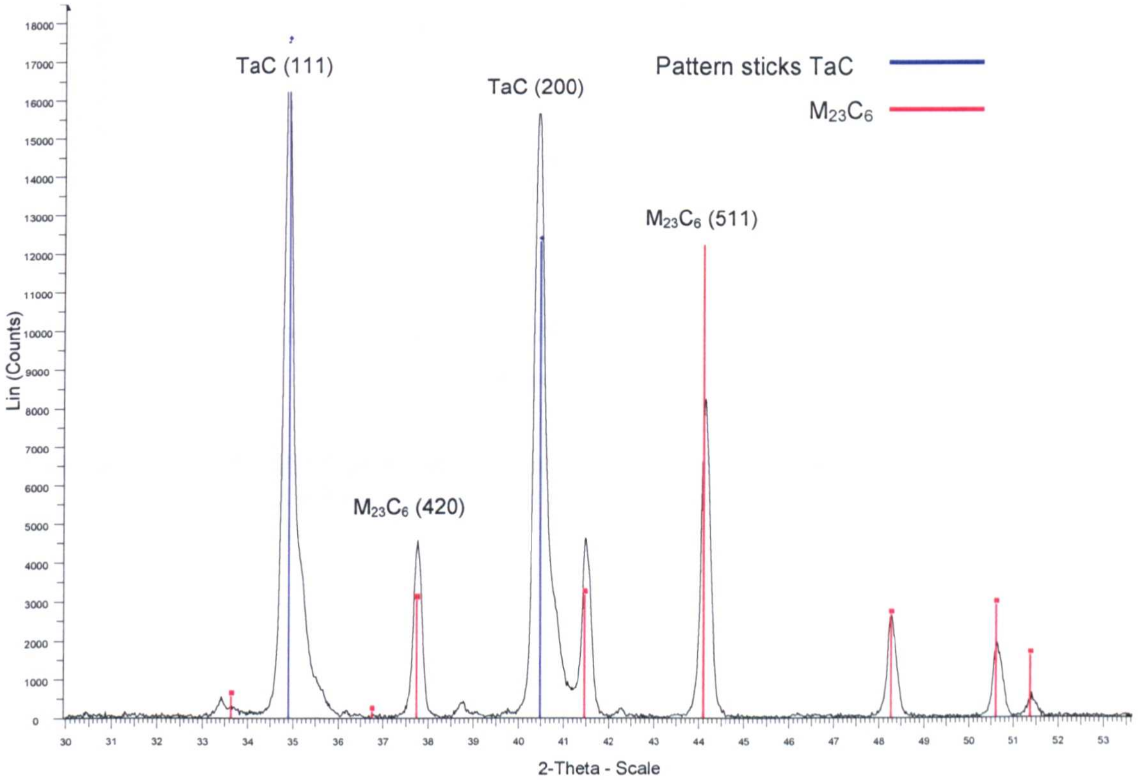

Figure 6.19 MAR M509 XRD trace illustrating peaks used for MC:$M_{23}C_6$ peak area and peak height measurements 859°C 5,000 hour sample.

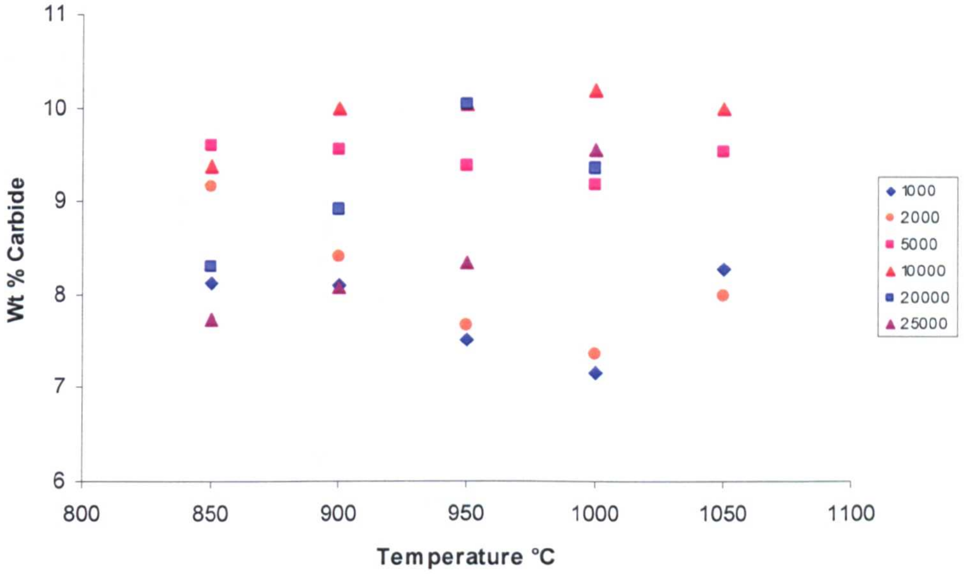

Figure 6.20 MAR M509 wt.% carbide extracted for all samples up to 25,000 hour plotted with temperature.

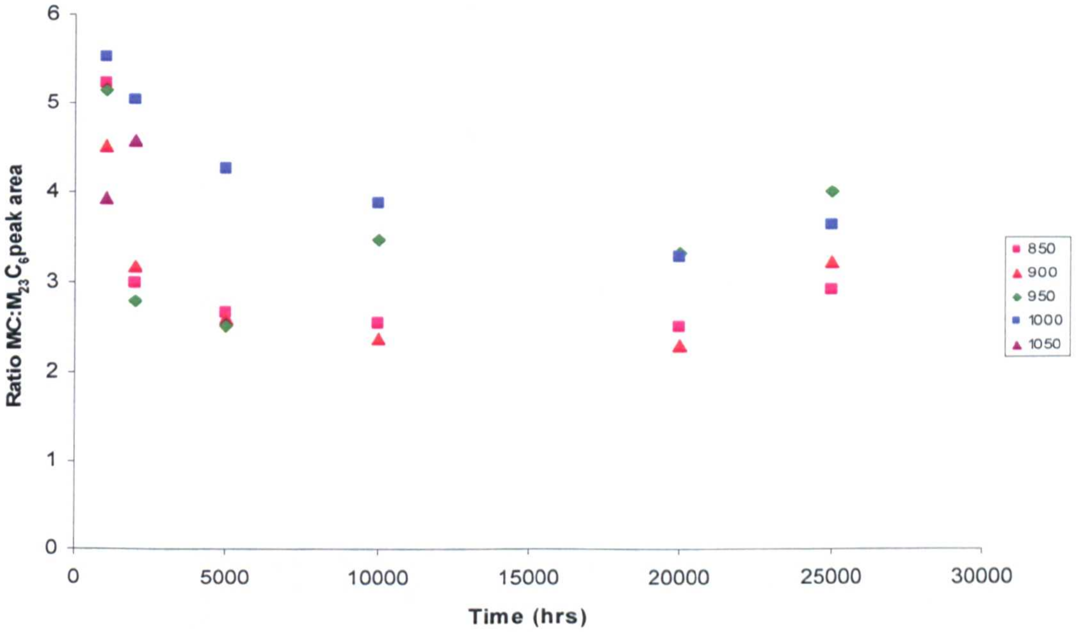

Figure 6.21 MAR M509 ratio of MC (111 and 200 peaks):$M_{23}C_6$ (420 and 511 peaks) peak area from XRD traces plotted with time.

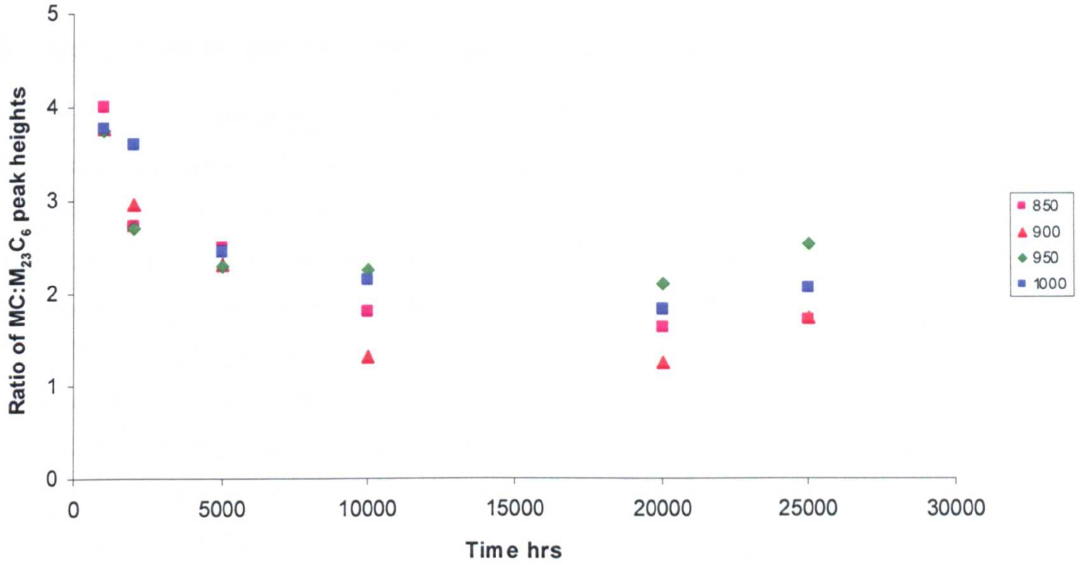

Figure 6.22 MAR M509 ratio of MC (111 and 200 peaks):$M_{23}C_6$ (420 and 511 peaks) peak heights from XRD traces plotted with time.

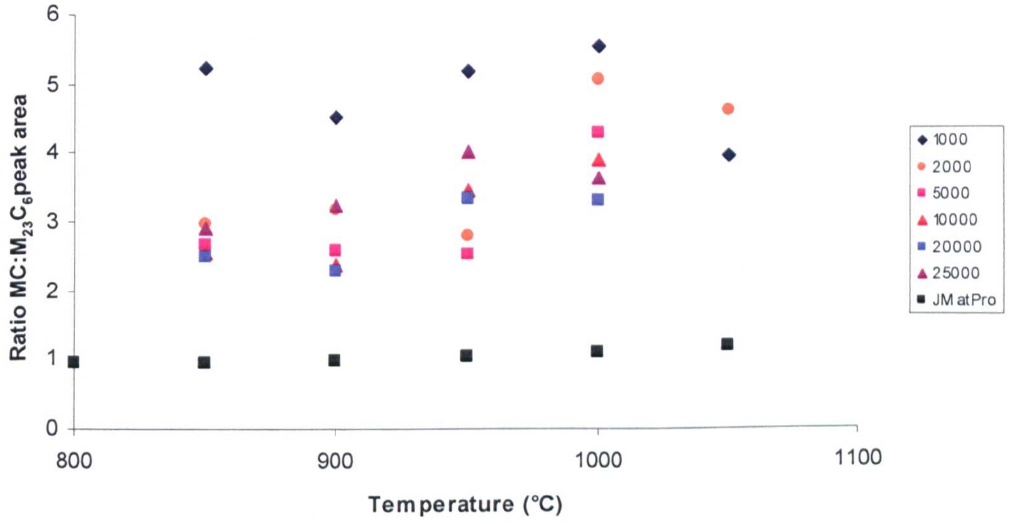

Figure 6.23 MAR M509 ratio of MC (111 and 200 peaks):$M_{23}C_6$ (420 and 511 peaks) peak area from XRD traces with JMatPro prediction plotted with temperature.

6.5 Unknown Phase Identification (Electron Diffraction)

Thin foil samples containing the tungsten rich and the tantalum rich phases in the $M_{23}C_6$ eutectic carbides were removed from the 1,000 hour 850°C and 15,000 hour 950°C samples by FIB SEM. Figure 6.24 shows the position of the thin foil in the FIB SEM 1,000 hour 850°C sample, a TEM image of the thin foil sample taken to include the tungsten rich phase in the $M_{23}C_6$ eutectic carbide and a selected area electron diffraction pattern from the tungsten rich phase. Figure 6.25 shows the position of the thin foil in the FIB SEM 15,000 hour 950°C sample, a TEM image of the thin foil sample which includes the tantalum rich phase found in the $M_{23}C_6$ eutectic carbide and a selected area electron diffraction patterns from the tantalum rich phase. The patterns were indexed using the Cambridge University Practical Crystallography software Version 1.6(79). The phases investigated were μ, η, σ, MC, M_6C, M_7C_3 and $M_{23}C_6$. Indexing of the pattern confirms the tungsten rich phase is M_6C (FCC, lattice parameter 11.08 Å) or Co_3W_3C (FCC, lattice parameters 10.897 Å). Sims(2) notes that M_6C carbides usually occur as M_3M_3C or M_4M_2C. The tantalum rich phase indexed as TaC (FCC, lattice parameter 4.455 Å).

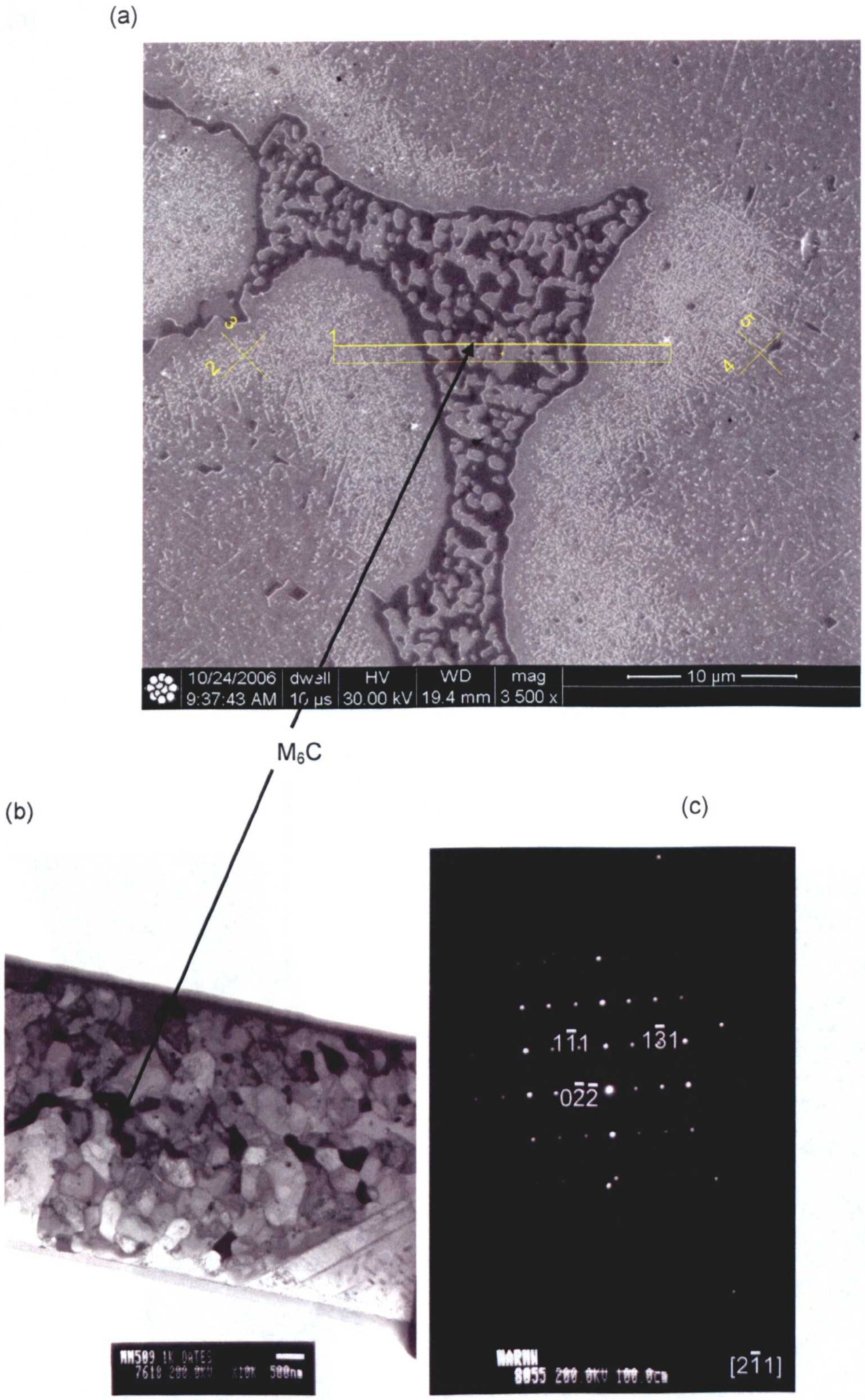

Figure 6.24 MAR M509 850°C 1,000 hour sample (a) FIB SEM image sample position (b) TEM image of thin foil and (c) diffraction pattern.

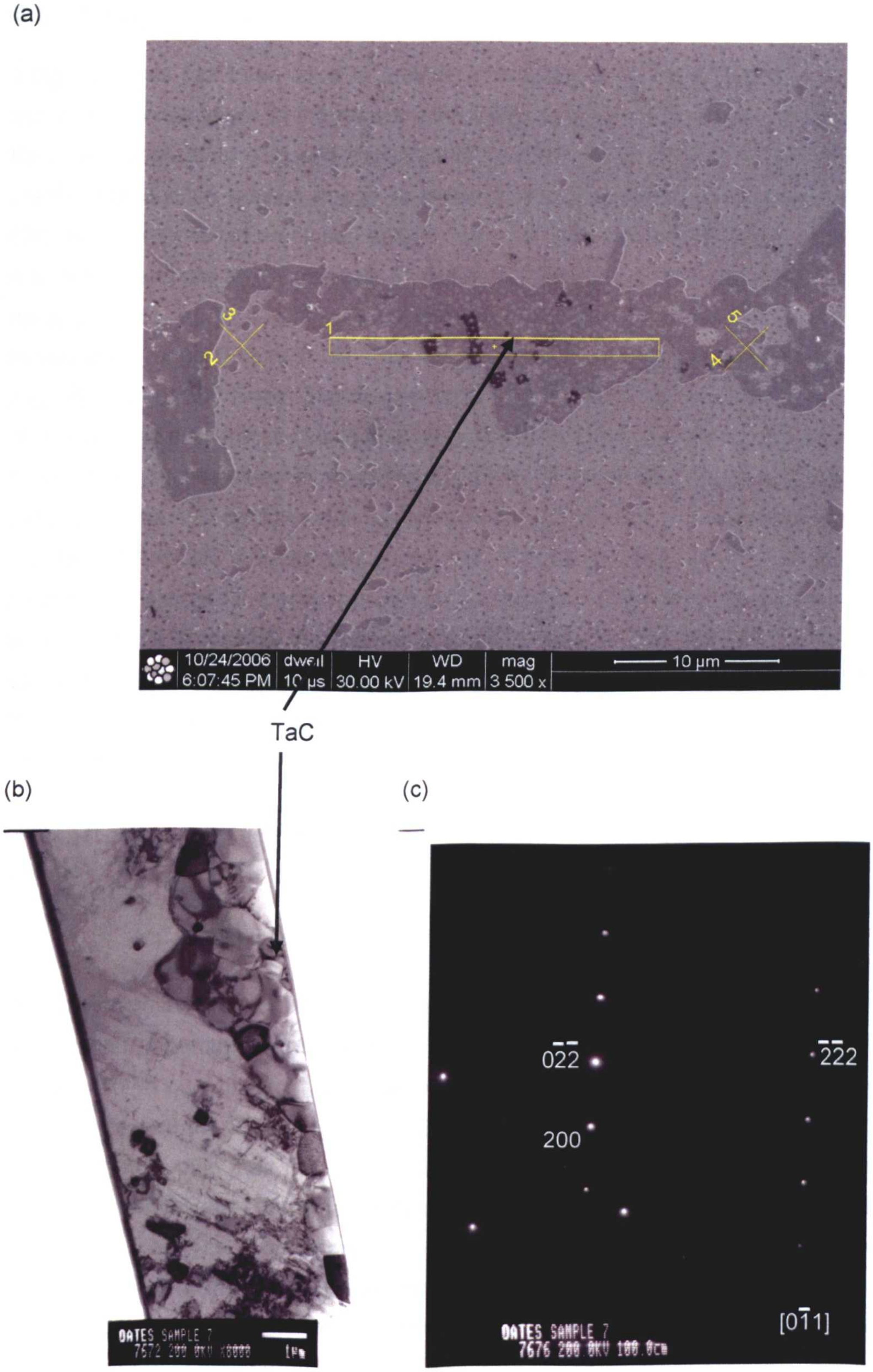

Figure 6.25 **MAR M509 20,000 hours 950°C sample (a) FIB SEM image sample position (b) TEM image of thin foil and (c) diffraction pattern.**

6.6 Image analysis

Image analysis has been used to provide a measure of the area fraction of carbide in the samples. The variations in the results from image analysis can be very significant. However, by careful application of sound experimental technique it is possible to limit the scatter and create reproducible results. Image analysis of the MC carbide is relatively simple as the carbide in the polished un-etched samples show white in SEM backscatter mode against the grey matrix and the $M_{23}C_6$ carbides (Figure 6.8). The results, from the image analysis of the aged samples, show a relatively uniform level of MC carbide of 5-6 area % across the temperature range (Figure 6.26). The image analysis was carried out on scans taken at a magnification of 500 times. The magnification is a compromise to allow the detection of any changes in the area fraction while minimising the effects of carbide segregation by including a minimum of 100 carbides in each image. Figure 6.13 (a) and (b) illustrate the significant variation in the MC carbides that can exist between samples. The results suggest that any changes in the MC carbide are minor and if present would only be evident at higher magnifications where the effects of carbide segregation would produce large variations in the area fraction. It is possible that there is a balance between any solutioning of the primary MC carbides and the precipitation of the secondary MC carbides in the matrix and the eutectic $M_{23}C_6$ carbides. The changes are too small to provide a robust measurement of service temperature from service exposed vanes.

Sims(2) notes that the MC carbides, under long service exposures, degenerate to a lower carbide:

$$\text{MC + austenite} \longrightarrow M_6C \text{ or } M_{23}C_6$$

For alloys high in chromium the predominant displacement reaction is from MC to $M_{23}C_6$. This provides an important secondary hardening effect from the MC carbide, which acts as a source of large quantities of $M_{23}C_6$ carbides. Figure 6.27 illustrates MC carbides from the as-cast sample and the 25,000 hour 950°C sample. The carbides in the aged sample have a more 'ragged' profile than the as-cast carbides. What cannot be determined is if this is the result of precipitation of secondary carbides on to the primary carbides, or the solutioning of the primary carbides. The impression from the samples is that it is more likely to be precipitation on to the MC carbides rather than solutioning of the carbides. The JMatPro equilibrium prediction (Figure 6.16) shows a slight increase in MC carbide across the temperature range 800-1100°C.

Image analysis of the $M_{23}C_6$ carbides proved to be impracticable due to the difficulty in producing the contrast required to differentiate between the $M_{23}C_6$ and the γ matrix. The more significant problem is the fine secondary carbides around the primary carbides (Figure 6.28) in the 850 and 900°C samples. At lower magnifications (<1000) the secondary carbides cannot be resolved and produce a halo around the primary carbides significantly increasing the measured area fraction.

Szala et al(86) report the results of an investigation to enhance the detection of the carbides in MAR M509 by selective etching to allow automated image analysis to provide a quantitative measure of the carbides in service exposed MAR M509. The report confirms the ease with which the MC carbides in MAR M509 can be detected in polished unetched samples and the difficulty of detecting the $M_{23}C_6$ eutectic carbides for image analysis. Techniques and etchants to improve the contrast between the $M_{23}C_6$ eutectic carbides and the matrix are reported. However, the report is only concerned with the primary $M_{23}C_6$ eutectic carbides. In aged samples, secondary $M_{23}C_6$ carbides precipitate around the primary $M_{23}C_6$ eutectic carbides and show, at low magnification, as a broad halo around the primary carbides (Figure 6.28). Images in the report appear to be from as-cast samples with small isolated areas of secondary $M_{23}C_6$ carbides. It is the halo of secondary $M_{23}C_6$ carbides around the primary carbides which have caused problems with image analysis of the aged MAR M509 in this work. At low magnification the carbides cannot be resolved and artificially increase the quantity of $M_{23}C_6$ carbides. At higher magnification where the carbides can be resolved, the overall carbide segregation leads to large variations in the measured $M_{23}C_6$ carbide.

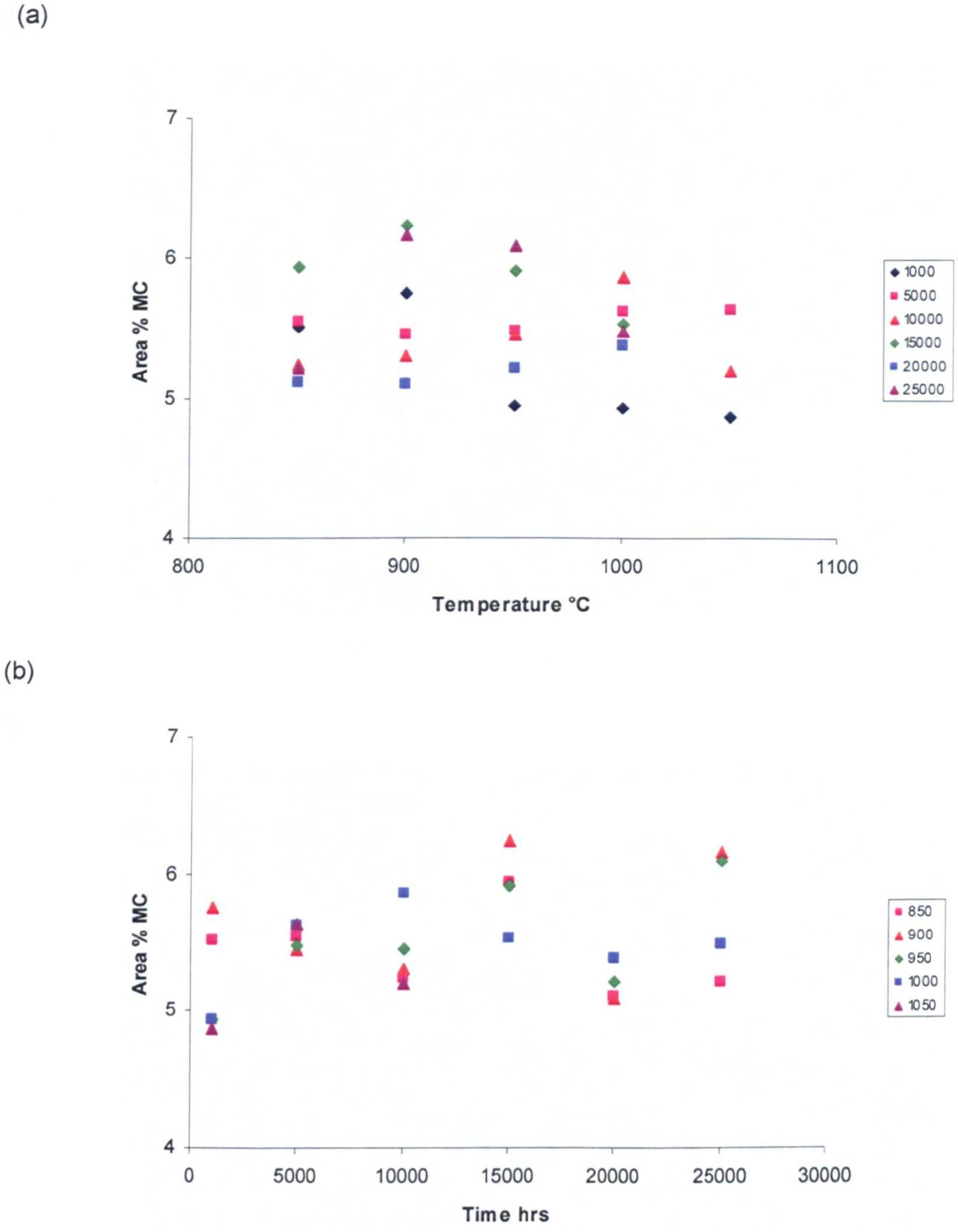

Figure 6.26 MAR M509 image analysis area % MC carbide plotted as a function of (a) temperature and (b) time.

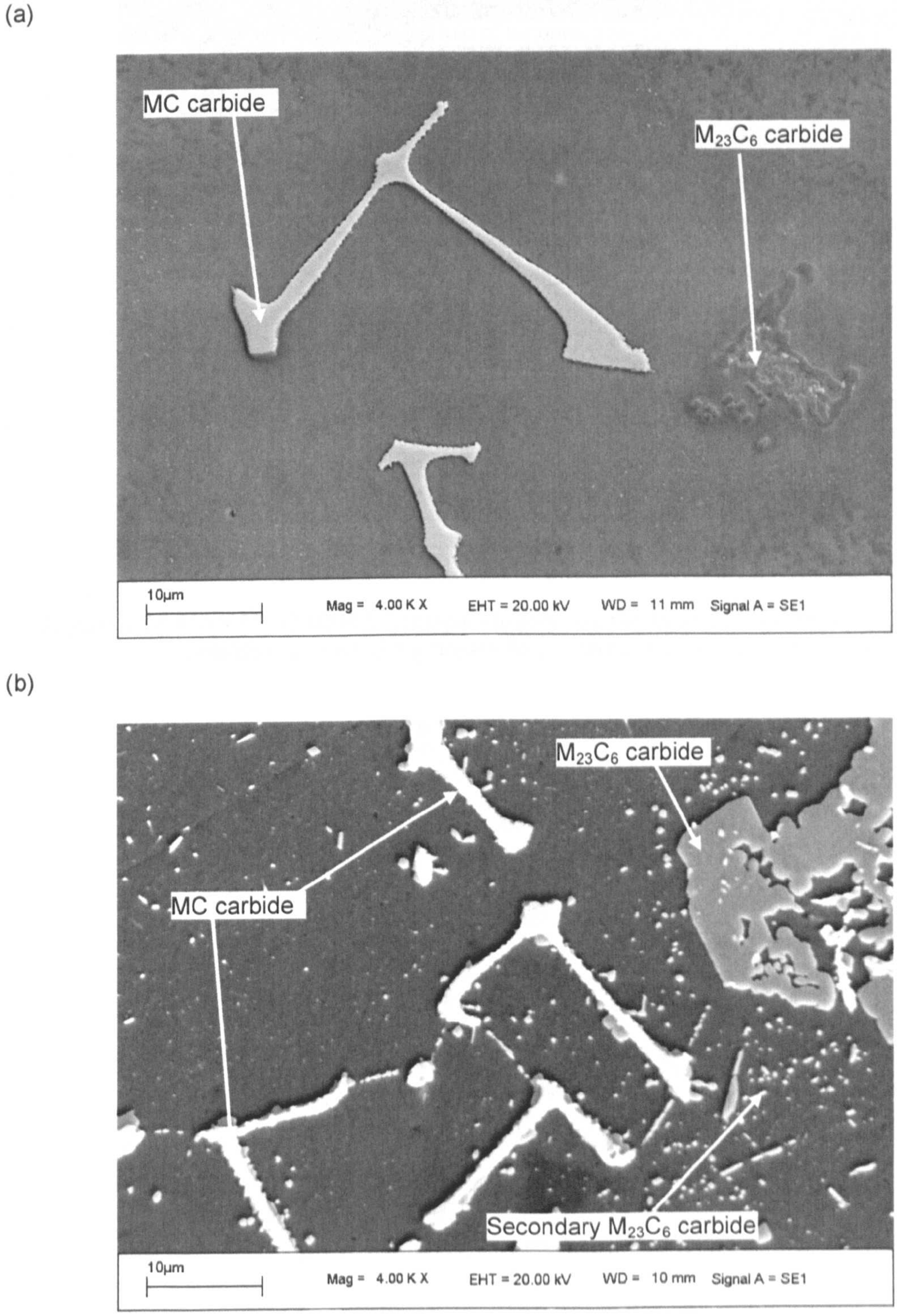

Figure 6.27 MAR M509 SEM SE images showing MC carbides in (a) as-cast sample and (b) 950°C 25,000 hour sample.

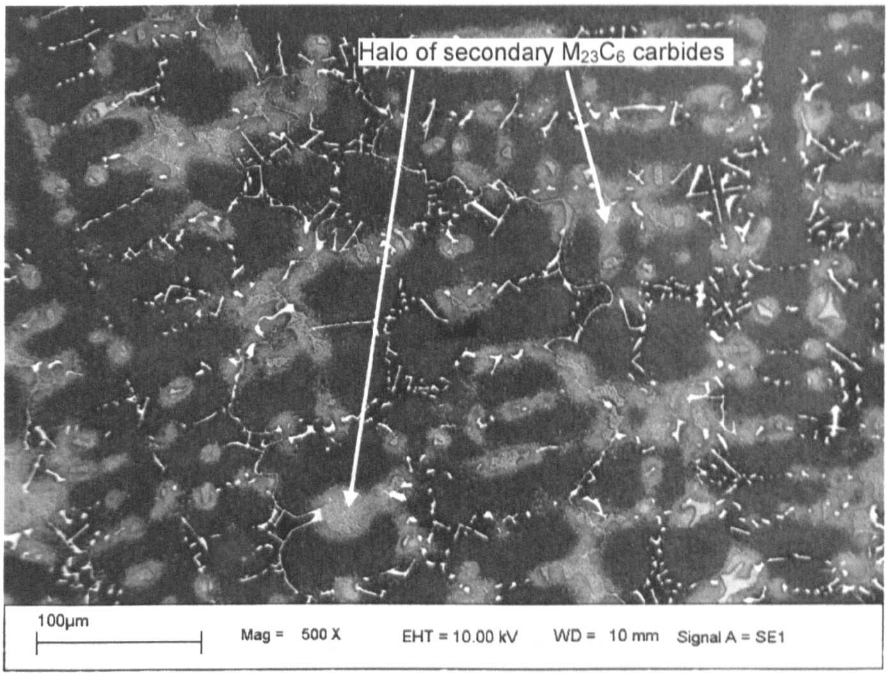

Figure 6.28 MAR M509 SEM SE image illustrating the halo of secondary $M_{23}C_6$ carbides around the primary $M_{23}C_6$ carbides 850°C 5,000 hour sample.

6.7 Hardness

Figure 6.29 shows plots of hardness against time and ageing temperature for the aged samples. The results show a drop in hardness with ageing temperature from ~365 to ~330 Hv_{20} with a maximum variation between samples at the ageing temperatures of ~15 Hv_{20} The hardness results plotted against time show at 1,000 hours a significant variation in hardness with ageing temperature with the 850°C sample at 385 Hv_{20} and the 1050°C sample at 330 Hv_{20}. The 850-1000°C samples show an increase in hardness from 1,000 to 2,000 hours followed by a drop in hardness from 2,000 hours to 15,000 hours. As the hardness drops the difference in hardness between samples, at the ageing temperatures, reduces. From 15,000 hours to 25,000 hours the overall hardness remains relatively constant with a continuing reduction in the hardness between the samples. The 1050°C sample shows a small increase in hardness with time from 1,000 to 15,000 hours.

Figure 6.30 shows the current hardness results and a plot taken from Drapier et al(62). The initial as-cast hardness ~350 Hv_{20} for the current sample is higher than the 330 Hv_{20} of the Drapier samples, indicating the wide range in hardness that may occur as a result of variations in casting conditions.. For the aged samples both plots show a similar range of hardness values at 1,000 hours. The Drapier hardness plot shows an increasing level of hardness for the 800°C samples with the hardness of the 900, 950 and 1100°C samples dropping. The current results show an initial increase in hardness at 2,000 hours which then falls to the 1,000 hour values at 5,000 and 10,000 hours. The 1050°C sample shows the initial rise evident in the lower ageing temperature samples, but then remains constant at the higher hardness.

A microhardness survey of the matrix was carried out on polished and etched samples, the results are shown graphically in Figure 6.31. Positioning of the micro-hardness indenter was carried out at a magnification of 400 times. At this magnification areas of matrix clear of primary and secondary carbides could be identified. The results with temperature show a wide variation in the micro-hardness with the 850°C samples showing a maximum hardness at 5,000 hours of ~375 $Hv_{0.5}$ and a minimum hardness of ~300 $Hv_{0.5}$ in the 20,000 hour sample. The results for the 850-950°C samples show an increase in hardness from 1,000 hour to 5,000 hours followed by a small drop to 10,000 hours with a larger drop to the 15,000 and 20,000 hour samples. The 1,000 hour samples have a relatively constant hardness across the range of ageing temperatures. However, the remaining samples all show a drop in hardness between the 950°C samples and the 1000°C samples. The only optical change evident between the 950°C and the 1000°C sample (Table 6.1) is the reduction in the secondary $M_{23}C_6$ carbides. It is not clear why this would affect the micro-hardness of the matrix. The plot of micro-hardness with time shows a drop in hardness from 1,000 hours to 15,000 hours with a recovery to the original 1,000 hour hardness at 25,000 hour.

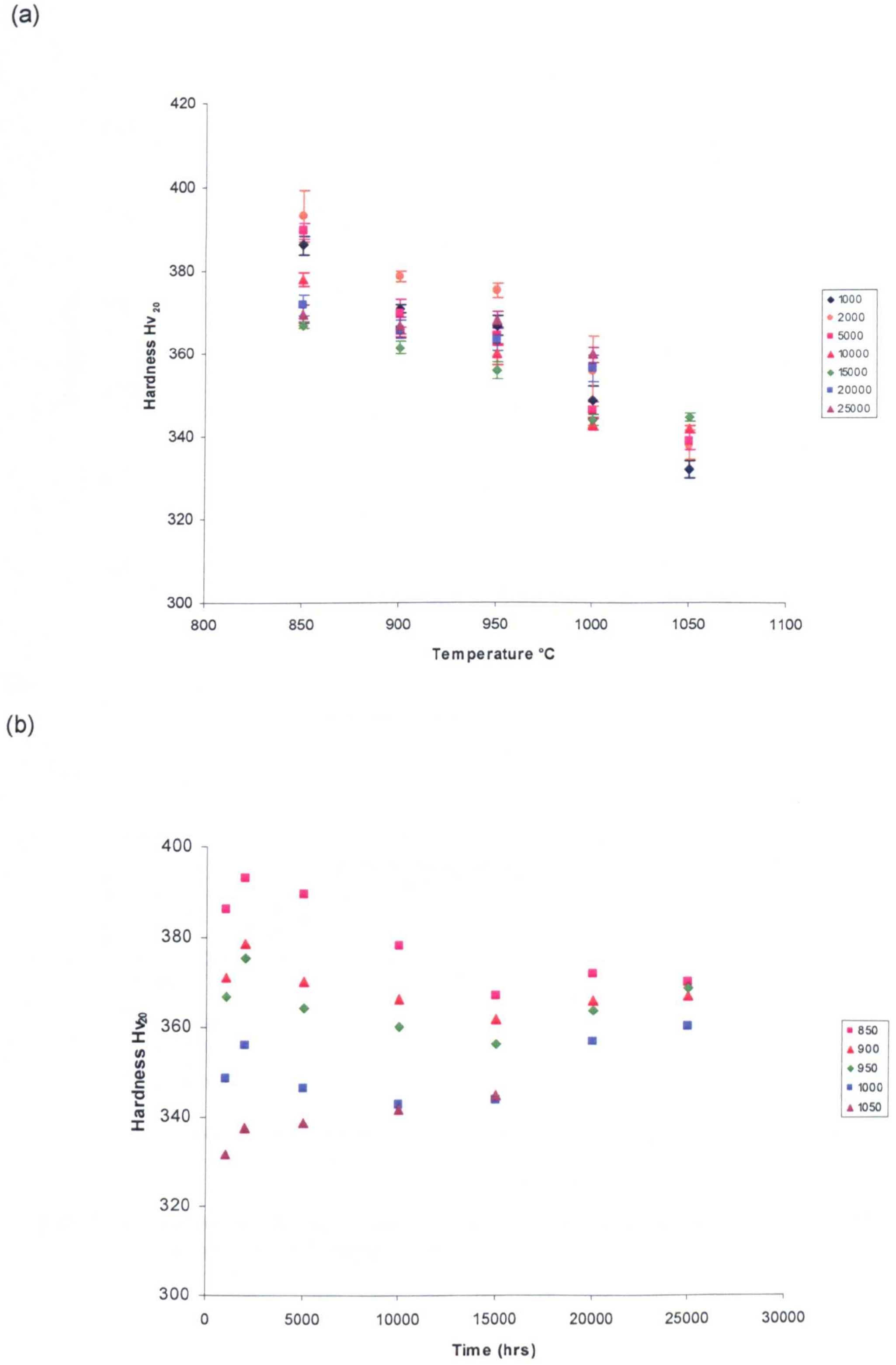

Figure 6.29 **MAR M509 aged samples Vickers hardness plotted as a function of (a) temperature (b) time.**

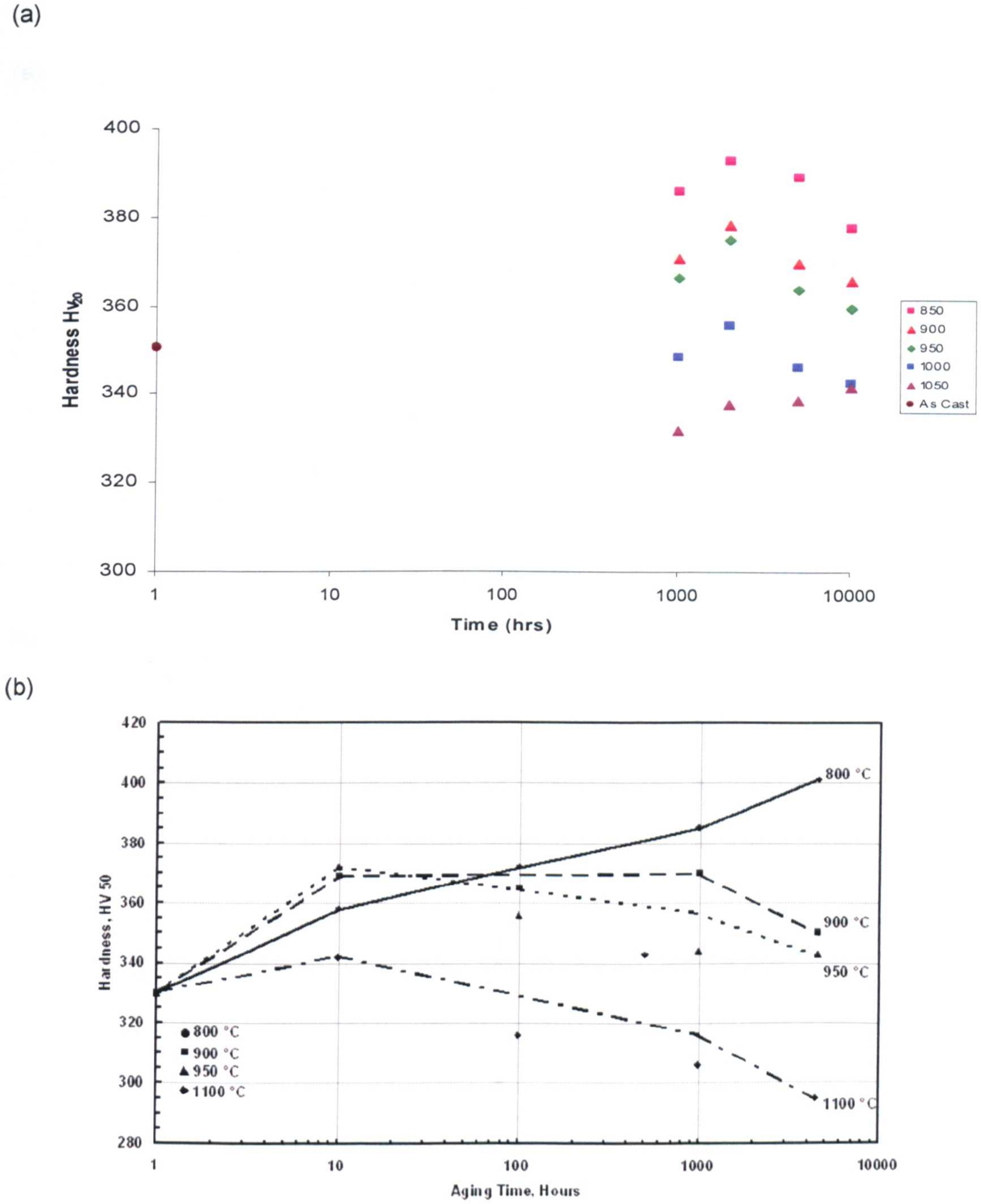

Figure 6.30 MAR M509 Hardness vs. time for the (a) aged samples (b) and similar graph from Drapier et al$^{(62)}$.

(a)

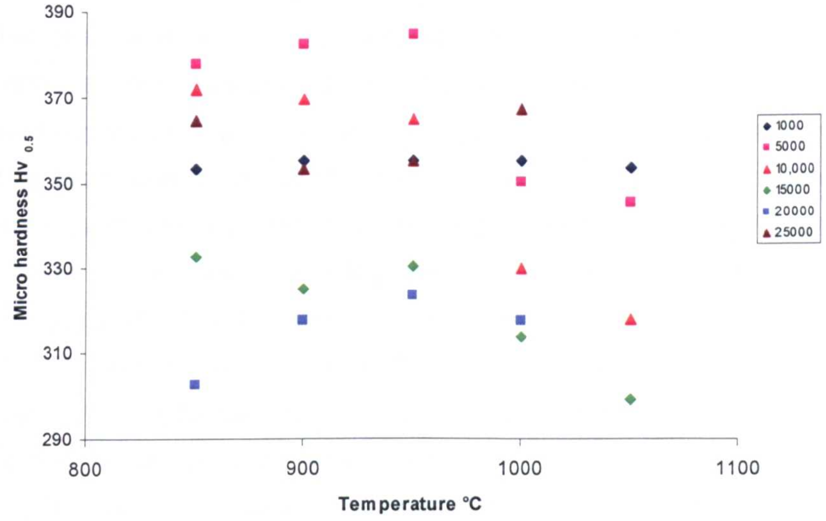

(b)

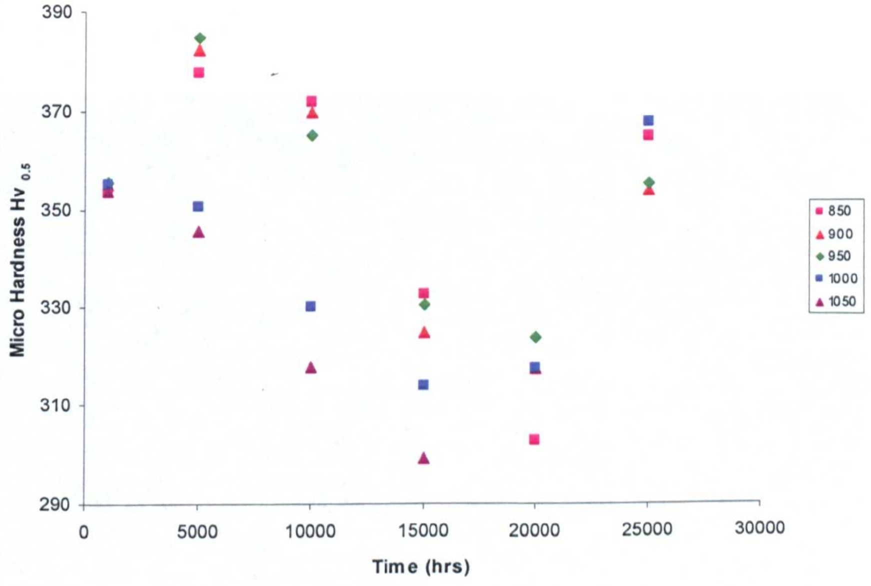

Figure 6.31 MAR M509 matrix micro-hardness results from the aged samples plotted as a function of (a) temperature and (b) time.

6.8 Denuded Layer

Figure 6.32 illustrates the denuded/oxidised layer formed on the exposed surfaces of the aged samples as a result of the oxidation of the carbides. Twenty measurements of the width of the denuded layer were taken along the sample. For the purpose of this investigation the width of the denuded layer was considered to be the distance from the outer surface to the first un-oxidised carbide (primary or secondary). Figure 6.33 is a plot of width of the oxidised layer evident on the exposed surface of the sample against temperature and time. The plots show a correlation with time which would allow the prediction of an operating temperature for an uncoated vane with a known operating history. However, the samples were held at a constant temperature with a very small of number cooling events. It was evident from the oxide scale in the furnace that spalling of the oxide occurred at temperature. In addition, violent spalling of the oxide occurred on cooling the samples to room temperature. The primary oxide that forms on cobalt superalloys is Cr_2O_3. To form this oxide chromium is required from the substrate resulting in preferential oxidation of the chromium rich carbides. Clearly, the more the oxide spalls, the wider the denuded/oxidised layer. Further work would be required to determine the effects of thermal cycling and composition of the substrate on the width of the denuded layer.

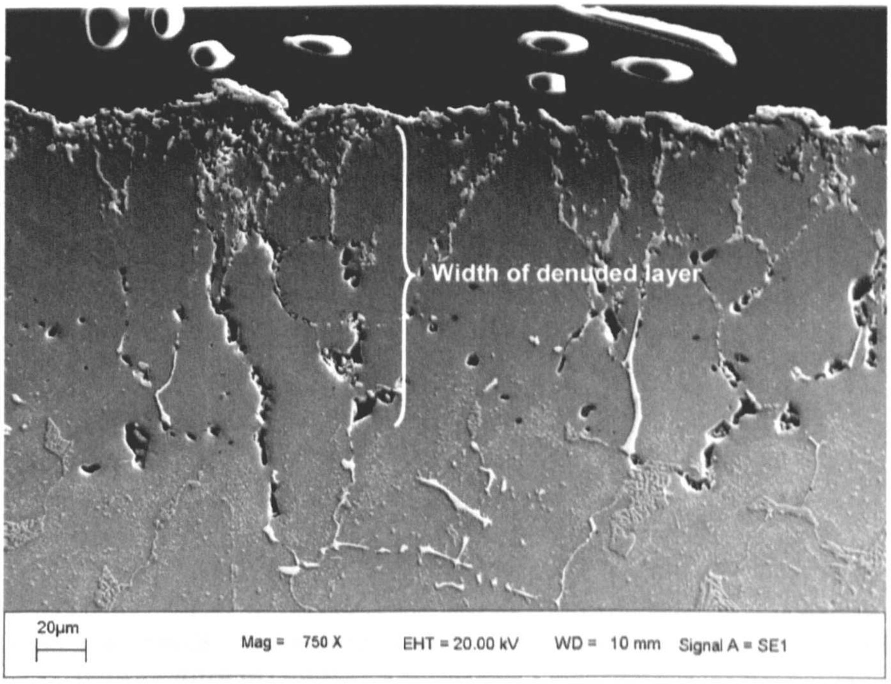

Figure 6.32 MAR M509 SEM SE image showing denuded/oxidised layer formed on the outer surface of the 850°C 25,000 hour sample.

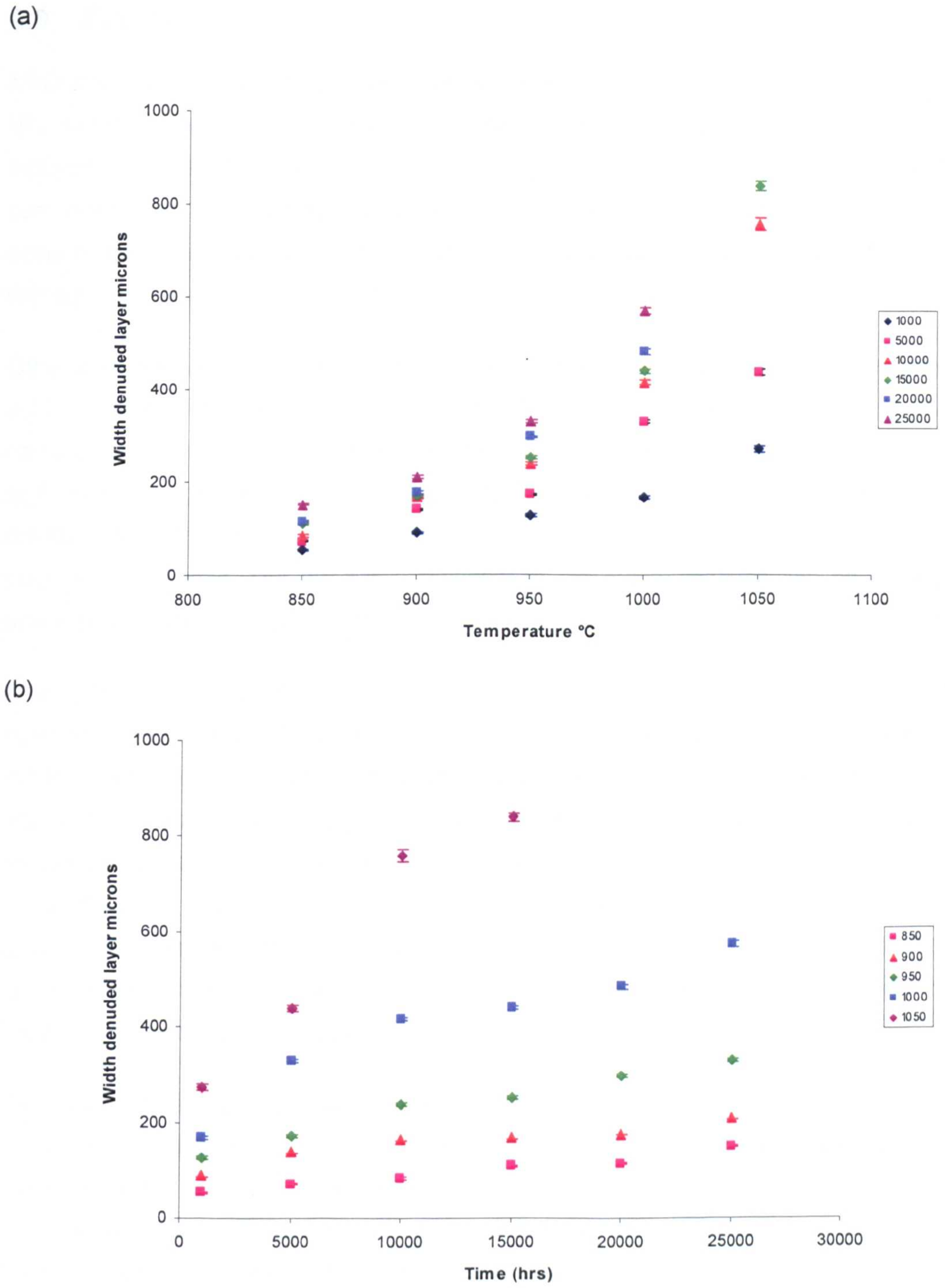

Figure 6.33 **MAR M509 aged samples width of denuded layer plotted against (a) temperature (b) time.**

6.9 Summary

XRD and EDS/WDS confirmed the carbides present in the aged samples are tantalum rich MC carbides and chromium rich eutectic $M_{23}C_6$ carbides. The MC carbides are primarily tantalum carbides but also contained zirconium, tungsten and titanium and the metallic component can be expressed as approximately $Ta_{53}Zr_{18}Ti_{12}Cr_8Co_8W_3$ (where the subscript describes the concentration in at.%). The carbide composition showed no significant changes with ageing time or temperature.

Other than the zirconium level, the EDS/WDS analysis was in reasonable agreement with the JMatPro predictions for MC carbide. The $M_{23}C_6$ eutectic carbides were primarily chromium carbides but also contained tungsten, cobalt and nickel, and the levels determined showed no significant changes with ageing time or temperature. The EDS analysis and the JMatPro predictions for the $M_{23}C_6$ eutectic carbides are similar, other than small differences in the tungsten and cobalt. The metallic component of the $M_{23}C_6$ carbides can be expressed as approximately $Cr_{82}Co_{10}W_5Ni_3$ (where the subscript describes the concentration in at.%).

A tungsten rich M_6C carbide was evident in the $M_{23}C_6$ eutectic carbides in all of the samples aged at 850°C and 900°C for times up to 25,000 hours. At 950°C the level of M_6C carbide reduced with increasing ageing time and could not be found in the samples after 15,000 hours, as increased levels of a tantalum rich phase precipitated in the $M_{23}C_6$ eutectic carbides. Electron diffraction identified the tantalum rich phase as tantalum carbide (MC). Other than the presence of M_6C phase in the eutectic carbides, which may not be an equilibrium phase, the results show that JMatPro using the nickel superalloy database has produced reasonable predictions of the equilibrium phases that would form in MAR M509 and the chemical composition of those phases.

An attempt to identify any changes in the volume fraction of the MC carbides and the $M_{23}C_6$ carbides using the peak area and peak heights of the XRD traces showed only a small increase in the ratio with time. Image analysis of the MC carbides showed no significant change with time or temperature. Image analysis of the $M_{23}C_6$ carbide was not carried out as a clear difference between the matrix and the carbide could not be achieved. However, it is considered that image analysis of the secondary $M_{23}C_6$ carbides may provide a correlation with time and temperature.

Measured Vickers and micro-hardness levels dropped from 365-390 Hv_{20} at 850°C to 332-344 Hv_{20} at 1050°C with ageing temperature but varied by less than 20 Hv_{20} with ageing time. The Vickers hardness levels measured were in reasonable agreement with those measured by Drapier et al(62) and showed a similar trend with time. The results from the tests show no significant variations that would allow the prediction of time and temperature.

The results from the denuded layer formed as a result of the oxidation of the exposed surfaces of the samples would provide a method of prediction ageing time and or temperature from uncoated components taken out of service. However, further work is required to determine the effect of thermal cycling and bulk composition of the component on the width of the denuded layer.

The results of all of the tests carried indicate that MAR M509 is a very stable material. However, it may be possible to make an assessment of ageing temperature based on the coarsening of the secondary $M_{23}C_6$ carbides which precipitate around the primary MC and $M_{23}C_6$ eutectic carbides.

7 Characterisation and discussion of NiCoCrAlTaY Coating on MAR M509

Higher turbine inlet temperatures have lead to the increased use of thermal barrier coatings on turbine components. A thermal barrier coatings (TBC) is formed from two layers; a metallic inner layer, the bond coat (BC) and an outer ceramic insulating layer. The purpose of the bond coat is to improve the adhesion of the ceramic coat to the substrate and prevent oxidation of the substrate, as the ceramic coating, typically yttria stabilised zirconia conducts oxygen. In service, a thermally grown oxide (TGO) develops between the bond coat and the top coat.

Both the method of application and the composition of the coatings vary from one supplier to another. In most commercial coatings, the main phases present are γ(Ni) and β(NiAl) although there are some γ′/β coatings. Depending on the composition and service temperature additional phases including γ′(Ni_3Al), α(Cr), σ(CoCr) and yttrium rich phases may be present. The microstructure and the nature of the interfaces therefore play a critical role in determining the life of turbine hot gas path components.

Mould reactivity or Intercarbidic Oxidation (ICO) is a problem with MAR M509 particularly in thick sections. 'ICO' is evident as particles of ZrO_2 close to the surface of the casting. 'ICO' is thought to be detrimental to the performance of a component since the oxidised carbide could act as a crack initiator at the grain boundaries, and because it can lead to poor coatability for both diffusion and overlay coatings.

This chapter presents and discusses the results of experimental work carried out on coated samples of MAR M509, with and without intercarbidic oxidation (ICO), focusing on; the phase changes within the coating, the interaction between the coating and the substrate, and the effect of 'ICO' on coating life. Samples were examined in both the as-received condition and the aged condition at temperatures between 800 and 1000°C for various times up to 25,000 hours as detailed in Chapter 3. The chemical composition of the coating and the substrate are given in Table 3.1 and Table 3.3 respectively. The results of thermodynamic equilibrium calculations on the coating materials are also presented and compared with experimental data.

7.1 Coating Characterisation

The starting point for the experimental investigation was to examine in detail the composition and morphology of the phases present in the coating both initially and as a function of ageing time and temperature. The identification of the coating phases was initially based on EDS chemical composition measurements and comparison with representative compositions found in the literature. Subsequent transmission electron microscopy (TEM) of samples and the analysis of electron diffraction patterns has confirmed, in part, the initial assumptions (see section 7.4).

The appearance of the coating phases in the scanning electron microscope (SEM), backscatter (BSE) mode, are detailed in Table 7.1. It should be noted that the shades are relative and subjective; the actual shades may vary depending on the SEM operating conditions, but are given as a guide to phase identification.

Phase	**Description**	**BSE (polished)**
Coating		
Gamma (γ)	Ni	Grey
Gamma Prime (γ′)	$Ni_3(Al,Ti)$	Light grey
Beta (β)	NiAl	Dark grey
Alpha-Cr (αCr)	Cr	Dark grey/black
TaC	MC	White
Yttria	Y-rich	Dark grey at coating/substrate interface
Substrate		
Gamma (γ)	Co	Grey
$Cr_{23}C_6$	$M_{23}C_6$	Blocky grey
TaC	MC	White

Table 7.1 Common coating/substrate phases and their appearance in SEM BSE mode.

7.1.1 Coating microstructure as-received

In the as-received samples, following the 1000°C diffusion heat treatment, the BSE images (Figure 7.1) show three phases in the bulk coating: γ (~4 wt.% Al), β (~18 wt.% Al) and a fine white phase typically less than 0.5 µm in size. The small size of the white phase prevented the determination of a quantitative analysis. However, EDS analysis of the phase indicated a high aluminium level of ~10 wt.%. The white phase was not evident in the layer adjacent to the substrate, although both γ and β were present together with a tantalum rich phase which decorated the interface between the coating and the MAR M509 substrate (Figure 7.2). No additional phases other than tantalum rich MC carbides and chromium rich $M_{23}C_6$ carbides were present in the MAR M509 local to the interface.

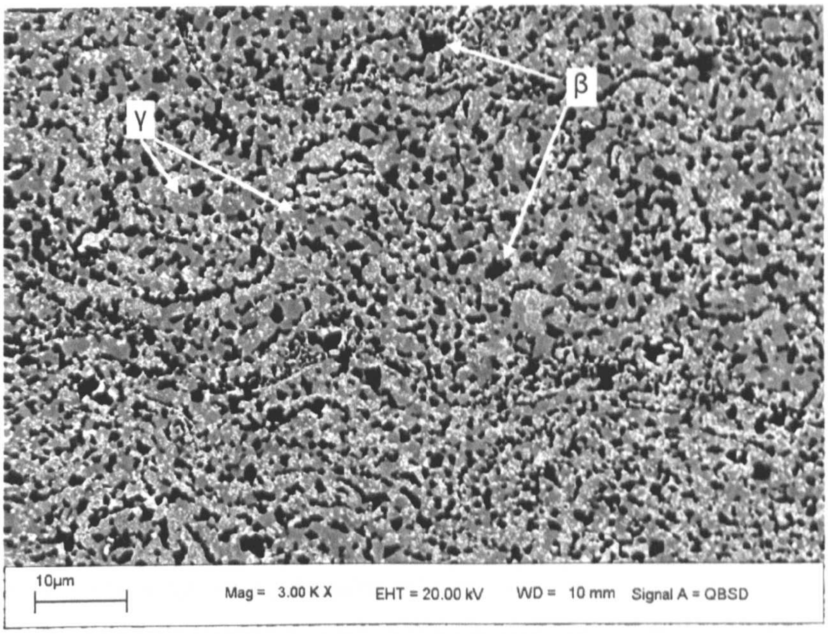

Figure 7.1 **SEM BSE image of bulk Amdry 997 coating microstructure after diffusion heat treatment prior to ageing.**

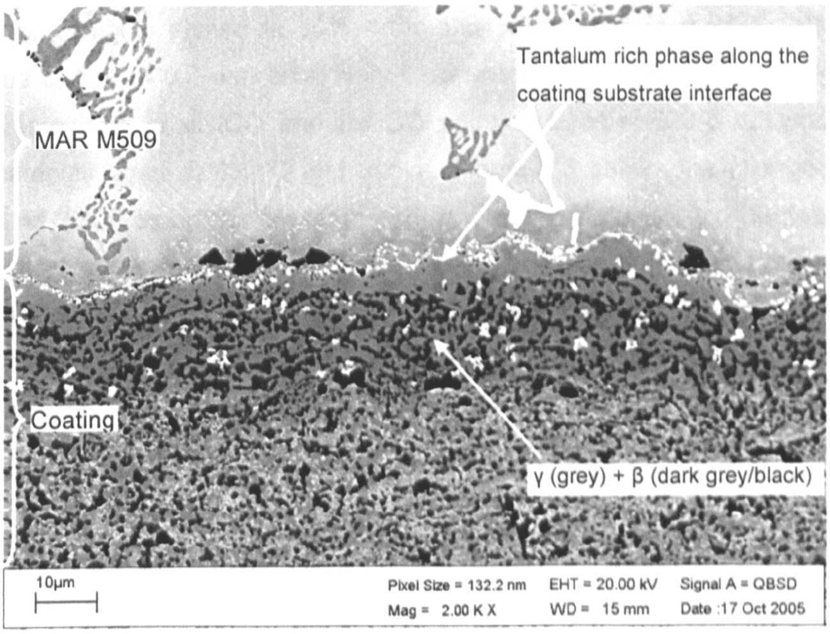

Figure 7.2 **SEM BSE image of Amdry 997 coating/MAR M509 interface and inner layer after diffusion heat treatment prior to ageing showing γ, β and tantalum rich phase.**

7.1.2 Coating microstructure samples aged at 800 - 850°C

The coatings on the aged 800°C and 850°C samples were similar to each other with only minor differences between the 'ICO' and 'no ICO' samples. No inner or outer denuded layers were noted on any of the 'no ICO' samples for ageing times up to 25,000 hours. An intermittent inner denuded layer was evident on the 850°C 15,000 hour 'ICO' sample with a continuous inner denuded layer present on the 20,000 hour and 25,000 hour 'ICO' samples.

The phases present in the bulk of the coating were γ, γ′, β and a chromium rich phase. The levels of the chromium rich phase in the coating increased with both time and temperature. β was evident in all of the 800°C 'no ICO' samples up to 25,000 hours but was not detected in the 'ICO' samples beyond 10,000 hours. At 850°C β was found in the 'no ICO' samples up to 15,000 hours but was not found in the ICO samples for ageing times greater than 5,000 hours. The tantalum carbide phase found in the as-received samples was not found in any of the samples other than the 1,000 hour 800°C samples. The small white particles observed in the as-received samples were no longer evident in the samples aged for 2,000 hours and above, where the light grey γ′ (8 wt.% Al) became more evident. γ′ and the chromium rich phase were the principal phases in the coating adjacent to the fusion boundary with the chromium rich phase the principal phase at the boundary. An yttrium rich phase was evident at the interface in both the 'ICO' and 'no ICO' samples at times above 2,000 hours at 850°C. This phase was evident as small discrete groups, of ~1 μm particles in general, but not exclusively, associated with oxide particles at the interface between the coating and the MAR M509 substrate. In the inter-diffusion zone the phases present were γ, γ′ and blocky $M_{23}C_6$ carbide.

Examination of samples etched in 10% ortho-phosphoric acid in a FEG SEM showed at 800°C clusters of fine (< 0.3 μm) secondary γ′ between the larger γ′ phase (Figure 7.3 (a)). The fine γ′ was evident in all 'ICO' and 'no ICO' samples aged at 800°C but was not found in any of the samples aged at 850°C and above. Figure 7.3 shows the changes in γ′ in the 5,000 hour 'no ICO' sample with temperature. An investigation by Baufeld et al(87) of microstructural changes in heat treated samples of a NiCoCrAlY coating on a directional solidified IN 100 substrate confirmed, by TEM electron diffraction patterns, that fine spherical precipitates in the γ phase in both the diffusion zone and the NiCoCrAlY coating were the γ′ phase. The investigation showed that the precipitates were evident in samples aged for 24 hours and subsequently water quenched from temperatures between 840 and 970°C and in slowly cooled samples aged for 24 hours at 1100°C.

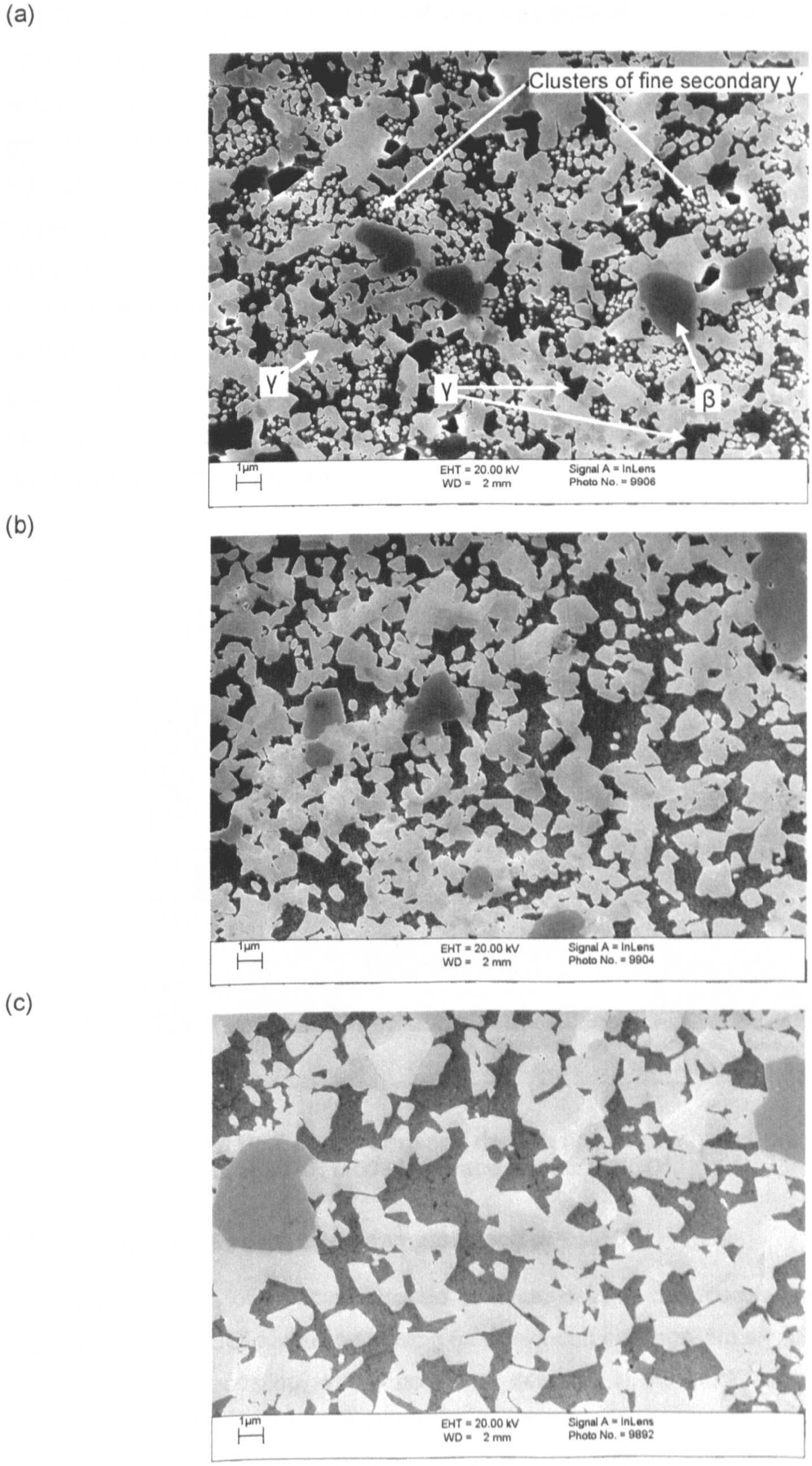

Figure 7.3 FEG SEM SE images from Amdry 997 coating showing growth of secondary γ´ in 5,000 hour sample (a) secondary γ´ at 800°C (b) coalescing γ´ at 850°C and (c) γ´ at 900°C respectively.

7.1.3 Coating microstructure samples aged at 900°C

At 900°C an intermittent inner denuded layer was evident on all the samples with 'ICO' up to 10,000 hours, with a continuous denuded layer on samples aged for 15,000 hours and longer. At the lower ageing times it was evident that the denuded layer was forming in the coating at positions local to the 'ICO' phase in the MAR M509 substrate (Figure 7.4).The samples with 'no ICO' showed an intermittent denuded layer at 15,000 hours with a continuous layer forming at ageing times above 20,000 hours. Within the bulk coating the levels of the chromium rich phase increased with time and the levels of β decreased with time until β was no longer detected. In the samples with 'no ICO', β was not detected in the samples beyond 10,000 hours and in the 'ICO' samples, at times up to 5,000 hours. γ, γ', the chromium rich phase and the yttrium rich phase were evident at the interface in all of the 'ICO' and 'no ICO' samples. In the inter-diffusion zone, the only phase present in all of the samples was blocky $M_{23}C_6$ carbide and the γ matrix.

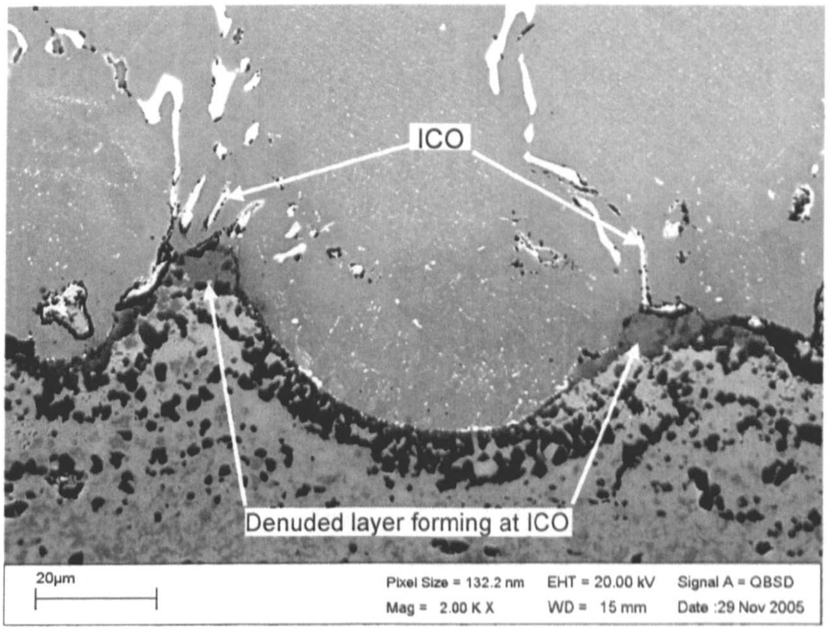

Figure 7.4 SEM BSE image showing denudation of coating at the Amdry 997 coating/MAR M509 interface opposite 'ICO'.

7.1.4 Coating microstructure samples aged at 950°C

At 950°C both sets of samples showed continuous inner denuded layers, with the 20,000 hours and above 'ICO' samples showing fully denuded coatings. No significant changes were evident in the bulk coating, with β no longer detected in the 'ICO' samples aged for times greater than 2,000 hours and in the 'no ICO' samples for ageing times greater than 10,000 hours. All of the 'ICO' and 'no ICO' samples showed tantalum carbide along with a chromium rich phase in the inner denuded layer and tantalum carbide along with the yttrium rich phase along the interface. In the interdiffusion zone the only phase present was blocky $M_{23}C_6$ carbide and the γ matrix.

7.1.5 Coating microstructure samples aged at 1000°C

At 1000°C all of the samples showed inner and outer denuded layers. The 'ICO' 1,000 hour and 2,000 hour samples and the 'no ICO' 1,000, 2,000 and 5,000 hour samples showed within the coating two distinct layers in addition to the inner and outer denuded layers (Figure 7.5). Adjacent to the outer denuded layer is a layer containing γ, γ´ and a chromium rich phase. Between this layer and the inner denuded layer is a second layer containing γ, β, a chromium rich phase and TaC. The 'ICO' samples aged for times longer than 5,000 hours were fully denuded. The phases present in the coating of the fully denuded samples were γ and TaC. None of the 'no ICO' samples up to 15,000 hours were fully denuded, howeve,r the layer of γ´ phase present in the coating of the 10,000 hour sample was very thin and at 15,000 hours was intermittent. The yttrium rich phase was evident at the interface in all of the 'ICO' and 'no ICO' samples (Figure 7.6). In the interdiffusion zone the only phase present was $M_{23}C_6$ carbide and the γ matrix.

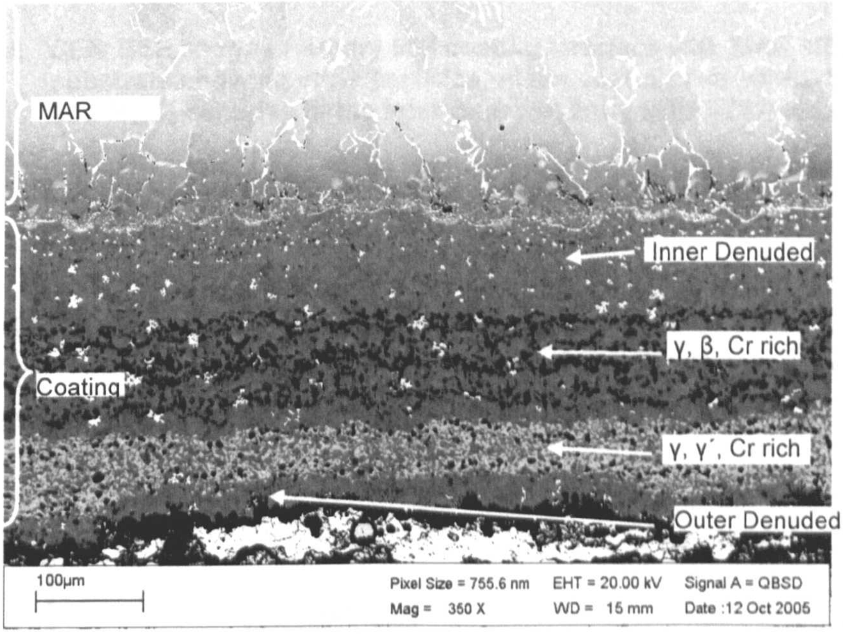

Figure 7.5 SEM BSE image showing Amdry 997 coating γ´ layer, β layer, inner and outer denuded layers 1000°C 2,000 hour 'ICO' sample.

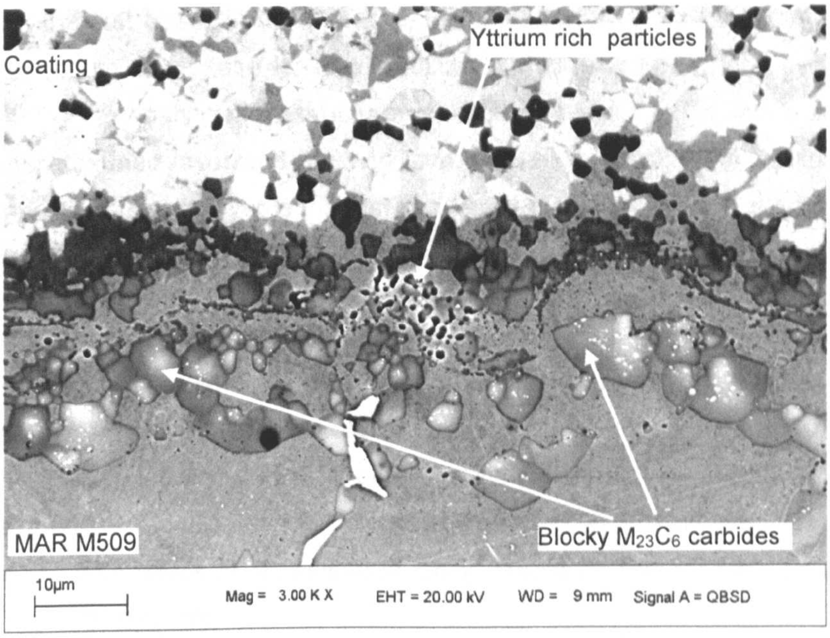

Figure 7.6 SEM BSE image of Amdry 997 coating interface with MAR M509 substrate showing yttria particles on the coating side of the interface and $M_{23}C_6$ carbides in the inter diffusion zone 950°C 25,000 hour sample.

The results of the ageing trials show, in very broad terms, the degradation of the coating occurs as follows:

Ageing temperature 800 - 950°C

	Bulk	Inner denuded
Initial coating	γ β (γ′ minor)	
Increasing time/temp	γ γ′↑ β↓ Cr rich↑	
↓	γ γ′↓ Cr rich	γ Cr rich
	γ Cr rich↓ TaC	γ Cr rich TaC
Fully denuded	γ TaC	γ TaC

Ageing temperature 1000°C

Initial coating	γ β (γ′ minor)	
Increasing time/temp		
↓	γ γ′↓ Cr rich↑ TaC and γ β↓ Cr rich↑ TaC	γ Cr rich TaC
	γ γ′↓ Cr rich↓TaC	γ Cr rich TaC
Fully denuded	γ TaC	γ TaC

The results indicate at temperatures from 800-950°C initially as β goes into solution, γ′ and a chromium rich phase (not evident in the original microstructure) initiate/grow. As ageing continues, β is the first phase to disappeared, this is followed by the loss of γ′ and then the loss of the chromium rich phase leaving tantalum carbide the last phase evident in the γ matrix. At 1000°C the coating microstructure developed as two distinct layers a γ′ rich layer below the outer denuded layer and a β rich layer with no γ′ adjacent to the inner denuded layer. The inner β rich phase layer is the first to disappear followed by the γ′ rich layer leaving tantalum carbide in the γ matrix.

If the absence of β(2) is considered to indicate the end of coating life, then with 'no ICO' present the coating has a useful life in excess of 25,000 hours at temperatures of 800°C or less. At temperatures above 800°C the coating life is reduced from 15,000 to 10,000 hours at 850°C and 900°C respectively. If 'ICO' is present then the coating life is between 10,000 and 15,000 hours at 800°C reducing to 5,000 hours at 850 and 900°C. However, it is possible that as a result of the high levels of aluminium in the γ′ phase (~ 7 wt.%) the loss of β may not indicate the end of coating life.

Table 7.2 and 7.3 detail the phases found in the Amdry 997 coating in the 'no ICO' and 'ICO' samples. Representative SEM micrographs, from the middle of the coating, from the 1,000, 5,000, 15,000 and 25,000 hour samples are shown Figure 7.7 - 7.11 and show more clearly the changes in the microstructure with time and temperature.

Temp		1,000 hrs	2,000 hrs	5,000 hrs	10,000 hrs	15,000 hrs	20,000 hrs	25,000 hrs
800°C	**Outer Denuded**	No denudation	No denudation	No denudation	No denudation	No denudation	No denudation	No denudation
	Bulk	γ, β, Cr rich, white phase < 0.5μm	γ, γ´, β, Cr rich	γ, γ´, β, Cr rich	γ, γ´, β, Cr rich	γ, γ´, β, Cr rich	γ, γ´, β, Cr rich	γ, γ´, β, Cr rich
	Inner layer	γ, γ´ Cr rich	γ, γ´ Cr rich	γ, γ´, Cr rich	γ, γ, Cr rich	γ, γ´, Cr rich	γ, γ´, Cr rich	γ, γ´, Cr rich
	Interface	γ, γ´, Cr rich	γ´, Cr rich, Y	γ´, Cr rich, Y	γ´, Cr rich, Y	γ´, Cr rich, Y	γ´, Cr rich, Y	γ´, Cr rich, Y
	Interdiffusion	$M_{23}C_6$	$M_{23}C_6$, γ´	$M_{23}C_6$, γ´	$M_{23}C_6$, γ´	$M_{23}C_6$, γ´	$M_{23}C_6$, γ´	$M_{23}C_6$, γ´
850°C	**Outer Denuded**	No denudation	No denudation	No denudation	No denudation	No denudation	No denudation	No denudation
	Bulk	γ, γ´, β, Cr rich	γ, γ´, β, Cr rich	γ, γ´, β, Cr rich	γ, γ´, β, Cr rich	γ, γ´, β, Cr rich	γ, γ´ Cr rich	γ, γ´ Cr rich
	Inner layer	γ, γ´, Cr rich	γ, γ´, Cr rich	γ, γ´, Cr rich	γ´, Cr rich	γ´, Cr rich	γ, γ´, Cr rich	γ, γ´, Cr rich
	Interface	γ, γ´, Cr rich, Y	γ, γ´, Cr rich, Y	γ´, Cr rich, Y	γ´, Cr rich, Y	γ´, Cr rich, Y	γ´, Cr rich, Y	γ´, Cr rich, Y
	Interdiffusion	$M_{23}C_6$, γ´	$M_{23}C_6$, γ´	$M_{23}C_6$, γ´	$M_{23}C_6$, γ´	$M_{23}C_6$, γ´	$M_{23}C_6$, γ´	$M_{23}C_6$, γ´
900°C	**Outer Denuded**	No denudation	No denudation	No denudation	No denudation	γ (slight)	γ (slight)	γ (slight)
	Bulk	γ, γ´, β, Cr rich	γ, γ´, β, Cr rich	γ, γ´, β, Cr rich	γ, γ´, β, Cr rich	γ, γ´, Cr rich	γ, γ´, Cr rich	γ, γ´, Cr rich
	Inner layer	γ, γ´, Cr rich	γ, γ´ Cr rich	γ´ Cr rich	γ´, Cr rich	γ, γ', Cr rich	γ, Cr rich	γ, Cr rich
	Interface	γ, γ´, Cr rich, Y	γ, γ´ Cr rich, Y	γ´, Cr rich, Y	γ´, Cr rich, Y	γ, γ', Cr rich, Y Inter denuded	γ, Cr rich, Y	γ, Cr rich, Y
	Interdiffusion	$M_{23}C_6$, γ'	$M_{23}C_6$, γ´	$M_{23}C_6$, γ ´	$M_{23}C_6$, γ´	$M_{23}C_6$,	$M_{23}C_6$	$M_{23}C_6$
950°C	**Outer Denuded**	No denudation	γ (slight)	γ (slight)	γ (slight)	γ, Ta	γ, Ta	γ, Ta
	Bulk	γ, γ´, β, Cr rich	γ, γ´, β, Cr rich,	γ, γ´, β, Cr rich	γ, γ´, β, Cr rich	γ, γ´, Cr rich	γ, γ´, Cr rich	γ, γ´, Cr rich
	Inner layer	γ, Cr rich, Ta	γ, Cr rich, Ta	γ, Cr rich, Ta	γ Cr rich, Ta	γ, Cr rich, Ta	γ, Cr rich,Ta	γ, Cr rich,Ta
	Interface	γ, Ta, Y	γ, Ta, Y	γ, Ta, Y	γ, Ta, Y	γ, Ta, Y	γ, Ta, Y	γ, Ta, Y
	Interdiffusion	$M_{23}C_6$,	$M_{23}C_6$,	$M_{23}C_6$	$M_{23}C_6$	$M_{23}C_6$	$M_{23}C_6$	$M_{23}C_6$
1000°C	**Outer Denuded**	γ, Cr rich, Ta	γ, Cr rich, Ta	γ, Cr rich, Ta	γ, Ta	γ, Ta	No Sample	No Sample
	Bulk	1. γ, γ´ Cr rich 2. γ, β, Cr rich, Ta	1. γ, γ´ Cr rich 2. γ, β, Cr rich, Ta	1. γ, γ´, Cr rich 2. γ, β, Cr rich, Ta	1. γ, γ´, Cr rich, Ta 2. γ, β, Cr rich, Ta (int)	γ, γ´, Cr rich, Ta (int)		
	Inner layer	γ Cr rich, Ta	γ, Cr rich, Ta	γ, Cr rich, Ta	γ, Cr rich, Ta	γ, Cr rich Ta		
	Interface	γ, Ta, Y	γ, Ta, Y	γ, Ta, Y	γ, Ta, Y	γ, Ta, Y		
	Interdiffusion	$M_{23}C_6$	$M_{23}C_6$	$M_{23}C_6$	$M_{23}C_6$	$M_{23}C_6$		

Table 7.2 Amdry 997 coating phases evident in the 'no ICO' samples, table highlighted to show presence of β phase in coating.

ICO		1,000 hrs	2,000 hrs	5,000 hrs	10,000 hrs	15,000 hrs	20,000 hrs	25,000 hrs
800°C	**Outer Denuded**	No denudation	No denudation	No denudation	No denudation	No denudation	No denudation	No denudation
	Bulk	γ, β, Cr rich white phase < 0.5μm	γ, γ´, β, Cr rich,	γ, γ´, β, Cr rich,	γ, γ´, β Cr rich	γ, γ´ Cr rich	γ, γ´,Cr rich	γ, γ´,Cr rich
	Inner layer	γ, γ´, Cr rich,	γ, γ´, Cr rich	γ, γ´, Cr rich,	γ´, Cr rich	γ, γ´, Cr rich	γ´, Cr rich	γ´, Cr rich
	Interface	γ, γ´, Cr rich, Ta	γ, γ´, Cr rich	γ´, Cr rich, Y	γ´, Cr rich, Y	γ´, Cr rich, Y	γ´, Cr rich, Y	γ´, Cr rich, Y
	Interdiffusion	$M_{23}C_6$	$M_{23}C_6$, γ´	$M_{23}C_6$, γ´	$M_{23}C_6$, γ´	$M_{23}C_6$, γ´	$M_{23}C_6$, γ´	$M_{23}C_6$, γ´
850°C	**Outer Denuded**	No denudation	No denudation	No denudation	No denudation	No denudation	No denudation	No denudation
	Bulk	γ, γ´, β, Cr rich	γ, γ´, β, Cr rich	γ, γ´, β, Cr rich	γ, γ´, Cr rich	γ, γ´ Cr rich	γ, γ´, Cr rich	γ, γ´, Cr rich
	Inner layer	γ, γ´, Cr rich	γ, γ´, Cr rich	γ, γ´, Cr rich	γ´, Cr rich	γ, γ´, Cr rich int denuded	γ, Cr rich int denuded	γ, Cr rich int denuded
	Interface	γ, γ´, Cr rich, Y	γ, γ´, Cr rich, Y	γ´, Cr rich, Y	γ´, Cr rich, Y	γ, γ´, Cr rich, Y	γ´, Cr rich, Y	γ´, Cr rich, Y
	Interdiffusion	$M_{23}C_6$, γ´	$M_{23}C_6$, γ´	$M_{23}C_6$, γ´	$M_{23}C_6$	$M_{23}C_6$	$M_{23}C_6$	$M_{23}C_6$
900°C	**Outer Denuded**	No denudation	No denudation	No denudation	γ odd bit	γ	γ, Cr rich, Ta	γ, Cr rich, Ta
	Bulk	γ, γ´, β, Cr rich	γ, γ´, β, Cr rich	γ, γ´, β, Cr rich,	γ, γ´, Cr rich	γ, γ´ Cr rich	γ, γ´ Cr rich	γ, γ´ Cr rich
	Inner layer	γ, γ´, Cr rich	γ, γ´ Cr rich	γ´, Cr rich	γ, γ', Cr rich,	γ, Cr rich	γ, Cr rich	γ, Cr rich
	Interface	γ, γ´ Cr rich, Y Int denudation	γ, γ´, Cr rich, Y Int denudation	γ, γ', Cr rich, Y Int denudation	γ, Cr rich, Y Int denudation	γ, Cr rich Y	γ, Cr rich, Y	γ, Cr rich, Y
	Interdiffusion	$M_{23}C_6$	$M_{23}C_6$	$M_{23}C_6$	$M_{23}C_6$	$M_{23}C_6$,	$M_{23}C_6$	$M_{23}C_6$
950°C	**Outer Denuded**	No denudation	γ (slight)	γ, Ta	γ, Cr rich, Ta	γ, Cr rich, Ta	Fully denuded γ, Ta	Fully denuded γ, Ta
	Bulk	γ, γ´, β, Cr rich	γ, γ´, β, Cr rich,	γ, γ´, Cr rich,	γ, γ´, Cr rich	γ, γ´, Cr rich		
	Inner layer	γ, Cr rich, Ta	γ, Cr rich, Ta	γ, Cr rich, Ta	γ, Cr rich, Ta	γ, Cr rich,Ta		
	Interface	γ, Ta, Y	γ, Ta, Y	γ, Ta, Y	γ, Ta, Y	γ, Ta, Y	γ, Ta, Y	γ, Ta, Y
	Interdiffusion	$M_{23}C_6$	$M_{23}C_6$	$M_{23}C_6$	$M_{23}C_6$	$M_{23}C_6$	$M_{23}C_6$	$M_{23}C_6$
1000°C	**Outer Denuded**	γ Cr rich, Ta	γ, Cr rich, Ta	Fully denuded γ, Ta	Fully denuded γ, Ta	Fully denuded γ, Ta	No sample	No sample
	Bulk	1. γ, γ´, Cr rich, Ta 2. γ, β, Cr rich, Ta	1. γ, γ´, Cr rich, 2. γ, β, Cr rich, Ta					
	Inner layer	γ, Cr rich, Ta	γ, Cr rich, Ta					
	Interface	γ, Ta, Y	γ, Ta, Y	γ, Ta, Y	γ, Ta, Y	γ, Ta, Y		
	Interdiffusion	$M_{23}C_6$	$M_{23}C_6$	$M_{23}C_6$	$M_{23}C_6$	$M_{23}C_6$		

Table 7.3 Amdry 997 coating phases evident in the 'ICO' samples, table highlighted to show presence of β phase in coating.

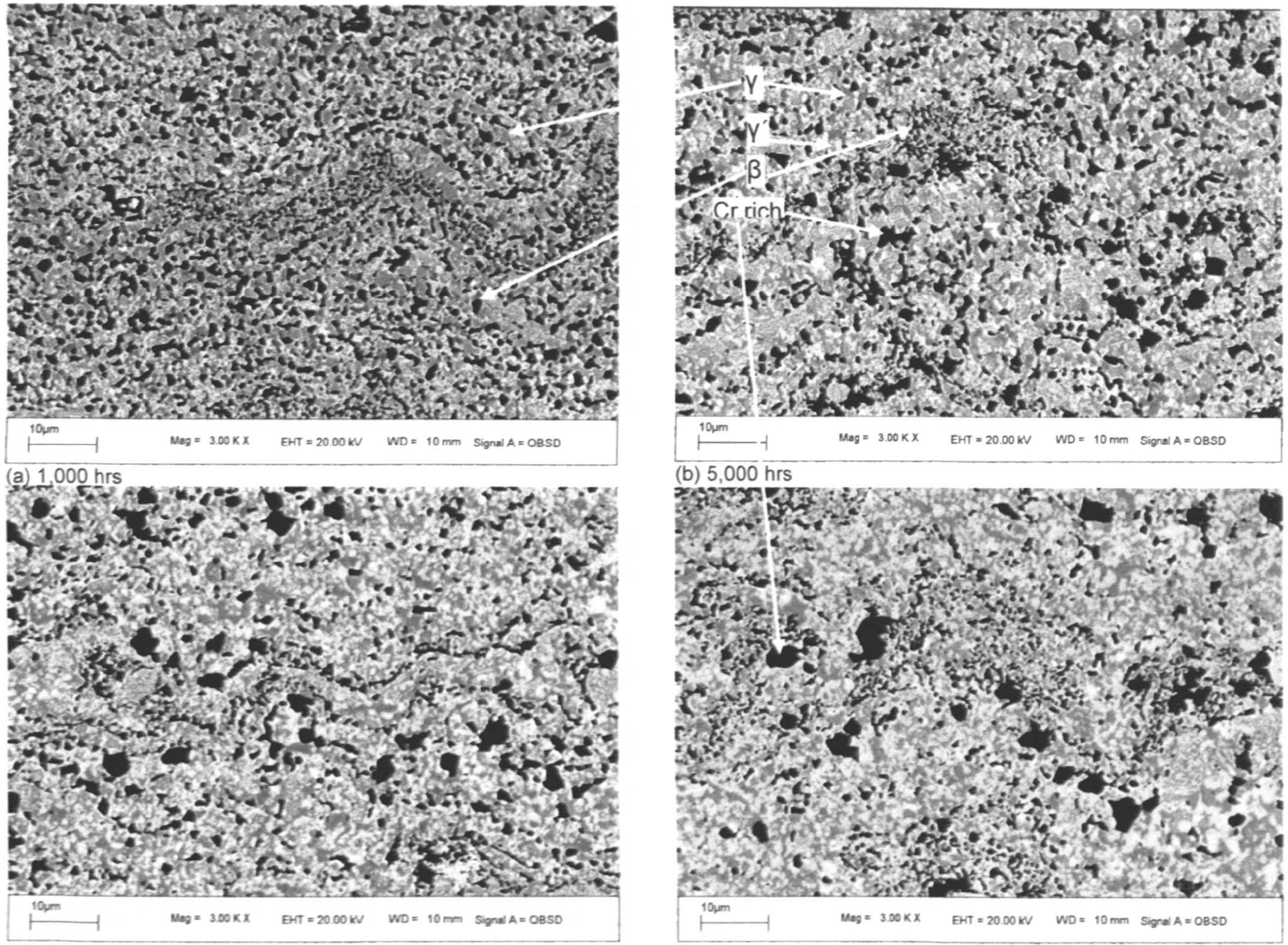

(a) 1,000 hrs

(b) 5,000 hrs

(c) 15,000 hrs

(d)25,000 hrs

Figure 7.7 **Amdry 997 coating SEM BSE images of samples aged at 800°C for (a) 1,000, (b) 5,000, (c) 15,000 and (d) 25,000 hours respectively.**

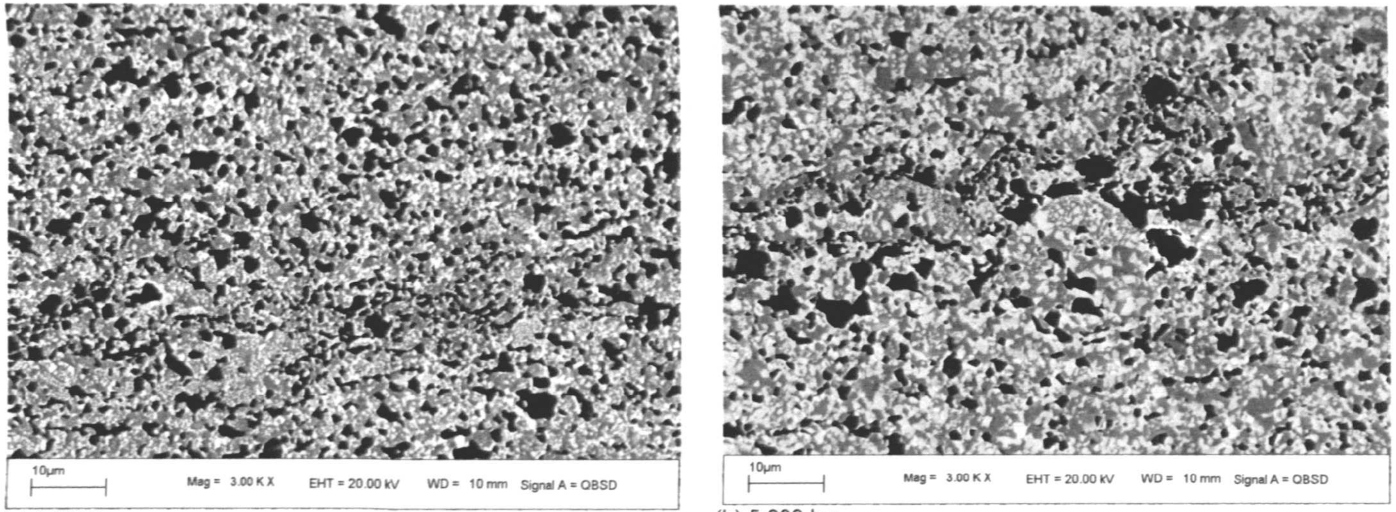

(a) 1,000 hrs (b) 5,000 hrs

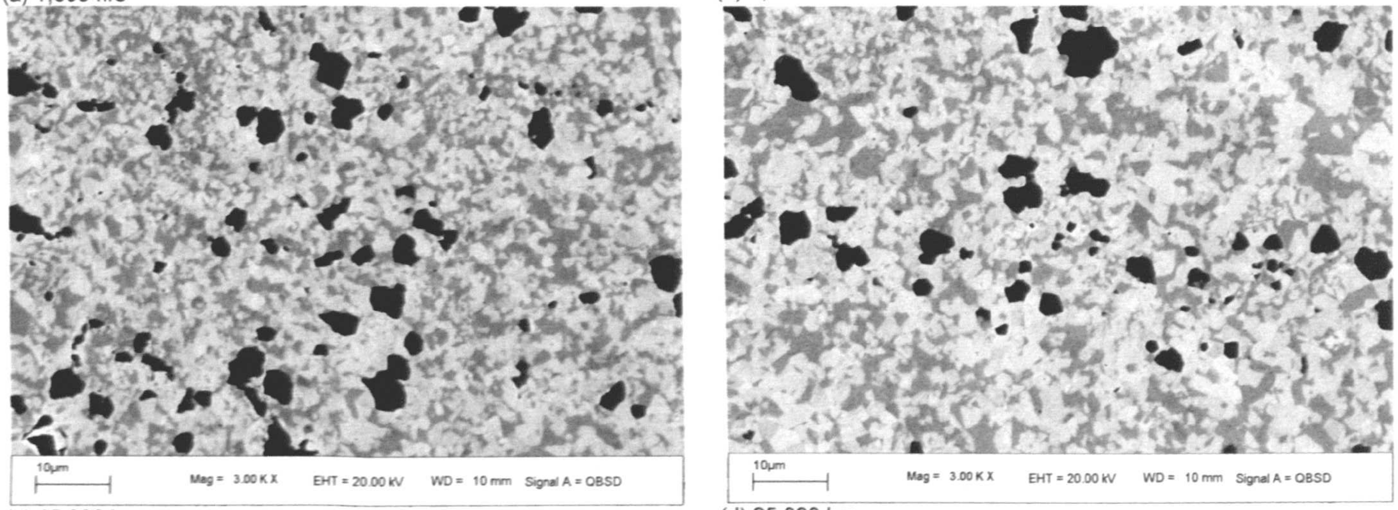

(c) 15,000 hrs (d) 25,000 hrs

Figure 7.8 **Amdry 997 coating SEM BSE images of samples aged at 850°C for (a) 1,000, (b) 5,000, (c) 15,000 and (d) 25,000 hours respectively.**

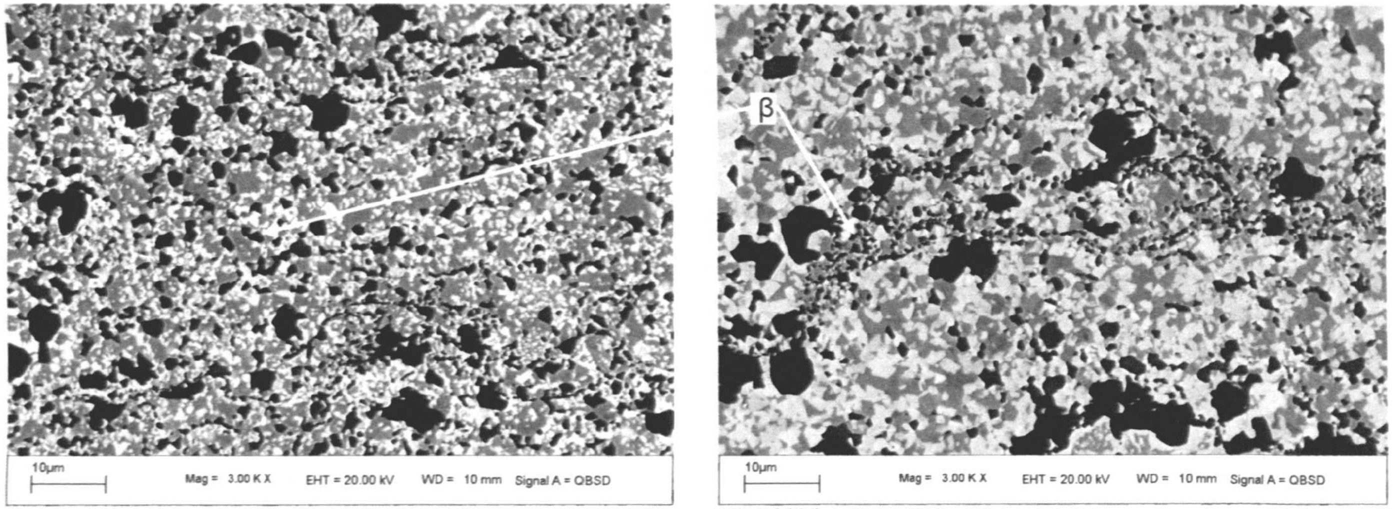

(a) 1,000 hrs

(b) 5,000 hrs

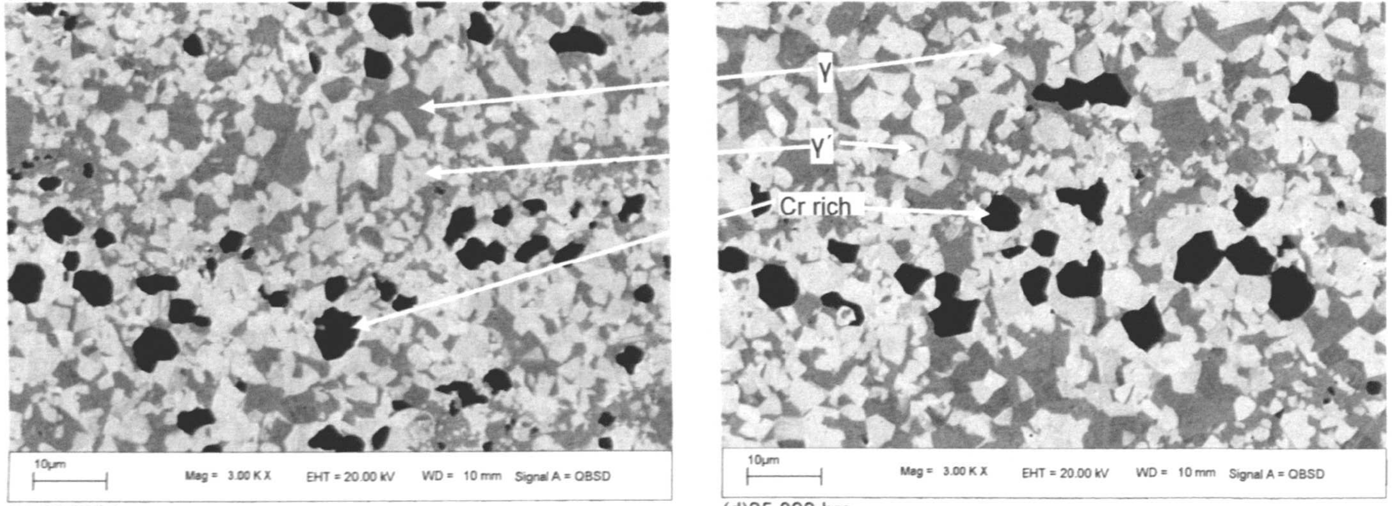

(c) 15,000 hrs

(d)25,000 hrs

Figure 7.9 Amdry 997 coating SEM BSE images of samples at 900°C for (a) 1,000, (b) 5,000, (c) 15,000 and (d) 25,000 hours respectively.

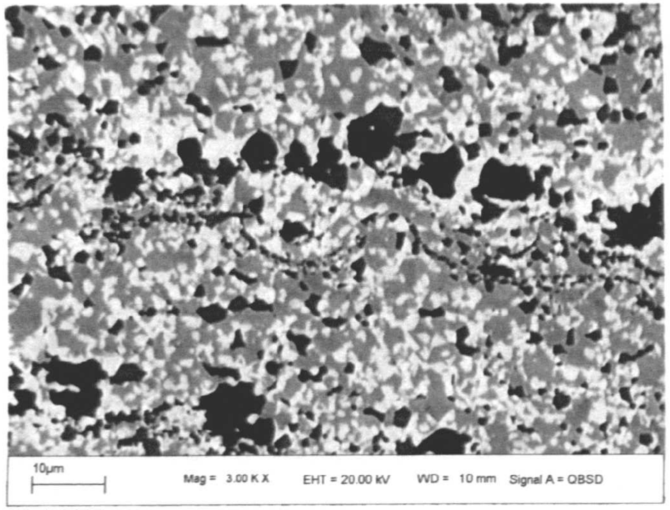

(a) 1,000 hrs

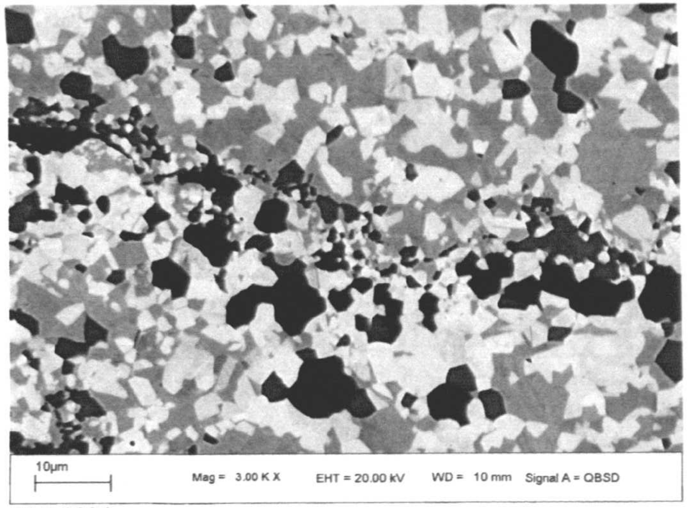

(b) 5,000 hrs

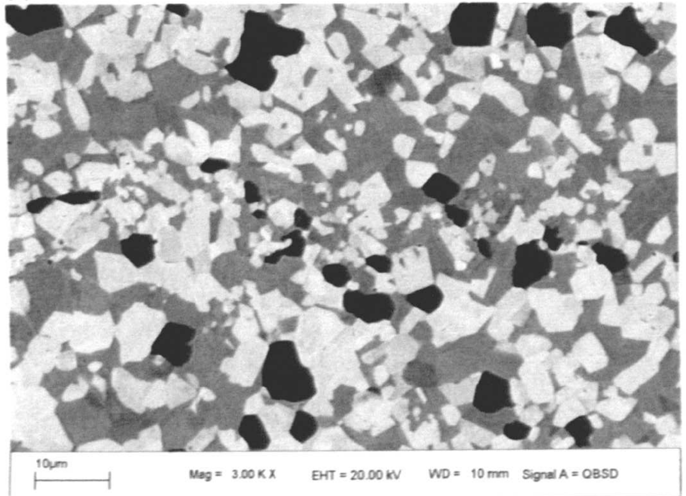

(c) 15,000 hrs

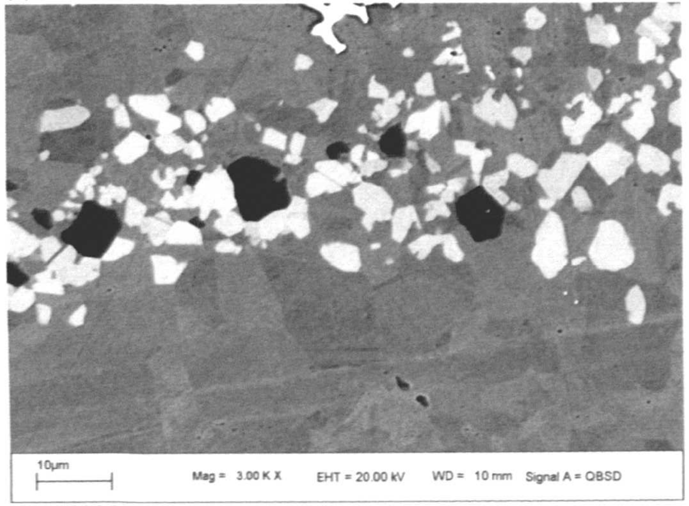

(d)25,000 hrs

Figure 7.10 Amdry 997 coating SEM BSE images of samples aged at 950°C for (a) 1,000, (b) 5,000, (c) 15,000 and (d) 25,000 hours respectively.

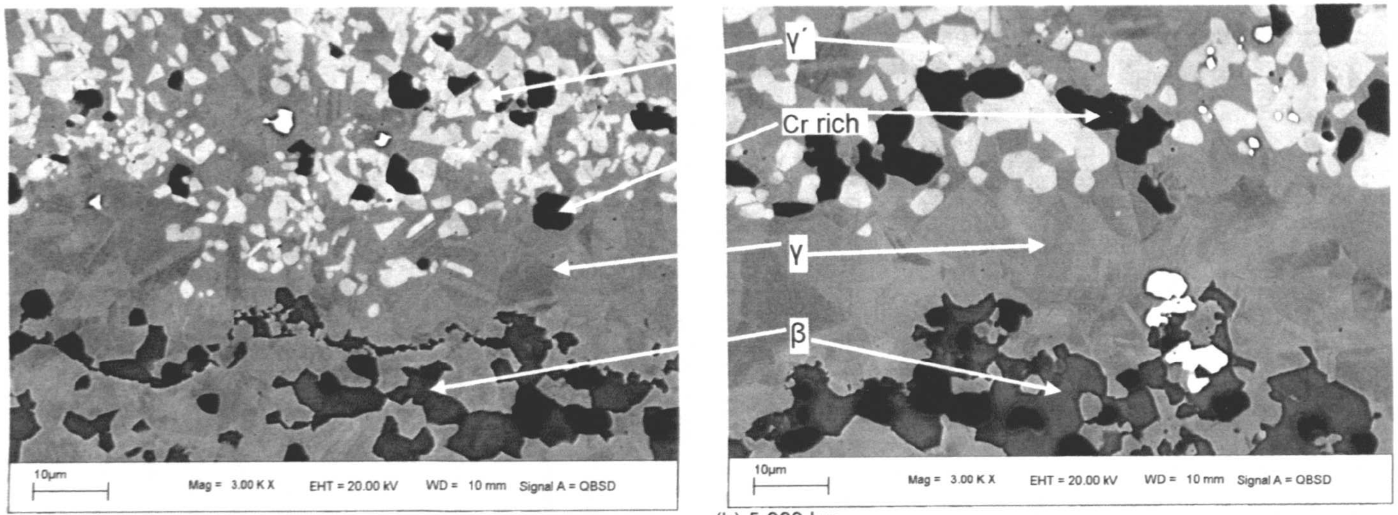

(a) 1,000 hrs

(b) 5,000 hrs

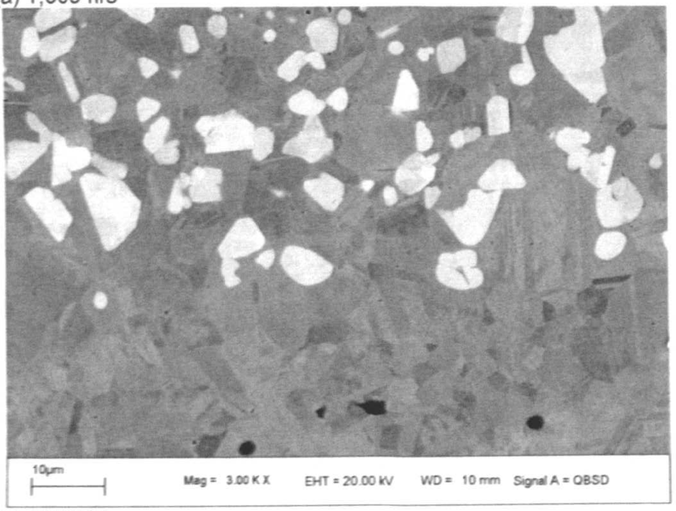

(c) 15,000 hrs

Figure 7.11 Amdry 997 coating SEM BSE images of samples aged at 1000°C for (a) 1,000, (b) 5,000, and (c) 25,000 hours respectively.

7.2 Phase Composition Determined by EDS Analysis

Table 7.4 details the coating bulk analysis for the aged 'no ICO' samples. The bulk analyses were taken from the coating γ′ layer (box measurement) at a minimum of four positions. The results (Figure 7.12) show the expected reduction of aluminium in the coating with both time and temperature however the reduction is less than 2 wt.% from 1,000 to 25,000 hours. The 1000°C aluminium EDS results show a constant 5.8 wt.% aluminium from 1,000 to 10,000 hours dropping to 5.1 wt.% aluminium at 15,000 hours. It should be noted from Table 7.2 that the coating microstructure at 1000°C is unusual in that there are two distinct layers (Figure 7.5); a γ′ layer on the TGO side of the coating and a β layer on the substrate side of the coating up to 10,000 hours. Beyond 10,000 hours the β layer is lost completely leaving a thin intermittent γ′ layer in a largely denuded coating. The bulk EDS measurements were taken from the γ′ layer. For all the samples, the bulk analysis aluminium levels remain above 5.1 wt.%. The cobalt EDS results show a linear rise with time ~4 wt.% where as the chromium results show a smaller reduction ~2 wt.% with time. The cobalt and chromium content of the γ′ layer in the coating show only minor changes with ageing temperature. The nickel results are constant with time.

Table 7.5 details the EDS composition of the phases within the Amdry 997 coating of the "no ICO" samples aged at 900°C. Table 7.5 and Figure 7.13 have been included to highlight the high levels of chromium in the chromium rich phase, the presence of tantalum and tungsten in γ′ and the aluminium content in γ, γ′ and β. A more comprehensive programme of analysis was carried out on the γ′ and the chromium rich phase in the "no ICO" coating (Table 7.6). Gaps in the table at low times and temperatures are where the phases within the coating were too small to obtain a reliable quantitative analysis. The results (Figure 7.14 for γ′ and Figure 7.15 for the chromium rich phase) show only small changes in the elemental analysis with no systematic changes with time or temperature.

A tantalum rich phase was evident in the denuded coating and at the interface between the coating and MAR M509 substrate (Figure 7.16). An EDS/WDS analysis was carried out to determine if the tantalum rich phases present within the denuded coating and at the interface between the coating and MAR M509 substrate were similar to the known tantalum rich MC carbides in the MAR M509 substrate (Figure 7.16). A similar exercise was also carried out to determine whether the blocky phase formed within the interdiffusion zone was chromium rich $M_{23}C_6$ carbide similar to the $M_{23}C_6$ carbide in the MAR M509 substrate. In both cases carbon was analysed by WDS and the remaining elemental analysis by EDS. The results were not normalised and are shown in Table 7.7.

It is considered that WDS can detect carbon but requires additional carbon standards to give a quantitative result. For the purpose of this investigation the carbon analysis is considered to be indicative only.

The carbon level of the tantalum rich phase in the bond coat (51 at.%) and the tantalum carbide in the substrate (55 at.%) are considered similar. The tantalum rich phase in the bond coat has a similar level of chromium (3 at.%) to that of the MAR M509 MC carbides but has none of the substitutional elements (Zr, Ti and W) found in the MAR M509 tantalum carbides. The formation of TaC in the coating would be dependant upon the diffusion of carbon from the MAR M509 substrate into the coating. The tantalum phase is not found in the aged samples until the inner and outer denuded layers have formed, suggesting that tantalum is being released by the solutioning of γ' (Table 7.5).

The results from the high chromium interdiffusion zone phase (29 at.% carbon) are similar to the values obtained from the $M_{23}C_6$ carbides (25 at.% carbon) in the substrate. The chromium required to form the carbides could, in part, occur as a result of the dissolution of the chromium rich phase in the coating. Baufeld et al(42) concluded that failure occurred along the coating/substrate interface of NiCoCrAlYRe coated MAR M509 thermal fatigue samples as a result of brittle chromium carbides which formed along the interface between the MAR M509 and the bond coat. For the purposes of this investigation, the tantalum rich phase will be considered to be tantalum carbide (MC) and the interdiffusion zone chromium rich phase to be chromium carbide ($M_{23}C_6$). This initial assumption was confirmed by the analysis of electron diffraction patterns from thin foils viewed in a TEM (see section 7.4).

		1,000 hrs	5,000 hrs	10,000 hrs	15,000 hrs	20,000 hrs	25,000 hrs
800°C	Al	7.3	7.1	6.6	6.2	5.7	5.6
	Cr	18.3	18.2	17.5	17.1	16.5	16.4
	Co	23.2	24.1	24.9	25.1	26.5	26.6
	Ni	44.4	44.3	44.7	45.2	44.7	45.2
	Ta	4.6	4.5	4.4	4.4	4.6	4.6
	W	1.2	1.2	1.2	1.1	1.2	1.1
	Y	1.0	0.9	0.7	0.9	0.8	0.8
850°C	Al	7.2	6.9	6.5	6.05	5.6	5.5
	Cr	17.9	17.2	17.2	16.8	17	16.8
	Co	23.7	24.5	25.5	26.1	27	26.5
	Ni	44.8	45.2	44.7	44.7	43.9	44.6
	Ta	4.5	4.4	4.5	4.5	4.6	4.6
	W	1.1	1.3	1.1	1.3	1.5	1.4
	Y	0.8	0.6	0.5	0.7	0.6	0.5
900°C	Al	7.1	6.8	6.3	5.9	5.5	5.4
	Cr	18.2	17.2	17.1	16.3	17.1	16.9
	Co	23.4	24.5	25.0	25.7	26.3	26.3
	Ni	44.7	45.1	44.8	45.6	44.1	44.1
	Ta	4.5	4.4	4.5	4.5	4.5	4.5
	W	1.4	1.3	1.4	1.5	1.9	1.7
	Y	1.0	0.6	0.8	0.3	0.6	0.5
950°C	Al	6.9	6.5	6.2	5.8	5.4	
	Cr	17.8	17.4	17.4	15.7	16.4	
	Co	23.4	24.5	25.4	25.8	26.8	
	Ni	45.6	44.7	44.3	45.2	45.6	
	Ta	4.4	4.4	4.5	4.5	3.9	
	W	1.2	1.4	1.6	1.7	1.7	
	Y	0.6	0.5	0.7	0.5	0.3	
1000°C	Al	5.8	5.9	5.9	5.1		
	Cr	18.5	15.6	14.9	17.7		
	Co	23.8	24.5	24.9	25.4		
	Ni	46.3	48.1	47.5	46.0		
	Ta	4.1	4.2	4.2	4.2		
	W	1.1	1.3	1.7	1.7		
	Y	0.4	0.5	0.4			

Table 7.4 Amdry 997 coating bulk analysis (γ' layer) 'no ICO' samples (wt.%).

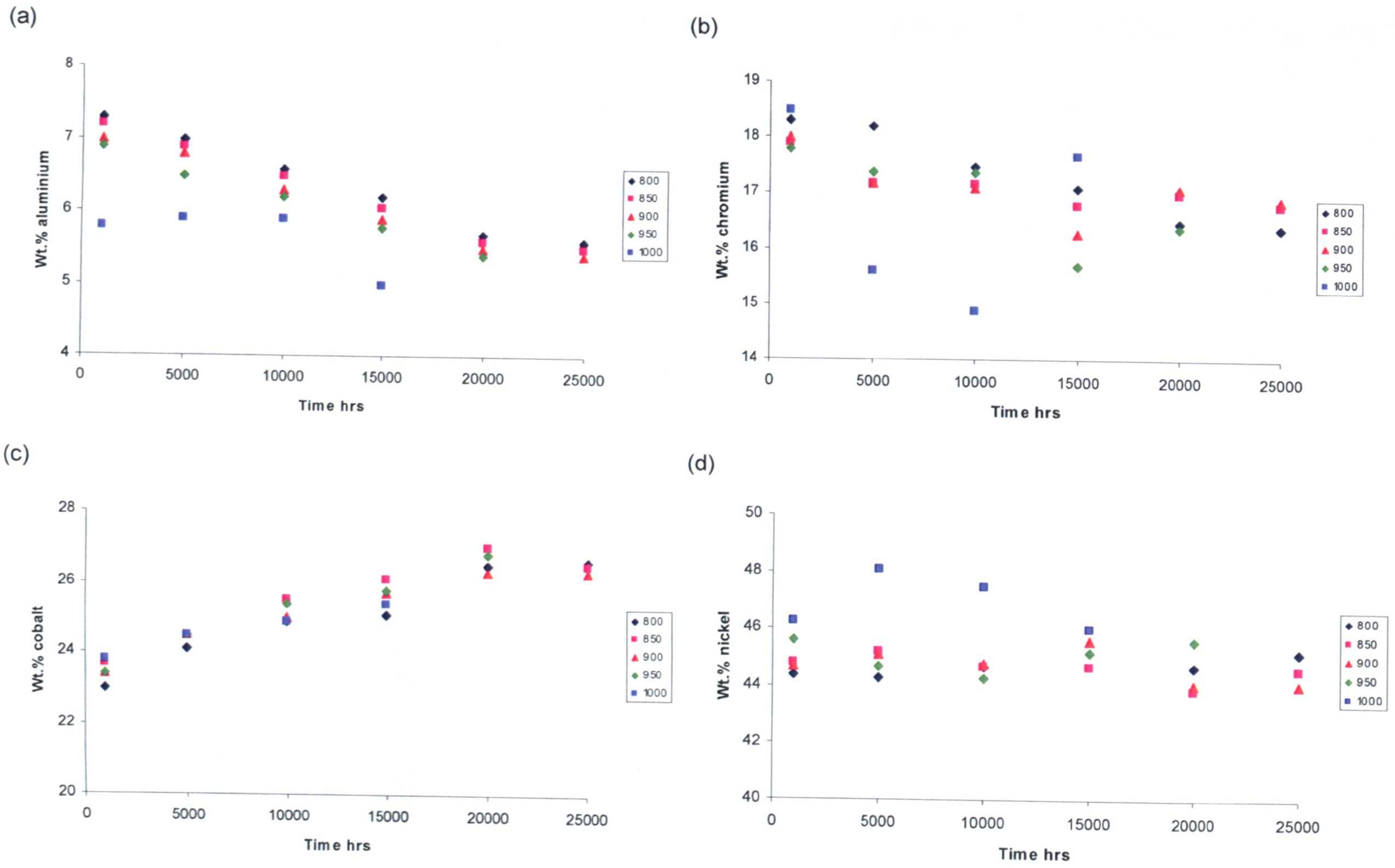

Figure 7.12 Amdry 997 coating EDS bulk analysis (a) aluminium and (b) chromium, (c) cobalt and (d) nickel respectively as a function of time and temperature (wt.%).

	1,000 hrs				5,000 hrs				10,000 hrs				15,000 hrs			20,000 hrs			25,000 hrs		
	γ	γ´	β	Cr rich	γ	γ´	β	Cr rich	γ	γ´	β	Cr rich	γ	γ´	Cr rich	γ	γ´	Cr rich	γ	γ´	Cr rich
Al	3.5	7.5	18.2		3.8	8.1	17.9		3.9	8.1	18.3		4.0	8.2		3.9	8.0		3.7	8.0	
Cr	24.7	6.7	6.1	87.6	21.3	5.8	5.2	90.6	19.5	6.1	6.1	90.3	19.3	6.1	88.2	19.2	5.5	86.3	19.4	56.1	87.5
Co	33.2	16.1	15.6	4.8	36.3	18.3	17.4	4.5	39.1	20.8	15.6	4.1	38.5	21.1	6.6	39.0	20.7	7.6	38.5	20.0	7.3
Ni	36.3	55.2	58.6	6.5	36.3	55.8	58.3	4.2	36.2	55.3	58.6	4.5	36.4	55.0	4.5	35.1	54.1	4.7	36.1	55.6	4.4
Y	0.3	0.7	0.2		0.3	0.7	0.1			0.6	0.2		0.1	0.6		0.5	0.6	0.2	0.2	0.5	
Ta	1.4	11.8	0.7	0.4	1.3	9.4	0.6	0.4	0.8	7.2	0.7	0.4	1.0	7.1	0.3	1.2	8.6	0.5	1.1	8.3	0.3
W	0.6	2.1	0.5	0.4	0.8	2.0	0.5	0.4	0.5	1.9	0.5	0.4	0.7	2.0	0.3	1.2	2.5	0.6	1.0	2.1	0.4

Table 7.5 EDS composition of Amdry 997 coating phases 900°C 'no ICO' samples (wt.%).

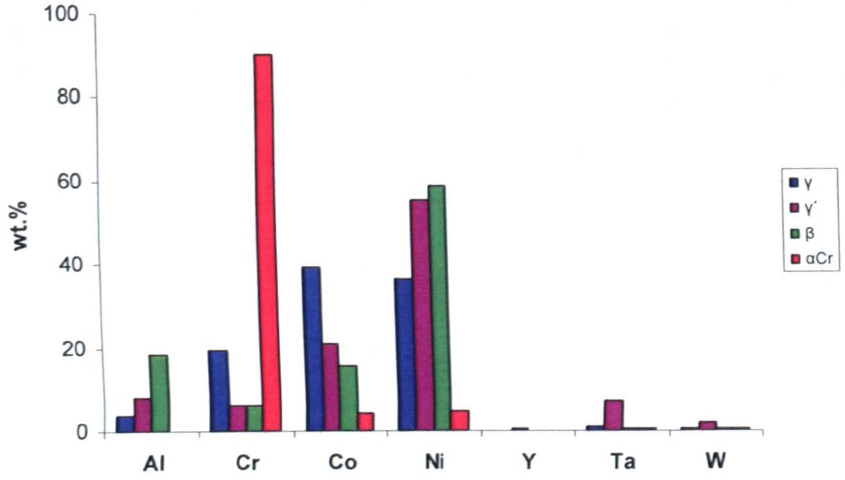

Figure 7.13 EDS composition of Amdry 997 coating phases from 900°C 10,000 hour sample.

Time hrs	1,000	5,000	10,000	15,000	20,000	25,000	1,000	5,000	10,000	15,000	20,000	25,000
800°C	γ′						Cr rich					
Al				8.2	7.9	8.4			0.1	0.2	0.2	0.1
Cr				6.4	7.1	6.4			90.9	89.6	90.5	91.2
Co				17.7	19.1	17.5			4.1	4.5	4.2	3.8
Ni				55.3	56.5	56.9			4.4	4.6	4.3	4.2
Y				0.7	0.6	0.8			0.1	0.3	0.3	0.1
Ta				9.6	7.4	8.3			0.1	0.6	0.2	0.2
W				2.2	1.6	1.8			0.3	0.4	0.4	0.3
850°C												
Al		7.9	8.3	8.4	8.1	8.4	0.2	0.1	0.2	0.2	0.2	
Cr		6.6	6.1	6.8	5.5	5.9	89.6	90.6	90.8	88.6	87.7	89.1
Co		18.6	18.9	21.3	19.6	20.9	4.2	4.3	4.3	5.7	6.3	5.8
Ni		53.7	55.9	54.6	56.1	55.3	5.4	4.3	4.2	4.6	5.3	4.3
Y		0.8	0.6	0.5	0.6	0.5	0.1				0.2	
Ta		10.1	8.3	6.7	8.2	7.3	0.3	0.3	0.2	0.4	0.5	0.3
W		2.3	1.9	1.7	2.2	1.7	0.3	0.3	0.3	0.5	0.3	0.4
900°C												
Al	7.5	8.1	8.1	8.2	8.2	8						
Cr	6.7	5.8	6.1	6.1	5.5	5.6	89.6	90.6	90.3	88.2	86.3	87.5
Co	16.1	18.3	20.8	21.1	20.7	20.0	4.8	4.5	4.1	6.6	7.6	7.3
Ni	55.2	55.8	55.3	55.1	54.1	55.6	5.5	4.2	4.5	4.5	4.7	4.4
Y	0.7	0.7	0.6	0.6	0.6	0.5						
Ta	11.8	9.4	7.2	7.1	8.6	8.3	0.4	0.4	0.4	0.3	0.5	0.3
W	2.1	2	1.9	2.2	2.5	2.1	0.4	0.4	0.4	0.3	0.6	0.4
950°C												
Al	7.8	8.1	8.4	7.9	7.8	7.4	0.1	0.1	0.1			
Cr	5.8	6.1	6 1	5.4	5.1	5.1	88.2	86.7	87.0	86.8	86.8	
Co	18.5	19.7	19.8	19.3	18.8	18.7	5.7	7.2	7.4	7.7	7.6	
Ni	55.3	55.4	54.8	55.3	55.7	56.1	4.9	4.7	4.6	4.6	4.7	
Y	0.7	0.5	0.5	0.6	0.4	0.5	0.2	0.2		0.1	0.1	
Ta	9.8	8.5	8.3	9.3	9.4	9.2	0.5	0.7	0.5	0.5	0.4	
W	2.1	1.9	2.1	2.3	2.7	3.1	0.5	0.5	0.5	0.4	0.3	
1000°												
Al	8.1	8.3	8.3	8.6			0.1		0.1			
Cr	5.8	5.8	5.8	5.5			87.4	86.2	86.6			
Co	17.7	17.8	18	17.3			6.7	7.4	7.4			
Ni	57.9	57.6	57.6	57.2	No sample		4.8	5.0	4.7	No sample		
Y	0.7	0.5	0.5	0.4			0.2	0.2	0.1			
Ta	7.9	7.9	7.4	8.5			0.4	0.7	0.4			
W	2.0	2.2	2.3	2.4			0.4	0.5	0.6			

Table 7.6 Amdry 997 coating EDS analysis γ′ and Cr rich phase 'no ICO' samples (wt.%).

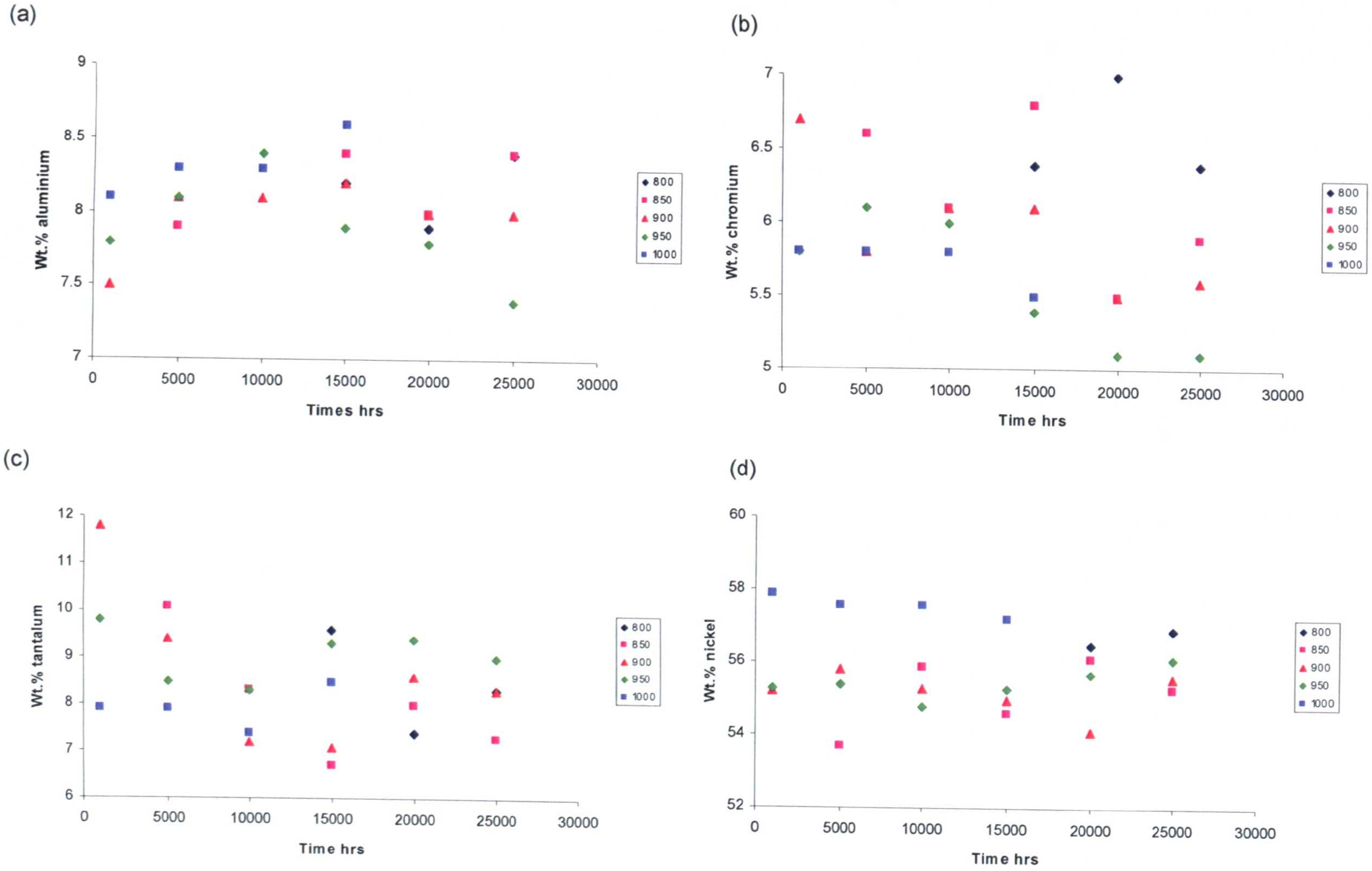

Figure 7.14 Amdry 997 coating EDS analysis γ′ ‘no ICO’ samples (a) aluminium, (b) chromium, (c) tantalum and (d) nickel respectively.

]

(a)

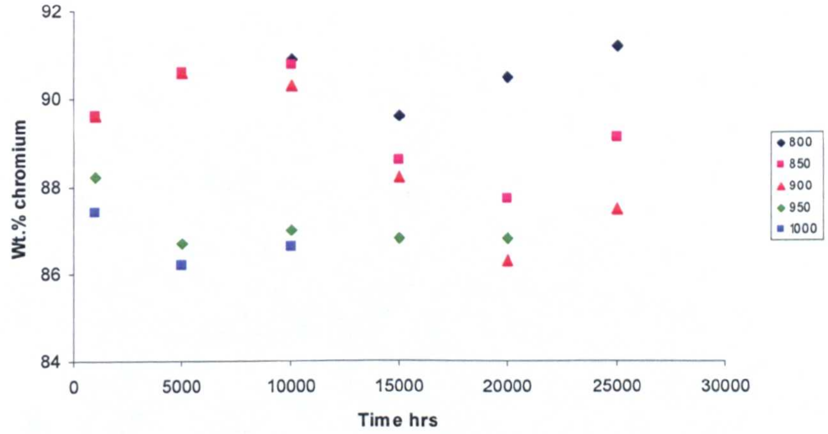

(b)

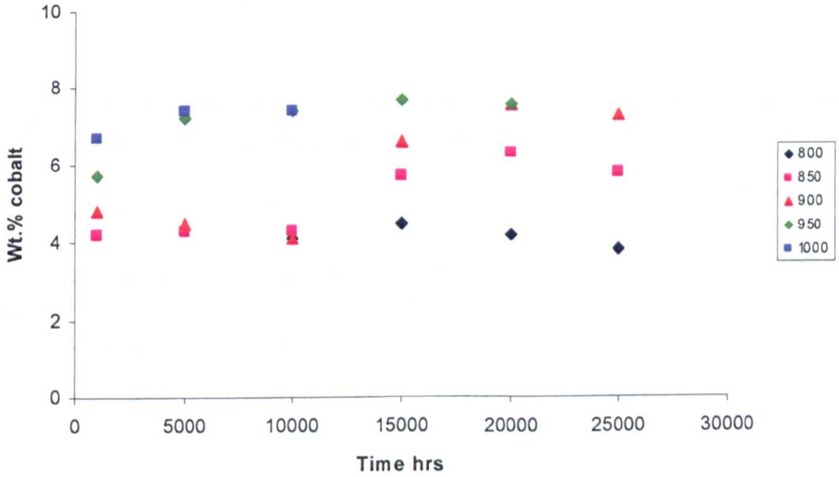

(c)

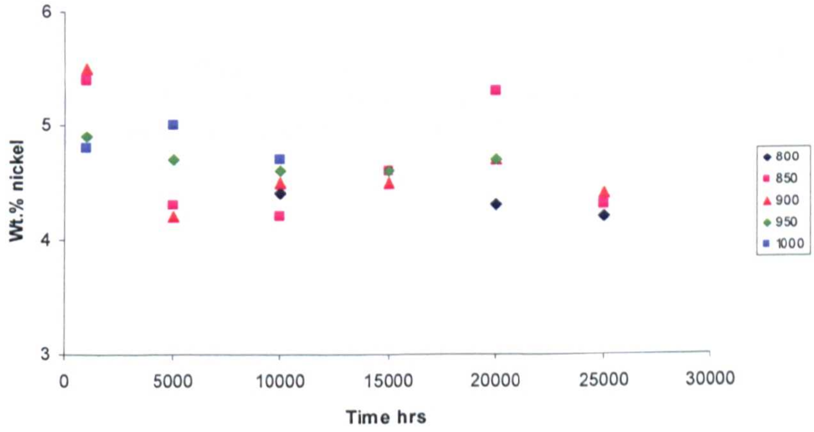

Figure 7.15 Amdry 997 coating EDS analysis Cr rich phase 'no ICO' samples (a) chromium, (b) cobalt and (c) nickel respectively.

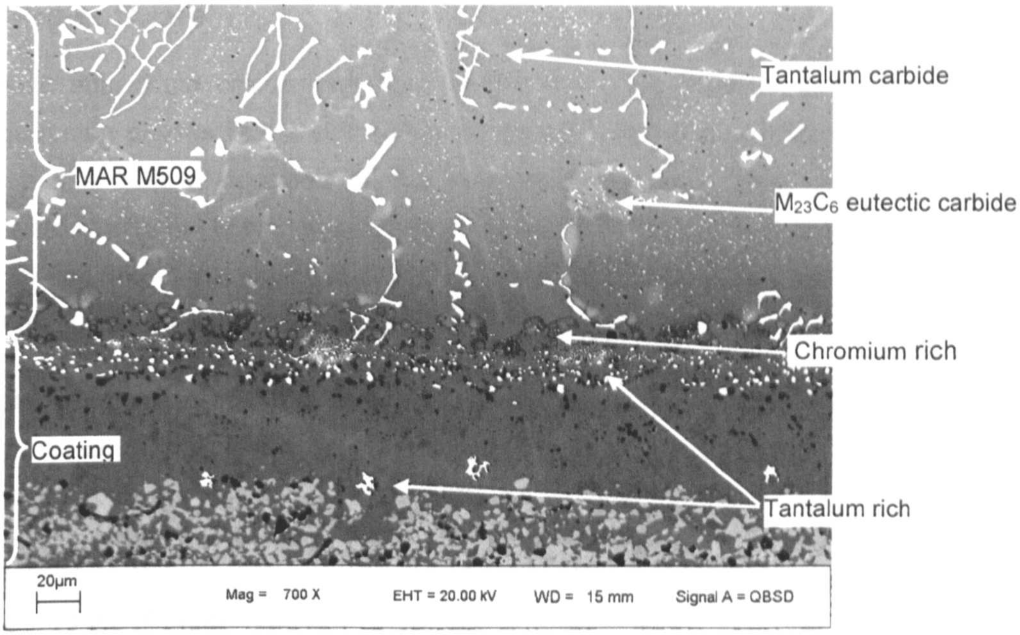

Figure 7.16 SEM BSE image showing tantalum and chromium rich phases in the Amdry 997 coating and carbides in MAR M509.

at.%	C	Ta	Zr	Ti	Cr	W	Co	Ni
MC (MAR M509)	55	25	6	5	3	1	4	1
Interface*	50	35		1.6	4		4	5
Coating*	51	36		0.6	3		4	5
$M_{23}C_6$ (MAR M509)	28				59	4	8	1
Interdiffusion	29				61	2	5	3

* small particles, analysis affected by beam spread

Table 7.7 EDS/WDS analysis of tantalum and chromium rich phases in the Amdry 997 coating and known carbides in the substrate (at.%). Results are the average of five analyses for each phase.

7.3 Thermodynamic Equilibrium Calculations for Amdry 997 Utilising JMatPro software

Thermodynamic equilibrium calculations were carried out using JMatPro to indicate the predicted equilibrium phases in the coating for Amdry 997. The composition used for the calculations is the bulk composition of the as-received samples, see Table 3.3. All calculations were carried out in the temperature range 800 - 1100°C. Initially no phases were excluded from the nickel superalloy database. Unless otherwise stated nickel was the balancing element in all calculations.

Yttrium is not a compositional input in JMatPro. It is considered that the omission of yttrium, which is only present in small amounts (0.6 wt.%), would not lead to substantial errors in the thermodynamic predictions. Yttrium is not considered to impact upon the thermodynamic stability of any of the major phases expected to be present (i.e. γ, γ' and β).

Figure 7.17 shows the JMatPro predicted equilibrium phases in Amdry 997 over the selected temperature range. The predictions show that γ' and σ decrease as the temperature increases, with γ and to a lesser extent β (NiAl) increasing with temperature. σ is not predicted at temperatures above 940°C with γ, γ' and β (NiAl) present, to a greater or lesser extent, over the temperature range of 800-1050°C. The thermodynamic equilibrium compositions of the predicted phases are presented in Figure 7.18 showing significant changes in nickel, cobalt and chromium in γ, cobalt and tantalum in β (NiAl) and tantalum in γ' with temperature. The predicted aluminium content of, γ is less than 5 wt.%, γ' ~10 wt.% and β ~18 wt.%. The predicted chromium and cobalt for σ are ~60 and 34 wt.% respectively at 900°C.

A small number of investigations have identified the phases present in aged samples of Amdry 997 coating on nickel based superalloys (Table 7.8). The results of the investigations show that both σ and αCr have been reported in Amdry 997 on nickel based superalloy substrates. For JMatPro to predict αCr (BCC phase in JMatPro) as an equilibrium phase it is necessary to remove both σ and $M_2(C,N)$ from the phases present. The JMatPro equilibrium phase predictions (Figure 7.19), with σ and $M_2(C,N)$ removed, show increased levels of γ and β in the temperature range 800 - 920°C with reduced levels of γ' over the same temperature range when compared to the original JMatPro predictions. αCr (BCC) is predicted below 825°C. The thermodynamic equilibrium compositions of the predicted phases are presented in Figure 7.20. The changes in composition noted previously for γ and β (NiAl) are still present, however, the change in tantalum in γ' is reduced. The predicted chromium level in αCr (84 wt.%) is significantly higher than the chromium content of σ (57 wt.%) shown in Figure 7.18.

Table 7.9 compares the EDS results from the 900°C 1,000 hour and 10,000 hour samples with the JMatPro equilibrium predictions at 900°C (800°C for αCr). The results are also plotted in Figure 7.21, showing reasonable agreement between predicted and experimental measurements other than a higher chromium content predicted by JMatPro in γ with higher nickel lower chromium and cobalt in γ'. The results for β are similar with slightly higher tantalum predicted by JMatPro and higher cobalt in αCr.

Table 7.10 details the composition of σ and αCr predicted by JMatPro at 800°C and the composition of σ found by Frances(76) at 850°C and the composition of the chromium rich phase at 800°C from the current investigation. The composition of σ predicted by JMatPro is similar to the composition of σ detailed by Frances. The JMatPro predicted composition of αCr (83 wt.% Cr, 14 wt.% Co) shows a higher cobalt content than the composition of the chromium rich phase (91 wt.% Cr, 4 wt.% Co) determined from this investigation.

The current investigation has shown that a chromium rich phase is present in the majority of the samples investigated and in some cases is the last phase present in the denuded coating after the solutioning of both γ' and β. JMatPro predicts that at equilibrium β will be present at ~20 wt.% at all temperatures, the current investigation shows that β is no longer evident in the coating after 10,000 hours at ageing temperatures above 800°C. Coatings are a dynamic system and it may be possible as a result of the outward diffusion from the coating and the inward diffusion from the substrate that equilibrium in the coating may never be achieved.

Figure 7.22 and Figure 7.23 show JMatPro equilibrium predictions for increased levels of carbon in the coating and reduced levels of aluminium in the coating at 800°C and 900°C. The prediction for carbon increasing in the coating (Figure 7.22 (a) and (b)) is that at 800°C in addition to γ, γ' and β, a chromium rich (Figure 7.22 (c)) $M_{23}C_6$ carbide would be present. At 900°C JMatPro predicts that in addition to γ, γ', β and $M_{23}C_6$ carbide, a tantalum rich MC carbide is formed (Figure 7.22 (d)) above 0.2 wt.% carbon. Figure 7.23 (a) and (b) show the effect of varying aluminium on the equilibrium phases predicted by JMatPro. The results show that αCr (BCC) disappears rapidly as the aluminium content decreases, and is not evident at 900°C, γ and γ' increase as β decreases as the aluminium concentration reduces. With the loss of β, γ continues to increase at the expense of γ'. Both γ and γ' would remain at 3 wt.% aluminium with β removed at ~5.6 wt.% aluminium. Figure 7.23 (c) and (d) show the effect of the inclusion of 0.2 wt.% carbon in the coating analysis on the predicted equilibrium phases as aluminium is reduced. At 800°C, 4 wt.% $M_{23}C_6$ carbide is present as the aluminium reduces from 7.5 to 4 wt.%. After this the $M_{23}C_6$ carbide reduces and MC carbide is predicted. At 900°C a very low level of MC carbide is predicted from 7.5 to 6.5 wt.% aluminium and ~3 wt.% $M_{23}C_6$ carbide is predicted from 7.5 to 6 wt.% aluminium. Below 6 wt.% aluminium the $M_{23}C_6$ carbide reduces, the MC carbide increases to ~3 wt.% and remains constant down to 3 wt.% aluminium. The effect of the addition of 0.2 and 0.4 wt.% carbon to the coating analysis is shown in Figure 7.24. The presence of 0.2 wt.% carbon slightly reduces the levels of γ, γ' and β, and introduces low levels of MC (~4 wt.%) and $M_{23}C_6$ (~5 wt.%) carbide. As would be expected, increasing the carbon from 0.2 – 0.4 wt.% increases the amounts of the predicted carbides.

The results show that if carbon is diffusing into the coating from the substrate then chromium rich $M_{23}C_6$ carbide is likely to form within the coating, and tantalum carbide would form at lower aluminium levels in the denuded coating layers. The presence of tantalum carbide in the denuded coating has been confirmed by TEM/electron diffraction. The WDS results carried out on a small number of samples has confirmed that carbon is present in the phase identified as the chromium rich phase (Table 7.12). The presence of $M_{23}C_6$ carbide in the coating is still to be proved conclusively. The EDS results show that aluminium is diffusing from the coating and that as the β content decreases, the γ′ content increases. The lowest aluminium content at which β was found was 5.6 wt.% (25,000 hour 800°C 'no ICO'). This is in agreement with the JMatPro prediction of β removed at 5.8 wt.% at 800°C. The lowest measured aluminium content at which γ′ was evident was 5.1 wt.%, which is significantly higher than the JMatPro predictions of γ′ still evident at 3 wt.%.

JMatPro was developed for the prediction of equilibrium phases in nickel based superalloys and has been 'tweaked' using the results from various research programmes. The composition of MCrAlY coatings are generally outside of the compositions normally found in nickel based superalloys and for this reason JMatPro may not be directly applicable to MCrAlY coatings. It is also considered that as a result of the inward diffusion from the substrate to the coating and outward diffusion from the coating to the TGO and substrate that the coating may never achieve equilibrium. The results of this investigation show that the dynamics of the system, NiCoCrAlTaY coating on a high carbon cobalt superalloy, may be beyond the current limits of the JMatPro software. However, although there may be limitations to JMatPro, it provides a good first indication of the phases that might be present in the coating. In addition, given knowledge of the system, it is possible to carry out useful calculations to provide an insight in to the effect of compositional variations. A model which combines the kinetics of diffusion with thermodynamic equilibrium predictions is required to fully explain the experimental data.

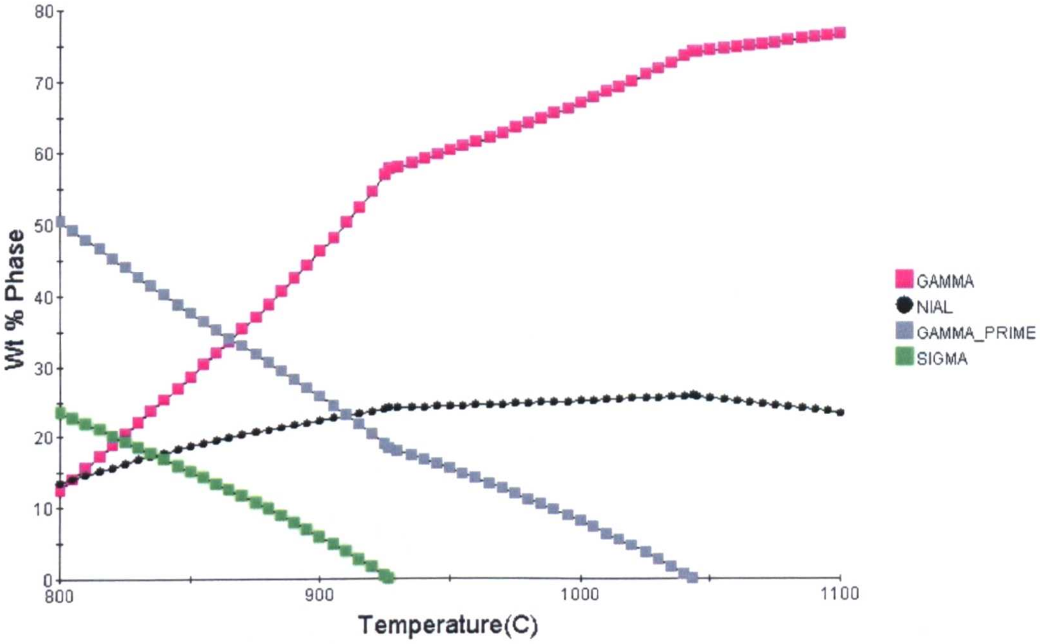

Figure 7.17 JMatPro thermodynamic equilibrium predictions of phases in Amdry 997 coating (no phases excluded).

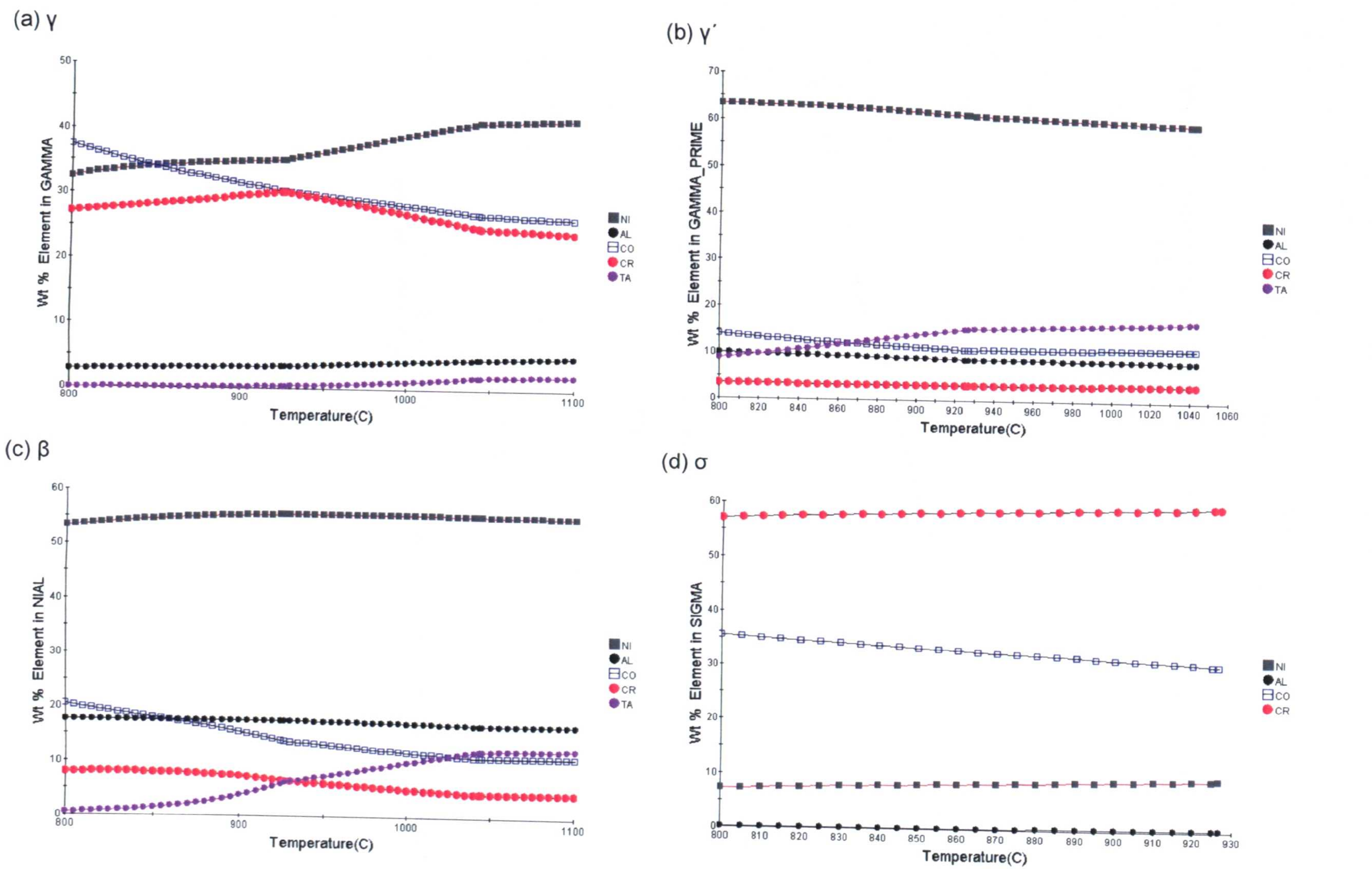

(a) γ

(b) γ´

(c) β

(d) σ

Figure 7.18 **JMatPro thermodynamic equilibrium predictions of phase composition in Amdry 997 (a) gamma, (b) gamma prime, (c) NiAl (β) and (d) σ respectively.**

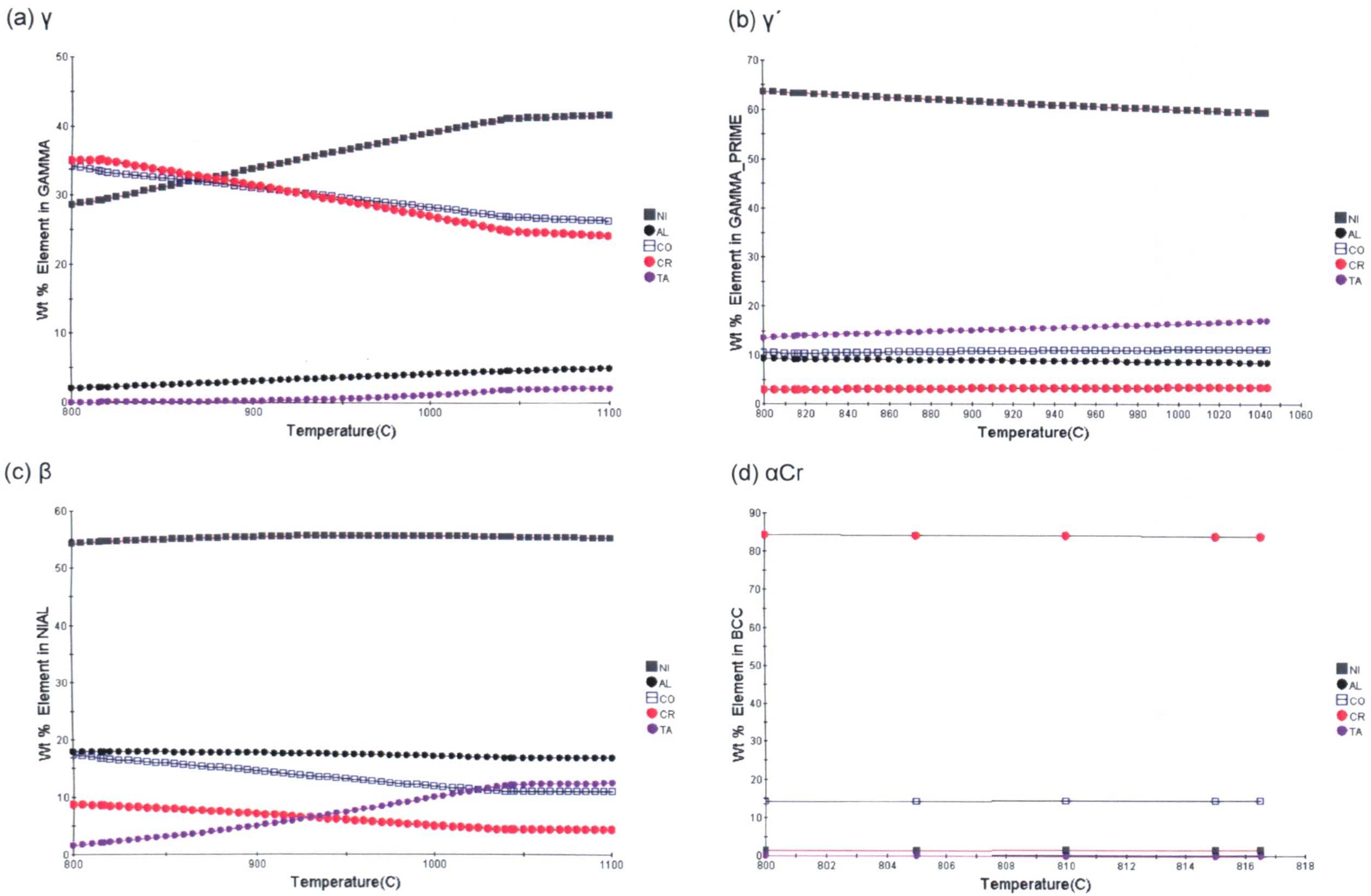

(a) γ

(b) γ´

(c) β

(d) αCr

Figure 7.20 JMatPro thermodynamic predictions for composition of equilibrium phases in Amdry 997 following the removal of σ and M (C N) from the initial calculation (a) gamma, (b) gamma prime, (c) NiAl and (d) BCC (alpha Cr) respectively.

	1,000 hrs				JMatPro				10,000 hrs			
	γ	γ′	β	Cr rich	γ	γ′	β	αCr	γ	γ′	β	Cr rich
Al	3.5	7.5	18.2		3.1	8.9	17.7	0.1	3.9	8.1	18.3	
Cr	24.7	6.7	6.1	87.6	32.0	3.3	7.1	84.3	19.5	6.1	6.1	90.3
Co	33.2	16.1	15.6	4.8	31.3	10.9	14.6	14.2	39.1	20.8	15.6	4.1
Ni	36.3	55.2	58.6	6.5	34.2	61.7	55.6	1.4	36.2	55.3	58.6	4.5
Y	0.3	0.7	0.2							0.6	0.2	
Ta	1.4	11.8	0.7	0.4	0.3	15.2	5.0		0.8	7.2	0.7	0.4
W	0.6	2.1	0.5	0.4					0.5	1.9	0.5	0.4

Table 7.9 Comparison of EDS compositions Amdry 997 coating at 1,000 and 10,000 hour 900°C with JMatPro predicted compositions at 900°C (αCr at 800°C) (wt.%).

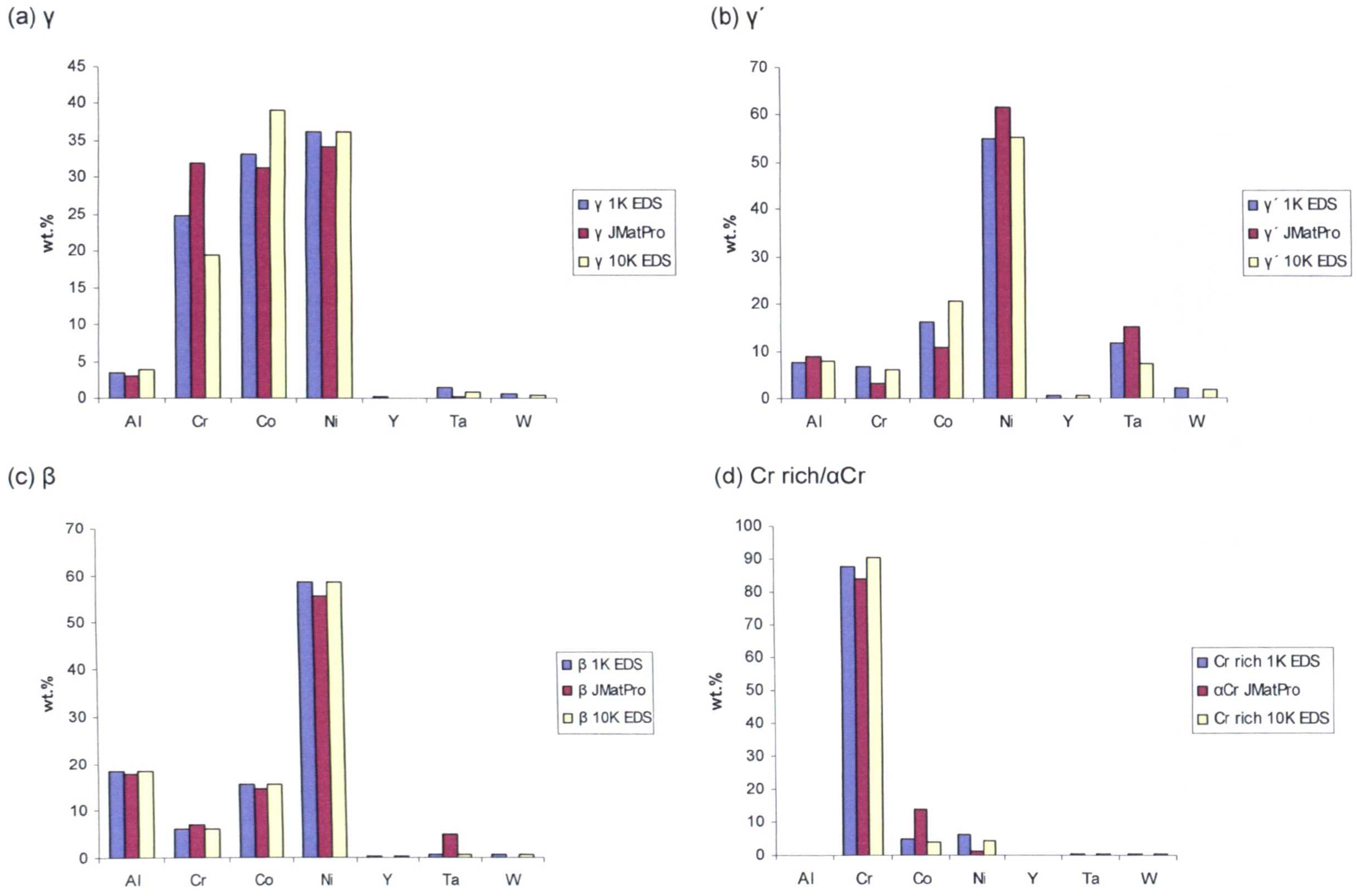
(a) γ

(b) γ´

(c) β

(d) Cr rich/αCr

Figure 7.21 Amdry 997 coating EDS analysis at 1,000 hours and 10,000 hours and JMatPro equilibrium predictions at 900°C (a) γ, γ´, β and αCr respectively.

Wt.%	Cr	Co	Ni	W
JMatPro σ	56	36	8	
Frances(76) σ	56	29	14	
JMatPro (αCr)BCC	84	14	2	
Cr rich this programme (10,000 hours)	91	4	4	0.4

Table 7.10 JMatPro predicted equilibrium compositions for Amdry 997 coating phases σ and αCr (850°C), together with the composition quoted by Frances(76) for σ and the SEM EDS composition of the Cr rich phase from this programme (850°C 10,000 hrs).

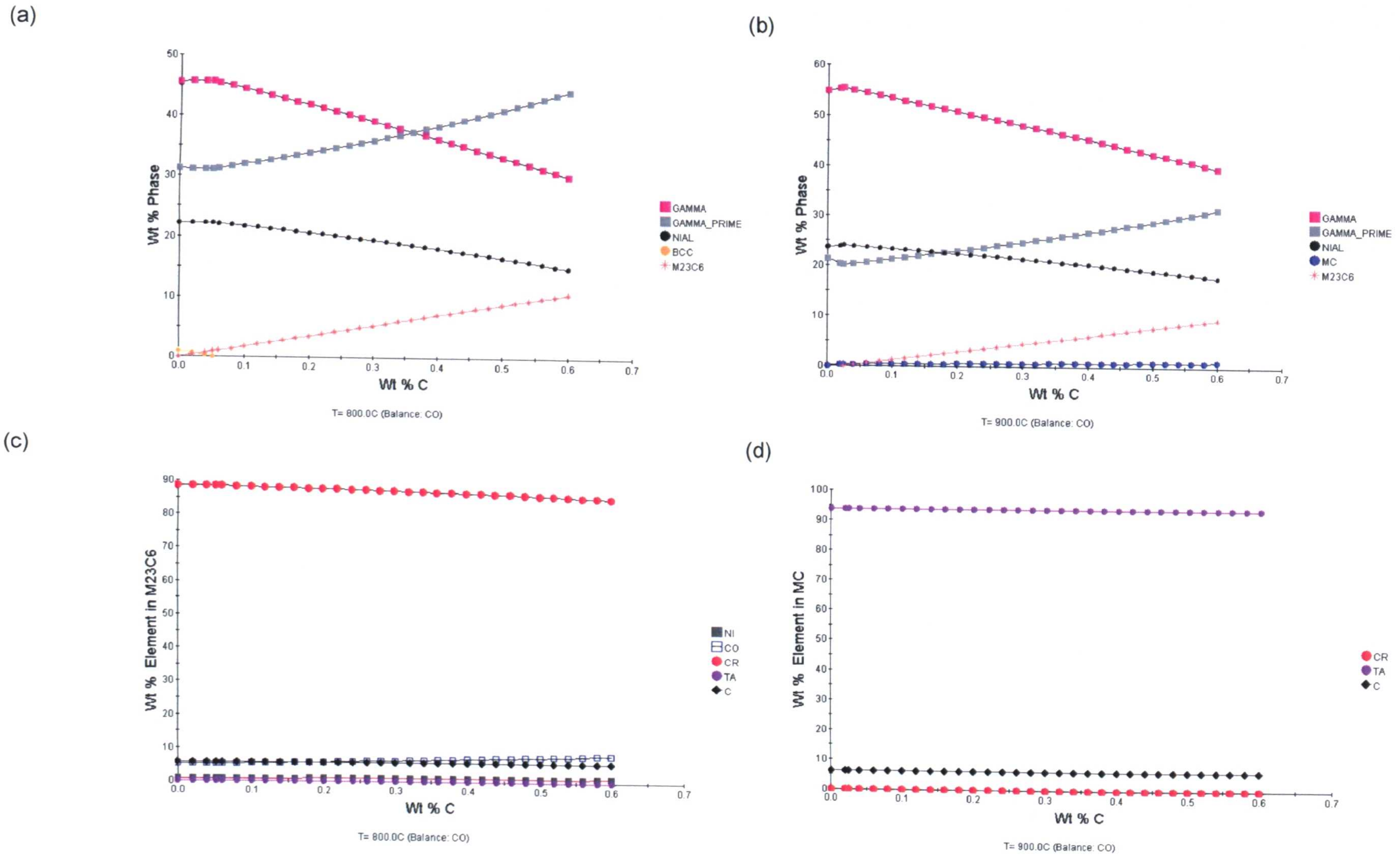

Figure 7.22 Amdry 997 JMatPro equilibrium predictions (a) 800°C carbon varied balance Co, (b) 900°C carbon varied, balance Co, (c) 800°C $M_{23}C_6$ carbide composition (d) 900°C MC carbide composition respectively (with σ and $M_2(CN)$ removed for all of these calculations).

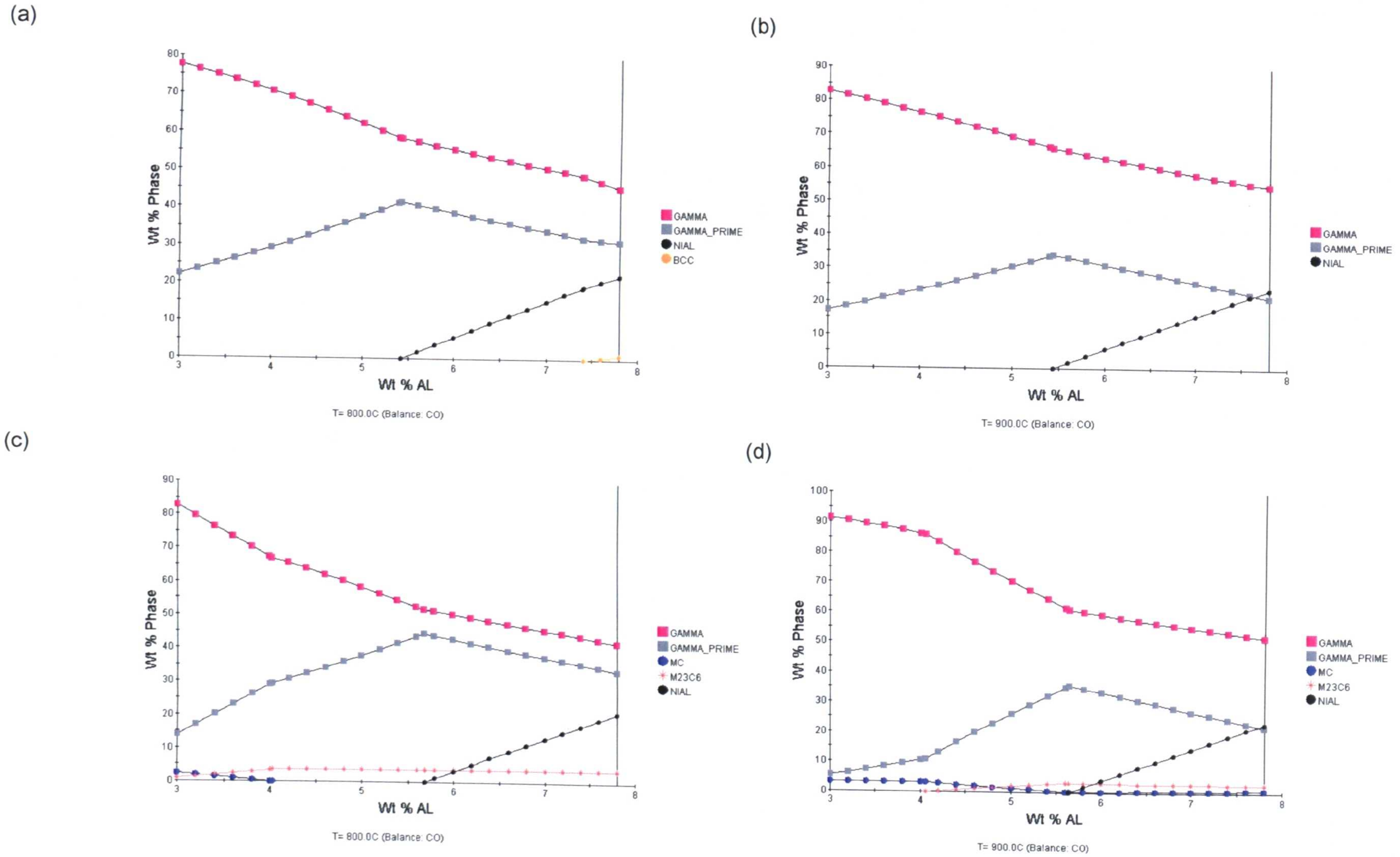

Figure 7.23 Amdry 997 JMatPro equilibrium predictions (a) 800°C aluminium varied, balance Co, (b) 900°C aluminium varied, balance Co, (c) 800°C 0.2 wt.% carbon, aluminium varied, balance Co and (d) 900°C 0.2 wt.% carbon, aluminium varied, balance Co respectively (with σ and $M_2(CN)$ removed for all calculations).

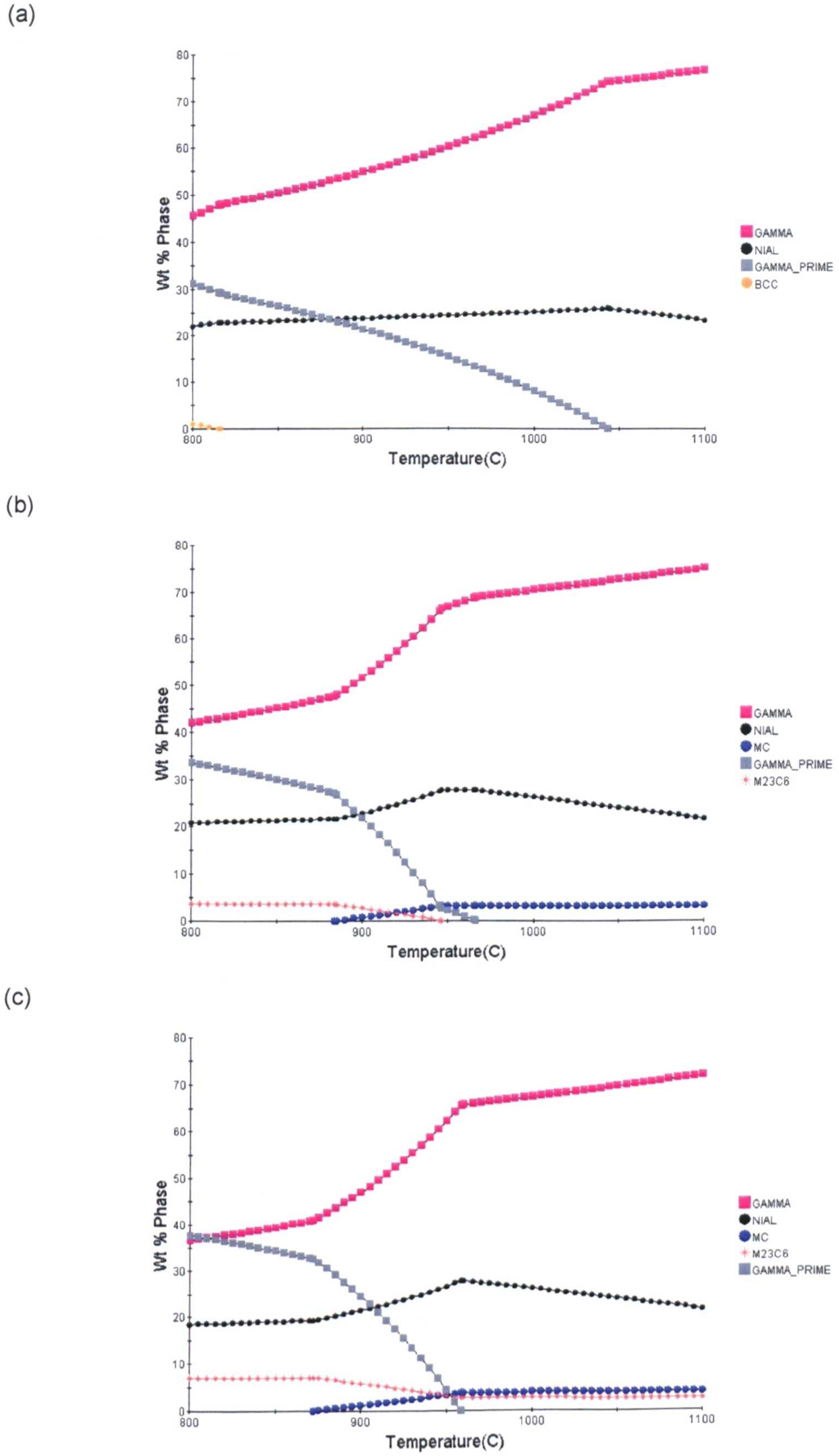

Figure 7.24 **Amdry 997 JMatPro thermodynamic equilibrium predictions for (a) coating analysis, no carbon (b) coating analysis with 0.2 wt.% carbon (c) coating analysis with 0.4 wt.% carbon respectively (with σ and $M_2(CN)$ removed for all calculations).**

7.4 Identification of Unknown Phase

During the course of this research, a number of phases have been identified which required more detailed investigation. Three microscopes were used for this work, a fei Nova Nano Lab 600 dual beam (FEG-SEM/FIB) system, a Jeol 2000FX TEM and a Philips Tecnai F20 FEG TEM fitted with a GATAN DigiPEELS spectrometer. Thin foil samples were produced in the FEG-SEM FIB for examination in the TEM and FEG TEM.

7.4.1 Electron diffraction

The thin foil samples taken from the aged samples for electron diffraction are as follows;

a) Tantalum rich phase from the denuded region of the coating 20,000 hours 950°C 'no ICO' sample (Figure 7.25).

b) Yttrium rich phase from the interface and the chromium rich phase in the inter diffusion zone 10,000 hour 850°C 'no ICO' sample (Figure 7.26).

c) Chromium rich phase in the bulk of the coating 10,000 hour 850°C 'no ICO' sample (Figure 7.28).

d) Chromium rich phase at the interface 10,000 hour 850°C 'no ICO' sample (Figure 7.29).

The TEM EDS composition of the phases investigated are detailed in Table 7.11. Figure 7.25 – 7.29 show for each phase the position of sample within the bulk sample, a TEM image of the thin foil and the diffraction pattern from the phase of interest. The patterns were indexed using the Cambridge University Practical Crystallography software Version 1.6(79). The crystallography of the phases which were investigated are detailed in Table 3.4. Indexing of the patterns confirms the tantalum rich phase as tantalum carbide (FCC lattice parameter 4.46Å), the yttria rich phase as Y_2O_3 (BCC lattice *parameter 10.6Å), the chromium rich phase* in the interdiffusion region as $M_{23}C_6$ (FCC lattice parameter 10.66Å).

The electron diffraction patterns taken from the chromium rich phase thin foils (c) and (d) could not be indexed as αCr (BCC, lattice parameter 2.8839 Å). The electron diffraction patterns could be indexed to $M_{23}C_6$ (FCC lattice parameter 10.66 Å). A series of WDS/EDS analyses were carried out to identify if carbon was present in the bulk and interface chromium rich phase in the 10,000 hour 850°C sample, from which the thin foils had been cut. Table 7.12 details the WDS/EDS analysis results showing that both the bulk and the interface chromium rich phase contained ~11 wt.% carbon, similar to the 10 wt.% obtained from a $M_{23}C_6$ carbide in the MAR M509 substrate. In both cases the carbon was determined by WDS and the remaining elements by EDS. It is considered that in a dirty SEM, carbon can be deposited on to the surface of the sample and therefore in order to rule out the possibility that the observed carbon was the result of contamination. Spot analyses were carried out on the γ' phase around the chromium rich phase. The γ' phase analysis in Table 7.12 is typical of the results showing no evidence of carbon. Further work has been carried out by parallel electron energy loss spectroscopy (Chapter 7.4.2) to confirm the presence of carbon in the chromium rich phase.

Wt.%	Cr	Co	Ni	Ta	Ti	W	Y	O
Sample (a) Tantalum rich				92	8			
Sample (b) Yttrium rich							39	60
Sample (b) Chromium rich	72	14	6			8		
Sample (c) Chromium rich bulk	77	15	8					
Sample (d) Chromium rich interface	75	14	6			5		

Table 7.11 Amdry 997 coating - TEM EDS composition from the phases in the thin foil samples (no carbon taken into account) (wt.%).

	C	Al	Cr	Co	Ni	Ta	W
chromium rich phase bulk	11.8		79.8	4.2	4.2		
γ'		8.3	7.9	23.7	52.9	7.2	
chromium rich phase interface	10.9		79.1	5.2	4.8		
$M_{23}C_6$ MAR M509	10.0		56.5	16.1	3.3	0.5	13.6

Table 7.12 SEM EDS/WDS to determine carbon content of Cr rich phase in the bulk of the Amdry 997 coating and local to the interface with the substrate and compare this with the carbon content of the $M_{23}C_6$ carbide in the MAR M509. γ' analysis carried out as control (wt.%).

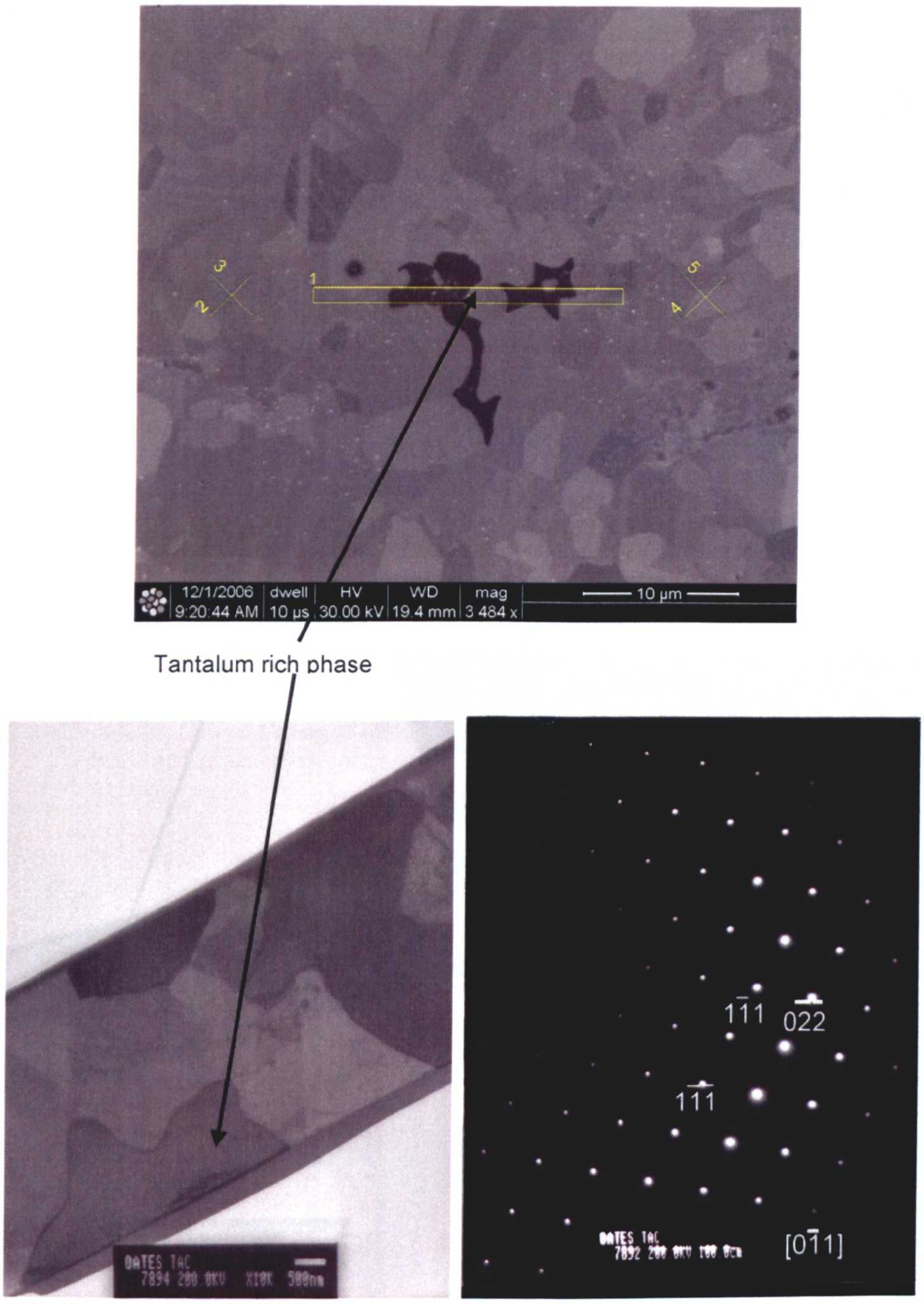

Figure 7.25 **Amdry 997 coating 20,000 hours 950°C tantalum rich phase (a) FIB SEM image of sample position (b) TEM image of thin foil and diffraction pattern indexed as TaC.**

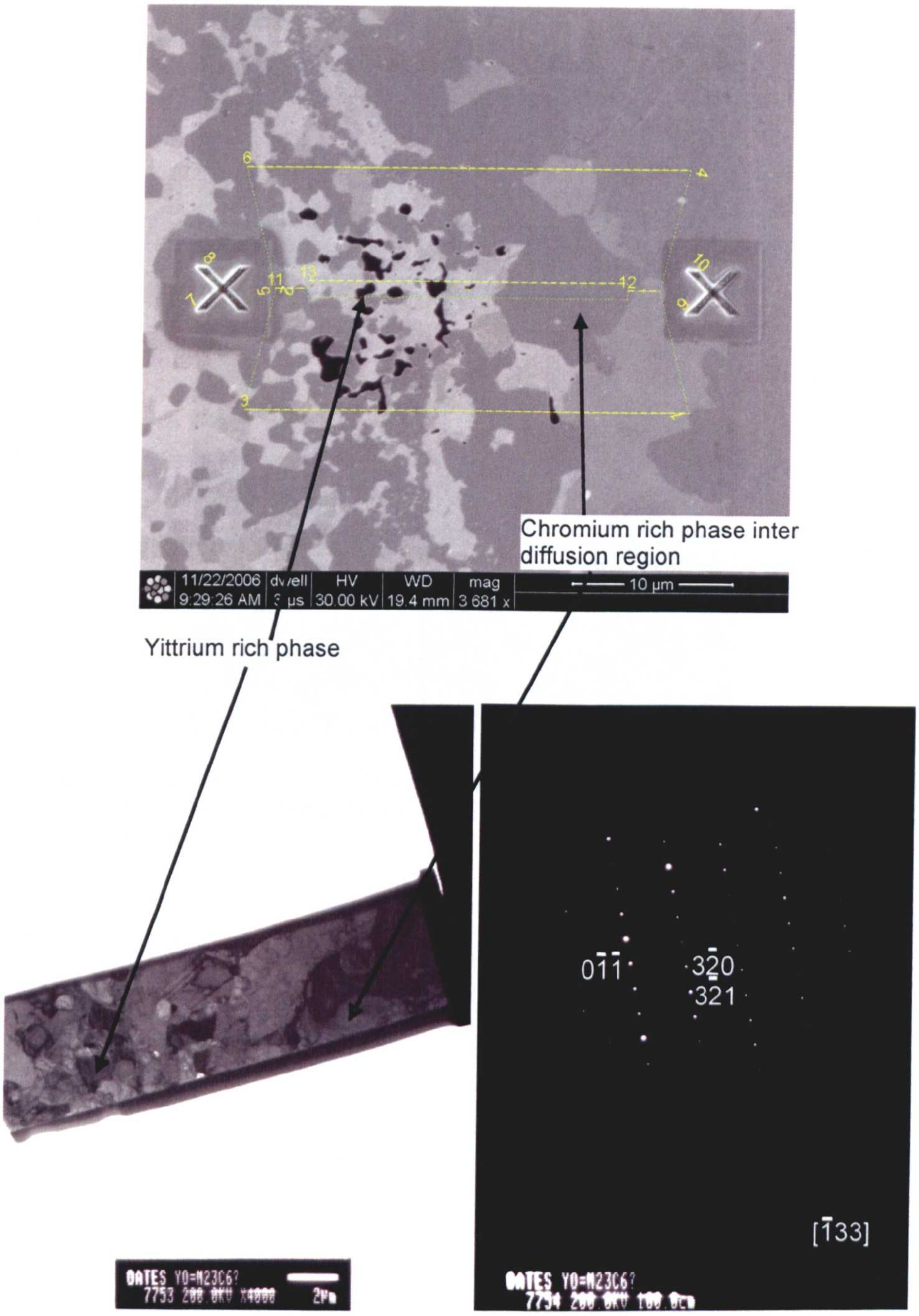

Figure 7.26 Amdry 997 coating 10,000 hour 850°C yttria rich interface phase (a) FIB SEM image of sample position (b) TEM image of thin foil and diffraction pattern indexed as Y_2O_3.

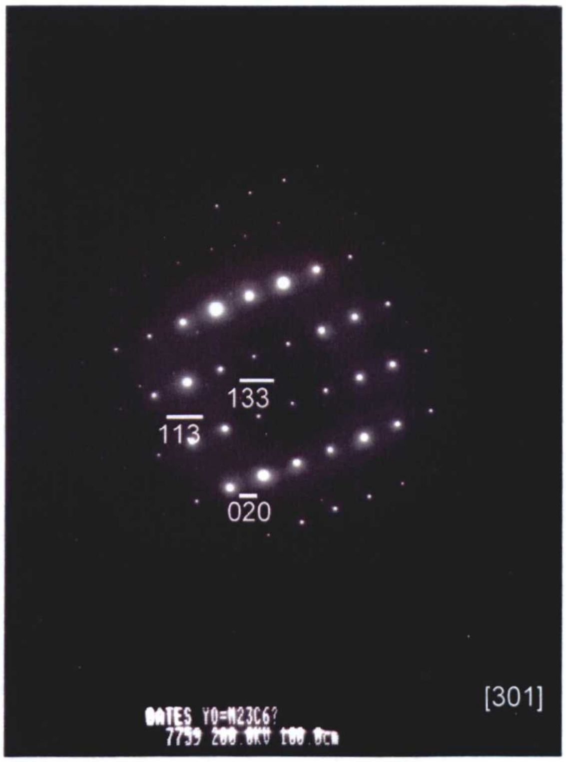

Figure 7.27 **Amdry 997 coating electron diffraction pattern for blocky phase in interdiffusion zone shown in Figure 7.26. Pattern indexes as $M_{23}C_6$ carbide.**

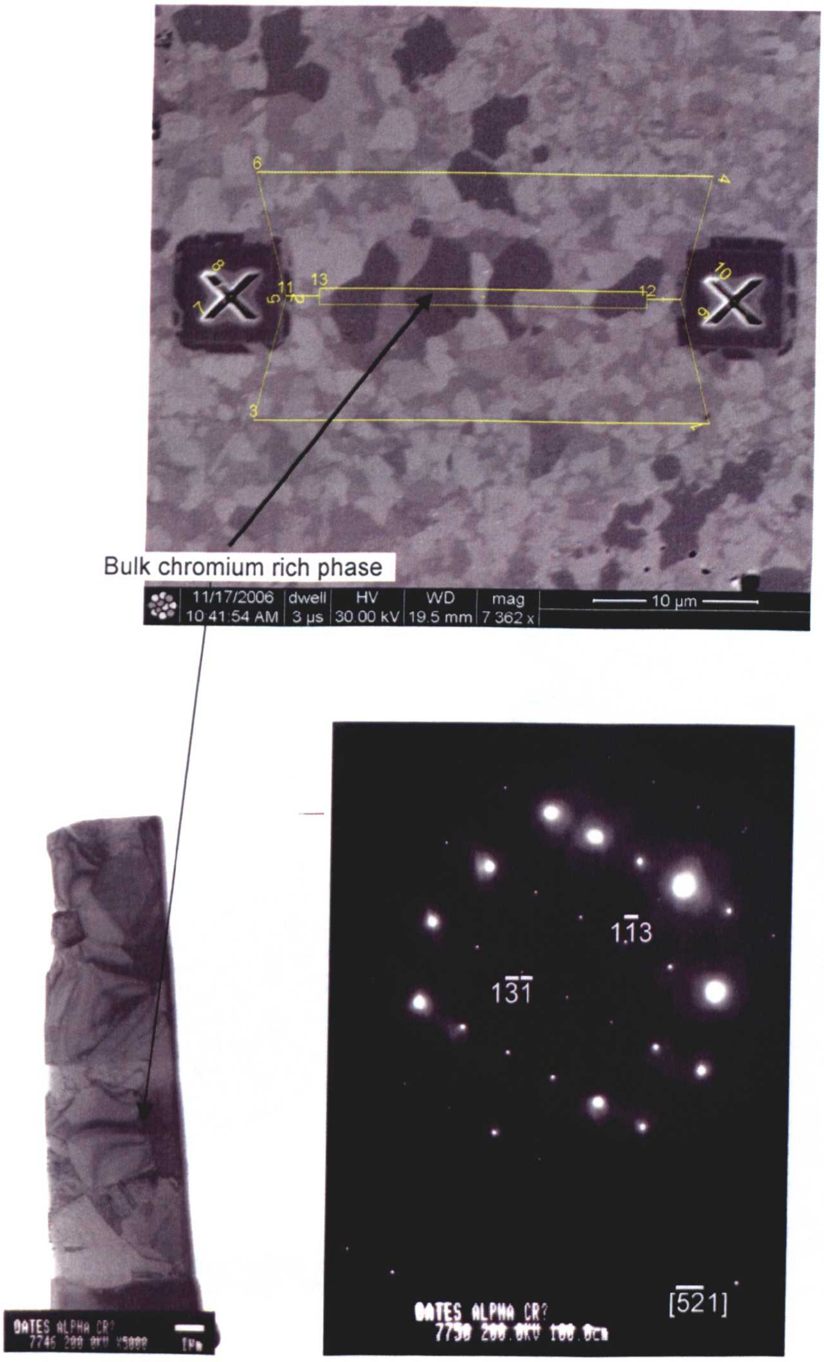

Figure 7.28 Amdry 997 coating 10,000 hour 850°C 'no ICO' sample, chromium rich phase (a) FIB SEM image of sample position (b) TEM image of thin foil and diffraction pattern indexed as $M_{23}C_6$ (FCC lattice parameter 10.66Å).

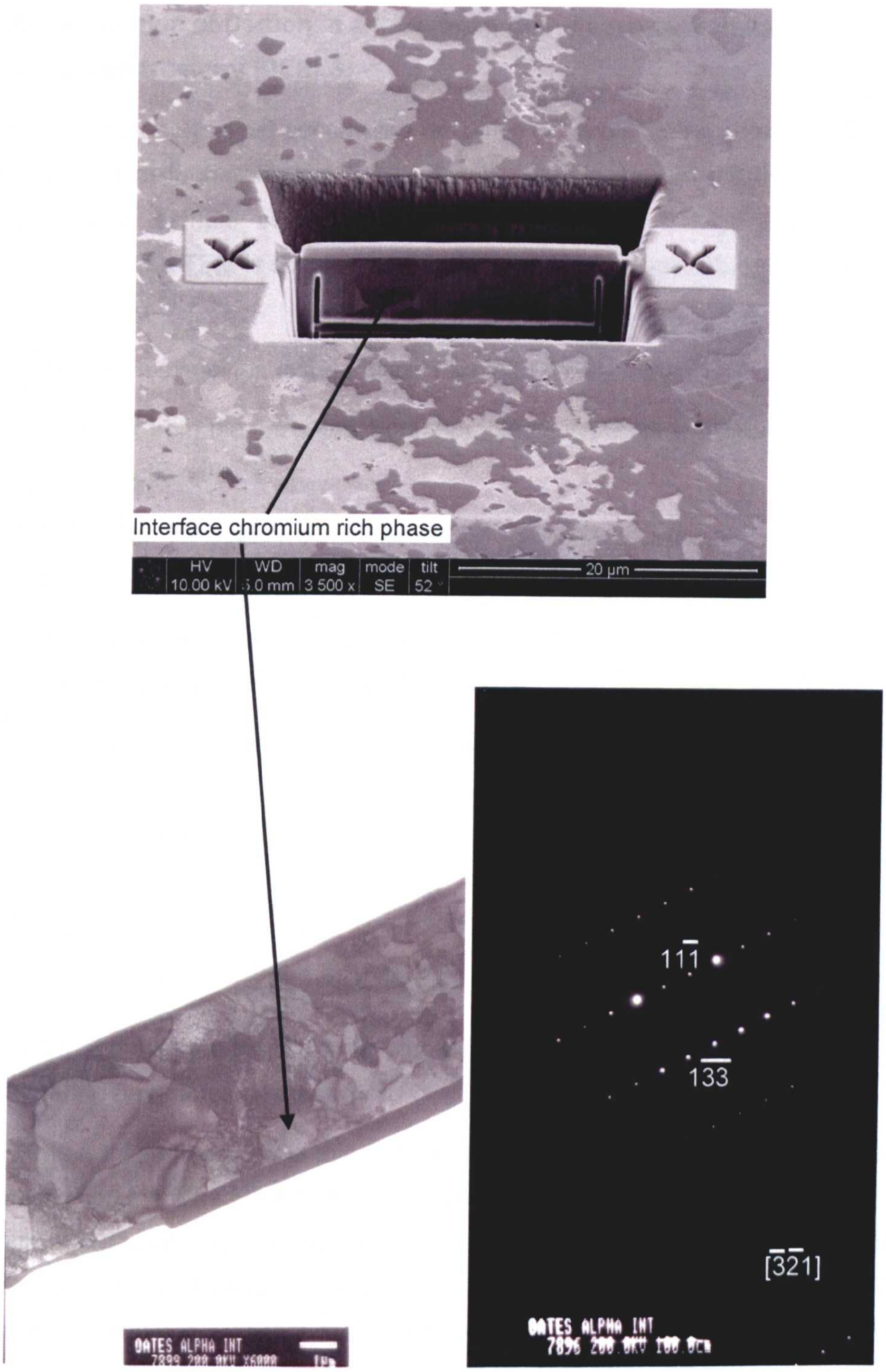

Figure 7.29 Amdry 997 coating 10,000 hour 850°C 'no ICO' sample, interface chromium rich phase (a) FIB SEM image of sample position (b) TEM image of thin foil and diffraction pattern.

7.4.2 Determination of Carbon in a Chromium Rich Phase by Parallel Electron Energy Loss Spectrometry (PEELS)

Although the WDS analysis did confirm the presence of carbon in the chromium rich phase, it was considered that further work was required to substantiate the WDS results due to the possibility of bulk sample contamination. Parallel Electron Energy Loss Spectroscopy (PEELS) attached to a TEM is considered a positive method for identifying low atomic number elements.

Three samples were examined in the Philips Tecnai F20 FEG TEM;

a) Thin foil cut from the uncoated 1,000 hour 850°C MAR M 509 sample taken through a $M_{23}C_6$ eutectic carbide.

b) Thin foil from the coated 10,000 hour 850°C sample through the chromium rich phase in the bulk of the coating.

c) Thin foil from the coated 10,000 hour 850°C sample through the chromium rich phase at the interface with the MAR M509 substrate.

From the EELS atlas(81) the expected peak positions are as follows;

Carbon = 283.8 eV

Chromium = 574 eV

Nickel = 854 eV

Cobalt = 779 eV

It was noted that during the tests a small amount of drift occurred within the system. This was not considered to have affected the results.

Figure 7.30 is a micrograph of the thin foil taken through the 1,000 hours 850°C MAR M509 $M_{23}C_6$ eutectic carbide. The FEG TEM EDS X-ray maps (Figure 7.31) show the chromium and carbon rich $M_{23}C_6$ carbides, the tungsten and carbon rich M_6C carbides and the nickel and cobalt rich γCo matrix. The PEELS trace from the carbide (Figure 7.32) show a small carbon and a larger chromium ionisation edge, whereas the PEELS trace from the γCo between the $M_{23}C_6$ eutectic carbide shows no evidence of a carbon peak (Figure 7.33).

Figure 7.34 shows a FEG TEM image of the chromium rich phase bulk sample removed from the 10,000 hour 850°C 'no ICO' sample. Three PEELS traces were taken from this sample, one from each of the two chromium rich particles and one from the γ phase between the chromium rich particles. The PEELS traces (Figure 7.35) show carbon peaks for the two chromium rich particles tested and no carbon peak on the γ trace. The process was repeated for the thin foil removed from the 10,000 hour 850°C sample which included an interface chromium rich particle (Figure 7.36). FEG TEM EDS X ray maps (Figure 7.37) show the interface chromium rich phase is rich in chromium with higher levels of carbon than the surrounding γ' phase. PEELS traces taken from the interface chromium rich phase and the γ' phase show carbon and chromium ionisation edges on the interface chromium rich phase trace and no carbon but chromium, cobalt and nickel ionisation edges on the γ' trace (Figure 7.38).

The results from the electron diffraction patterns, the SEM WDS/EDS analysis and the PEELS traces all indicate that the chromium rich phase in the 10,000 hour 850°C 'no ICO' sample contains carbon and is therefore considered to be chromium $M_{23}C_6$ carbide. However, only very limited analysis of one sample has been carried out in this investigation. Further work is required to confirm if the chromium rich phase identified in the coated samples is chromium carbide in all of the samples or if there is a transition, possibly from αCr phase to chromium carbide at a point during the ageing process. In addition, further work would be required to determine if the presence of chromium carbide in the coating is found for nickel based superalloys which have a lower carbon content than MAR M509.

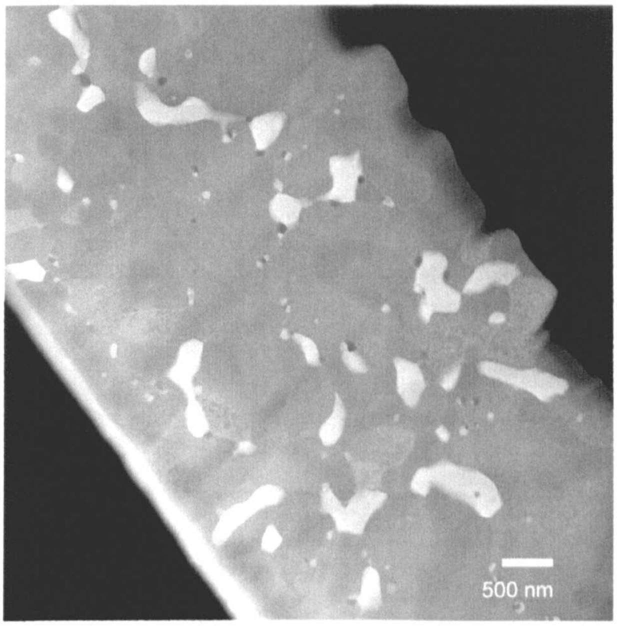

Figure 7.30 FEG TEM micrograph of MAR M509 thin foil cut through a $M_{23}C_6$ eutectic carbide from the 1,000 hour 850°C sample.

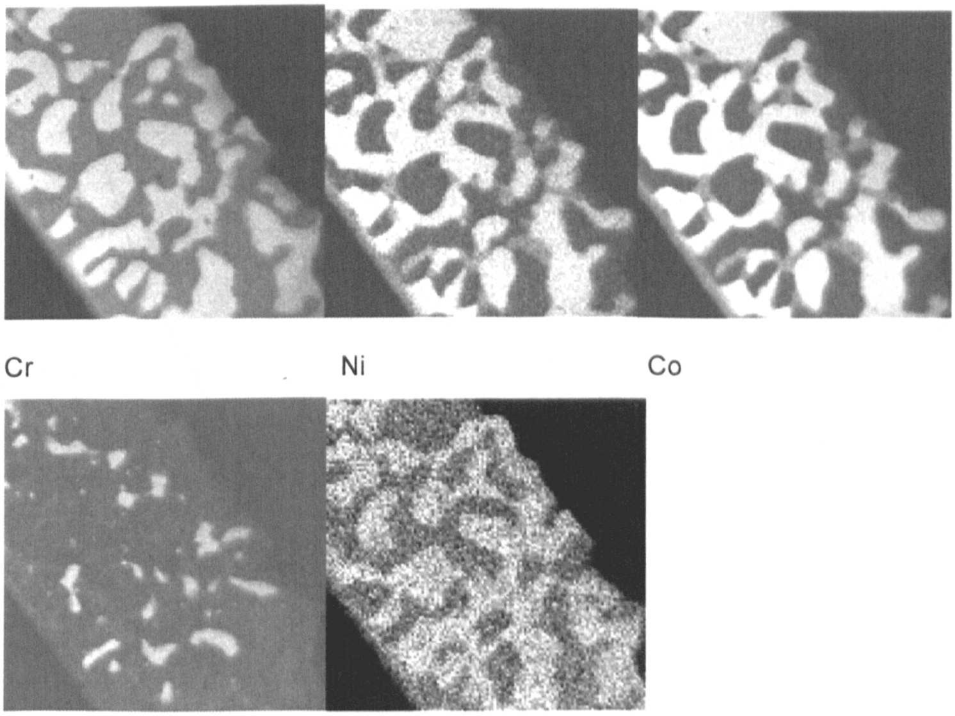

Cr Ni Co

W C

Figure 7.31 FEG TEM EDS X-ray maps from the 1,000 hours 850°C MAR M509 thin foil Cr, Ni, Co, W and C respectively.

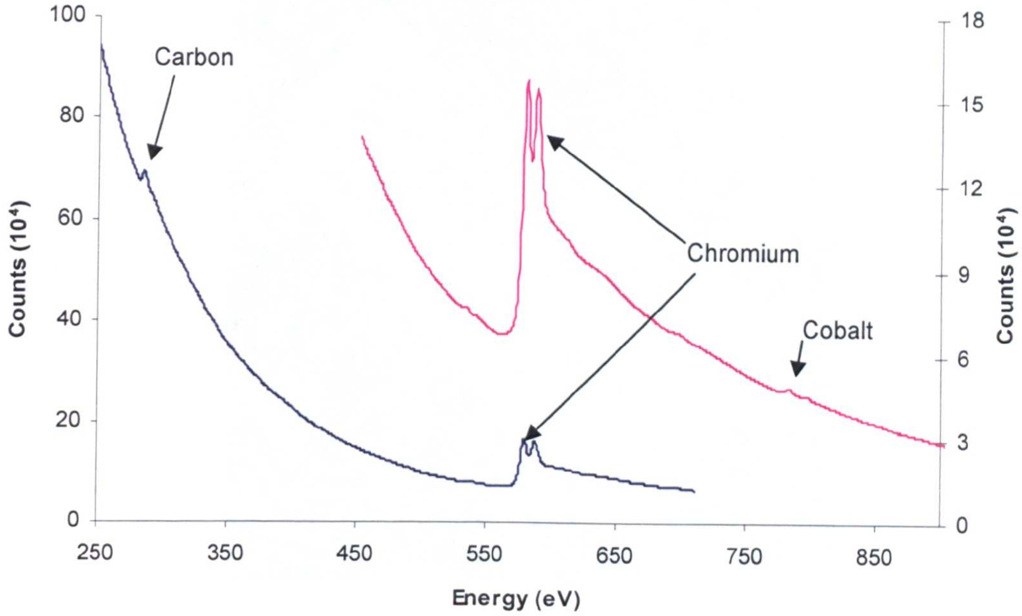

Figure 7.32 PEELS result from $M_{23}C_6$ eutectic carbide showing carbon and chromium peaks, MAR M 509 1,000 hour 850°C thin foil.

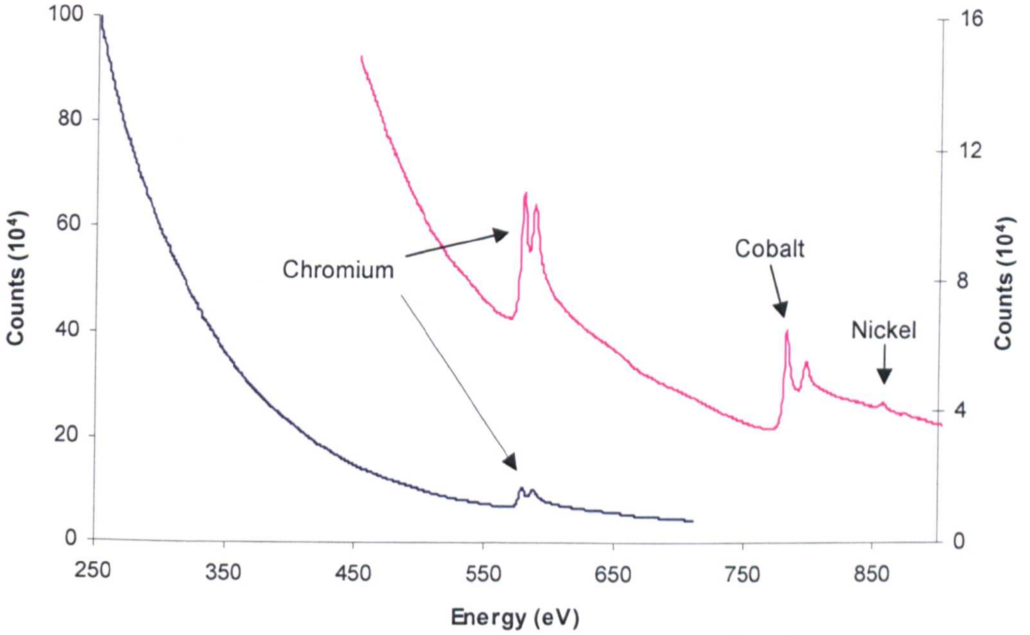

Figure 7.33 PEELS trace from γCo matrix between the $M_{23}C_6$ eutectic carbide, MAR M509 1,000 hour 850°C thin foil.

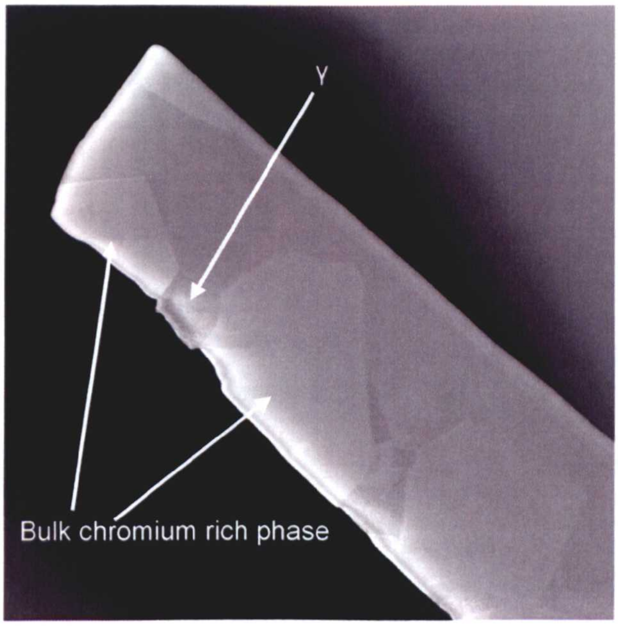

Figure 7.34 FEG TEM micrograph of thin foil cut through the bulk chromium rich phase, 10,000 hour 850°C 'no ICO'

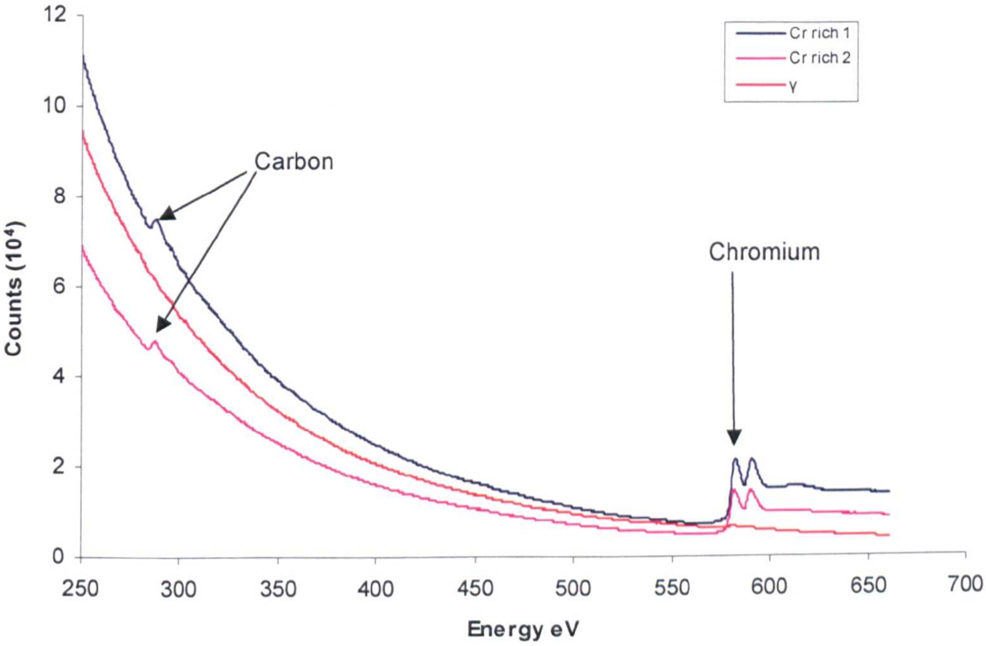

Figure 7.35 PEELS traces from bulk chromium rich phase and γ, 10,000 hour 850°C 'no ICO' thin foil.

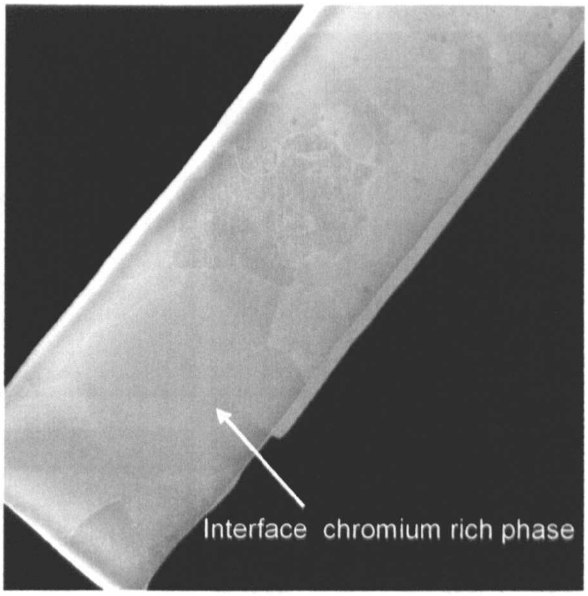

Figure 7.36 FEG TEM micrograph of thin foil cut through the Amdry 997 interface chromium rich phase, 10,000 hour 850°C 'no ICO'.

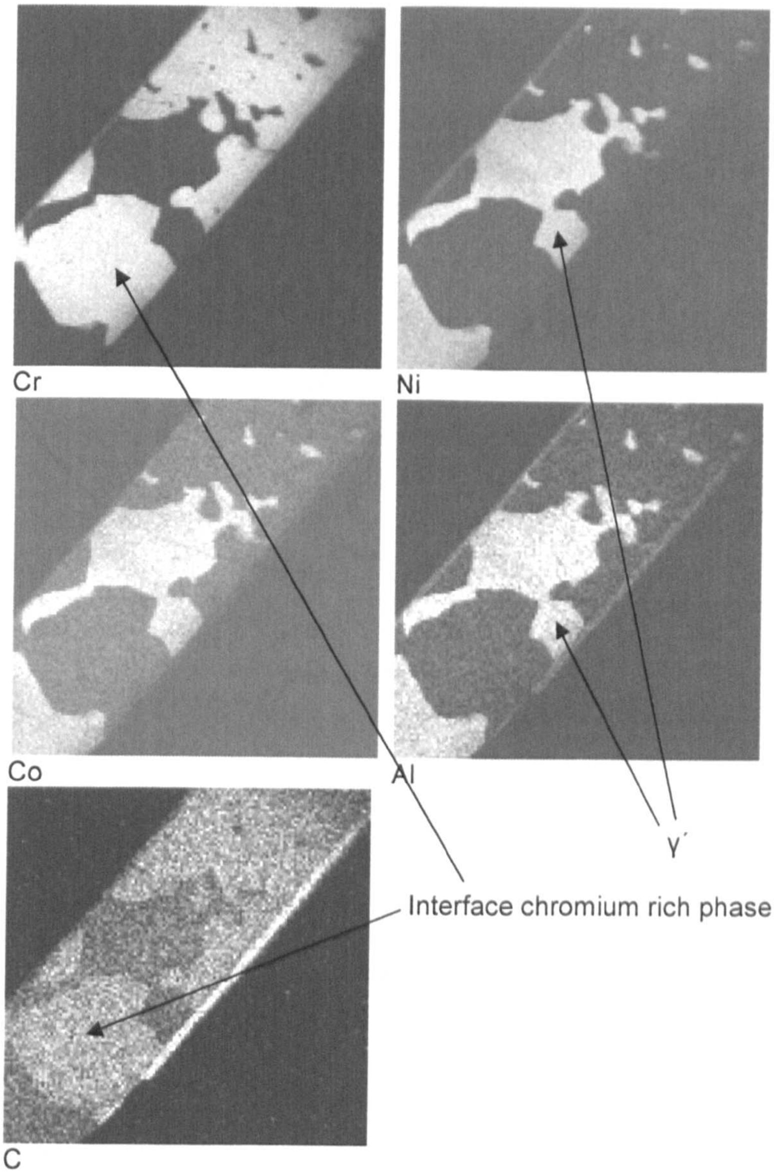

Figure 7.37 **FEG TEM EDS X-ray maps of Cr, Ni, Co, Al and C from the Amdry 997 interface chromium rich phase thin foil, 10,000 hour 850°C 'no ICO'.**

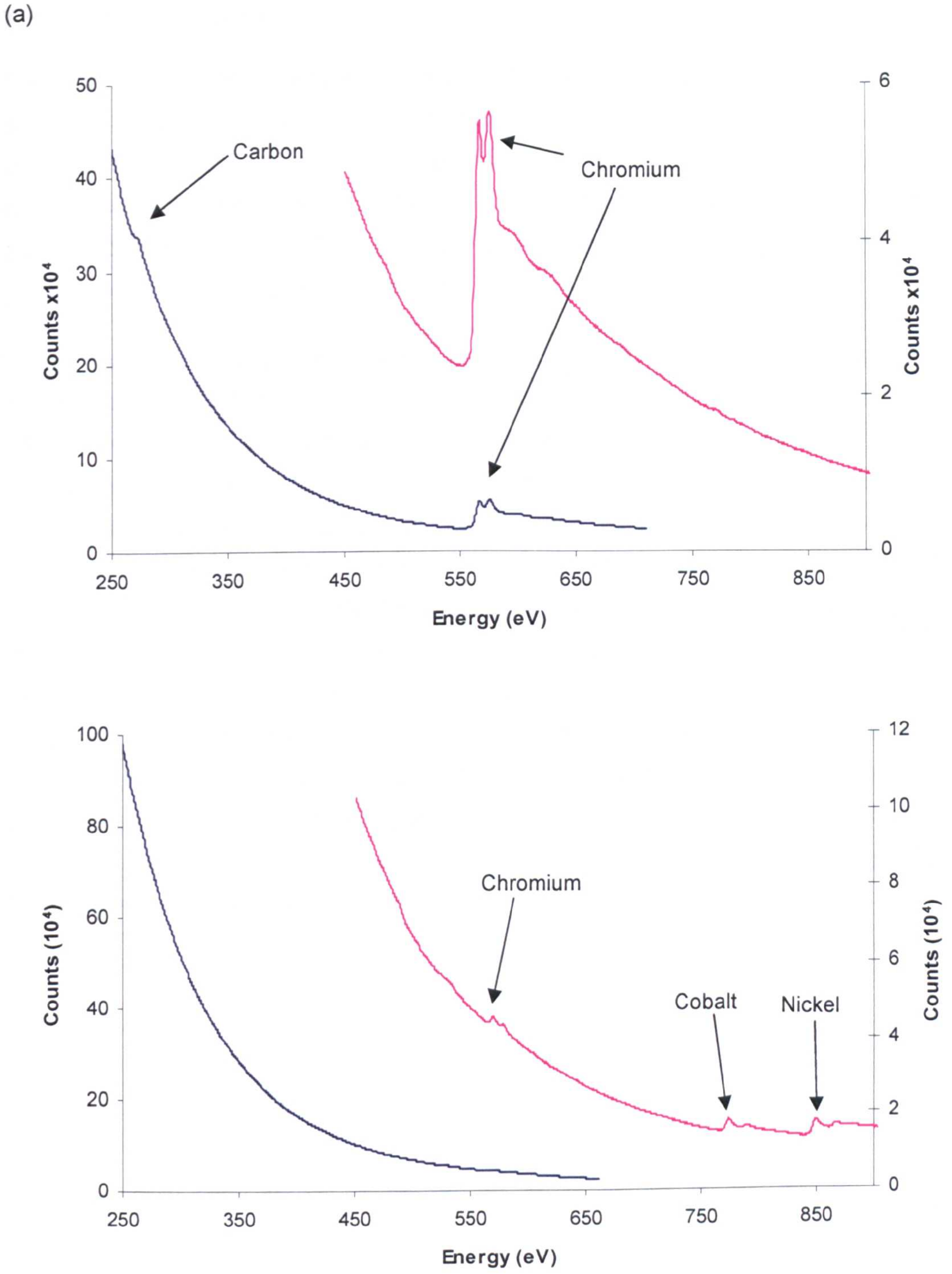

Figure 7.38 FEG TEM PEELS traces from interface chromium rich phase thin foil (a) interface chromium rich phase and (b) γ phase, 10,000 hour 850°C 'no ICO'.

7.5 γ′ image analysis

The images presented in Figure 7.39 are BSE images from the 'no ICO' samples aged at 900°C for times up to 25,000 hours. The images show visually an increase in the size of γ′ with time up to 15,000 hours. At 25,000 hours there is an apparent reduction in the level of γ′ when compared to the 15,000 hour sample. In addition the samples show the loss of β (dark grey particles) evident in the 1,000 – 15,000 hours samples and the increase in the chromium rich phase (black particles) across all times.

Image analysis of the γ′ phase was carried out on ten mid coating images, taken at a magnification of 3000 times, from each of the 'no ICO' coating samples. The results (Figure 7.40) show that in general there is a small increase in the γ′ area fraction from 1,000 hours to 15,000 hours with an approximately constant area fraction at 20,000 and 25,000 hours. The 1000°C samples show a relatively constant γ′ area fraction. The plot of γ′ area fraction against ageing temperature shows a small change in γ′ area fraction with temperature. This is significantly different from the JMatPro predictions which show a drop from ~60 wt.% at 800°C to 13 wt.% at 1000°C. Although the results are in area fraction and the JMatPro predictions are in wt.% such a significant change in γ′ would be detectable by image analysis assuming that equilibrium has been reached. However, as a result of the diffusion taking place from the coating to the TGO and substrate and diffusion from the substrate to the coating this is a dynamic system and as such may never reach equilibrium. The measured variation of γ′ area fraction in the coating is too small to allow this measure to be used for the prediction of operating temperature of coated samples.

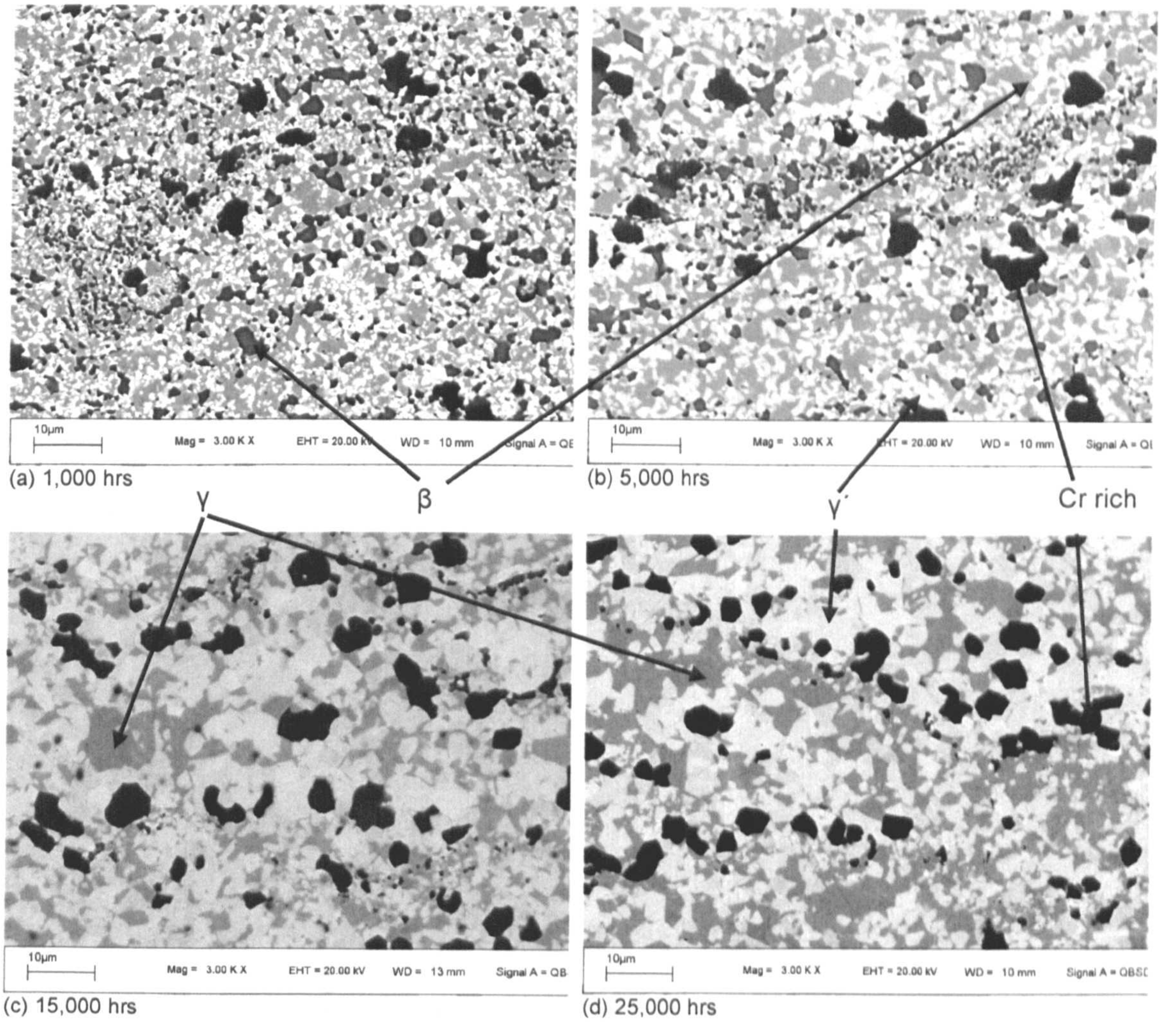

(a) 1,000 hrs

(b) 5,000 hrs

(c) 15,000 hrs

(d) 25,000 hrs

Figure 7.39 SEM BSE images of Amdry 997 coating microstructure from 'no ICO' samples aged at 900°C (a) 1,000, (b) 5,000, (c) 15,000 and (d) 25,000 hours respectively.

(a)

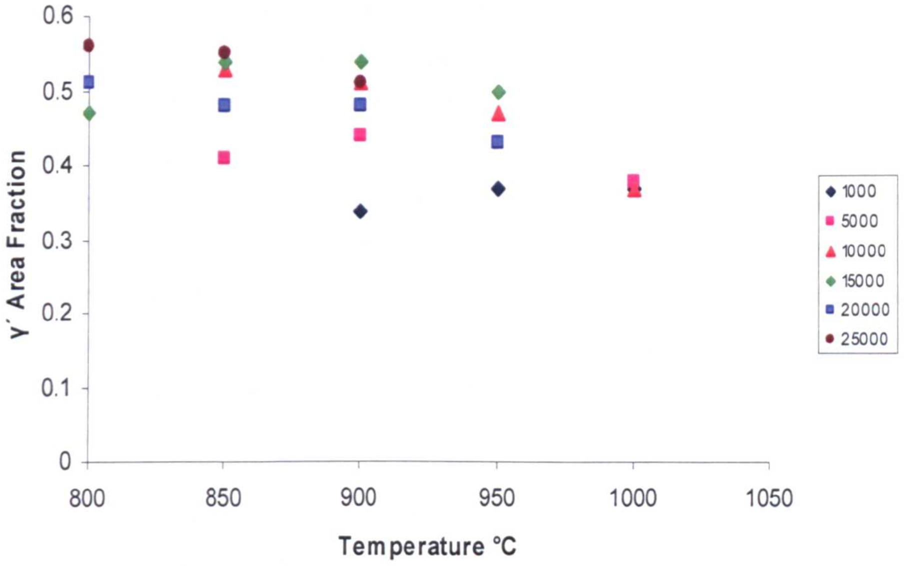

(b)

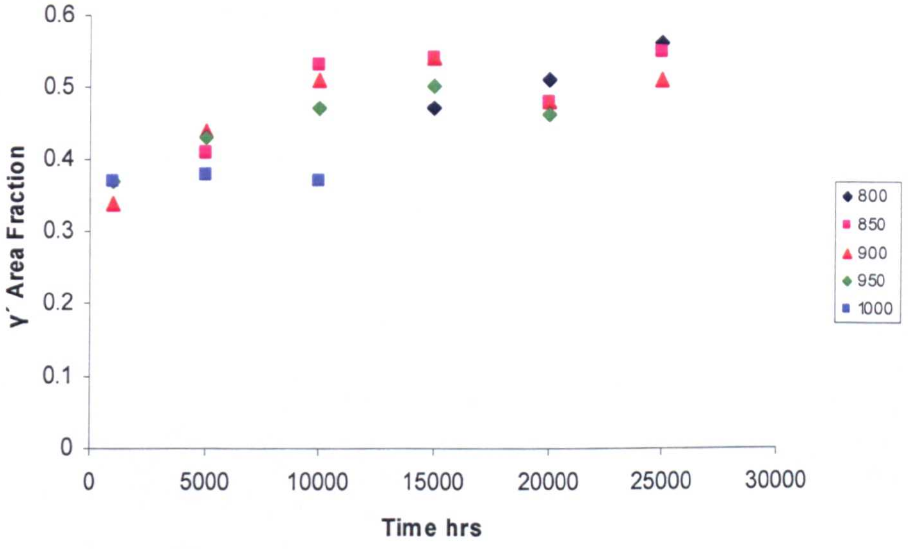

Figure 7.40 Amdry 997 coating γ´ image analysis results 'no ICO' sample plotted as a function of (a) temperature and (b) time s.

7.6 Coating Denudation

It was apparent from observation of the samples that the width of the denuded layer on the substrate side of the coating was wider than the denuded layer on the TBC side of the coating (Figure 7.41). This would suggest that the life of the coating in these samples is limited by the diffusion of aluminium into the substrate rather than the formation of thermally grown oxide. It was considered that the variation in the width of the inner denuded layer with time and temperature could be used to predict time/temperature of coated components and could be used to indicate the effect of 'ICO' on coating life. However, it is also apparent from Figure 7.41 that the width of the coating on the 'ICO' samples was thinner than the coating on the 'no ICO' samples. This may have influenced the outcome of the coating denudation. However, it was considered that the results would be valid where a layer of γ' separates the inner and outer denuded layers of the coating.

The width of the coating and the width of the inner denuded layer were measured at twenty positions along the samples using an optical microscope. Figure 7.42 is a plot of the fraction denuded with respect to the coating width against ageing temperature and shows that the rate of denudation of the coating on the 'ICO' samples was approximately three times faster than the coating on the 'no ICO' samples. Plots (c) and (d) show the results plotted against time$^{1/2}$ seconds and show that denudation in the coating is approximately linear with time$^{1/2}$. However, there is a deviation in the line at higher temperatures which is more evident in the 'no ICO' samples. The deviation indicates an increased rate of denudation and for the 'no ICO' samples broadly occurs following the removal of β phase from the coating (Table 7.2) Measurement of the width of the denuded layer could be used to predict the operating temperature of the component if the time in service is known.

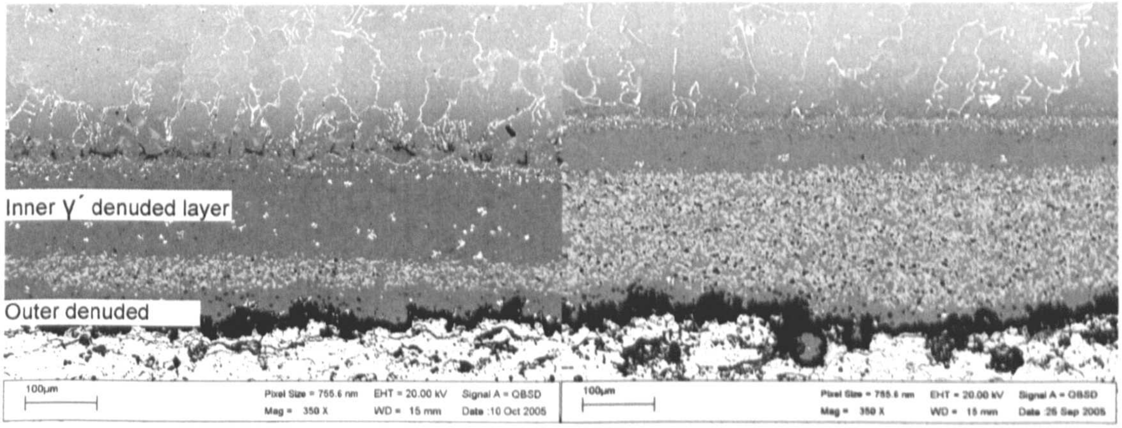
(a) (b)

Figure 7.41 SEM BSE images illustrating the variation in Amdry 997coating width for 15,000 hour 950°C samples (a) 'ICO' (b) 'no ICO' and the wider inner denuded layers on both samples.

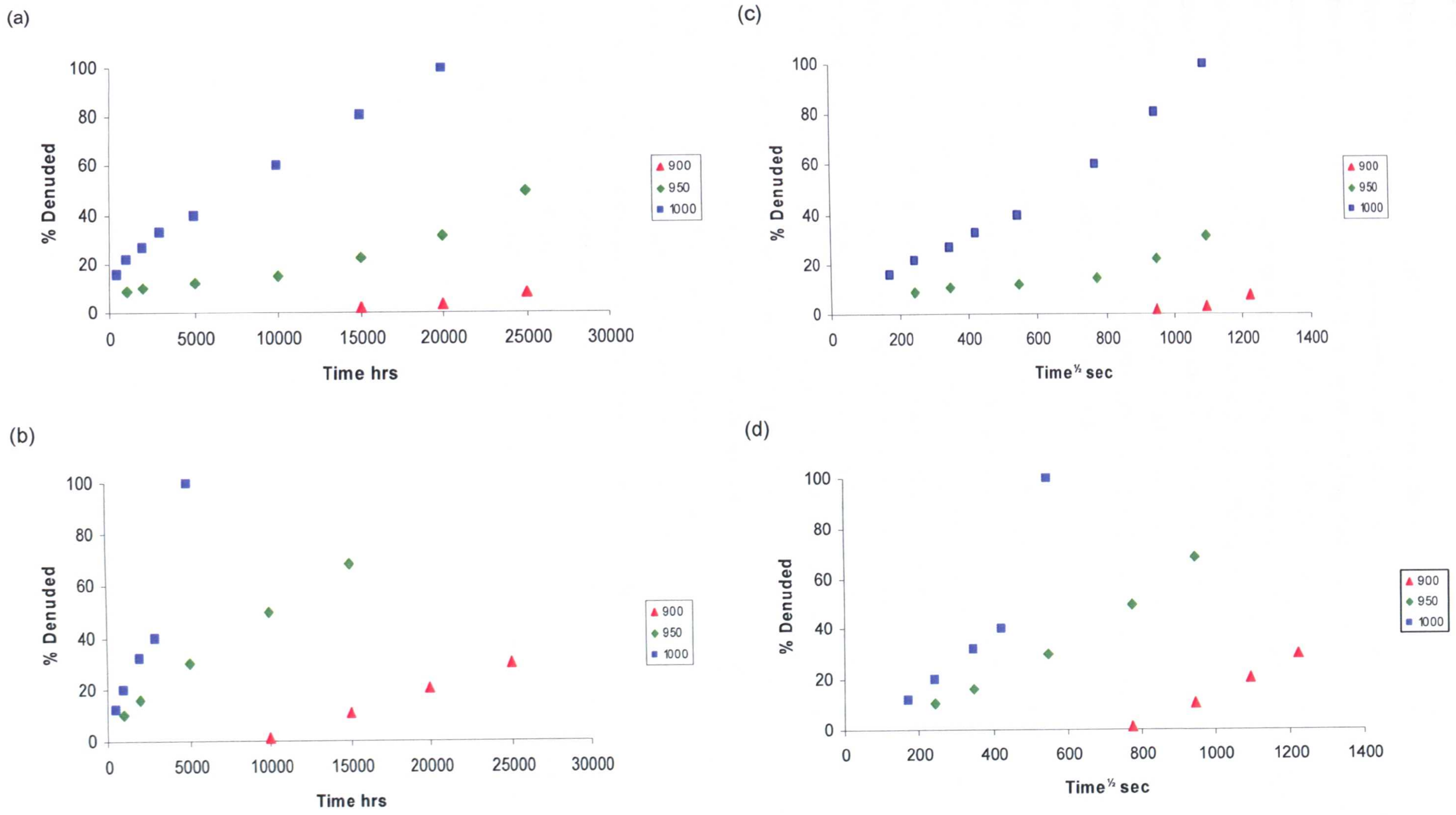

Figure 7.42 Amdry 997 coating inner denuded layer percent denude for (a and c) 'no ICO' samples (band d) 'ICO' samples respectively.

7.7 Aluminium diffusion in γ

To understand the diffusion of elements from the coating into the substrate and from the substrate into the coating, EDS spot analysis were carried out in a line from the coating γNi phase through the interdiffusion layer into the γCo of the MAR M509 substrate, at a minimum of three positions along each sample. Figure 7.43 illustrates the results from the 950°C samples at 1,000 hour and 20,000 hour. The results show there are significant changes across the interdiffusion zones where a balance is achieved between the composition of the coating and the bulk composition of the substrate. Of note are the increased levels of aluminium and nickel and the reduced levels of tungsten and cobalt in the interdiffusion zone when compared to the coating and substrate analysis. The interdiffusion zone of the 1,000 hour and 20,000 hour samples were measured as approximately 52 μm and 140 μm respectively.

Figure 7.44 is a plot of the aluminium content (wt.%) against distance from the interface for the 20,000 hours 950°C sample with 'ICO' showing four aluminium traces and the reproducibility of the technique. Figure 7.45 illustrates the changes in the aluminium traces with time. The traces have been used very simply to investigate the diffusion of aluminium from the coating into the γ Co MAR M509 substrate by taking the distance from the interface to the point at which the aluminium is at 1 wt.%. and plotting this against temperature (Figure 7.46) for both the 'ICO' and 'no ICO' samples. The results do show the expected increase in the diffusion of aluminium with time. However, there is very little difference between the 'ICO' and 'no ICO' samples. Figure 7.47 details the results from the 1,000 hour, 10,000 hour and 20,000 hour samples showing the small variations, both positive and negative, between the 'ICO' and 'no ICO' samples. Error bars are plotted in Figure 7.47. The increase in the width of the error bars at longer times and higher temperatures is considered to be a result of the flattening of the curves through 1 wt.% aluminium. The results show there is no significant difference between the 'ICO' and 'no ICO' samples with regards to the diffusion of aluminium through the γNi in the coating into the γCo substrate. However, it has been shown (Chapter 7.6) that denudation of the coating occurs three times faster for the 'ICO' samples than the 'no ICO' samples.

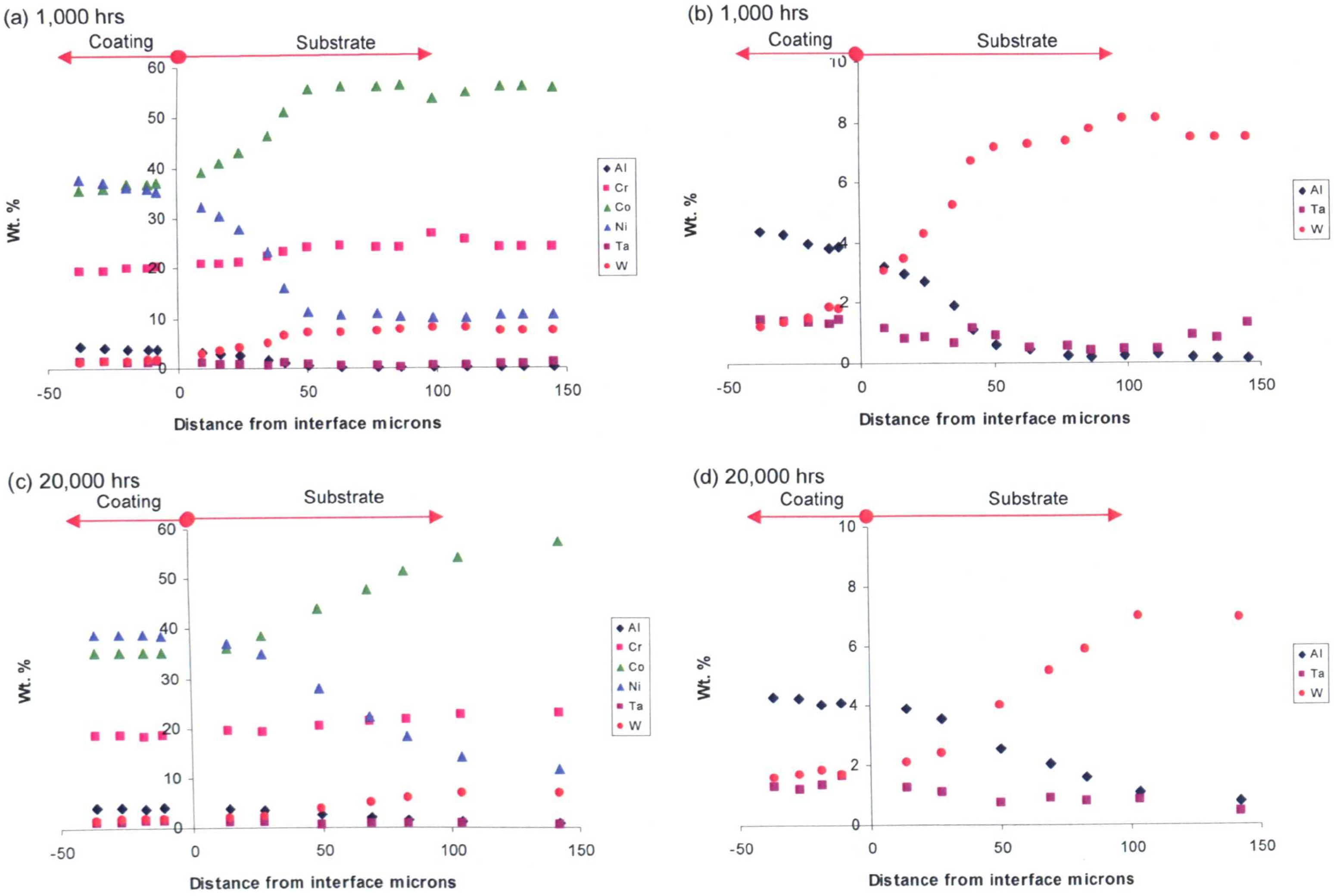

Figure 7.43 **Amdry 997 coating EDS spot traverses from denuded layer into substrate 950°C samples (a) 1,000 hour (b) 1,000 hour rescaled, (c) 20,000 hour and (d) 20,000 hour rescaled respectively.**

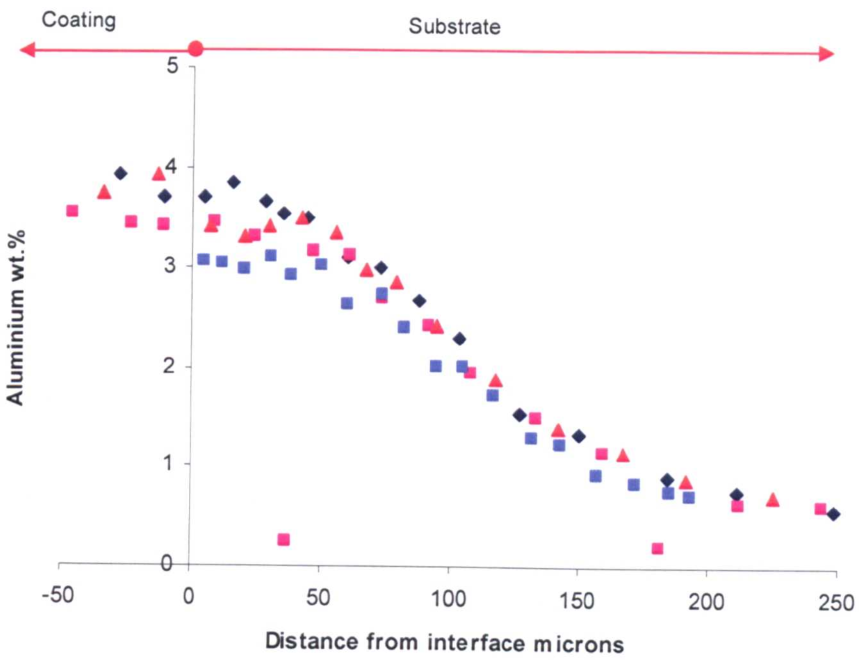

Figure 7.44 Aluminium measurements from the 20,000 hour 950C 'ICO' sample showing repeatability of the spot analysis measurements.

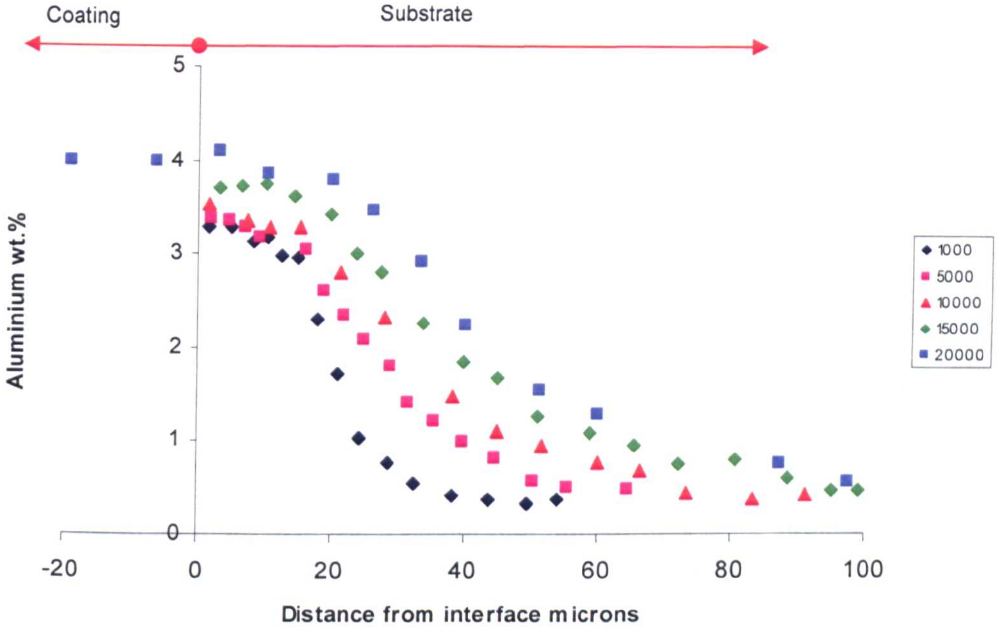

Figure 7.45 Aluminium traces from Amdry 997 coating into substrate for the 950°C 'no ICO' samples for various ageing times.

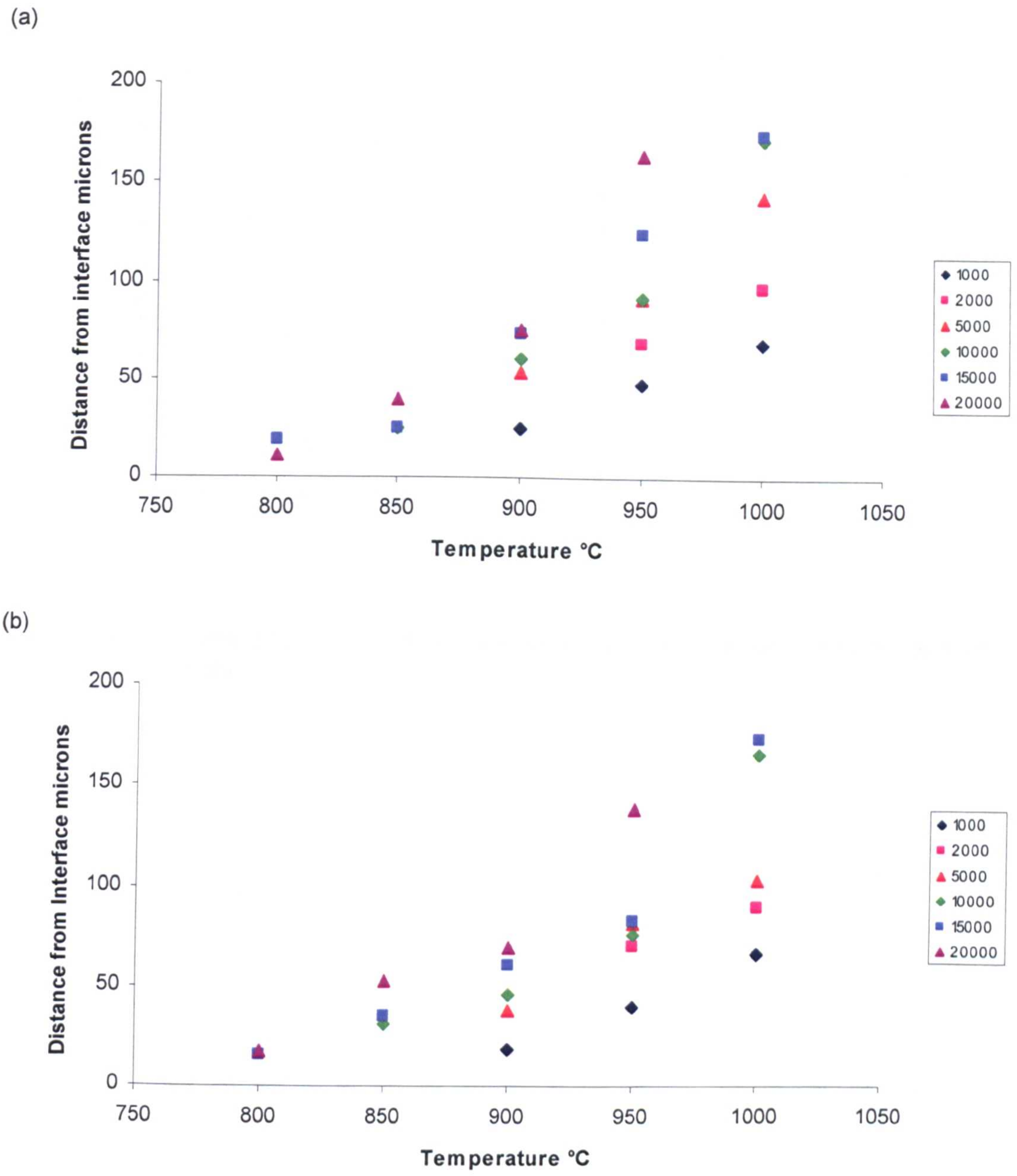

Figure 7.46 Aluminium EDS trace position of measured 1 wt.% aluminium from interface (a) 'no ICO' samples and (b) 'ICO' samples.

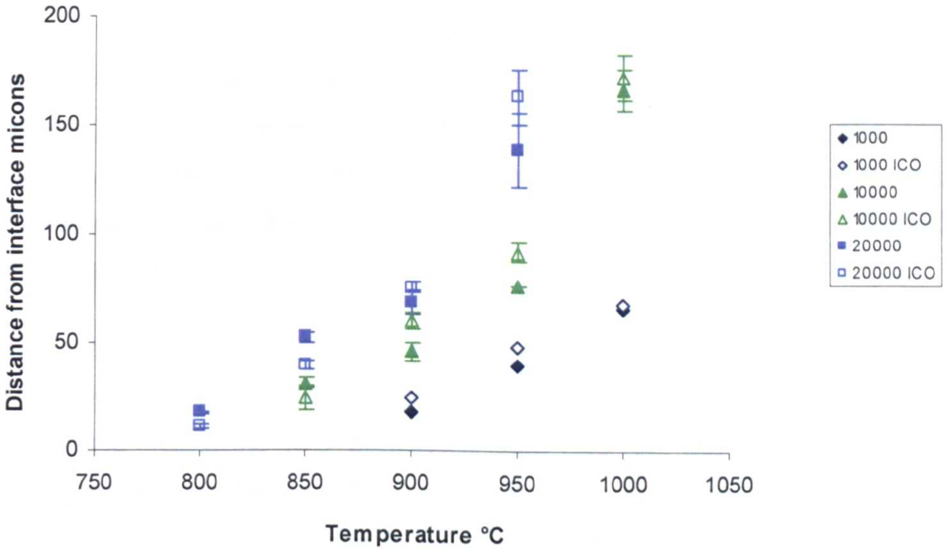

Figure 7.47 Comparison of 1 wt.% aluminium 'ICO' and 'no ICO' samples with error bars.

7.8 Effect of Inter-Carbidic Oxidation on Aluminium Diffusion

The results from the previous chapter show there is no significant difference between the 'ICO' and 'no ICO' samples with regards to the diffusion of aluminium through the γNi in the coating into the γCo substrate. However, it has been shown (Chapter 7.6) that denudation of the coating occurs three times faster for the 'ICO' samples than the 'no ICO' samples. In order to show why the coating denudes faster on the 'ICO' samples further SEM, FEG-SEM FIB and TEM work was carried out.

'ICO' in the original cast plates is evident as particles of zirconia (ZrO_2) close to the surface of the casting (Figure 7.48 (a)). The SEM images of the aged 'ICO' samples show in SEM BSE mode a black phase around the 'ICO' particles (Figure 7.48 (b)). SEM EDS mapping of the aged 'ICO' sample (Figure 7.49) show the black phase to be rich in aluminium with a central core rich in zirconium. The EDS detector attached to the Leo 1455 VP SEM has a beryllium widow which precludes the quantitative analysis of oxygen. However, if oxygen is present it will be detected and will show as an oxygen peak on the EDS trace. EDS spot analysis of the aged 'ICO' samples confirmed the presence of oxygen in the outer aluminium rich layer and in the zirconium rich core. The results of the EDS analysis suggest that aluminium diffusing from the coating into the substrate leaches oxygen from the zirconia to form Al_2O_3 leaving a central core of zirconium/zirconia.

$$3ZrO_2 + 4Al = 2Al_2O_3 + 3Zr$$

A thin foil sample was removed from the inter-diffusion zone of the 15,000 hour 900°C 'ICO' sample (Figure 7.50) to investigate further the aluminium rich phase around the 'ICO' and the nature of the zirconium rich core. X-Ray mapping of the 'ICO' phase in the foil (Figure 7.51) showed within the zirconium rich core a large area rich in oxygen and a second smaller area low in oxygen (Figure 7.51). TEM selected area diffraction patterns were taken from the aluminium rich phase and from the two areas within the zirconium core.

The aluminium rich phase around the aged 'ICO' Figure 7.50 was considered to be Al_2O_3 (Hexagonal, lattice parameters 5.54 and 9.02Å). Electron diffraction patterns from the two areas were considered to be zirconia, however, it was not possible to differentiate between ZrO (FCC lattice parameter 4.62Å) and ZrO_2 (Tetragonal lattice parameters 5.12 and 5.25Å).

Ellingham diagrams are plots of the free energy of formation of a metal oxide per mole of oxygen (O_2) against temperature (°K). The diagram is a useful pictorial representation of the relative stability of metal oxides (Figure 7.53). The metals in the more stable oxides (lower on the chart) can chemically reduce the metals in the less stable oxides (higher on the chart). The Ellingham diagram shows that above 800°C the ZrO_2 line is below the Al_2O_3 line and as such aluminium would not remove oxygen from the zirconia. However, there are drawbacks to the Ellingham diagram in that the G° values do not take into account chemical activities which may be different from unity, and no account of the kinetics of the reaction is taken in measurements of thermodynamic quantities.

In summary it is considered that the increased denudation in the coating on the 'ICO' samples (Figure 7.40) is a direct result of the formation of Al_2O_3 around the 'ICO' particles.

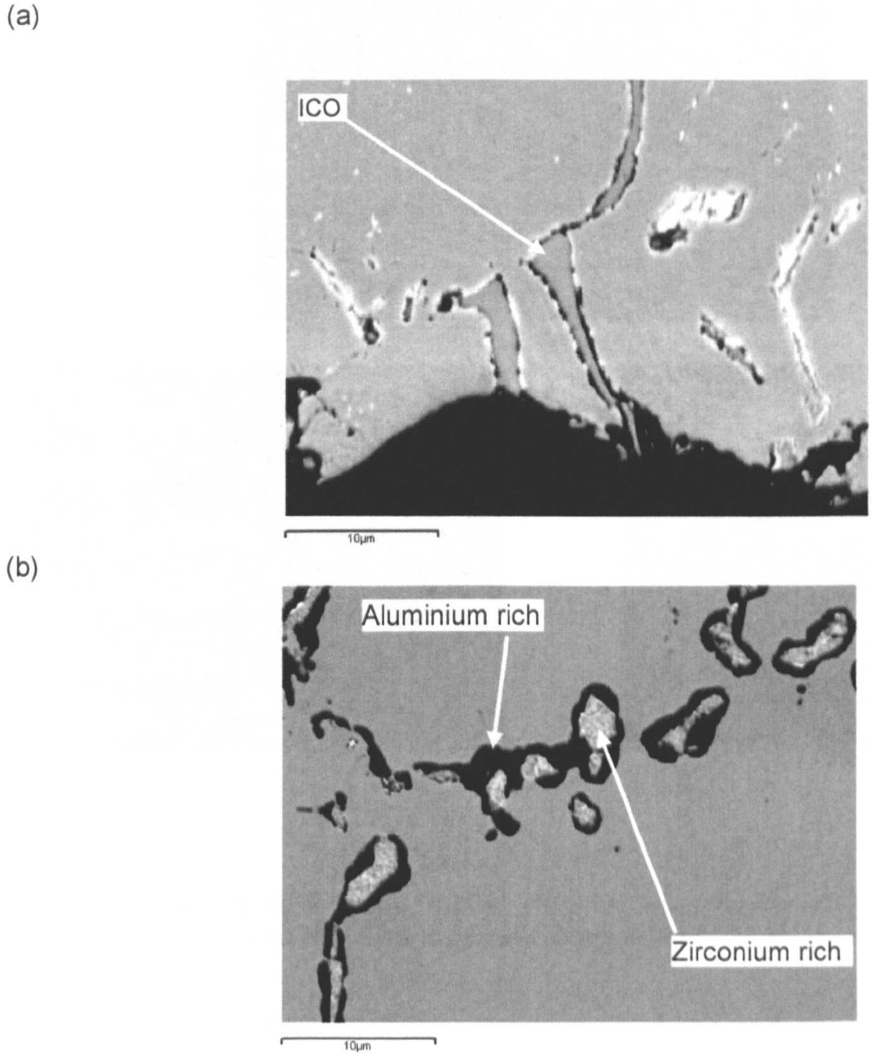

Figure 7.48 SEM BSE images of (a) 'ICO' in the as-cast MAR M 509 sample and (b) 'ICO' surrounded by a black phase in the Amdry 997/MAR M509 950°C 15,000 hour sample.

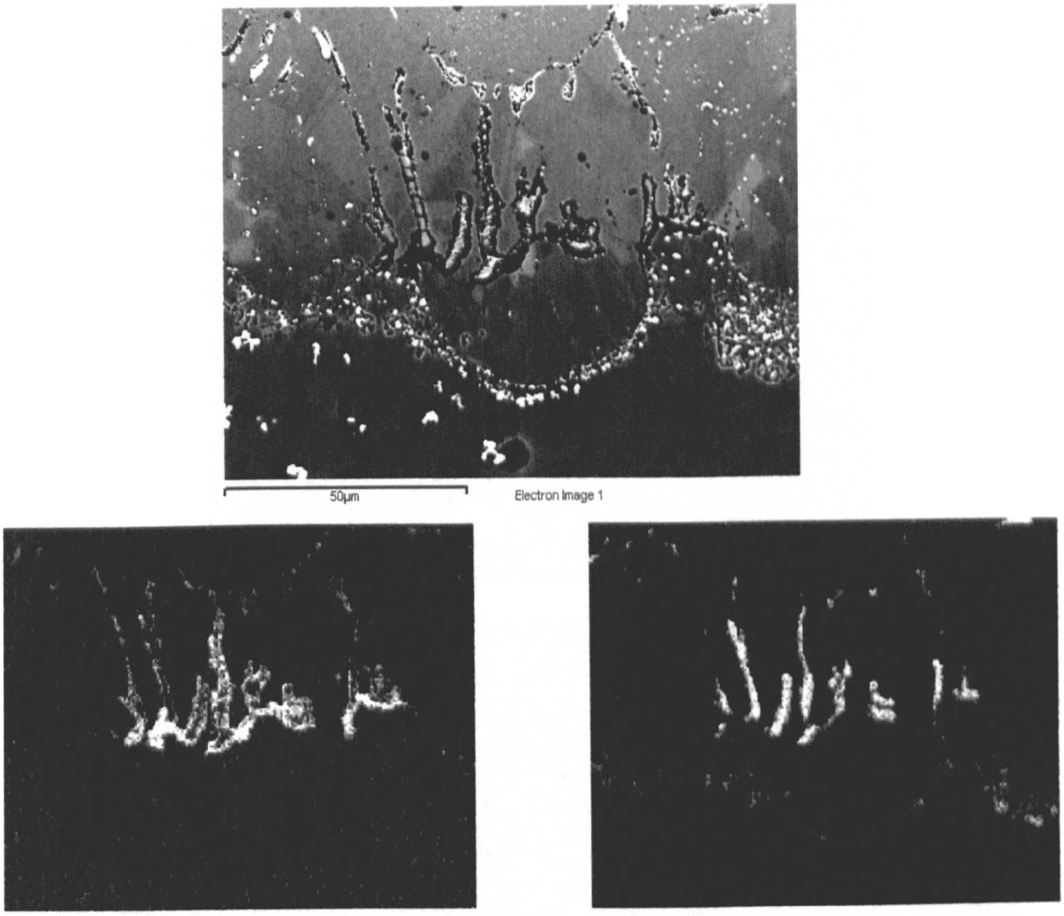

Al Ka1

Zr La1

Figure 7.49 SEM BSE image from 950°C 5,000 hour Amdry 997/MAR M509 'ICO' sample and EDS maps showing aluminium and zirconium.

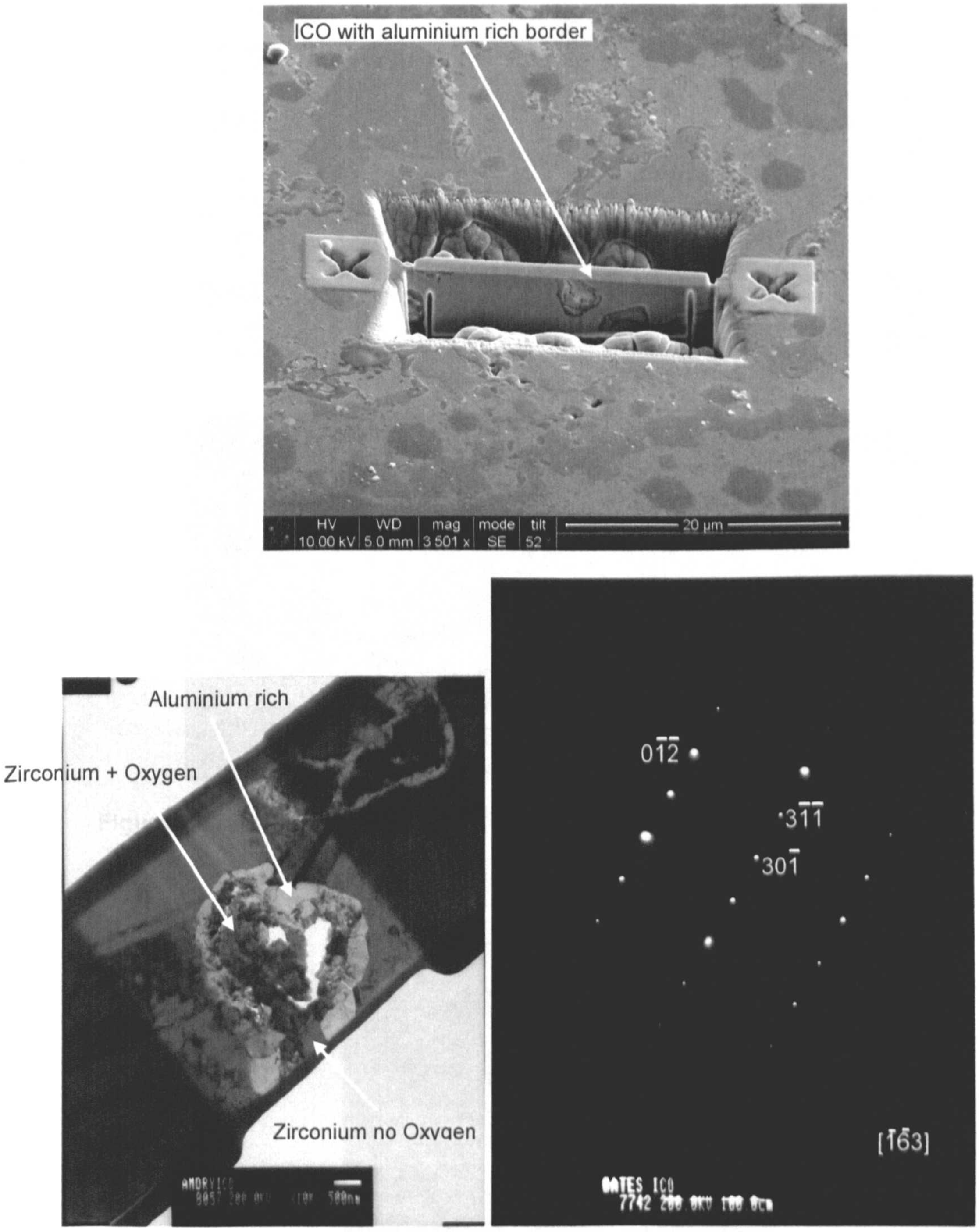

Figure 7.50 Amdry 997/MAR M509 900°C 15,000 hour 'ICO' sample (a) FIB SEM image of sample position (b) TEM image of thin foil and diffraction pattern of aluminium rich phase around 'ICO' indexed as Al_2O_3.

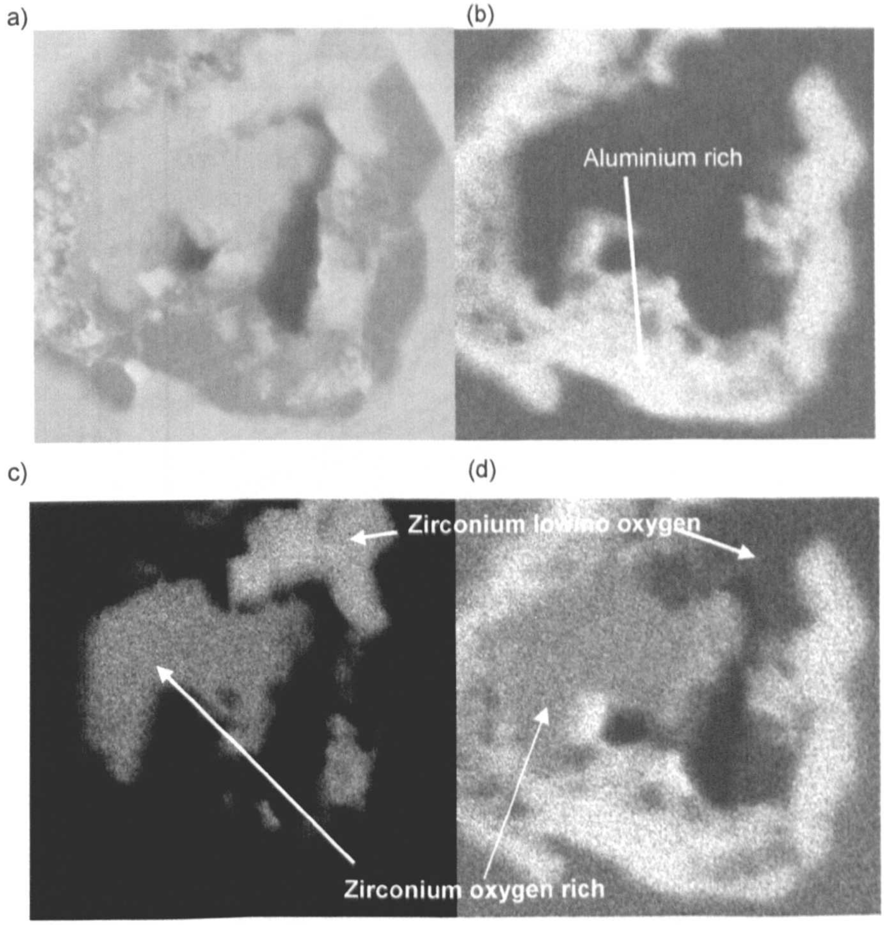

Figure 7.51 Amdry 997/MAR M509TEM EDS X-ray mapping of 900°C 15,000 hour 'ICO' sample showing (a) TEM image, (b) aluminium map, (c) zirconium map and (d) oxygen map.

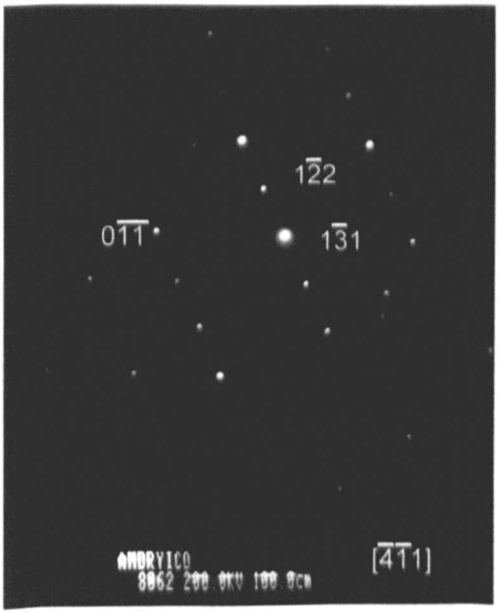

Figure 7.52 Electron diffraction patterns from Amdry 997/MAR M509 900°C 15,000 hour 'ICO' sample, zirconium rich with oxygen indexed as ZrO (FCC lattice parameter 4.62Å).

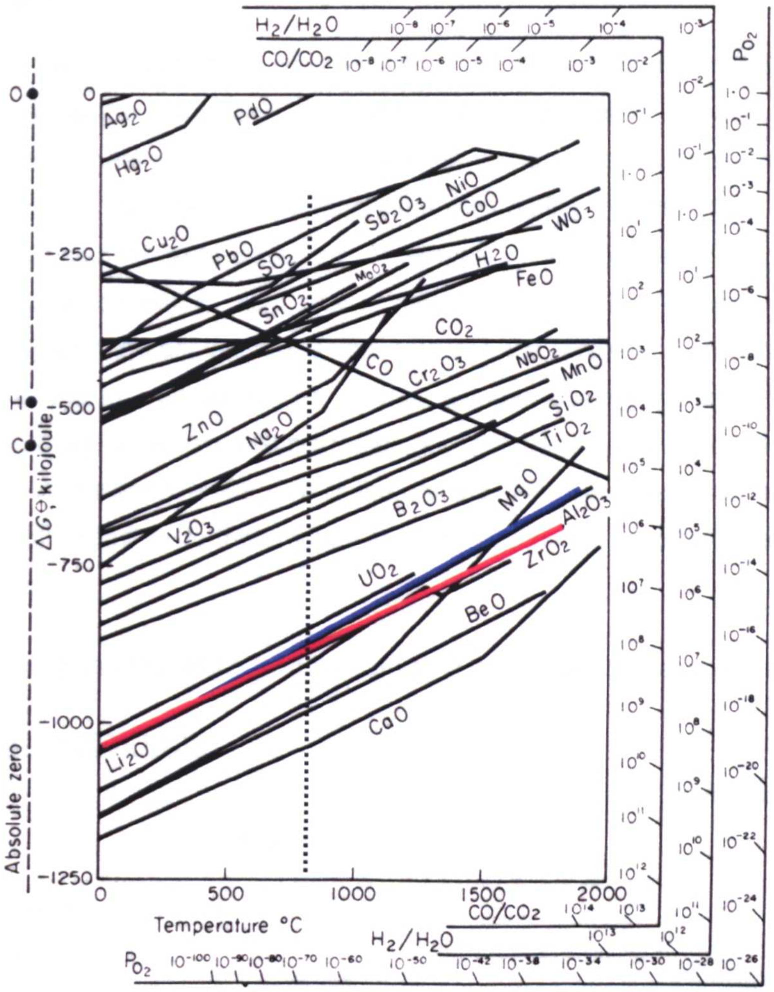

🟦 Al_2O_3

🟥 ZrO_2

Figure 7.53 Ellingham diagram highlighting the Al_2O_3 and ZrO_2 lines.

7.9 Summary

The results of the microstructural investigations carried out on the coated MAR M509 samples, both with and without 'ICO', showed that the initial coating microstructure, following the 1000°C diffusion heat treatment, comprised fine γ and β with an indeterminate very fine aluminium rich phase. With time and temperature the coating microstructure coarsened and changes in phase stability were observed. At temperatures from 800-950°C as β goes into solution, γ′ and a chromium rich phase (not evident in the original microstructure) initiate/grow. Following the depletion of β phase, γ′ and the chromium rich phase reduce, with tantalum carbide the last phase evident in the denuded coating γ matrix. At 1000°C the coating microstructure shows two distinct bands; a γ′ rich band on the TBC side of the coating and β rich band on the MAR M509 side of the coating. With time the β rich layer disappears leaving the γ′ rich band to further reduce in size with tantalum carbide remaining in the denuded γ matrix.

The effect of ageing on the coating microstructure, in very broad terms, is as follows:

<u>Ageing temperature 800 - 950°C</u>

	Bulk	Inner denuded
Initial coating	γ β (γ′ minor)	
Increasing time/temp	γ γ′↑ β↓ Cr rich↑	
↓	γ γ′↓ Cr rich	γ Cr rich
	γ Cr rich↓ TaC	γ Cr rich TaC
Fully denuded	γ TaC	γ TaC

<u>Ageing temperature 1000°C</u>

Initial coating	γ β (γ′ minor)	
Increasing time/temp		
↓	γ γ′↓ Cr rich↑ TaC and γ β↓ Cr rich↑ TaC	γ Cr rich TaC
	γ γ′↓ Cr rich↓TaC	γ Cr rich TaC
Fully denuded	γ TaC	γ TaC

If the absence of β is considered to indicate the end of coating life, then with 'no ICO' present the coating has a useful life in excess of 25,000 hours at temperatures of 800°C or less. At temperatures above 800°C the coating life is reduced to less than 15,000 hours at 850-900°C. If 'ICO' is present then the coating life is less than 15,000 hours at 800°C reducing to less than 10,000 hours at 850 -900°C. However, it is possible that as a result of the high levels of aluminium in the γ′ phase (~ 7 wt.%) the loss of β may not indicate the end of coating life.

EDS of the γ′ and the chromium rich phase in the coating showed no significant trends with time or temperature that would allow the prediction of ageing temperature or time. Subsequent investigation of the chromium rich phase confirmed the presence of carbon within the phase. Indexing of electron diffraction patterns showed the phase was probably $M_{23}C_6$. However, further work is required to determine if the chromium rich phase is chromium carbide in all of the samples or if a transition occurs from αCr to $M_{23}C_6$ with time and temperature.

JMatPro did, in part, predict the coating equilibrium phases and their composition. Of interest were the microstructural changes predicted for the simulated "diffusion" of aluminium from the coating and the diffusion of carbon into the coating. The results show that if carbon is diffusing into the coating from the substrate, then chromium rich $M_{23}C_6$ carbide is likely to form within the coating, and that tantalum carbide would form at lower aluminium levels in the denuded coating layers. However, it is considered that as a result of the changes in the coating composition from outward diffusion from the coating to the TGO and the substrate and the inward diffusion from the substrate to the coating that the system would not reach equilibrium and as such JMatPro was of limited use. A model which combines the kinetics of diffusion with the thermodynamic equilibrium predictions is required to fully explain the experimental data.

Measurement of the width of the denuded layer in the coating adjacent to the MAR M509 substrate showed denudation (removal of γ′) of the coating in the 'ICO' samples was approximately three times faster than in the 'no ICO' samples. Measurements of the aluminium diffusion from the coating into the substrate showed very similar profiles between the 'ICO' and 'no ICO' samples. However, it was noted that an aluminium rich layer had formed around the 'ICO' phase in the aged samples. It was proposed that the aluminium formed around the 'ICO' extracting oxygen from the zirconia 'ICO' particles. Electron diffraction patterns confirmed the aluminium rich phase as Al_2O_3 surrounding ZrO/ZrO_2 'ICO'.

Measurement of the width of the inner denuded layer showed potential for estimating the time temperature history of a NiCoCrAlTaY coating on MAR M509 substrate. The investigation of the coated MAR M509 has shown that there is a commercial benefit to be gained from the removal of 'ICO' from the surface of MAR M509 vanes prior to coating.

8 Conclusions and Further Work

The conclusions which arise from the various investigations carried out as part of this work are discussed below in separate sections. The first three sections refer to the study of the microstructural changes in two cobalt-based superalloys FSX 414 and MAR M509 and one high cobalt nickel based superalloy NP 222 in order to produce a method to allow the prediction of operating time and temperature of service exposed superalloy vanes. The fourth section refers to the second part of the programme investigating the effect of inter-carbidic oxidation (ICO) on coating life, and the microstructural changes within the coating and the inter-diffusion layer with the intention of producing a method to enable the prediction of operating time and temperature for a NiCoCrAlTaY coating on a cobalt-based substrate.

8.1 FSX 414 Predicting time and temperature from microstructural changes

FSX 414 is a conventionally cast cobalt-based superalloy. The as-cast microstructure consists of dendrites of FCC (γ-Co) solid solution and interdendritic eutectic $M_{23}C_6$ carbides at the grain boundaries and within the γ matrix. As a result of heat treatment or service the carbides can be partially solutioned and precipitated as more finely divided $M_{23}C_6$ carbides around the original carbides(5).

XRD and EDS have confirmed that the carbides present in the samples of FSX 414 are primary chromium rich $M_{23}C_6$ eutectic carbides and secondary $M_{23}C_6$ carbides in the aged samples. The chromium rich $M_{23}C_6$ eutectic carbides contain tungsten, cobalt and nickel and can be expressed as approximately $Cr_{80}Co_{11}W_7Ni_2$ (where the subscript describes the concentration in at.%). The composition of the $M_{23}C_6$ eutectic carbides determined by EDS in the SEM was similar to the thermodynamic equilibrium predictions using JMatPro. However, the measured cobalt values decrease with JMatPro predicting an increase and a significant difference exists between the measured (~16 wt.%) and predicted (~12 wt.%) tungsten. Two additional phases were evident in the samples aged at temperatures less than 950°C; a large blocky phase and a high tungsten phase, both phases were associated with the eutectic $M_{23}C_6$ carbides. The phases were identified as σ and Laves phase respectively by selected area electron diffraction in a TEM. Representative EDS compositions for Laves phase and σ is: Laves 55 wt.% W, 25 wt.% Co, 14 wt.% Cr and 3 wt.% Ni, σ 43 wt.% Cr, 36 wt.% Co, 15 wt.% W and 5 wt.% Ni.

JMatPro initially predicted σ and μ to be present at equilibrium. By removing μ from the allowed phase list in the calculation, JMatPro predicted σ and Laves phase at lower temperatures with predicted compositions similar to that determined by EDS. The secondary phases σ and Laves could be used to indicate qualitatively the operating temperatures and service time experienced. The presence of σ in a sample would indicate service temperatures of 850°C and 900°C for times greater than 5,000 hours, whereas the presence of Laves phase would indicate service temperatures of between 850°C and 950°C for 1,000 to 25,000 hours. Therefore the presence of Laves with no σ evident would indicate a service temperature between 900°C and 950°C for 1,000 to 25,000 hours. Further work would be required to determine the effect of alloy composition on the formation of Laves and σ in FSX 414.

Image analysis of the $M_{23}C_6$ carbides was inconclusive and would require further extensive work to differentiate the $M_{23}C_6$ from the matrix and from the Laves and σ phases. In addition, problems were encountered with the coarse highly segregated primary eutectic carbides which required low magnification images to overcome the effects of segregation, and the fine secondary carbides which could not be resolved at the lower magnification. However, it is considered that image analysis of the secondary $M_{23}C_6$ carbides may provide a correlation with time and temperature. Image analysis of the Laves phase did show an increase in Laves phase with increasing time and a reduction in Laves phase with increasing temperature. However, the low levels of Laves in the aged samples would prohibit the use of Laves phase for the prediction of time and or temperature in practice. Additional samples aged at lower temperatures may have increased levels of Laves phase.

The measured Vickers hardness levels dropped slightly with ageing temperature and ageing time, however, the changes were not sufficient to allow the prediction of time or temperature.

The width of the oxidised layer evident on the exposed surfaces of the sample would allow the prediction of operating temperature on uncoated samples. The width of the denuded layer, over the period from 1,000 hours to 25,000 hours, increased from 21 to 64 microns at 850°C and from 100 to 350 microns at 1000°C. However, further work should be undertaken to determine the effect of temperature cycling and composition on the width of the denuded layer.

8.2 NP 222 Predicting time and temperature from microstructural changes

NP 222 is a conventionally cast γ' (~20%) strengthened nickel based superalloy with a high level, ~19 wt.%, of cobalt. The alloy exhibits a primary tantalum, titanium, niobium rich MC carbide and a chromium rich grain boundary $M_{23}C_6$ carbide(55).

XRD and EDS/WDS confirmed the carbides in the aged samples are a tantalum, titanium, niobium rich MC carbide and a chromium rich $M_{23}C_6$ carbide. From the SEM EDS measurements the metallic component of the MC carbide can be expressed as approximately $Ti_{48}Nb_{26}Ta_{16}W_3Cr_3Ni_3Co$ (where the subscript describes the concentration in at.%). Due to the small size of the $M_{23}C_6$ carbide, EDS measurements were considered qualitative and were only used to confirm the presence of the carbide. The $M_{23}C_6$ carbide is evident in all the samples aged at 800 and 850°C, and the 900°C samples aged for times less than 10,000 hours. η phase was evident in all samples aged in the range 800 - 1000°C for times greater than 5,000 hours. γ′ reduced and coarsened with both time and temperature and was not evident in any of the samples aged at 1000°C and 1050°C.

The changes in microstructure could be used as a maximum temperature indicator, with $M_{23}C_6$ carbide indicating a temperature below 850°C; the presence of γ′ also indicates temperatures of less than 950°C and the absence of γ′ indicating temperatures in excess of 1000°C. η in the microstructure together with no γ′ would indicate an effective temperature between 1000°C and 1050°C.

JMatPro has been used to study the effect of varying the composition of NP 222 on the formation of η. The predictions would suggest that η would not be formed in NP 222 vanes, with titanium and niobium levels at the bottom end of the specified composition range below 900°C. The predicted temperatures at which η would be present are considered to be above the normal operating temperatures for stage 2 and 3 vanes. Therefore, the presence of η in a NP 222 vane is likely to indicate a fault condition.

The EDS/WDS analysis results for the MC carbide in the aged samples show similar levels of tantalum, titanium and niobium (~31 wt.%) with tungsten at ~3 wt.%. The JMatPro predictions, over the temperature range from 850°C to 1050°C, show significant changes in the composition of the MC carbide with tantalum reducing from ~46 wt.% to ~30 wt.% and titanium increasing from ~11% to ~29% wt.%. Niobium is predicted to remain relatively constant at ~29 wt.% with tungsten at less than 1 wt.% and zirconium reducing over the temperature range from ~4 wt.% to 1 wt.%. The EDS/WDS results show none of the large changes in the MC carbide composition predicted by JMatPro for tantalum and titanium. No prediction of time or temperature could be made with the small changes in composition found in the MC carbide.

The limitations imposed by the spot size precluded the quantitative EDS measurement of γ′, η and $M_{23}C_6$ carbides. However, EDS was used to confirm the presence of $M_{23}C_6$ carbides in the samples where the η phase peaks dominated the XRD traces.

The reduction in the measured mean hardness between 800 and 950°C could provide a coarse prediction of operating temperature but would require knowledge of the microstructure to confirm the samples contained γ′. Correlations were also evident between η needle length and the γ′ denuded layer formed on the exposed surfaces of the sample. Further work would be required to understand the effects of composition on η needle initiation and growth and the effects of composition and thermal cycling on the formation of denudation zones on free surfaces.

8.3 MAR M509 Predicting time and temperature from microstructural changes

MAR M509 is a high carbon, high strength, vacuum cast cobalt-based superalloy which is generally used in the as-cast condition. The microstructure is typically composed of dendrites of the FCC (γ-Co) solid solution and an interdendritic network of "Chinese script" MC carbides and interdendritic eutectic $M_{23}C_6$ carbides consisting of mixtures of the γ Co solid solution and carbide.

XRD and WDS/EDS confirmed the carbides present in the aged samples are tantalum rich MC carbides and chromium rich $M_{23}C_6$ carbides. The MC carbides are primarily tantalum carbides but also contained zirconium, tungsten and titanium and the metallic component can be expressed as approximately $Ta_{53}Zr_{16}Ti_{12}Cr_8Co_8W_3$ (where the subscript describes the concentration in at.%).

From the EDS/WDS results the composition of the MC carbides shows only minor changes in composition with no significant variations with time or temperature. A typical composition would be tantalum (~75 wt.%), zirconium (~11.5 wt.%), titanium (~4.5 wt.%), tungsten (~3.5 wt.%) and cobalt (~2.5 wt.%). The variations in analysis predicted by JMatPro from 850°C to 1050°C are tantalum reducing from 78 to 76 wt.%, tungsten increasing from 2.8 to 4.6 wt.% with zirconium, carbon and titanium remain relatively constant at 7 wt.%, 7.4 wt.% and 4 wt.% respectively. Other than the zirconium level, the WDS/EDS analysis was in reasonable agreement with the JMatPro predictions for MC carbide.

The $M_{23}C_6$ eutectic carbides were primarily chromium carbides but also contained tungsten, cobalt and nickel and the metallic component can be expressed as approximately $Cr_{82}Co_{10}W_5Ni_3$ (where the subscript describes the concentration in at.%). From the EDS results a typical composition would be chromium (~70 wt.%), tungsten (~15 wt.%), cobalt (~12 wt.%) and nickel (~2 wt.%). The variations predicted by JMatPro from 850°C to 1050°C are that chromium reduces from 67 to 63 wt.%, cobalt increases from 14.3 to 17.8 wt.%, nickel increasing from 1.1 to 1.8 wt.% with tungsten and carbon at 12 wt.% and 5 wt.% respectively. The EDS analysis and the JMatPro predictions for the $M_{23}C_6$ eutectic carbides are similar, other than small differences in the tungsten and cobalt. The measured levels of elements in the $M_{23}C_6$ carbides showed no significant changes with ageing time or temperature.

A tungsten rich phase found within the $M_{23}C_6$ eutectic carbides was identified as M_6C carbide by selected area electron diffraction. The tungsten rich M_6C carbide was evident in all of the samples aged at 850°C and 900°C for times up to 25,000 hours. At 950°C M_6C reduced with increasing ageing time and could not be found in the samples after 15,000 hours as increased levels of a tantalum rich phase precipitated in the $M_{23}C_6$ eutectic carbides. The tantalum rich phase in the $M_{23}C_6$ eutectic carbides was noted in all of the samples other than the 1,000 hour 850°C sample. The level of tantalum carbide in the $M_{23}C_6$ eutectic carbides increased with both ageing time and ageing temperature. Selected area electron diffraction identified the tantalum rich phase as tantalum carbide (MC). Other than the presence of M_6C phase in the eutectic carbides which may not be an equilibrium phase the results show that JMatPro using the nickel superalloy database has produce reasonable predictions of the equilibrium phases that would form in MAR M509 and the chemical composition of those phases.

An attempt to identify any changes in the volume fraction of the MC carbides and the $M_{23}C_6$ carbides using the peak area and peak heights of the XRD traces showed only a small increase in the peak area ratio with time. Image analysis of the MC carbides showed no change with time or temperature. Image analysis of the $M_{23}C_6$ carbide was not carried out as a clear difference between the matrix and the carbide could not be achieved. In addition the segregation effects and the presence of fine secondary carbides caused similar problems to those identified in FSX 414.

Measured Vickers and micro-hardness levels dropped from 365-390 Hv_{20} at 850°C to 332-344 Hv_{20} at 1050°C with ageing temperature but varied by less than 20 Hv_{20} with ageing time. The Vickers hardness levels measured were in reasonable agreement with those measured by Drapier et al(62) and showed a similar trend with time. The results from the tests show no significant variations that would allow the prediction of time and or temperature.

Micro sections from the aged samples showed a denuded/oxidised layer on the outer exposed surface of the samples. Measurements of the width of the denuded/oxidised layer showed a correlation with time which would allow the prediction of an operating temperature for an uncoated vane with a known operating history. However further work is required to determine the effect of thermal cycling and bulk composition on the width of the denuded layer.

8.4 NiCoCrAlTaY Predicting time and temperature from microstructural changes

A thermal barrier coating for protection against the high temperature exposures was applied to MAR M509 samples both with and without intercarbidic oxidation (ICO). The bond coat was a NiCoCrAlTaY coating and the outer ceramic coating was yttria stabilised zirconia. Prior to the deposition of the ceramic coating the samples were heat treated in vacuum at 1000 ± 10°C for 4 hours followed by an argon gas fan quench. The investigation of the coating has focused on the effects of ageing on the phase changes within the coating, the interaction between the coating and the substrate, and the effect of 'ICO' on coating life.

The results of the microstructural investigations showed that the initial coating microstructure comprised fine γ and β with an indeterminate very fine aluminium rich phase. With time and temperature the coating microstructure coarsened and changes in phase stability were observed. At temperatures from 800-950°C as β goes into solution, γ' and a chromium rich phase (not evident in the original microstructure) initiate/grow. Following the depletion of β phase, γ′ and the chromium rich phase reduce with tantalum carbide the last phase evident in the denuded coating γ matrix. At 1000°C the coating microstructure shows two distinct bands, a γ′ rich band on the TBC side of the coating and β rich band on the MAR M509 side of the coating. With time the β rich layer disappears leaving the γ′ rich band to further reduce in size with tantalum carbide remaining in the denuded γ matrix.

If the absence of $\beta^{(2)}$ is considered to indicate the end of coating life then with 'no ICO' present the coating has a useful life in excess of 25,000 hours at temperatures of less than 800°C. At temperatures above 800°C the coating life is reduced to between 10,000 and 15,000 hours at 850-900°C. If 'ICO' is present then the coating life is between 10,000 and 15,000 hours at 800°C reducing to 5,000 – 10,000 hours at 850 and 900°C. However, it is possible that as a result of the high levels of aluminium in the γ′ phase (~ 7 wt.%) the loss of β may not indicate the end of coating life.

EDS analysis of the γ′ and the chromium rich phase in the coating showed no significant trends with time or temperature that would allow the prediction of ageing temperature or time. Subsequent investigation of the chromium rich phase, in the 10,000 hour 850°C 'no ICO' sample, confirmed the presence of carbon within the phase. Indexing of selected area electron diffraction patterns showed the phase was probably $M_{23}C_6$. However, further work is required to determine if the chromium rich phase is chromium carbide in all of the samples or if a transition occurs from αCr to $M_{23}C_6$ with time and temperature.

The JMatPro predictions were in general limited to the range of temperatures used for the ageing trials. The initial predictions identified the equilibrium phases as γ, γ′ β (NiAl) and σ. Previous investigators of this coating had reported both σ and αCr to be present. The current investigation has identified in the coating a chromium rich phase with a chromium content significantly higher than predicted by JMatPro for σ. For JMatPro to predict αCr (BCC phase in JMatPro) as an equilibrium phase it is necessary to remove both σ and $M_2(C,N)$ from the phases present. The JMatPro equilibrium phase predictions, with σ and $M_2(C,N)$ removed, show increased levels of γ and β with reduced levels of γ′ when compared to the original JMatPro predictions. αCr (BCC) was only predicted below 825°C. The predicted chromium level of αCr (84 wt.%) is significantly higher than the predicted chromium content of σ (57 wt.%).

Within JMatPro it is possible to carry out concentration step calculations in which the composition range of a single element is varied at a fixed temperature. In this case the aluminium composition was lowered to simulate the loss of aluminium from the coating. The change in aluminium content was balanced by cobalt. The current investigation has also confirmed the presence of carbon within the coating. For the concentration step calculations carbon contents of 0.2 wt.% and 0.4 wt.% were included in the coating composition. The results of the concentration step calculation show that a chromium rich $M_{23}C_6$ carbide and tantalum rich MC carbide are predicted to form in the coating, in addition to the γ, γ' and β phases.

However, it is considered that as a result of the changes in the coating composition from outward diffusion from the coating to the TGO and the substrate and inward diffusion from the substrate to the coating that the system would not reach equilibrium and as such JMatPro was of limited use. A model which combines the kinetics of diffusion with the thermodynamic equilibrium predictions is required to fully explain the experimental data.

Measurement of the width of the denuded layer in the coating adjacent to the MAR M509 substrate showed that denudation (removal of γ') of the coating in the 'ICO' samples was approximately three times faster than in the 'no ICO' samples. Measurements of the aluminium diffusion from the coating into the substrate showed very similar profiles between the 'ICO' and 'no ICO' samples. However, it was noted that an aluminium rich layer had formed around the 'ICO' phase in the aged samples. It was proposed that the aluminium formed around the 'ICO' extracting oxygen from the zirconia 'ICO' particles to produce an alumina layer. Selected area electron diffraction patterns confirmed the aluminium rich phase around the 'ICO' (ZrO/Zr_2O) as Al_2O_3.

Measurement of the width of the denuded layer showed potential for estimating the time temperature history of a NiCoCrAlTaY coating on MAR M509 substrate. The investigation of the coated MAR M509 has shown that there is a commercial benefit to be gained from the removal of 'ICO' from the surface of MAR M509 vanes prior to coating.

8.5 Further work

A number of areas of further work have been identified as a result of this research and are discussed below

The current investigation attempted to carry out image analyses on both the primary and secondary carbides in MAR M509 and FSX 414 and found problems as a result of segregation and the contrast required between the $M_{23}C_6$ carbides and the matrix. It is considered that image analysis of the secondary $M_{23}C_6$ carbides could provide a method of predicting time and temperature.

Additional samples aged at lower temperatures are required to identify at what temperatures σ and Laves phase do not form in FSX 414 and the ageing temperatures where η does not form in the current NP 222 samples. Further work is required to determine the effect of composition on η initiation and growth in NP 222 and the effects of composition and temperature cycling on the width of the denuded/oxidised zone in all of the alloys examined.

Image analysis of the chromium rich phase in the coating may provide a method of predicting time and temperature. The chromium rich phase in the NiCoCrAlTaY coating was identified in one sample as $M_{23}C_6$. Further work is required to confirm if the chromium rich phase is $M_{23}C_6$ in all of the samples or there is a point at which the chromium rich phase is αCr and reverts to $M_{23}C_6$. This work could be extended to lower carbon cobalt or nickel based superalloys.

Should a cobalt-based database be developed for use with JMatPro the results should be used to validate the predictions.

8.6 Industrial Application of Microstructural Time/Temperature Correlations

There are a number of practical considerations that need to be addressed with regards to the use of microstructural changes to predict time and temperature for service exposed vanes. The first, second and in some cases the third, stage vanes are generally cooled by air from the compressor. For air cooled vanes the surface temperature of the vane will vary not only along the length of the vane but, dependant on the cooling configuration, will show significant variations from the leading edge to the trailing edge, with variations between the pressure surface and the suction surface of the vane. However, the through wall temperature gradient would be typically ~250°C from the outside of the vane to the cooled inner surface over a distance of ~3mm. This large through wall temperature gradient can lead to significant through wall microstructural changes. For this reason any technique developed using changes in microstructure to determine the operating temperature must be able to identify the changes in the microstructure, preferably, in a relatively narrow band immediately below the denude/oxidised layer.

For turbine vanes, the time in service is generally known and it is the operating temperature that is required. It should be noted that the operating temperature determined will be a metallurgical average temperature i.e. the temperature determined will be the result of metallurgical changes and may not be a "true" average temperature although it will be representative of an effective operating temperature. If the metallurgical change being measured is not active during significant periods of service lower metallurgical average temperatures will be predicted.

Generally metallurgists are asked to determine the temperature of a component with a known time in service. There are two main reasons for this:

- IGTs are controlled by exhaust temperatures, the temperatures of individual stages are back calculated from the exhaust temperatures. These calculated temperatures can be inaccurate and do not identify variations in metal temperatures around the components. Component metal temperatures are important for predicting component lives and determining if components can be run for longer service intervals or will be acceptable for refurbishment.
- Calculation of service temperatures for components that have failed in service (often due to elevated temperature conditions). This can then be used to help determine the root cause of the failure.

Less frequently, it is also necessary to determine the length of time a component has been in service, for example since a crack developed. The author can quote an instance where a change in the level of vibration of a gas turbine was identified from onboard transducers. The turbine continued to operate to a planned overhaul. A visual inspection noted that the top corner of a turbine blade had been removed as a result of foreign impact damage. An investigation was carried out to determine when the damage had occurred and if the vibration noted by the onboard transducers was the result of the loss of the blade section. The blade material was the nickel base superalloy GTD111 for which the microstructural changes as a function of time and temperature have been well characterised. An average metal temperature was calculated from the γ' morphology, based on the total length of time the blade had been in service. Using the width of the denuded layer across the fracture a time since impact was calculated based on the calculated metal temperature. The predicted time the damage occurred fell very close to the time when the change in vibration was detected by the onboard transducers.

One particular aspect of the investigation of the coated MAR M509 is noteworthy. It has been shown that there is a commercial benefit to be gained from the removal of 'ICO' from the surface of MAR M509 vanes prior to coating because the presence of the 'ICO' was found to reduce coating life by approximately one third.

8.6.1 Practical utilisation of the techniques described in this thesis

Qualitative assessment of microstructure in SEM.

The presence or absence of σ and Laves phase in FSX 414 and the presence or absence of $M_{23}C_6$, γ' and η in NP 222 would allow the prediction of maximum metal temperatures. Typical temperature limits would be ± 50°C from the ageing experiments carried out in this research.

XRD of carbide extraction

This process could be applicable to a solid vane where there is a limited through wall temperature gradient. It is difficult to see how this process could be used on a cooled vane as a through wall sample would present a gradation of microstructures and could include oxide or coating interdiffusion phases. For this technique to work there would have to be phases which form in a specific temperature range above the normal operating temperature. For FSX 414, the detection of Laves phase without σ would indicate a temperature between 950°C and 1000°C. This would of course indicate that at some point through wall the temperature has been between 950°C and 1000°C.

Hardness

This would be the optimum process for use in industry as it can be targeted in specific areas and is a relatively simple technique. Of the materials tested in this investigation NP 222 was the only material where the reduction in the measured mean hardness between 800°C and 950°C could provide a coarse prediction of operating temperature but would require knowledge of the microstructure to confirm the samples contained γ'. Typical temperature limits would be ± 50°C.

Denuded/oxidised layers

Measurement of the denuded/oxidised layer on the outer surface of uncoated superalloys would allow the predictions of the maximum surface temperatures. Measurement of the inner denuded layer of a NiCoCrAlTaY coating on a MAR M509 substrate would allow the prediction of operating temperature for this coating system. Typical temperature limits would be ± 50°C, although further work linked to combined thermodynamic/kinetic models may allow refinement of this temperature interval.

8.6.2 Specific Applications for Cobalt Alloys

There are two specific applications where the processes developed in this thesis will need to be applied:

1. A coating was applied to the platforms of FSX 414 row 1 vanes to reduce the amount of thermal fatigue cracking. This has largely been successful, but a few significant cracks have still developed and have resulted in some components being removed from service early. The investigation into the cracking will require a method of determining the temperature (with a known time) at various positions in the FSX414 component.

2. MAR M509 row 1 vanes have been refurbished and returned to service. During the refurbishment there has been considerable coat-down of the film cooling holes, however, a TBC has been applied over the whole gas-washed surfaces of the vanes. Following service, one of the vanes will be sectioned and compared to a vane sectioned after the first operating interval. A time temperature relationship for MAR M509 will be required to determine if there have been any significant changes in metal temperatures.

The work in this thesis has identified that denuded layers for uncoated surfaces and the inner denuded layer for coated surfaces offer the greatest potential for making accurate temperature estimates for cobalt-based superalloys.

9 References

1. Saunders N, Li X, Miodownik A P and Schille J P, "Computer modelling of materials properties", *Materials Design Approaches and Experiences*, Editors: *Zhao J-C, Fahrmann M and Pollock T*, TMS 2001, 185-197.

2. Sims C T, Stoloff N S and Hagel W C, "Superalloys II - High Temperature Materials for Aerospace and Industrial Power", John Wiley & Sons, 1987.

3. Rothman M F, Zordan R D and Muzyka D R, "Role of Refractory Elements in Cobalt-Base Alloys", Proceedings of *Refractory Alloying Elements in Superalloys*, Rio de Janeiro, 1984, 101-115.

4. Donachie M J and Donachie S J, "Superalloys - A Technical Guide", ASM International, 2002.

5. Sims C T, "Contemporary View of Cobalt-Base Alloys", *Journal of Metals*, **2**, 1969, 27-42.

6. "Technology Status Report - Review of Advanced Materials for Power Generation", Report No 018, 2002.

7. Schilke P W, Foster A D and Pepe J J, "Advanced Gas Turbine Materials and Coatings", GE Power Systems GER 3569.

8. Coutsouradis D, Davin A and Lamberigts M, "Cobalt-Based Superalloys for Applications in Gas Turbines", *Materials Science and Engineering*, **88** 1987, 11-19

9. Sullivan C P, Donachie M J and Morral F R, "Cobalt-Base Superalloys - 1970; A Critical Survey of Cobalt-Base Superalloy Development with Emphasis on the Relationship of Mechanical Properties to Microstructure, *Cobalt Monograph Series*, Brussels: Centre d'information du cobalt, 1970.

10. Rausch J J, McAndrews J B and Simcoe C R, "Effects of Alloying on the Properties of Wrought Cobalt", *High Temperature Materials II*, 1961, 259-279.

11. Jiang W H, Yao X D, Guan H R and Hu Z Q, "Secondary M_6C precipitation in a cobalt-base superalloy", *Journal of Materials Science Letters*, **18** 1999, 303-305.

12. Tien J K and Purushothaman S, "Metallurgy of High Temperature Alloys", *Properties of High Temperature Alloys, With Emphasis on Environmental Effects*, 1976, 3-41.

13. Wlodek S T, "The stability of superalloys", Proceedings of *Long Term Stability of High Temperature Materials*, San Diego, California, USA, Editors: Fuchs G E, Dannemann K A and Deragon T C, TMS, 1999, 3-40.

14. Steinberg B G and Perez-Daple W R, "Practical Approach to Gas Turbine Component Life Assessment - an Electric Utility's Perspective", Proceedings of *Life Assessment & Repair: Technology for Combustion Turbine Hot Section Components*, 1990, 41-53.

15. Lane J R and Grant N J, "Carbide Reactions in High Temperature Alloys", *Transaction of ASM*, **44** 1952, 113-120.

16. Jiang W H, Yao X D, Guan H R, Hu Z Q, "Secondary carbide precipitation in a directionally solidified cobalt-base superalloy", *Metallurgical and Materials Transactions A*, **30A** 1999, 513-520.

17. Jiang W H, Yao X D, Guan H R and Hu Z Q, "Carbide behaviour during high temperature low cycle fatigue in a cobalt-base superalloy", *Journal of Materials Science and Technology*, **15** 1999, 515-518.

18. Saunders N and Miodownik A P, "CALPHAD: Calculation of Phase Diagrams: A Comprehensive Guide", Pergamon, 1998.

19. Saunders N, "Ni-DATA Information", Thermotech, Surrey Technology Centre, Surrey, 2000.

20. Berthod P, Michon S, Aranda L, Mathieu S and Gachon J C, "Experimental and thermodynamic study of the microstructure evolution in cobalt-base superalloys at high temperature", *Calphad*, **27** 2003, 353-359.

21. Michon S, Berthod P, Aranda L, Rapin C, Podor R and Steinmetz P, "Application of Thermodynamic Calculations to Study High Temperature Behaviour of TaC-Strengthened Cobalt-base superalloys", *Calphad*, **27** 2003, 289-294.

22. RWE npower Private Communication.

23. Pomeroy M J, "Coatings for gas turbine materials and long term stability issues", *Materials & Design*, **26,** 2005, 223-231.

24. Kasik N and Hoffeiner W, "A Review of Service Life Assessment", *EPRI GS-7302 Project 2775-5*, 1991, 2.1-2.17.

25. Nicholls J R and Hancock P, "Advanced High Temperature Coatings for Gas Turbines", *Institute of Corrosion Science & Technology*, 1985, 5-24.

26. Rapp R A. and Zhang Y S, "Hot corrosion of materials: fundamental studies", *Journal of Coating Technology*, **66**, 1994, 47-55.

27. Stringer J, "High-Temperature Corrosion of Superalloys", *Materials Science and Technology*, **3** 1987, 482-493.

28. Grunling H W and Burgel R, "Influence on High Temperature Mechanical Strength of High Temperature Corrosion", *Werkst. Korros*, **34** 1983, 527-538.

29. Otsuka N and Rapp R A, "Local Salt Film Chemistry During Hot Corrosion of Preoxidized Nickel at 900 deg C", Proceedings of *Corrosion & Particle Erosion at High Temperatures*, 1989, 145-161.

30. Pettit F S and Meier G H, "Oxidation and Hot Corrosion of Superalloys", *Superalloys 1984*, TMS, 1984, 651-687.

31. Beltran A M, "The Oxidation and Hot Corrosion Resistance of Cobalt-base superalloys", General Electric Co., Schenectady N Y, USA, 1969.

32. Prescott R, Mitchell D F, Graham M J and Doychak J, "Oxidation mechanisms of beta -NiAl+Zr determined by SIMS", *Corrosion Science*, **37**, 1995, 1341-1364.

33. Adrain R S, "Gas turbine technology review - materials development", NP Restricted 1992.

34. Viswanathan R, "Damage Mechanisms and Life Assessment of High-Temperature Components", ASM International, 1989.

35. Nicholls J R, Simms N J, Chan W Y and Evans H E, "Smart overlay coatings - concept and practice", *Surface and Coatings Technology*, **149** 2002, 236-244.

36. Novak R.C, "Coating Development and Use: Case Studies." Presentation to the Committee on Coatings For High Temperature Structural Materials-, 1994.

37. Mazars P, Manesse D and Lopvet C, "Interdiffusion of MCrAlY coating with the substrate", Proceedings of *High Temperature Alloys for Gas turbines and Other Applications*, 1986, 1183-1192.

38. Quadakkers W J, "Coating system development for future, high efficiency gas turbines", *Ochrona Przed Korozja*, 2002, 79-86.

39. Nicholls J R, "Review of Coatings for Gas Turbines", Power Generation Technology Centre, Cranfield University, Report Number PGTC/0012, 2000,

40. Quadakkers W J, "High Temperature Coatings - Failure Mechanisms & Future requirements", Proceedings of *EPRI/DOE - Conference on Advances in Life Assessment and Optimisation of Fossil Power Plants*, 2002, 1-4.

41. West S, "High Temperature Protective Coatings in Gas Turbines", NP Engineering Report, 1999.

42. Baufeld B, Tzimas E, Mullejans H, Peteves S, Bressers J and Stamm W, "Thermal-mechanical fatigue of MAR-M 509 with a thermal barrier coating", *Materials Science and Engineering A*, **315** 2001, 231-239.

43. Chase T F and Beltran A M, "The High Temperature Properties of Welded Cast Co-Based Alloys", *American National Standards Institute,* Proceedings of *International Conference on Superalloys*, 1972.

44. Foster A D and Sims C T, "FSX-414 - An Alloy For Gas Turbines", *Metal Progress*, **96** 1969, 83-85.

45. Mezzedimi V, Giorni E, Tognarelli L and Pratesi F, "Assessment of Turbine Hot Gas Path Components", Proceedings of *Materials for Advanced Power Engineering*, 1988, 1699-1708.

46. Bicego V, Sampietri C, Taylor N, Giorni E, Pinzauti M and Giannozzi M, "Analysis of high temperature fatigue and creep damage for a FSX414 gas turbine nozzle", Proceedings of *Materials Ageing and Component Life Extension*, Milan, Italy, Editors: Bicego V, Nitta A and Viswanathan R, 1995, 1085-1094.

47. Morrow H, Danesi W P, and Sponseller D L, "Effects of Substituting Mo for W in Two Cast Co-Base Alloys", *Cobalt*, **4** 1973, 93-102.

48. Haafkens M H, "Blade Repair and Recovery", Proceedings of *High Temperature Alloys for Gas Turbines*, Belgium, Editors: Brunetaud R, Coutsouradis D, Gibbons T B, Lindblom Y, Meadowcroft DB, Stickler R, Kluwer 1982, 931-954.

49. Pratesi F, Giannozzi M, Innocenti M and Del Puglia A, "Characterisation of Metallographic Damage in Cobalt Superalloy", Proceedings of 3rd International Conference on *Engineering Structural Integrity Assessment*, Cambridge, UK, Editors: Edwards JH, Flewitt PEJ, Gasper BC, McLarty KA, Stanley P and Tomkins B, Sept. 1996, 637-646.

50. Foster A D and Sims C T, "FSX-414 - An Alloy for Gas Turbines", *Metal Progress* **96** 1969, 83-88.

51. Tien J K and Jarrett R N, "Effects of Cobalt in Nickel-Base Superalloys", Proceedings of *High Temperature Alloys for Gas Turbines*, Belgium, Editors: Brunetaud R, Coutsouradis D, Gibbons T B, Lindblom Y, Meadowcroft DB, Stickler R, Kluwer 1982, 423-446.

52. Nathal M V, MacKay R A and Miner R V, "Influence of Precipitate Morphology on Intermediate Temperature Creep Properties of a Nickel-Base Superalloy Single Crystal", *Metallurgical Transactions*, **20A** 1989, 133-141.

53. Maurer G E, Jackman L A and Domingue J A, "Role of Cobalt in Waspaloy", *Superalloys 1980*, TMS, 1980, 43-52.

54. Wood J H and Haydon J S, "Nickel-Base Alloy", *Ausz. Eur Patentanmeld*, **5** 1989.

55. Banik T, Deragon T C and Schweizer F A, "The effects of ingot composition and conversion on the mechanical properties and microstructural response of GTD-222", *Superalloys 1996*, TMS, 1996, 607-611.

56. Seavers D W. and Beltran A M, "Nickel-Base Alloy GTD 222, A New Gas Turbine Nozzle Alloy", *Journal of Engineering for Gas Turbines and Power,* Transactions of the ASME, **115** 1993, 155-159.

57. Prager M and Shira C S, "Welding of Precipitation – Hardened Nickel-Based Alloys", *Welding Research Council Bulletin*, **128** 1968.

58. Wheaton H L, "MAR-M 509, A New Cast Cobalt-Base Alloy For High - Temperature Service", *Cobalt*, **29** 1965, 163-170.

59. Woulds M J and Cass T R, "Recent Developments in MAR-M Alloy 509", *Cobalt*, **42** 1969, 3-13.

60. Klopp W D," MAR-M 509", *Aerospace Structural Metals Handbook*, **5** 1991.

61. Wahl J B and Harris K, "Superalloys in Industrial Gas Turbines – An Overview", Proceedings of 9th *World Conference on Investment Casting*, San Francisco, USA, 1996, 12.1-12.12.

62. Drapier J M, Leroy V, Dupont C, Coutsouradis D and Habraken L, "Structural Stability of MAR-M509, a Cobalt-base Superalloy", *Cobalt*, **41** 1968, 199-213.

63. Biss V, "Phase Analysis of Standard and Mo-Modified MAR-M509", *Microstructural Science*, **3A** 1975, 249-264.

64. Beltran A M, Sim C T and Wagenheim N T, "High-Temperature Properties of MAR-M Alloy 509", *Journal of Metals*, **21** 1969, 39-47.

65. Woulds M J, "Casting of Cobalt-Base Superalloys", *Metals Engineering Quarterly, American Society for Metals,* 1968, 42-45.

66. Czech N, "Mar M509 Heat Treatment", Report Prepared by NC Consulting, 2003,

67. Morral F R, Habraken L, Coutsouradis D, Drapier J M and Urbain M, "Microstructure of Cobalt-Base High Temperature Alloys", *Metals Engineering Quarterly, American Society for Metals*, 1969, 1-16.

68. "Data on World Wide Metals and Alloys, MAR-M Alloy 509.", *Engineering Alloys Digest*, 1967.

69. Reuchet J and Remy L, "High Temperature Low-Cycle Fatigue of MAR-M 509 Superalloy: I. The Influence of Temperature on the Low-Cycle Fatigue Behavior From 20 to 1100 deg C", *Materials Science and Engineering*, **58** 1983, 19-32.

70. Reuchet J and Remy L, "High-Temperature Low-Cycle Fatigue of MAR-M 509 Superalloy: II. The Influence of Oxidation at High Temperatures", *Materials Science and Engineering.*, **58** 1983, 33-42.

71. Czech N, Juez-Lorenzo M, Kolarik V and Stamm W, "Influence of the surface roughness on the oxide scale formation on MCrAlY coatings studied in situ by high temperature X-ray diffraction", *Surface and Coatings Technology*, **108-109** 1998, 36-42.

72. Rehfeldt T, Schumacher G, Vassen R and Wahi R P, "Order-disorder transformation in a NiCoCrAlY bond coat alloy at high temperature", *Scripta Materialia*, **43** 2000, 963-968.

73. Hasegawa M and Kagawa Y, "Microstructural and Mechanical Properties Changes of a NiCoCrAlY Bond Coat with Heat Exposure Time in Air Plasma-Sprayed Y_2O_3-ZrO_2 TBC Systems", *International Journal of Applied Ceramic Technology*, **3** 2006, 293-301.

74. Eskner M, "Mechanical Behaviour of Gas Turbine Coatings", Doctoral Thesis, Royal Institute of Technology, Sweden, 2004.

75. Fox P and Tatlock G J, "Effect of tantalum additions on oxidation of overlay coated superalloys", *Materials Science and Technology*, **5** 1989, 816-827.

76. Frances M, Vilasi M, Mansour-Gabr M, Steinmetz J and Steinmetz P, "Etude de l'Oxydation a 850°C de l'Alliage Ni-Co-Cr-Al(-Y)-Ta Coule et Projete au Chalumeau Plasma sous Pression Reduite", *Materials Science and Engineering*, **88** 1987, 89-96.

77. Di Martino I, "Microstructure Modelling of Coated Single Crystal Ni-Based Superalloys", PhD Thesis, Loughborough University, UK, 2004.

78. Vaughan D, "Energy Dispersive X-ray Microanalysis, An Introduction", Kevex, 1983.

79. Bhadeshia H K D H, "Worked examples in the Geometry of Crystals", Institute of Materials, London, 1987.

80. Zhao J-C and Henry M F, "CALPHAD - Is it Ready for Superalloys", *Advanced Engineering Materials*, **4** 2002, 501-507.

81. Ahn C C and Krivanek O L, "EELS Atlas: A Reference Guide of Electron Energy Loss Spectra Covering all Stable Elements", 1983.

82. Lukas H L, Weiss J and Henig E-T, "Strategies for the calculation of phase diagrams", *Calphad*, **6(3)** 1982, 229-251.

83. Kattner U R, Boettinger W J and Coriell S R, "Application of Lukas' phase diagram programs to solidification calculations of multicomponent alloys", *Zeitschrift fur Metallkunde*, **87** 1996, 522-528.

84. Biss V, "Phase Analysis of Standard and Mo-Modified MAR-M509", *Analysis Instrumentation:* Proceedings of *The Annual ISA Analysis Instrumentation Symposium*, **3** 1975, 249-264.

85. Cullity B D, "Elements of X-Ray diffraction", Second Edition, Addison Welsley, 1978.

86. Szala J, Szczotok A, Richter J, Cwajna J and Maciejny A, "Selection of methods for etching carbides in MAR-M509 cobalt-base superalloy and acquisition of their images", *Materials Characterization*, **56** 2006, 325-335.

87. Baufeld B, Bartsch M, Broz, P and Schmucker M, "Microstructural changes as postmortem temperature indicator in Ni-Co-Cr-Al-Y oxidation protection coatings", *Materials Science and Engineering A*, **384** 2004, 162-171.

88. Ogden S L and Thomson R C, "To be submitted to *Scripta Materialia*", 2007,

89. Wells J J and Williamson J, "Characterisation of Coatings on a Ni-Based Superalloy Using Optical and scanning Electron Microscopy", A report prepared for Innogy, 2000.